The Pennsylvania State University

The Graduate School

Department of Astronomy and Astrophysics

X-RAY FLARES IN GAMMA-RAY BURSTS

A Dissertation in

Astronomy and Astrophysics

by

David C. Morris

Submitted in Partial Fulfillment
of the Requirements
for the Degree of

Doctor of Philosophy

May 2008

The dissertation of David C. Morris was reviewed and approved* by the following:

David N. Burrows
Senior Scientist and Professor of Astronomy and Astrophysics
Thesis Adviser
Chair of Committee

Derek B. Fox
Assistant Professor of Astronomy and Astrophysics

Robert G. Melton
Professor of Aerospace Engineering

Peter Meszaros
Eberly Chair Professor of Astronomy and Astrophysics

John A. Nousek
Professor of Astronomy and Astrophysics

Larry W. Ramsey
Professor of Astronomy and Astrophysics
Head of the Department of Astronomy and Astrophysics

*Signatures are on file with the Graduate School.

Abstract

Data from the Swift mission have now shown that flares are a common component of Gamma-Ray Burst afterglows, appearing in roughly 50% of GRBs to which Swift slews promptly and in all phases of GRBs. Much has been learned from analysis of individual flares and from the recent first GRB flare surveys (Falcone et al. (2007); Chincarini et al. (2007)) which have focused primarily on properties of the X-ray emission from flares. The broadband spectral properties of flares, however, particularly at UV and optical wavelengths, have yet to be systematically studied. In this thesis, I discuss results from a multiwavelength survey of bright X-ray selected flares seen in Swift GRBs. Using simultaneous data from the UVOT, XRT and BAT, I have produced SEDs of flares from 0.002 keV to 150 keV and fit them using several different spectral models. My results show that a simple absorbed powerlaw is unable to fit flare spectra in the 0.002 keV to 150 keV energy range due, in large part, to a very low UV/X-ray emission ratio. I furthermore investigate the applicability to the data of several models for GRB flare production from the literature. I find that the internal shock model of flare production is the most likely model to explain any given flare, but that no single model is able to explain the complete taxonomy of GRB X-ray flares. I determine the approximate fraction of flares which are explained by each mechanism. I also use the flares in my sample to investigate the bulk Lorentz factor of GRB flares and to compare it to the bulk Lorentz factor of the prompt GRB emission. I find a likely range for the Lorentz factor of flares of $10 < \Gamma < 30$, significantly lower than the canonical value for the prompt emission of $\Gamma < 300$. Finally, I also investigate a discovered trend between the amount of flaring activity in GRBs and redshift.

Table of Contents

List of Tables

List of Figures

Acknowledgments

I owe thanks to many for making this work possible. For my parents, who told me continually that I could do whatever I wanted but may often have regretted those words as I frustrated them by repeatedly changing course, thank you for supporting me throughout my indirect path to this point. Without the work ethic I was taught as a child, I would not be here. For my thesis adviser, Dave Burrows, who took me on as a first year graduate student and immediately immersed me in research on the ground-breaking *Swift* mission which would lead to this dissertation work, thank you for granting me the latitude to find my thesis topic and the freedom to explore that topic fully while keeping me from straying too far afield. For the many members of the *Swift* collaboration, without whose hard work and dedication the *Swift* mission would not be the success that it is, and without whom my work, as well as that of many others, would never have been possible, I thank you all. For my many friends in State College and elsewhere who supported me with discussion, distraction, encouragement, companionship and, of course, a great deal of beer, I thank you all for your friendship. Finally, for my remarkable wife Cate, with whom a conversation over lunch a day after we met would lead us to State College 2 years later, I owe this all to you. Without your encouragement I would not have begun, and without your constant, unwavering and often superhuman support I could not have finished this. Thank you and I love you.

Chapter 1

Introduction

The Gamma-Ray Burst (GRB) phenomenon has been one of great interest and cosmological significance since its unanticipated discovery more than 35 years ago (Klebesadel et al. 1973; Strong et al. 1974) by the US Advanced Research Projects Agency Vela program, a series of gamma-ray sensitive satellite-borne instruments designed to enforce the Limited Nuclear Test Ban Treaty of 1963 by monitoring for the characteristic burst of gamma-rays which accompanies a (terrestrially based) nuclear explosion. It is in many ways remarkable that several of the signature characteristics which we know today to be hallmarks of the GRB phenomenon were noted from observations reported from this first generation of non-purpose designed GRB detectors, including:

- GRBs last from a few to a few 10s of seconds
- GRBs show a pulsed sub-structure
- later pulses tend to be softer than earlier ones
- peak energy νF_ν of the GRB spectrum is few 10^2 keV

GRBs were found to be non-repeating (excluding the Soft Gamma-Ray repeaters which would be a later discovered subclass of the phenomenon) and appeared at seemingly random locations in the sky, making the study of these sources difficult with the instrumentation of the day. Limited by what little data could be collected on this new class of object during the few seconds of observations made by the then current gamma-ray detectors, a host of potential physical models was proposed to explain the new transients ranging from such exotic models as Compton upscattering of CMB photons by spallation off cometary dust grains in the outer Solar System to the collision of binary neutron stars at cosmological distances (Meszaros & Rees 1992).

With the launch of the Compton Gamma-ray Observatory (CGRO) in 1991 with its suite of instruments designed specifically for the study of GRBs, including the 8 Burst and Transient Source Experiment (BATSE) detectors, the Energetic Gamma-ray Experiment Telescope (EGRET), and the Imaging Compton Telescope (COMPTEL), a new era in the study of GRBs was ushered in. CGRO was able to show definitively that the spatial distribution of GRBs was isotropic, but at the same time it showed that the log-N log-S distribution of the sources did not follow the characteristic -3/2 powerlaw slope expected of a complete and homogeneous isotropic distribution. The isotropic distribution suggested that GRBs were located either in an extended galactic halo or beyond (though they may also have been very local and intrinsically weak), while the flatter than expected slope of the log-N log-S distribution, showing fewer sources at the faint end of the distribution than expected, hinted that GRBs may have cosmological origins. The energy requirement of such a cosmological origin, however, was an enormous 10^{50}-10^{52} ergs, which argued in favor of a more local source population. With positional accuracy of only a few degrees, however, the BATSE experiment did not allow the rapid optical follow-up measurements which would be necessary to locate the predicted transient optical afterglow which could be used to measure the redshift of the source and thereby resolve the distance debate. Nevertheless, CGRO resulted in several significant conclusions about GRBs, including:

- GRBs are isotropically distributed on the sky but are not homogeneously distributed

- GRBs are divided in two classes, short-hard and long-soft, with a rough temporal break at $t \sim t_0 + 2$ s (Kouveliotou et al. 1993)

- GRBs show a hard to soft spectral evolution with peak energy in νF_ν at ~300 keV (Borgonovo & Ryde 2001)

- GRB spectra are well characterized by an approximate doubly broken powerlaw (Band et al. 1993)

- GRBs are capable of producing extremely energetic photons (>GeV), possibly as long as hours after the burst onset (Hurley et al. 1994)

This era also saw the development of the GRB fireball model (Meszaros & Rees 1992, 1993; Meszaros et al. 1994) as one of the leading candidates for the physical underpinning of the phenomenon. The fireball model proposes a central engine, likely a black hole surrounded by an accretion disk which ejects a highly relativistic jet into the surrounding circumstellar material. The model invokes collisions of separately ejected shells of material with varying Lorentz factors, Γ, to produce the promptly observed GRB gamma-ray emission through the synchrotron cooling of shocked electrons. A prediction of the model, beyond the capabilities of the operating instrumentation at the time, was that a secondary emission component should be produced. As the emission jet plows into the surrounding medium, it would sweep up the ambient material, gradually slowing the ejected jet and producing a blast wave shock front in the ambient medium. Shocked electrons in this external shock would emit synchrotron radiation as well, albeit at characteristically lower frequencies than the prompt emission due to the lower bulk Lorentz factor of the shocked electrons in the external shock as compared to those in the internal shocks which produce the prompt emission. This secondary, "afterglow" emission component was then expected to cool adiabatically, leading to emission which cascades to lower frequencies as the burst progresses, but possibly remaining visible for days or weeks at optical and radio wavelengths.

While CGRO continued to detect GRBs until May 26, 2000, it would be the Italian-Dutch Beppo-SAX satellite (Boella et al. 1997) which would provide the answer to the GRB distance debate and usher in yet another new era of GRB study. Beppo-SAX, launched on April 30, 1996, was a multi-instrument X-ray observatory with sensitivity (from various instruments) in the 0.1-600 keV energy range. The key capability of Beppo-SAX with regard to GRB science was the combination of a gamma-ray burst monitor (GRBM) with a pair of diametrically opposed X-ray imaging cameras with a large field of view, the Wide Field Cameras (WFC), and a set of four higher resolution X-ray telescopes, the Low and Medium Energy Concentrator Spectrometers (LECS and MECS). The GRBM was sensitive in the 60-600 keV energy range with approximately full sky coverage. The WFCs were sensitive in the 2-30 keV energy range with 5 arcminute positional accuracy and 800 square degrees of spatial coverage (Frontera et al. 1997; Jager et al. 1997). The LECS and MECS were sensitive in the 0.1-10 and 1.0-10 keV energy ranges respectively with positional accuracy of $\sim$1.5 arcminutes and a field of view of ∼1 square degree. When a GRB was detected by the GRBM, data from the WFCs were analyzed on the ground to determine whether a point source could be identified. If a point source was identified, the 5 arcminute accuracy from the WFC was still not sufficiently precise for large ground based telescopes (with their typically small fields of view) to successfully locate the predicted GRB afterglow before it faded below the sensitivity threshold of the instrument. Upon identification of a new X-ray point source in the WFC, a spacecraft maneuver would be commanded from the ground to repoint the spacecraft so that the LECS and MECS could image a region covering the GRB position error circle as derived from the WFC data. If a new point source could be identified in the LECS or MECS data, typically after a delay of a ∼ 10 hours, the presence of the predicted GRB afterglow emission would immediately be confirmed (supporting the fireball model) and the ∼ 1 arcminute accuracy of the LECS and MECS position determination would be accurate enough to allow searches for an optical afterglow to be performed by ground-based telescopes, potentially resulting in a redshift measurement of the source.

This sequence of events led to the first ever detected GRB afterglow detection on February 28, 1997. Detections in the X-ray (Costa et al. 1997) and optical (van Paradijs et al. 1997) confirmed the theoretically predicted presence of afterglow emission and followup observations by the Hubble Space Telescope showed evidence of a host galaxy associated with the afterglow (Sahu et al. 1997), confirming the extragalactic origin of GRBs. While the actual redshift determination of GRB970228 would be several years away (Bloom et al. 2001a) due to complications with the spectroscopy measurements, a second GRB localization by Beppo-Sax just over 2 months later led to a confirmed spectroscopic redshift for GRB970508 of z ≥ 0.835 (Metzger et al. 1997), finally confirming the cosmological nature of at least some and, by reduction, likely all GRBs (though later observations would show that a fraction of short GRBs may be due to nearby Soft Gamma-Ray Repeaters, this was not realized at the time).

During the following 5 years, approximately 250 more GRBs were discovered through a combination of triggers by Beppo-SAX, the Rossi X-ray Timing Experiment (RXTE), the Interplanetary Network (IPN - a network of gamma-ray detecting satellites, each with little or no spatial resolution but which can be used together to trigger on and triangulate a moderate resolution position for GRBs), the High Energy Transient Explorer (HETE-2) and the International Gamma-ray Astrophysics Laboratory (INTEGRAL). Among these, more than 50 X-ray afterglows and more than 50 optical afterglows were identified (some but not all having both an X-ray and optical afterglow) with typical delays of hours. Detailed analysis of these bursts helped to confirm many of the predictions and refine the physical underpinnings of the fireball model of GRBs. Among the features observed in GRBs during this epoch were: *i)* optical flashes from the reverse shock as the blastwave reaches a critical point of deceleration (Mészáros & Rees 1999; Sari & Piran 1999a,b) supporting the presence of a moderately dense ($n \sim cm^{-3}$) circumburst medium, *ii)* achromatic breaks in the observed lightcurves (Berger et al. 2000; Jensen et al. 2001), supporting the relativistically jetted nature of the initial GRB ejecta and thereby greatly easing the energy constraints relative to isotropic emission models and *iii)* the identification of GRBs with counterpart supernovae (Kulkarni et al.

1998), supporting the association of (long) GRBs with core collapse events, termed Hypernovae. During this period, discussion of the mechanism and site of GRB emission intensified.

We here define four common emission mechanism and location concepts which will be often repeated throughout this thesis; the forward shock, the reverse shock, internal shocks and external shocks. The forward shock (FS) is the shock front set up by the relativistic outflow of the prompt GRB emission propagating into the circumburst medium. The FS is generally believed to be responsible for the long-lived afterglow of GRBs and the cascading nature of the associated emission frequency due to the progressive slowing of the FS. The reverse shock (RS) is a front that is propagating backwards (toward the central engine) with respect to the ejecta. It is created when the blast wave rapidly decelerated by interaction with the circumburst medium at the deceleration radius (see, e.g., Mészáros & Rees (1999); Sari & Piran (1999a)). The RS has a characteristically lower Lorentz factor than the FS and lasts as long as it takes the RS front to cross the width of the ejecta shell associated with the FS. Internal shocks (IS) are created by collisions between highly relativistic shells of ejecta, generally believed to be responsible for the prompt GRB emission and possibly (as will be argued later in this thesis) also for the majority of GRB X-ray flares. ISs occur at smaller radii from the central engine than the FS does (typically 10^{13}-10^{15} cm) and last only as long as it takes for the shock front to cross the width of the ejecta shells. Due to the high Lorentz factors and relatively narrow widths of the shells involved, IS are preferred as an explanation for the rapid, bright increase in flux seen in many GRB X-ray flares. External shocks (ES) are created by collisions between a relativistic shell of ejecta and a stationary circumburst medium or clump in the circumburst medium. The FS and RS are both components of the ES, the former propagating into the unshocked circumburst medium and the latter propagating into the unshocked jet. The ES mechanism is generally less preferred to explain GRB X-ray flares due to the longer interaction times (slower rise and decay times) implied by interaction with a relatively diffuse and stationary medium and also by time-of-flight delays due to the large size of the shock front (though see Dermer (2007)).

The afterglow era of GRBs had clearly brought a revolution in understanding of the phenomenon, yet a significant time period in the evolution of GRBs remained effectively unexplored. More accurately, a significant region in the luminosity-time phase space of GRBs remained unexplored. Due to the need for manual analysis of initial wide-field, low-sensitivity X-ray imaging data to identify an initial point source in the primary GRB trigger image and the subsequent need to manually command a spacecraft to repoint itself to observe with narrow-field, high sensitivity detectors, an unassailable barrier existed against the detection of the, generally faint, GRB afterglow signature between the first few minutes of a GRB and several hours later. Motivated by the promise of catching afterglows in their earliest stages, when the emission levels would be orders of magnitude higher than what had been observed to date, a new satellite mission concept was formed in which all human intervention in the GRB follow-up procedure would be removed.

The Swift mission consists of three instruments mounted on an autonomously slewing spacecraft platform, capable of slewing through 180 degrees in approximately 200 seconds (Gehrels et al. 2004). The three instruments include the Burst Alert Telescope (BAT), a highly sensitive coded aperture mask detector with energy sensitivity from 15-350 keV and capable of providing GRB positions accurate to ~ 3 arcminutes from anywhere within its ~ 1.5 sr field of view (FOV) within seconds of the burst trigger (Barthelmy et al. 2005a). Upon a GRB trigger, onboard screening is performed to determine whether the trigger is due to a known or new source. In the event of a new source and that the location of the trigger is in a safe viewing orientation for all instruments on-board, the satellite autonomously repositions itself, generally in 60-120 s, to observe with its pair of narrow field instruments. The X-ray telescope (XRT) is sensitive to energies from 0.2 to 10 keV with a FOV of $\sim$ 20x20 arcmin and is capable of automatically identifying and transmitting the position of a bright X-ray source to ground based observers. In the presence of a sufficiently bright source, positional accuracy of a few arcseconds is achieved (Burrows et al. 2005a). The third instrument on-board is the UV/Optical telescope, a 30 cm telescope with a detector which is sensitive from 170-650 nm, selectable through the use of a filterwheel. The combination of the highly sensitive BAT detector (5 times more sensitive than BATSE) and the rapid followup of observations of the XRT and UVOT promised to unveil a phase of GRB evolution never before seen and it would do so for ~ 100 bursts per year.

Swift was launched on November 20, 2004. Following turn-on and activation procedures, *Swift* performed its first automated slew to a GRB on January 17th, 2005, taking sensitive XRT observations of GRB050117A just 193 s after the burst trigger. While it was not recognized initially, due to sparse data collection (due, in turn, to the close proximity of *Swift* to the South Atlantic Anomaly during the burst observations), this very first GRB observed using *Swift's* automated observing sequence revealed a lightcurve unlike anything which had been observed before (Hill et al. 2006), but which would shortly become recognized as the new universal shape of GRB afterglows in the *Swift* era (see Nousek et al. (2006)). Two phases of the GRB afterglow not seen before were captured in the observation of GRB050117 and *Swift's* prompt observations of other GRBs to follow. The rapid decay of the gamma-ray and X-ray emission seen typically at $T_0 + \sim 100$ s has been taken as evidence of the geometric curvature of the shock front which produces the prompt GRB emission. As the prompt emission, produced through internal shocks, ends, emission from the shock front at small angles with respect to the observer is seen to end first, while there is a delay in arrival of photons from regions of the shock front at larger angles with respect to the observer, which have to travel a longer path. The steepness of this decay phase is set purely by the spectrum of the shocked electrons themselves, having the characteristic decay slope $\alpha = 2 + \beta$ where β is the spectral index of a powerlaw spectrum fit to the burst decaying emission. This steep decay phase suggests that the production of prompt emission ends abruptly, supporting IS as the likely emission mechanism rather than ES which are expected to decay more slowly. The duration of this rapid decay phase may also be used as a constraint on the beaming angle of the jetted ejecta (if the radius of emission is also known). The flat phase, seen typically at times from $T_0 + \sim 1000$s to $T_0 + \sim 10000$s, is generally interpreted as a period of energy injection to the forward shock blast wave (Zhang et al. 2006). The flat phase generally breaks to the (pre-*Swift*) expected normal GRB decay at $T_0 + \sim 10000$ s and is possibly followed at later times by a jet break as was discussed previously in reference to pre-*Swift* observations.

A third, as yet unobserved, phase of GRB afterglows which would be initially revealed with the *Swift* observations of GRB050406 (Romano et al. 2006) and made clear to be a common component of GRBs by several observations to follow (Falcone et al. 2006; Pagani et al. 2006; Morris et al. 2007) is X-ray flares. Beginning with the first clear detection in GRB50406, these often rapid rises in X-ray flux followed by a similarly rapid decay, seen temporally separated from the end of the gamma-ray prompt emission, have become recognized as a common component of GRB X-ray afterglows in the *Swift* era, being observed in some $\sim$50% of GRBs to which *Swift* slews promptly to begin observing with the NFI within a few hundred seconds (Burrows & The XRT Team 2006).

Occasional observations suggestive of late (ie, temporally separated from the prompt emission phase) flaring activity had been observed prior to the *Swift* mission (Piro et al. 1998, 2005; Galli & Piro 2006), but it is with the vastly improved X-ray sensitivity provided by the *Swift* XRT at times between T_0+100 to T_0+10000 s over what was available previously (an improvement of $\sim 10^3 - 10^4$ over the BeppoSAX WFC) that these late, bright x-ray flares were recognized as a common characteristic of GRB afterglows. Flares seen in BeppoSAX observations have been interpreted as either 1) continued energy injection events into the synchrotron emission associated with the forward shock deceleration in the context of a model in which both the prompt gamma-ray emission and the afterglow are due to the external shock scenario (Piro et al. 1998) or 2) the signature of the onset of synchrotron emission associated with the forward shock deceleration in the context of a model where the gamma-ray prompt emission is produced through internal shocks and the afterglow component of the emission is observed to begin later (Galli & Piro 2006), at a time after the fireball forward shock has swept up an amount of circumburst mass approximately equal to the mass of the expanding ejected shell itself. Evidence from BeppoSAX in favor of the former interpretation was that 1) the afterglow appeared to fit a single powerlaw decay from the end of the prompt emission to the later (2×10^4 s later) observations of the afterglow, taken as indication that the afterglow was following pure synchrotron cooling from the moment of the initial energy injection of the prompt phase and 2) there was a second x-ray outburst seen above this afterglow powerlaw decay at $\sim 10^5$ s, containing a smaller but significant amount of energy with respect to the initial burst itself, taken as indication of a second, smaller episode of synchrotron emission occurring at the same site (namely the forward shock deceleration site) as the prompt emission itself. In the latter interpretation, the prompt emission is attributed to the internal shock mechanism and evidence that the flare, seen at earlier time ($\sim 10^3$ s), is associated with the onset of the external shock generated afterglow comes from temporal fits which appear to smoothly connect the flare to the later afterglow data (shifting T_0 to the start time of the flare) and a spectrum of the flare seen softer than the prompt emission and more comparable to the later afterglow spectrum.

In earlier observations from the EGRET detector aboard CGRO, one instance of a single GeV photon observed at T_0+4500 s was observed (Hurley et al. 1994). While not immediately interpreted as evidence of flaring activity separate from the prompt burst emission, recent theoretical work examining the potential contribution from the synchrotron self-Compton process during both the prompt GRB phase and later episodes of X-ray flaring suggest that this event may have been due to first or second order inverse Compton scattering of photons from internal shocks, scattered by interactions with shocked electrons on passage through the forward shock (Wang et al. 2006). This observation has spurred much study of the extreme high energy emission potential of GRBs and is a topic of great current interest due to the impending launch of the next generation NASA gamma-ray observatory, GLAST, in late 2008.

Since being recognized as a common component of GRB afterglows in the *Swift* era, much work, both observational and theoretical, has followed on the subject of X-ray flares. Early observational work revealed the first recognized flare in GRB050406 (Romano et al. 2006), the steepness of the rise and decay of which staged the argument for flares as a product of the internal shock mechanism. Later detections would reveal some of the extremes of the *Swift* observational parameter space occupied by flares and thereby suggest constraints on the possible production mechanism at work. Observations of the giant flare in GRB050502B (Falcone et al. 2006) showed that X-ray flares may contain as much energy as the total prompt emission itself while also showing evidence for a flare or outburst at much later times (apparently similar to such outbursts as seen by Piro et al in GRB970508), potentially due to the interaction of the outward-moving, combined flare shell with the forward shock of the GRB fireball. Observations of GRB050713A (Morris et al. (2007), Chapter 3) showed the first simultaneous observations of flares in both the XRT and BAT energy range, showing that flares are better fit by spectral models with curvature or a spectral break (which is usually used to fit the prompt emission of GRBs) than with a simple powerlaw fit (which is usually used to fit the GRB afterglow component). We will discuss these observations in greater detail in Chapter 3. Observations of GRB050724 (Campana et al. 2006) showed the first conclusive evidence of X-ray flaring in a short hard burst (though see also Fox et al. (2005)), indicating that the flaring mechanism needs to be capable of operating in short as well as long bursts (or that there are, at least, mechanisms capable of operating in long GRBs and others capable of operating in short GRBs). Observations of GRB050904 (Tagliaferri et al. 2005; Cusumano et al. 2007), the GRB with the highest redshift measured to date at z=6.29, showed multiple bright flares extending to extremely late times ($3\text{x}10^4$ s, $\sim 4\text{x}10^3$ s in the rest frame), indicating the need for the X-ray flare mechanism to produce emission at times very far separated from the end of the putative prompt gamma-ray emission phase.

Theorists have been no less active in their efforts to unravel the various, sometimes conflicting, observations of X-ray flares onto a consistent physical framework. While the general physics of the evolution of the GRB fireball had been worked out in detail well before the discovery of X-ray flares (Meszaros & Rees 1992; Sari et al. 1996; Panaitescu & Kumar 2000), the identification of flares at late times prompted the reconsideration of the details of the model as it applied to producing bright X-ray emission separate from the prompt GRB phase. Even prior to the first *Swift* observations, Kobayashi et al. (2004) had discussed the potential of an X-ray flare due to synchrotron self Compton emission of optical/IR photons produced at the time of the reverse shock crossing (see also Kobayashi et al. (2007)). More recently, many authors have proposed the production of late time X-ray flares in GRBs through a variety of physical models including, magnetic support of infalling matter and subsequent magnetic instabilities in the accretion disk (Proga & Zhang 2006), external shocks in the interaction of the forward shock with a clumpy external medium (Dermer 2007), external shocks at the onset of the afterglow phase (Piro et al. 2005), internal shocks due to late time central engine activity (Zhang et al. 2006; Burrows et al. 2005b; Fan & Wei 2005) and internal shocks due to late interacting shells of material which were ejected at early times with a distribution of Γ which leads to their interaction at late times (Rees & Meszaros 1998). Each of these models has been applied in detail to the observations of at least a single GRB from either the BeppoSAX or *Swift* observational era and shown to produce agreeable results.

In Chapter 3 of this work, we will present an analysis of GRB050713A, mentioned above, in which we present such a case of a single flaring GRB which we will discuss in the context of one of these theoretical models, namely the late internal shock model. As the first GRB that presented well-sampled, overlapping XRT and BAT (as well as ground based optical) data and also as the first GRB to portray a series of (three) bright flares suitable to be tested against higher order (than a simple powerlaw) spectral models (though see also Pagani et al. (2006)), discussion of this burst (Chapter 3) will serve as an introduction to the characteristics of flares which we will investigate in greater detail in the later chapters of this thesis.

It remains to be shown, however, whether all of the processes cited above are required to explain the catalog of X-ray flares observed by *Swift* to date, or whether a subset of the models is sufficient, and if so, what subset is required and in what proportions. A pair of recent, complementary GRB X-ray flare survey papers (Chincarini et al. (2007); Falcone et al. (2007); see also Chapter 4) have made an initial, and at the time of this writing the most comprehensive, attempt to examine a large set of GRB X-ray flares both temporally and spectrally using the 0.3-10 keV XRT dataset, with the goal of identifying which mechanism(s) are best supported by the observational data. We detail the general methodology and some specifically designed software tools developed to perform the spectral survey portion of this work, as well as a refinement of the method to be considered later, in Chapter 2. In Chapter 4, we will present the main results of the spectral analysis from Falcone et al. (2007) and discuss the temporal results from the work of Chincarini et al where appropriate. We will find, at the conclusion of Chapter 4, that some useful constraints on the models can be drawn from this work, but that uncertainty will remain with regard to how many of the theoretically suggested models are required to explain the *Swift* results seen to date. We will also note, where appropriate, the work of other flare surveys, related to but different from that which will be presented here (Butler & Kocevski (2007); Kocevski et al. (2007) among others). This will lead us to a refined flares analysis, presented in Chapter 5, using broadband data from all three instruments aboard *Swift* to better constrain the parameters characterizing X-ray flares. In Chapter 6, we will use the aggregate of the results obtained in the studies of Chapters 4 and 5 to argue against a single mechanism as sufficient to produce all GRB X-ray flares observed by *Swift*. We will, furthermore, present conclusions regarding the approximate relative fractions of *Swift* X-ray flares explainable by each mechanism and discuss the requirements thereby imposed on the GRB central engine and circumburst environment.

Finally, in the course of this work, an intriguing relationship between the GRB redshift and the relative extent of X-ray flaring behavior has been discovered. As this discussion is somewhat distinct from the main focus of this thesis but is nevertheless interesting, we include it here as Appendix C.

Chapter 2

Methods

In any study, but particularly one which will distill as large an amount of raw data as this one will, it is important to develop and utilize a consistent method of data analysis which can be applied to each component dataset of the overall work. The goal of such a method should be to minimize the biases introduced to the work by the analysis techniques themselves. Insomuch as different datasets cannot necessarily be analyzed in completely identical fashion, it is furthermore important to recognize and quantify the biases introduced to the final data products resultant from the analysis method so that these biases can later be considered in relation to the analysis results.

In this section we detail several extensive coding efforts designed to produce as consistent a set of level 3 data products as possible from which to begin our analysis. The level 3 data products produced are lightcurves from each of the 3 Swift instruments and spectral fits to the broadband (UVOT-XRT-BAT) spectra of each flare that we analyze.

2.1 Data Analysis

All data are processed to level 1 products via the standard processing at the Swift Data Center (SDC) and are further processed to level 2 products using the standard Swift Software tools version 2.6 (build 19) which are included as part of HEADAS version 6.2 and are available on the SDC public website.

2.1.1 BAT

BAT data processing begins with level 1 event lists from the standard SDC product download and mask weighting is applied via the task *batmaskwtevt* using the spacecraft attitude file, detector quality map file, and ray tracing file found in the standard SDC products. The source position applied is determined from the XRT two-dimensional image data and default corrections are applied for flat fielding, exposure correction, partial coding correction and the mask weighting technique correction. The task *batbinevt* is then used to produce spectral files appropriate for analysis using XSPEC. Start and stop times for input to *batbinevt* are identical to the start and stop times of the XRT and UVOT data for each segment analyzed. The standard detector quality map is applied and spectral files are produced in seven energy bins, 15-20, 20-25, 25-35, 35-50, 50-75, 75-100 and 100-150 keV. The task *batupdatephakw* is run to update the raytracing header keywords in the resulting spectral files, the standard BAT spectral systematic error vector from the CALDB is applied by running the *batphasyserr* task and BAT detector response matrix files are generated for each spectral file using the *batdrmgen* task.

In addition to this customized BAT processing of the data associated with individual flares, the BAT standard data products produced by the *batgrbproduct* task were collected to be used in parts of this work (see Appendix C: BAT properties of Flaring Bursts). The *batgrbproduct* script is a specialized processing script written by the BAT instrument team which links individual BAT processing tasks together to produce a standardized set of data products describing the BAT response to each burst. These standard products include the T90 and T50 burst duration in the 15keV-350keV energy band, 1-s peak and time averaged flux measurements and 1-s peak and time averaged spectral fits to a simple powerlaw model, a cutoff powerlaw model and a Band function.

2.1.2 XRT

XRT data processing begins with level 1 event lists from the standard SDC product download. In order to determine start and stop times for the flares and to determine the best data extraction aperture to use for each flare segment, an XRT lightcurve is first produced from the complete XRT data set associated with the burst. Using an automated lightcurve generation program, written in IDL, corrections are applied to the XRT data to account for data lost due to defective pixels on the XRT CCD as defined in the CALDB badpixel files. Corrections are also applied for pileup effects (a more detailed explanation of the pileup phenomenon is included later in this chapter in §2.2.1) at high count rates by excluding events collected in the inner portion of the XRT point spread function (PSF) and scaling up the remaining counts accordingly as specified in Moretti et al. (2005) and through our own spectral curve of growth analysis.

In cases where pile-up is not a concern, XRT spectral files are extracted from a region of 30 pixel radius centered on the source position determined from analysis of the XRT two dimensional image data. In cases in which pile-up is significant, a central region is excluded of radius as designated in Table 2.1 resulting in an extraction annulus with outer radius of 30 pixels and inner radius as in Table 2.1. Spectral files are created using the *grppha* task, grouping a minimum of 20 events per spectral bin so that χ^2 statistics may be used. The task *xrtmkarf* is used to generate ancillary response files and the standard response matrix function (RMF) files are used from the CALDB.

2.1.3 UVOT

UVOT data processing begins with level 1 event lists and images from the standard SDC product download. For each data segment to be analyzed, data are sought in each of the six narrow filters as well as white (unfiltered). The task *uvotimsum* is used to co-add multiple images if more than a single image exists in a single filter during the time segment of interest. The task *uvot2pha* is then used to create a spectral file from either a co-added image file, individual image file or eventlist file. If the data do not form a 3 σ detection, a spectral file is created with a flux level equal to the source level minus the background level (regardless of the significance level of the detection) with appropriately large associated uncertainties. If the background level is higher than the source level (due to random fluctuations), a flux level of zero is entered into the spectral file with the appropriate associated one sigma uncertainty. Background measurements in each filter are determined by following a similar procedure as for the source measurement, but are centered on a hand-selected region away from the source position and free of apparent background source contamination. This procedure is performed for each filter in which data exists during the time segment of interest.

2.2 Lightcurve Generation

The generation of lightcurves from level 1 data products, while straightforward in principle, merits discussion due to: 1) instrumental peculiarities which are not addressed during the level 1 data processing; 2) issues related to signal to noise ratio (S/N) maximization and; 3) data binning issues. All three of these factors can significantly impact the final lightcurve produced.

2.2.1 XRT Lightcurves

The XRT lightcurve generation (XLG) program is written in IDL and controlled by an input parameter file requiring only the most basic information about the burst to be analyzed such as the level 1 fits file names, GRB celestial coordinates, background region celestial coordinates and Swift-BAT trigger time. A high-level flow diagram of the XLG is shown in Figure 2.1.

Given the celestial coordinates of the source and background position, an approximation to the tangent plane projection of each orbit of each level 1 fits file is performed to map celestial coordinates into detector coordinates and events are extracted corresponding to the GRB source and associated background region from each file.

The source counts extracted in each region are not an accurate representation of the true point spread function of the XRT instrument, however, because both individual pixels and entire columns of pixels within the detector are defective, hence unusable for scientific measurements and are therefore never telemetered to the ground from the spacecraft. As a result, any flux measurement made near one or several of these defective pixels will be attenuated by its or their presence. To correct for this effect, a model of the XRT PSF, as defined in the PSF standard calibration file distributed by the Swift Data Center, is created and centered at the position corresponding to the GRB celestial coordinates translated to detector coordinates as just described. Using information from the badpixel extension, which is appended to level 1 fits files output from the Swift XRT pipeline (Swift Data Center standard software), pixel locations in the modeled PSF which are set as 'bad' in the level 1 data products (examined on an orbit-by-orbit basis) are set to a value of 0 in the PSF model. A ratio is then made of the modeled PSF including 'bad' pixels and a modeled PSF without 'bad' pixels. This ratio is stored as a PSF correction factor to be applied to the events extracted from each orbit. Calculation of a correction factor to be applied to the background region is performed in a similar manner except that rather than using the XRT PSF model, a flat distribution of events is assumed. (Note that a PSF correction algorithm has been implemented in the Swift XRT standard processing pipeline as part of the HEASOFT release 6.0.5 on April 26th, 2006. Analysis of the PSF correction performed by the algorithm described here in comparison to the HEASOFT PSF correction shows the two methods to be effectively equivalent. In the interest of maintaining better control over the operation of the processing software, we have processed our data with the HEASOFT PSF correction turned off, relying on the internal PSF correction implemented within our software described here.)

The Swift XRT has two primary modes of operation (Hill et al. 2004) which are employed during burst observations, Photon Counting (PC) mode and Windowed Timing (WT) mode. In WT mode, the entire 600x600 CCD is effectively read out as a single 600 element row by rapidly clocking 10 rows at a time into the readout register, then clocking out the readout register. This method of operation provides only 1 dimensional positional information but yields rapid frame repetitions (2.2 ms frametime), limiting the potential for multiple photons to be recorded within the same pixel during a single frame, an effect known as pile-up in the high energy astronomy community (also known by other terms such as coincidence loss in the optical community). For a readout time of 1 ms, a detector countrate of ∼1000 cts/s will begin to produce a noticeable pile-up effect. In the Photon Counting mode of operation, the central 500x500 pixels of the XRT CCD are exposed for 2.5s and, subsequently, each row is individually clocked into the readout register and then clocked out serially. This mode of operation produces a complete 2 dimensional image of the sky, but is necessarily slow and therefore much more susceptible to pile-up effects than WT mode. Without correcting for the pile-up effect, lightcurves produced with WT and PC mode data would show a discontinuity at transitions between the two readout modes and the overall fluxes measured would, furthermore, be inaccurate. In addition to the different thresholds of susceptibility to pile-up effects, PC and WT modes differ in their ancillary response files, their instrumental and sky background levels and their susceptibility to bad pixels. Because of these differences, the PC and WT mode data are handled separately at the level 1 and level 2 fits file stages and are only combined into a single data product at the level 3 stage when the data are written into count rate tables and lightcurve figures.

For data in each of the two XRT modes of operation (PC and WT), a similar binning algorithm is separately applied to produce a binning solution which is optimized to achieve a lightcurve with high temporal resolution and precision during periods where the flux level is high and to achieve, during periods of low flux, a lightcurve composed of data points which represent enough photons to constitute a significant source detection but which do not unnecessarily span large periods of deadtime (i.e., time when the detector was not observing the source region). Techniques such as Bayesian blocking were considered for use in the binning algorithm, but no existing algorithm was found which satisfactorily accommodates both the extremely large dynamic range in flux level (ranging from 10^3 counts/s to 10^{-4} counts/s) and the extremely irregular observational duty cycle (approximately 30 minute observations are made every 90 minutes during the first 24 hours after the burst trigger, but the observation frequency then becomes rather unpredictable, due to complicated scheduling priorities, often leading to sparse observational sampling or large temporal gaps in the observation pattern, or both). To produce the desired precision and temporal resolution, a straightforward, rule-based binning algorithm was developed to divide the lightcurves into regions of significantly different flux level and to avoid including large amounts of deadtime within lightcurve datapoints.

The binning algorithm described is operated on the input events list to produce a table of bin start and stop times and associated count rates and errors. At this stage, however, the count rates and errors have been derived from source counts extracted from a uniform extraction region of 20 pixels in radius and are only preliminary estimates of the actual source flux level since we have not yet accounted for pile-up effects nor have we attempted to optimize the source extraction region to maximize the signal to noise ratio in the aperture. Using the initial count rates associated with each time bin region from the first pass of the binning algorithm, the XLG consults two tables, one which specifies, as a function of source count rate, the radius of an inner annular region within which pile-up effects will contaminate the data and another which specifies, as a function of source count rate, the source extraction aperture which maximizes the source signal to noise ratio. Each of these tables is discretized into 5-10 levels as shown in Table 2.1.

Table 2.1. Pileup parameters

XRT cts/s	exclusion radius (pixels)	correction factor
0.5	1.	1.25
2.0	3.	1.76
5.0	5.	2.66
10.	7.	3.69
25.	13.	7.20
70.	15.	8.46

The pile-up correction table is derived from a calibration publication describing pile-up analysis performed on the XRT as referenced previously (§2.1.2). It should be noted that the table used is specifically related to a source with a prescribed spectrum (a powerlaw with photon index of 2) but the true pile-up correction values for any given source will actually be a function of the spectrum of the source as well as the count rate. However, since we will not always be able to collect enough photons to produce a high-precision spectrum, and furthermore since we cannot be certain that the spectrum of the GRB we wish to analyze will remain constant during the duration (or any given period) of the burst, it is impractical and will often be impossible to perform spectral analysis in support of pile-up corrections to be made throughout each GRB analyzed. Furthermore, differences in the pile-up correction factors produced for different spectral types are small, so the XLG refers throughout to a single pile-up correction factors table taken from the reference noted previously. The signal to noise optimization table is derived by simulating a point source in the XRT at several threshold count rates, summing it with a canonical XRT sky background level, and maximizing the resulting signal to noise ratio.

Based on the preliminary count rates and the information in the tables just described, a new extraction annulus is then defined for each preliminary data bin, with an inner radius ranging from 0 to 15 pixels and an outer radius ranging from 15 to 30 pixels, along with the appropriate correction factors to account for the excluded portion of the PSF in each case. Event extraction is performed completely anew using these new source extraction annuli and the binning algorithm is run a second time. Bin start and stop times, rates and errors are recalculated, applying the noted PSF correction factors as appropriate. In principle, the binning solution could be further improved by performing repeated iterations of the pile-up and signal to noise optimization loop, but in practice the first iteration corrects the greatest part of the inaccuracy and further iterations are unnecessary.

2.2.2 BAT and UVOT Lightcurve Generation

In addition to XRT lightcurves, both BAT and UVOT lightcurves are generated for each burst. In the case of the BAT lightcurves, they will be used to measure the relative duration of the BAT prompt emission (Appendix C) as well as the relative flux and fluence level of the BAT prompt emission. The UVOT lightcurves are used both as a 'sanity check', to insure that any possible coincident flaring behavior in the UVOT is not overlooked as well as to insure that statistical fluctuations in the UVOT data are not erroneously identified as flares. The BAT lightcurves are created by summing the 5 BAT channel lightcurve files produced by the *batgrbproduct* task and then performing a smoothing of the 64ms data with a 1-s square filter. The UVOT lightcurves are produced

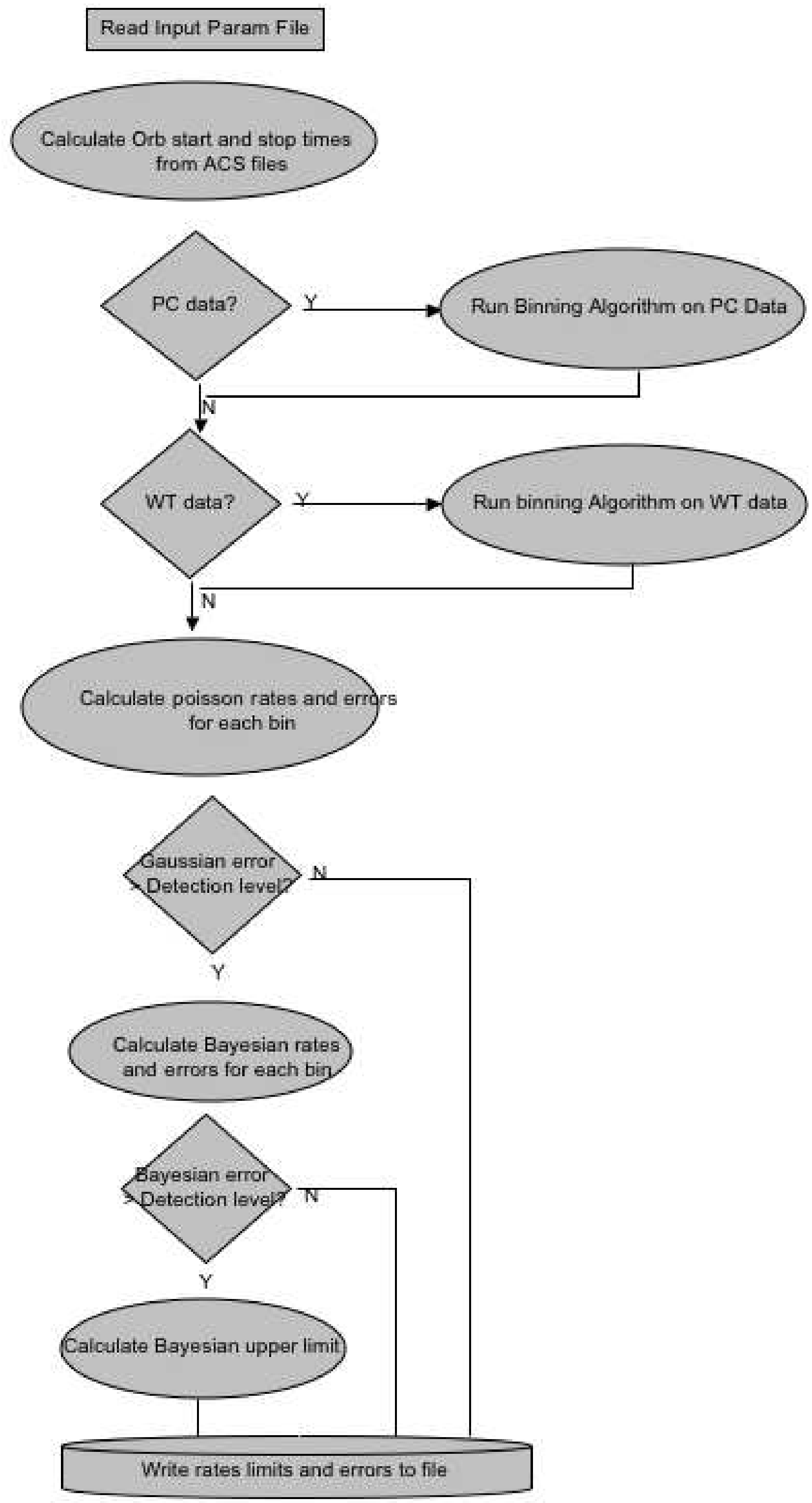

Fig. 2.1 X-ray lightcurve Processing Flowchart. All flares in the samples to be discussed in Chapters 4 and 5 are processed using the software outlined in this flowchart.

using the *uvotevtlc* and *uvotmaghist* tasks depending on whether event or image data are present at the time of interest.

2.3 Flare Identification

Once the XRT lightcurve has been produced for a burst, it is searched, by manual inspection, for periods which show excess emission above the GRB underlying afterglow decay (hereafter, UAD). All periods that show evidence of excess emission are then fit with three (temporal) powerlaws, with the BAT trigger time taken as the burst start time; one powerlaw is fit to the datapoints which represent the UAD (ie, excluding the datapoints showing excess emission); a second powerlaw is fit to the datapoints characterizing the rising leg of the flare; and a third powerlaw is fit to the datapoints characterizing the decaying leg of the flare. The intersections of the second powerlaw (rising leg) and third powerlaw (decaying leg) with the powerlaw describing the UAD define the start and stop time of the flare respectively.

The square root of the sum of the integrated flux (in units of instrumental counts) from the start time to stop time under the UAD powerlaw and the integrated flux from the start time to stop time under the powerlaws describing the flare is then taken as the measure of the "noise" associated with the flare. The integrated flux (also in instrumental counts) from start time to stop time under the powerlaws describing the flare and above the UAD powerlaw is taken as the measure of the flare "signal". Flares are then categorized by signal to noise ratio with excesses leading to $S/N < 3$ rejected as insignificant (see Figure 2.2).

2.4 SED Generation

The generation of Spectral Energy Distributions (SEDs) from Swift data is a straightforward but labor intensive process. The degree of labor required makes generation of such SEDs a prohibitively arduous (as well as prone to inconsistency and error) task when repeated on tens of flares and over tens of time segments within each flare. In the same way that there is a need to produce consistent X-ray lightcurves with a standard and traceable creation logic, there is a similar need to produce consistent SEDs of the flares using a standard and traceable logic. The creation of SEDs is significantly more laborious than the creation of X-ray lightcurves due to the fact that SEDs require inclusion of UVOT, XRT and BAT data together. It should also be noted that analysis of an individual X-ray flare requires the creation of two SEDs, one to characterize the flare itself and one to characterize the spectrum of the GRB UAD beneath the flare, as will be discussed in §2.5.

To create an SED for each time interval of interest, we begin by extracting the XRT data from the cleaned events files output from the XRT pipeline. Events below 0.3 keV and above 10.0 keV are excluded, a systematic 3% uncertainty is added to the spectrum to account for residual imprecision in the XRT redistribution matrix file (RMF; private communication Sergio Campana) and the data are spectrally binned to have a minimum of 20 events per bin. BAT data in 7 energy channels (see description of BAT data processing above) are added as are UVOT data in all filters that have data during the time segment over which the SED is to be produced. During extended time intervals (such as those corresponding to the time interval used to describe the UAD) the UVOT will typically cycle through all of its filters. During shorter time intervals, however (such as those corresponding to a typical flare duration of 100-1000 s), UVOT data will typically only be collected in one or two filters. Thus, the SED of the UAD will typically be well sampled in the UVOT energy range (due to the long temporal baseline of the observation), somewhat poorly sampled in the XRT energy range (due to generally lower XRT count rates at the time when the underlying component is measured) and not sampled at all in the BAT energy range since BAT event data are generally not available at the (late) time at which the UAD is measured. The SED of the flare, on the other hand, will be typically poorly sampled in the UVOT energy range (due to the short duration of the flare), well sampled in the XRT energy range (due to the high XRT flux) and possibly also well sampled in the BAT energy range if the flare occurs early enough that the BAT is still collecting event data. An important result of the nature of the flare SEDs is that they typically do not have the spectral fidelity necessary to accurately measure dust reddening, which would be observed as curvature of the spectrum between the UVOT and XRT energy ranges. For this reason, the dust reddening is tied to the measured value of the N_H column density, as will be discussed in the following section.

2.5 SED Spectral Fitting

Once a consistent SED has been created, the final stage of the processing chain is to perform a set of spectral fits to the SED, with the goal of determining the spectral parameters that most accurately and precisely characterize the spectrum of the flare emission. A flowchart of the SED fitting algorithm is shown in Figure 2.3. It is important to make the distinction between the overall spectral characteristics of the SED and the spectral characteristics of the flare emission alone. We make the assumption that, in the case of each flare in our sample, the SED that we analyze is a composite spectrum of the emission from the flare and the emission from an underlying component, dominated either by the tail of the prompt emission (the high latitude emission or rapid decay phase) or by the afterglow (either during the energy injection phase or the 'normal' afterglow phase). Because the flare spectral parameters that we are trying to determine are characteristic of only a portion of the emission in the SED which cannot be isolated from the SED as a whole, we must attempt to define the spectrum that is characteristic of the non-flaring emission component through means other than direct observation. We can then separate the observed SED into the non-flaring emission component and flaring emission component. To do this, we begin by making the assumption that either 1) we can find a segment of data in the afterglow observations of each flaring GRB that is spectrally representative of the non-flaring emission component that lies beneath the flaring data we want to analyze or 2) if no data are available that are likely to be representative of the non-flaring emission component, a useful approximation to the non-flaring emission component can be assumed to be an absorbed powerlaw with galactic extinction and photon index of 2.0. Once we have determined the spectrum characteristic of the non-flaring emission component, through one of these two methods, we can then solve the following equation to determine the model spectrum of the flaring emission component

$$M_{data}(J) = \int_{E_{j-1}}^{E_j} (M_{under}(E) + M_{flare}(E))dE \tag{2.1}$$

where $M_{data}(J)$ is the observed SED in the discrete energy bin J, $M_{under}(E)$ is the model spectrum of the non-flaring emission determined as discussed above, and $M_{flare}(E)$ is the model spectrum of the flaring emission component.

If data exist within the GRB dataset which contain enough fluence to make a good representation of the non-flaring component (roughly 500-1000 events in the 0.3-10 keV energy range is used as a minimum requirement), this is naturally preferable to using an assumed canonical spectrum for the non-flaring component. The time ranges which are representative of the non-flaring part of the burst are defined by inspection of the X-ray lightcurve, preferably being taken from the same phase of the lightcurve (see the phases of GRB afterglows in the Swift era as defined in the introduction and in, e.g., Nousek et al. (2006)) as that in which the flare is found. If no appropriate data are found within the same phase, data from another phase (energy injection or normal phase) may be selected. Since there is generally little or no observed spectral evolution from the energy injection phase of the afterglow to the 'normal' afterglow phase (Nousek et al. 2006), it is reasonable to use data from either of these phases to represent the spectrum of the non-flaring emission component during the flaring segment. Within the time range of the flare defined as described previously, all overlapping data from the UVOT are extracted and added to the SED of the non-flaring emission. BAT data for the non-flaring emission are not available because at these late times in the burst evolution the BAT no longer collects event data (in which each photon is recorded and can be back-propagated through the coded-mask to identify its position on the sky and perform accurate background subtraction) so we are limited to using the BAT detector plane histogram (DPH) data (in which photons are not position tagged and the background estimation becomes much more uncertain, see the Swift BAT User's Guide, version 6.3, available at http://swift.gsfc.nasa.gov/docs/swift/analysis/ for further detail). Since the 15-150 keV emission will also be faint at these times, however, background sources will generally dominate the BAT field, causing confusion problems in analysis of the BAT DPH data. Therefore BAT data are included only when event data are available.

The non-flaring SED is then fit with both a simple absorbed powerlaw and an absorbed broken powerlaw model. In each case, a local absorption component fixed to the galactic value (Dickey & Lockman 1990), a local reddening component fixed to the galactic value (Schlegel et al. 1998) and a redshifted absorption component and redshifted reddening component are included. A selection is then made between these two model fits based on the 95% threshold values of the f-test. While the validity of the f-test has been debated in some astronomical contexts (specifically with regards to line detection but more broadly with regards to the applicability of the test to non-nested model families; Protassov et al. (2002)), it is appropriate in this context since we are selecting between nested models with only a single additional degree of freedom. Once the non-flaring spectrum is defined, it is then necessary to determine the projection of the normalization level of the non-flaring component that is appropriate at the time segment during which the flaring emission occurs. To do this we take advantage of the knowledge that the X-ray lightcurves of GRBs, when not in a flaring state, are generally well approximated by a temporal powerlaw with a fixed exponent. This fixed exponent will change with the phase of the GRB afterglow, but within a particular afterglow phase, the exponent is generally observed to remain constant, and therefore within a particular afterglow phase, we are able to confidently interpolate (or sometimes extrapolate) the flux normalization of the afterglow from one time to another. After selecting data to temporally represent the afterglow behavior near to but separated from the flaring segment (these data may be the same as those used to spectrally represent the non-flaring spectral component, but need not be) we then fit a simple temporal powerlaw to these lightcurve data and project the normalization of the non-flaring spectrum along this temporal powerlaw to the level it would have had at the time of the flare.

If sufficient x-ray data are not available to produce a spectrum of the non-flaring emission, we assume the non-flaring data to have an absorbed powerlaw spectrum with photon index of 2.0 and a neutral hydrogen absorption column equal to the galactic value. Such a spectrum has commonly been found to be representative of (non-flaring) GRB afterglows in both the energy injection phase and 'normal' decay phase where many of the flares being analyzed are found. Simulated data with the aforementioned spectrum are generated in XSPEC (using the task *fakeit*), the normalization of the simulated spectrum is scaled to reproduce the flux level of the X-ray lightcurve during a non-flaring segment (note here that though sufficient counts are not available to create an accurate spectrum, sufficient counts may, and generally do, exist to define the temporal powerlaw behavior of the afterglow) and the normalization value is then projected along the afterglow temporal powerlaw to the value it would have had at the time of the flare, similarly to what is done when the non-flaring spectrum is fit from the data.

With the non-flaring emission spectrum now determined, either through observation or by assumption of the canonical spectrum, the parameters describing the non-flaring emission (with normalization projected to the time of the flaring data) are fixed and the flaring dataset is fit in XSPEC trying 5 different families of spectral models, 1) an absorbed powerlaw, 2) an absorbed cutoff powerlaw, 3) an absorbed Band function, 4) an absorbed powerlaw plus blackbody and 5) an absorbed broken powerlaw. In each case a local absorption component and local reddening component, each fixed to the galactic value, as well as a redshifted absorption component and redshifted reddening component, local to the GRB, are included. To avoid misidentifying local minima in the parameter space as global minima, XSPEC fit minimizations are performed using several different starting parameter values for each of the models noted above. The starting parameter values are chosen, by experience, to roughly span the expected parameter range of the more poorly constrained parameters and are detailed in Table 2.2. The best fit within each model type (as determined by comparison of reduced χ^2 values) is selected to represent the parameters of the flaring data as fit by that model type. We note here (and this point will be discussed in greater detail in later chapters) that the reddening component is added (multiplied, in fact) to each spectrum when UVOT data are included as part of the SED but not if UVOT data are absent. The reason for this is that the SED above 0.3keV (the lower limit of the XRT energy response) is largely unaffected by dust reddening. In cases where reddening is added in the spectral fit, the redshifted reddening component (E(B-V)) parameter is tied to the neutral hydrogen absorption column density, a parameter which is generally better constrained by the data than reddening is, as in Schady et al 2007.

Table 2.2. Flare Fit Parameter Starting Guesses

Powerlaw					
guess no.	N_H	Γ	norm		
1	galactic	2.0	1.0		
2	0.1	1.0	0.1		
3	0.1	2.0	0.1		
4	0.1	3.0	0.1		
5	0.1	2.0	0.01		
Band Function					
guess no.	N_H	α	β	E_0[a]	norm
1	galactic	-1.0	-2.0	2.0	1.0
2	0.1	-1.0	-2.0	1.0	0.1
3	0.1	-0.5	-2.0	1.0	0.1
4	0.1	-1.0	-2.0	5.0	0.1
5	0.1	-1.0	-2.0	0.1	0.1
Powerlaw + Blackbody					
guess no.	N_H	Γ	norm_{PL}	kT[a]	norm_{BB}
1	galactic	2.0	1.0	1.0	1.0
2	0.1	1.0	0.1	1.0	0.1
3	0.1	2.0	0.1	1.0	0.1
4	0.1	3.0	0.1	1.0	0.1

Table 2.2—Continued

5	0.1	2.0	0.1	0.1	0.1
Broken Powerlaw					
guess no.	N_H	Γ_1	E_{break} [a]	Γ_2	norm
1	galactic	1.0	2.0	2.0	1.0
2	0.1	1.0	2.0	2.0	0.1
3	0.1	0.5	2.0	1.5	0.1
4	0.1	1.0	5.0	2.0	0.1
5	0.1	0.5	5.0	1.5	0.1

[a] Fit range set to 0.1keV to 1000 keV

For completeness, I list below the form of the 5 families of models used.

Powerlaw:

$$A(E) = E_{BV}e^{(-N_H\sigma(E))} * (E_{BV1}e^{(-N_{H_1}\sigma(E))}K_1E^{\alpha} + E_{BV2}e^{(-N_{H_2}\sigma(E))}K_2E^{\alpha_1}) \tag{2.2}$$

Cutoff Powerlaw:

$$A(E) = E_{BV}e^{(-N_H\sigma(E))} * (E_{BV1}e^{(-N_{H_1}\sigma(E))}K_1E^{\alpha} + E_{BV2}e^{(-N_{H_2}\sigma(E))}K_2E^{\alpha_1}e^{(-E/\beta)}) \tag{2.3}$$

Band Function:

$$A(E) = E_{BV}e^{(-N_H\sigma(E))} * (E_{BV1}e^{(-N_{H_1}\sigma(E))}K_1E^{\alpha} + E_{BV2}e^{(-N_{H_2}\sigma(E))}K_2E^{\alpha_1}e^{(-E/E_c)}); E < (\alpha_1 - \alpha_2)E_c \tag{2.4}$$

$$A(E) = E_{BV}e^{(-N_H\sigma(E))} * (E_{BV1}e^{(-N_{H_1}\sigma(E))}K_1E^{\alpha} + E_{BV2}e^{(-N_{H_2}\sigma(E))}K_2[(\alpha_1 - \alpha_2)E_c]^{\alpha_1-\alpha_2}e^{[-(\alpha_1-\alpha_2)E^{\alpha 2}]}); E > (\alpha_1 - \alpha_2)E_c \tag{2.5}$$

Powerlaw + BB:

$$A(E) = E_{BV}e^{(-N_H\sigma(E))} * (E_{BV1}e^{(-N_{H_1}\sigma(E))}K_2E^{\alpha} + E_{BV2}e^{(-N_{H_2}\sigma(E))}K_2E^{\alpha_1} + \frac{K_3}{(kT)^4[e^{e/kT} - 1]}) \tag{2.6}$$

Broken Powerlaw:

$$A(E) = E_{BV}e^{(-N_H\sigma(E))} * (E_{BV1}e^{(-N_{H_1}\sigma(E))}K_1E^{\alpha} + E_{BV2}e^{(-N_{H_2}\sigma(E))}K_2E^{\Gamma_1}); E < E_{break} \tag{2.7}$$

$$A(E) = E_{BV}e^{(-N_H\sigma(E))} * (E_{BV1}e^{(-N_{H_1}\sigma(E))}K_2E^{\alpha} + E_{BV2}e^{(-N_{H_2}\sigma(E))}K_2E_{break}^{\Gamma_2-\Gamma_1}E); E > E_{break} \tag{2.8}$$

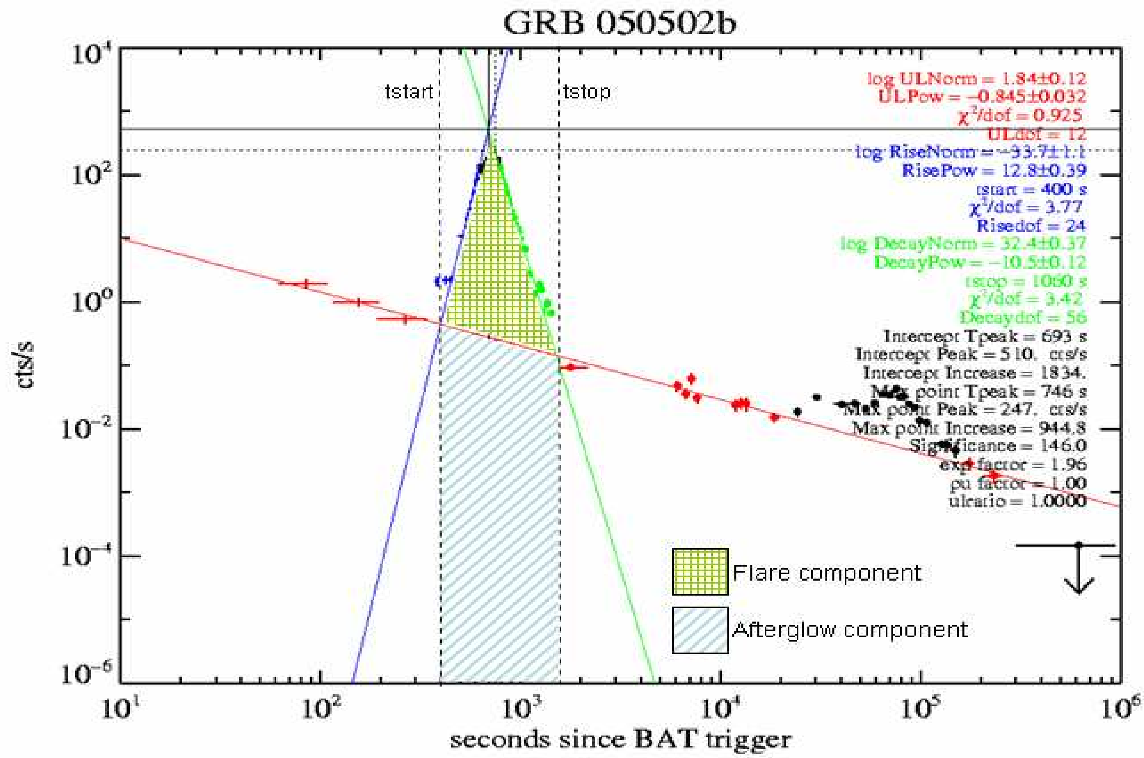

Fig. 2.2 The X-ray lightcurve of GRB050502B is shown with temporal powerlaws fit to the UAD (red), rising leg of the flare (blue) and decaying leg of the flare (green) as described in the text. The intersection of the UAD and rising leg of the flare defines the start time while the intersection of the UAD and the decaying leg of the flare defines the stop time. The contribution of the UAD beneath the flare (blue shaded region) is fit simultaneously with a separate component to account for the X-ray flare itself (green shaded).

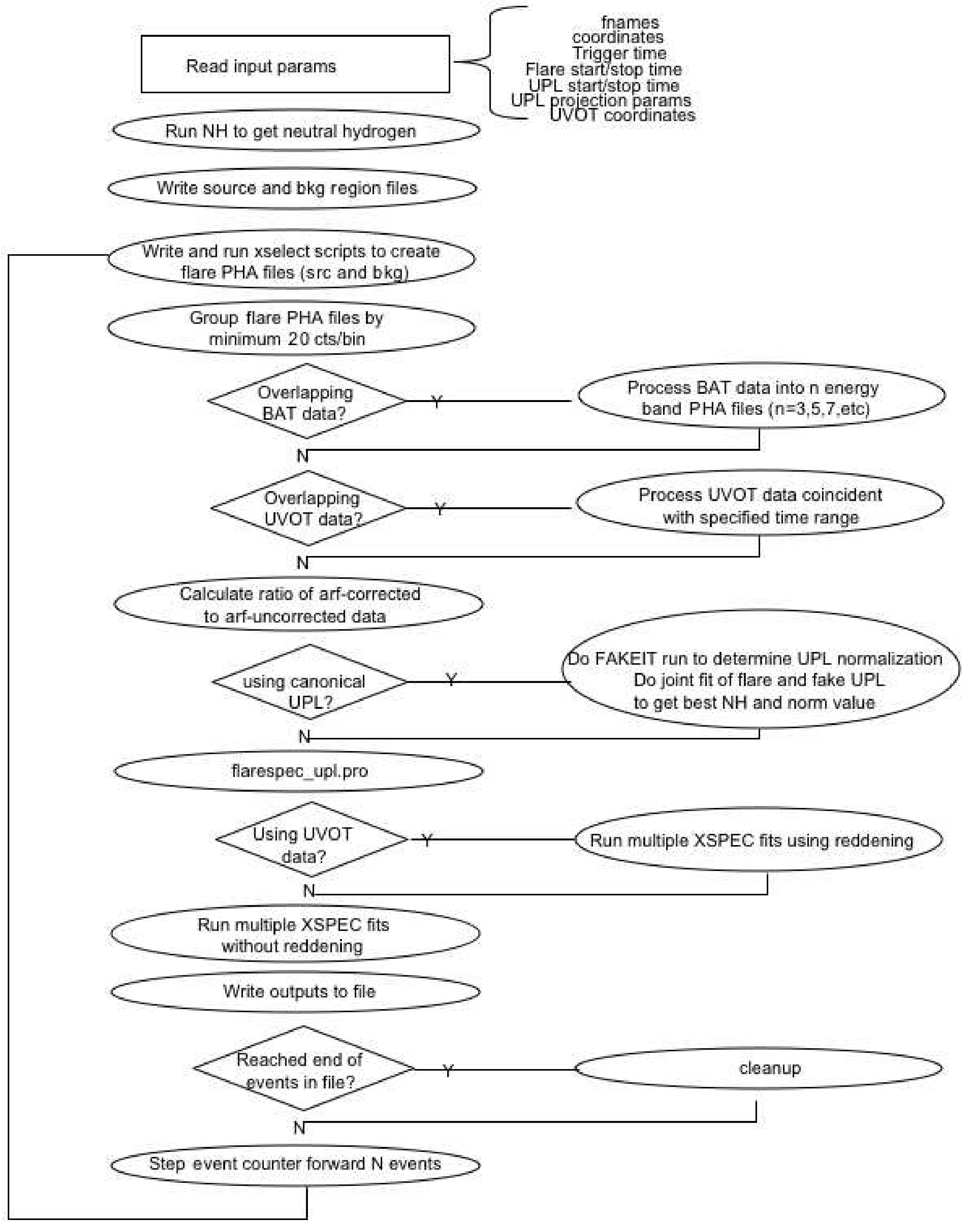

Fig. 2.3 SED spectral fitting flow chart. All flares in the samples to be discussed in Chapters 4 and 5 are processed using the software outlined in this flowchart.

Chapter 3

GRB 050713A: A Case Study

(published as Morris et al. (2007), ApJ, 654, 413)

We begin our detailed discussion of the *Swift* data on flaring GRBs with a case study of GRB 050713A. GRB 050713A is a burst of T_{90} = 70 seconds to which *Swift* slewed and began collecting data with the narrow field instruments (NFIs) in just 72.6 seconds, while the prompt gamma ray emission was still detectable by the BAT. This burst marked just the second time that the BAT and XRT had collected simultaneous data on a burst and it marked the first time that both instruments produced a well sampled, simultaneous dataset covering multiple flares in the prompt emission. This burst displays many of the hallmarks of the GRB X-ray flare phenomenon and so a detailed analysis of this GRB will serve as a useful primer for the discussion of the flare surveys that will comprise the rest of this thesis.

GRB 050713A is also a worthy burst to study on its own merits due to the extremely wide energy range over which it was observed, thanks to prompt measurements and rapid follow-up observations by Konus-Wind, MAGIC, *XMM-Newton* and ground based optical observatories. As will be discussed in greater detail in Chapter 5, broad spectral coverage is important in order to distinguish between the various possible spectral models thought to characterize the flare emission and thereby to gain insight into the possible emission mechanism responsible for flares. Since we will be treating this burst on its own merits in this chapter and furthermore because we will be combining data from several instruments other than *Swift*, we will analyze it outside the pipeline method discussed in Chapter 2 in order to allow the greatest flexibility to incorporate all the data available. Therefore, in §3.1 we describe the observations and data analysis from all instruments including ground follow-up. In §3.2 we discuss the implications of the observations on the models proposed for the production mechanism for flares. In §3.3 we summarize the analysis, discuss its relevance looking forward to the flare surveys to be discussed in the following 2 chapters and present our conclusions. As throughout this thesis, quoted uncertainties are at the 90% confidence level for one interesting parameter (i.e., $\Delta\chi^2$=2.71) unless otherwise noted.

3.1 Observations and Data Analysis

Many different observatories and instruments observed GRB 050713A. We devote the following section to a description of the observations and analysis carried out by each instrument team. All spectral fits were performed using XSPEC v11.3.

3.1.1 *Swift* BAT

The *Swift* BAT (Barthelmy et al. 2005a) triggered on GRB 050713A at 04:29:02.39 UT, measuring a peak 1-second flux of 6.0 ± 0.4 photons cm^{-2} s^{-1}. T_{90} measured in the 15–350 keV energy range is 70 ± 10 s (Palmer et al. 2005). The onset of the burst as defined by the BAT trigger is preceded by a weak, hard (photon index = 1.26) precursor at T_0–60 s. BAT data were processed using the BAT ground software build 11 and BAT Calibration Database files build 11.

At the time of the BAT trigger, the flux rose rapidly and remained elevated during a 12 s long, multipeaked burst (Figure 3.1). At T_0+12 s, the BAT flux rapidly decayed as a powerlaw f(t) = nt^{α}, with $\alpha \sim 8$ for 5 seconds before breaking to a more shallow decay of $\alpha \sim 2.5$ at T_0+17 s. This decay continued until T_0+40 s at which point the BAT flux had decayed to near background levels. At T_0+50 s, a flare is seen with peak flux 2×10^{-8} ergs cm^{-2} s^{-1}, extrapolated into the XRT 0.2–10.0 keV bandpass, followed by a flare with peak flux 3.5×10^{-8} ergs cm^{-2} s^{-1} at T_0+65 s, another at T_0+105 s with peak flux 1×10^{-8} ergs cm^{-2} s^{-1} and some hint of further emission at the onset of a flare seen in the XRT at T_0+160 s. A weak but statistically significant precursor is seen at T_0–70 s to T_0–50 s followed by a period of no significant emission from T_0–50 s to the burst trigger.

The spectrum of the entire BAT dataset is well fit by a power-law spectrum with photon index = 1.58 ± 0.07, though there is evidence for a slightly harder index of 1.45 during the plateau and a softening to $\Gamma = 1.60$ during the rapid decay, and further softening to $\Gamma = 2.0$ during the weak flares. Using the global fit of $\Gamma = 1.58$, the fluence is $9.1 \pm 0.6 \times 10^{-6}$ ergs cm^{-2} in the 15–350 keV energy range.

3.1.2 Konus-Wind

GRB 050713A triggered Konus-Wind (K-W) (Aptekar et al. 1995) at T_0(K-W)= 04:29:01.745 UT. It was detected by the S2 detector, which observes the north ecliptic hemisphere, with an incident angle of $18.^{\circ}1$. The K-W lightcurve in 3 bands is shown in Figure 3.2. The propagation delay from Wind to *Swift* for GRB 050713A is 1.387 s. Correcting for this factor, one sees that the K-W trigger time corresponds to T_0+0.742 s.

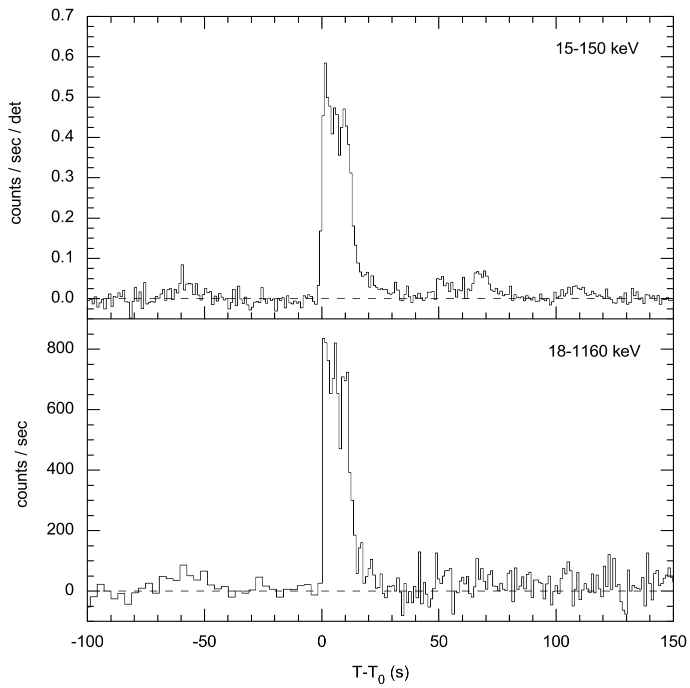

Fig. 3.1 Background subtracted BAT (top panel) and Konus-WIND (bottom) light curves on the same time scale. The plots have been adjusted so that the trigger time for both plots is the same relative to the burst. T_0 in the lower plot is T_0(BAT) plus the propagation time between the spacecrafts (0.742 s). BAT data are binned to 1 s resolution throughout. K-W data are binned to 2.94 s resolution in survey mode prior to the burst trigger and are binned to 1 s resolution in GRB follow-up mode after the trigger. Note that the precursor at T_0–65 s is detected in both BAT and K-W while post-trigger flares seen in the BAT at T_0+50 s, T_0+65 s and T_0+105 s are not clearly detected by K-W. This suggests a harder spectrum for the precursor than the post-trigger flares, which is confirmed by joint BAT/K-W spectral fits. The main burst consists of 3 closely spaced, overlapping pulses in both the BAT and K-W energy ranges. The K-W lightcurve decays rapidly to background level by T_0+15 s while the BAT lightcurve continues to show low level emission out to T_0+ ∼200 s.

Prior to T_0(K-W)-0.512 s data were collected by K-W in a survey mode with lower time resolution of 2.944 s and only 3 broad spectral channels, 18–70 keV, 70–300 keV and 300–1160 keV. From T_0(K-W) to T_0(K-W)+491.776 s, 64 spectra in 101 channels were accumulated on time scales varying from 64 ms near the trigger to 8.19 s by the time the signal became undetectable. The multichannel spectra cover the 18 keV–14 MeV energy range but no statistically significant emission is seen above 2 MeV. Data were processed using standard Konus-Wind analysis tools.

Joint spectral analysis was carried out using the BAT data between 15 and 150 keV and the KONUS data from 20 to 2000 keV. The spectra were fit by a power law model with an exponential cut off: dN/dE $\propto$ $E^{-\alpha}$ $e^{(-(2-\alpha)E/E_p)}$ where E_p is the peak energy of the ν F_ν spectrum and α is the photon index. The spectrum of the main pulse is well fit (Figure 3.3) with photon index $= 1.26 \pm 0.07$ and $E_p = 421^{+119}_{-80}$ keV (χ^2=138/119 dof). Joint fits between BAT and Konus were also made for other time intervals, including one which shows the faint precursor detected by both instruments at T_0 $\sim$–60 s, and will be addressed in greater detail in §3.3.

The main pulse fluence in the 20 keV to 2 MeV range is $8.08^{+0.55}_{-1.77} \times 10^{-6}$ erg cm^{-2}. The 256-ms peak flux measured from T_0+1.2 s in the 20 keV to 2 MeV band is $1.34^{+0.11}_{-0.45} \times 10^{-5}$ erg cm^{-2} s^{-1} and the T_{90} durations of the burst in the G1, G2 and G3 energy bands are 17 ± 2 s, 14 ± 4 s and 12 ± 2 s, respectively.

3.1.3 *Swift* XRT

The XRT (Burrows et al. 2005a) performs an automated sequence of observations (Hill et al. 2004) after *Swift* slews to a GRB detected by the BAT. When the spacecraft

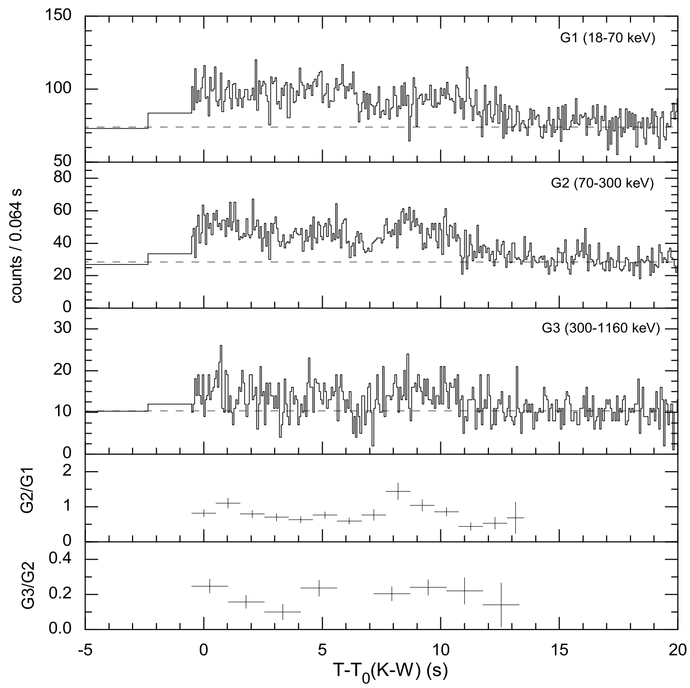

Fig. 3.2 Plot of Konus-Wind data in 3 bands and associated band ratios during burst prompt emission. Data binning is 64ms.

first settles on the target, a short image (0.1 s followed by a longer 2.5 s image if a position is not determined in 0.1 s) is taken to determine an accurate position. Following the image, the XRT switches into either Windowed Timing (WT) mode (a high timing accuracy mode with 1 dimensional position information) if the source count rate is above 2 counts s^{-1}, or Photon Counting (PC) mode (the more traditional operating mode of X-ray CCDS in which full 2 dimensional position information is retained but with only 2.5 s timing resolution) if the count rate is below 2 counts s^{-1}.

XRT collected a 0.1 s Image Mode frame upon settling on GRB 050713A 73 seconds after the BAT trigger, which yielded a count rate of 314 counts s^{-1}. Following the Image Mode frame, XRT cascaded down through its automated mode sequence and collected its first WT frame 4.5 seconds later. At the onset of the WT data, the XRT

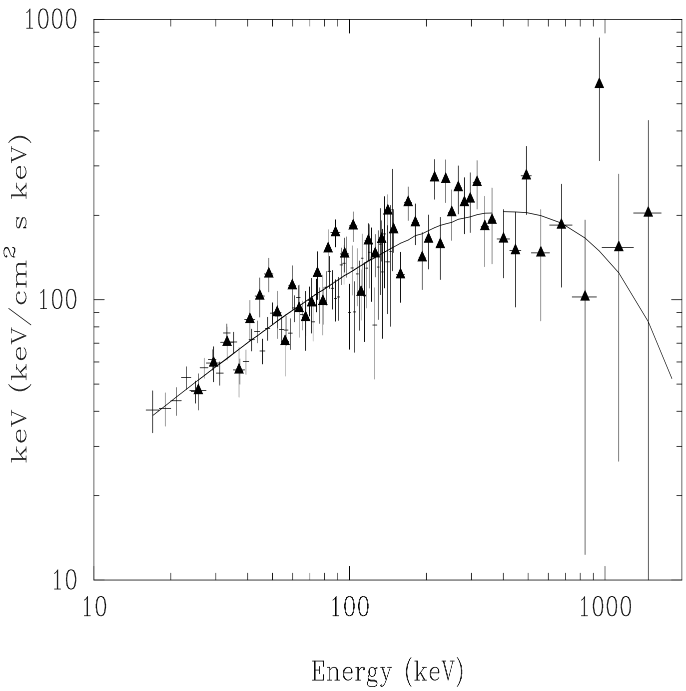

Fig. 3.3 Plot of joint spectral energy distribution of Konus-Wind and BAT data during burst prompt emission, showing $E_{peak} = 421$ keV. K-W data are filled triangles, BAT data are crosses. Data channels have been grouped where appropriate to produce significant data points.

count rate was about 100 counts s^{-1} and decaying as a powerlaw. This initial powerlaw decay in the XRT WT data together with the Image Mode data point measured at a flux level $\sim$3 times higher just 4.6 s earlier clearly indicates that the XRT settled and began taking data during the latter portion of the flare detected in the BAT at T_0+65 seconds (see Figure 3.4). XRT remained in WT mode throughout the entire first orbit of data collection on GRB 050713A, also observing the flare detected by the BAT at T_0+105 and a lower level flare not clearly detected by the BAT at T_0+155 s.

Following a 65 minute period of occultation by the Earth, XRT began observations again at T_0+4300 s, now observing in PC mode since the count rate of the source had decayed below 2 counts s^{-1}. A small flare at T_0+10 ks and the indication of another flare at T_0+45 ks are seen in the late time XRT lightcurve data, superimposed on an otherwise steady powerlaw decay. XRT observations continue to monitor the source until $T_0+1.8\times10^6$ s, a total exposure time of 178 ks, at which time the source had decayed below the XRT detection threshold.

XRT data are processed using the *xrtpipeline* software version 0.9.9, the redistribution matrices swxwt0to2_20010101v007.rmf (WT) and swxpc0to12_20010101v007.rmf (PC), and ancillary response files generated with the *xrtpipeline* task *xrtmkarf*.

3.1.3.1 XRT GRB Position Analysis

The X-ray afterglow position determined from ground processing of the data is RA(J2000) = $21^{\mathrm{h}}22^{\mathrm{m}}9.8$ Dec(J2000) = $+77^\circ4'29''\!.0$ with an uncertainty of 3.2 arcseconds. This is 10.5 arcseconds from the reported BAT position, 0.5 arcseconds from the optical counterpart reported by Malesani et al. (2005), and 1.5 arcseconds from the initial XRT position calculated onboard the satellite and automatically distributed via the GCN network (Falcone et al. 2005). An X-ray image compiled from the first segment of XRT PC data is shown as Figure 3.5 with the BAT, XRT and optical counterpart error circles displayed. A faint background source is detected 30 arcseconds due south of the GRB afterglow at a constant flux level of $7 \pm 2 \times 10^{-4}$ counts s^{-1}. The contribution of this steady source has been removed from the calculation of the afterglow lightcurve.

3.1.3.2 XRT Temporal Analysis

A timeline of the XRT (as well as other) observations of GRB 050713A is shown in Table 3.1. The lightcurve will be broadly treated in two parts. The first part is the initial orbit of data, during which the lightcurve is characterized by bright flares which are simultaneously observed by the BAT as well as the K-W instrument at higher energies. Due to the extreme variability in this portion of the lightcurve, a global decay index cannot be determined from the XRT data. The second part is the remainder of the XRT data from the second orbit onward, which is characterized primarily by a broken powerlaw decay, though at least one small flare is seen superimposed atop this global decay.

3.2.3.2.1 First Orbit *Swift* finished slewing to GRB 050713A at T_0+73 s, during the flare which began at T_0+65 s. The XRT short image frame is collected just after the peak of this flare, at a flux of 1.2×10^{-8}ergs cm^{-2} s^{-1}, and the first 20 frames of WT data record the decay of the flare. Fitting a simple powerlaw to this decay from T_0+79 s

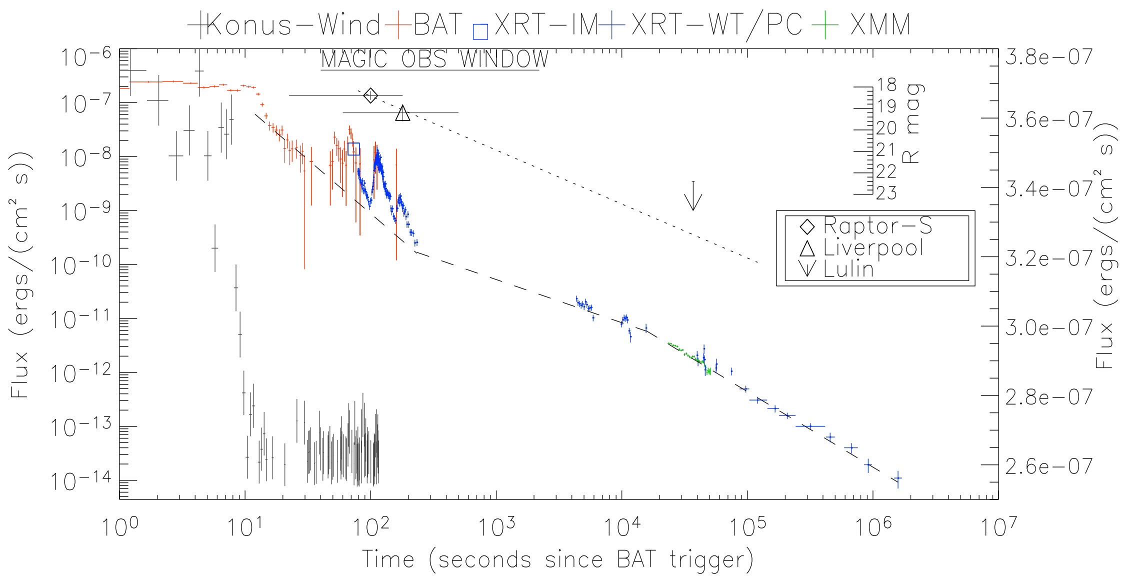

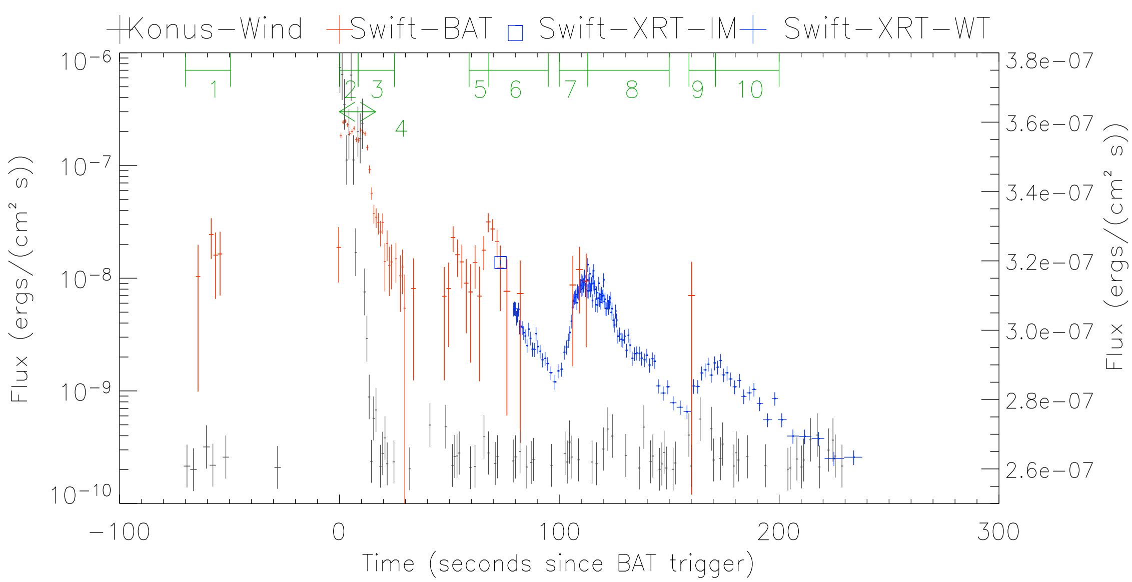

Fig. 3.4 X-ray/gamma-ray/optical lightcurve of GRB 050713A. Top: multicolored points are *Swift* and XMM data scaled to the left Y-axis. Black crosses are K-W data scaled to the right Y-axis. Fluxes are extrapolated into the 0.2–10 keV energy range. The diamond, cross and arrow are optical observations and scaled to the inset Y-axis. The scaling of the inset Y-axis is consistent with the outer, left Y-axis such that 1 magnitude is equal to a factor of 2.5 in flux. The window of MAGIC observations is shown by the horizontal bar. The dashed line is the supposed underlying powerlaw decay. Data from T_0+4 ks to T_0+16 ks are well fit by a flatter powerlaw of slope $t^{-0.8}$, implying an energy injection phase. A break to a steeper decay of $t^{-1.45}$ occurs at T_0+∼25 ks. We note the similar decay slopes in each of the three flares seen by XRT. Optical data are plotted with a fitted powerlaw decay of $t^{-1.0}$. Bottom: a close-up of the flares. Green bars indicate the segments of joint spectral fits.

Table 3.1. A Summary of High Energy Observations of GRB 050713A

Observatory /Instrument	Start Time (UT)	Stop Time (UT)	Live-time (Seconds)	Time Since BAT Trigger (Seconds)
Swift-BAT	05-07-13-04:29:02.4	05-07-13-04:32:00	178	0
Konus-Wind	05-07-13-04:29:03.1*	05-07-13-04:37:14.8	491.8	0.7
MAGIC(limit)	05-07-13-04:29:42	05-07-13-05:06:45	2223	40
Swift-XRT	05-07-13-04:30:14	05-08-01-04:37:02	167740	72
XMM-Newton	05-07-13-10:17:00	05-07-13-18:22:00	20900	21000

*The Konus-Wind trigger time corrected for the propagation time from Wind to Swift

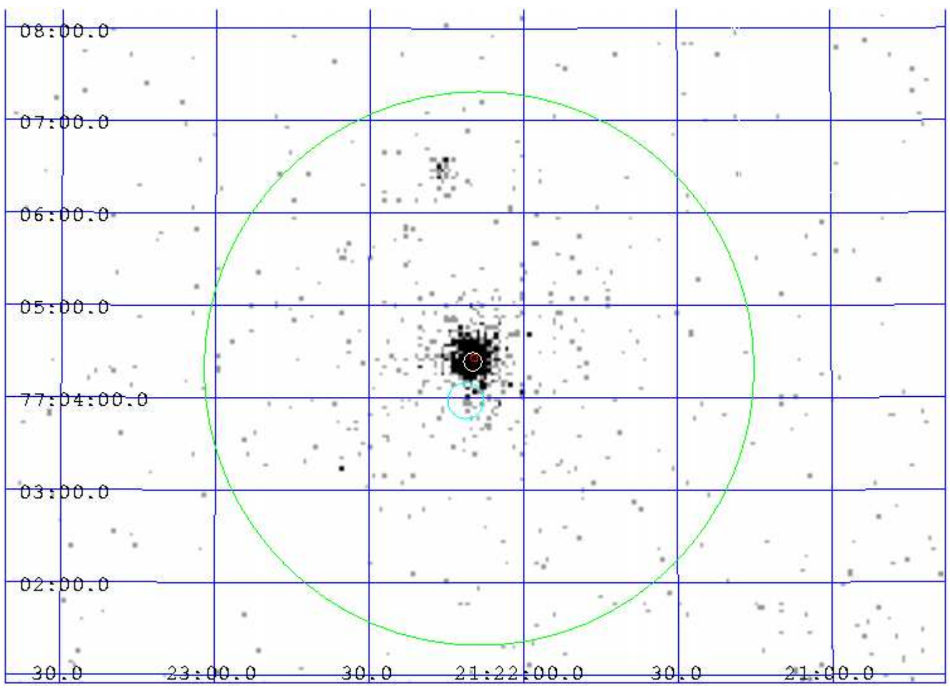

Fig. 3.5 XRT image with BAT and XRT optical error circles plotted. Green = BAT; White=XRT; Red=optical. The light blue circle indicates the location of the serendipitous source located 30 arcseconds south of the GRB which has been subtracted from the data.

to T_0+100 s, setting T_0 to be the BAT burst trigger time, we find a powerlaw index of 5.6 ± 1.8 (1 σ). At T_0+105 s a new flare begins, which rises with a powerlaw index of 23.3 ± 4.5 for 5-10 s, flattens at the peak of $\sim 9 \times 10^{-9}$ ergs cm^{-2} s^{-1} for 5-10 s, then decays with a more shallow powerlaw index of 8.4 ± 1.7 for about 30 s. At T_0+165 s a third flare is detected, which rises with a powerlaw slope of 8.9 ± 3.1 for 5-10 s, flattens at the peak of $\sim 1.5 \times 10^{-9}$ ergs cm^{-2} s^{-1} for 5-10 s, then decays with a slope of 6.1 ± 1.1 for 70 s before the end of the observing window due to Earth occultation.

3.2.3.2.2 Second Orbit and Later The second orbit of data in the XRT is the only single orbit of data in which the afterglow is characterized by a well sampled (greater than 100 events total) lightcurve devoid of any obvious flaring activity. During the 1600 seconds of data in this orbit, from T_0+4360 s to T_0+5952 s, the lightcurve decays steadily as a powerlaw with decay index of about 1.0. The third orbit of data is characterized by another flare, beginning at T_0+10 ks, lasting throughout the entire orbit (about 2 ks) and reaching a peak flux of 1×10^{-11} ergs cm^{-2} s^{-1}. A powerlaw fit to the rising portion of the flare yields a slope of 5.8 ± 1.8 while the decaying portion yields a slope of 11.0 ± 2.5. This flare seems to be superposed atop the underlying afterglow decay with powerlaw index $\alpha \sim 1$. Observations were interrupted after 150 s during the fourth orbit due to the occurrence of GRB 050713B, and observations of GRB 050713A remained suspended until T_0+40 ks. Some suggestion of another flare is seen in the orbit of data beginning at T_0+45 ks, though the statistics are poor. While afterglow data from the XRT alone do not clearly require a break in the afterglow powerlaw, *XMM-Newton* data (see §3.1.4) from T_0+21 ks to T_0+50 ks provide an accurate measure of the late-time decay slope

($\alpha = 1.45$) which cannot fit the XRT data from orbits 2 and 3 without a break in the powerlaw. The joint XRT-*XMM-Newton* lightcurve will be further discussed in §3.1.4. Table 3.2 summarizes the flares and their temporal fits.

Table 3.2. GRB 050713A: X-ray Flares Parameters.

Start Time (s)	Stop Time (s)	Duration (s)	Rise Index α^a (unitless)	Decay Index α^b (unitless)	Peak Flux (ergs cm^{-2} s^{-1})
79	101	22	NA	5.6 ± 1.8	3×10^{-8} (from BAT)
101	161	60	23.3 ± 5	8.4 ± 1.8	9×10^{-9}
161	304	143	8.9 ± 3	6.1 ± 1.2	1.5×10^{-9}
9751	11840	2089	5.76 ± 1.8	11.0 ± 2.4	1×10^{-11}

[a]Index α of a powerlaw fit to the rise of the flare with T_0=BAT trigger time; $\Gamma_\nu \propto (t\text{-}T_0)^{\alpha}$

[a]Index α of a powerlaw fit to the decay of the flare with T_0=BAT trigger time; $\Gamma_\nu \propto (t\text{-}T_0)^{-\alpha}$

3.1.3.3 XRT Spectral Analysis

The XRT spectral analysis is somewhat complicated by the high degree of flaring activity seen. In all cases, spectra are binned to a minimum of 20 counts per bin in order to use χ^2 statistics. Fitting the entire first orbit of data, the spectrum is well fit by a highly absorbed powerlaw with photon index $= 2.28 \pm 0.04$ and $N_H = 4.8 \pm 0.2 \times 10^{21}$ cm^{-2}, which is significantly above the galactic column (1.1×10^{21} cm^{-2}) in the direction of GRB 050713A (Dickey & Lockman 1990). We are also able, due to the large number of counts in each of the early flares in the dataset, to fit a spectrum to both the rising and decaying portions of the flares. In doing so we see the typical hard to soft evolution of the flares (Zhang & Mészáros 2004).

The second orbit of data shows a significantly different spectrum from the first, with a harder photon index of 1.9 ± 0.13 and a lower N_H value of $3.1 \pm 0.43 \times 10^{21}$, possibly indicating a period of energy injection (Nousek et al. 2006). The third orbit is well fit by a softer powerlaw similar to that which fit the first orbit with photon index $= 2.25 \pm 0.23$ and $N_H = 4.1 \pm 0.7 \times 10^{21}$.

During the period of overlapping coverage between *Swift* and *XMM-Newton* , XRT has 3.5 ks of exposure time at a mean countrate of 0.04 counts s^{-1} for a total of about 150 events during the simultaneous observing period. Fitting a spectrum to this overlapping coverage yields a photon index $= 1.9 \pm 0.30$ and $N_H = 4.0 \pm 0.15 \times 10^{21}$. The corresponding mean unabsorbed 0.2–10.0 keV flux during the overlap period as measured by XRT is $3.4 \pm 0.34 \times 10^{-12}$ ergs cm^{-2} s^{-1}.

The data collected after the third orbit (i.e., after the temporal break in the lightcurve at $T_0 + \sim 20$ ks) are too sparse to justify fitting with higher order models, but a simple absorbed powerlaw fit yields a spectrum of photon index $= 2.8 \pm 0.6$ with $N_H = 5.6 \pm 0.2 \times 10^{21}$. This is consistent with the X-ray photon index found in orbits 1 and 3 and is marginally softer than the photon index found during orbit 2 which, as noted above, suggests a period of energy injection.

3.1.4 *XMM-Newton*

XMM-Newton follow-up observations of GRB 050713A commenced at T_0+23.6 ks (for the EPIC-PN) and T_0+20.9 ks (for the two EPIC-MOS cameras). The *XMM-Newton* data were processed with the *epproc* and *emproc* pipeline scripts, using the *XMM-Newton* SAS analysis package, version 6.5. A bright rapidly decaying source is detected near the aimpoint of all three EPIC detectors, localized at RA(J2000)=$21^{\mathrm{h}}22^{\mathrm{m}}9.4$ Dec(J2000)=$+77^{\circ}4'28''.1$. The net exposures after screening and deadtime correction are 24.1 ks (PN) and 27.0 ks (MOS). All three EPIC cameras (PN and 2 MOS) were used in Full Window Mode with the medium filter in place.

Source spectra and lightcurves for all 3 EPIC cameras were extracted from circular regions of 20 arcseconds radius centered on the afterglow. Background data were taken from a 60 arcseconds circle on the same chip as the afterglow, but free of any X-ray sources. Fitting the afterglow lightcurve with a simple power-law decay results in a decay index of $\alpha = 1.45 \pm 0.05$. Several proton flares are present in the background lightcurve, so as a conservative check, we also excluded times where the background rate is $> 0.1\,\mathrm{counts\,s^{-1}}$. The afterglow decay rate is then $\alpha = 1.39 \pm 0.09$, consistent with the above value. The decay rate from the MOS lightcurve (for the two detectors combined) is also consistent at $\alpha = 1.35 \pm 0.06$.

3.1.4.1 *XMM-Newton* Spectral Analysis

Afterglow and background spectra were extracted with the same regions used for the lightcurves, while ancillary and redistribution matrix files were generated with the SAS tasks *arfgen* and *rmfgen* respectively. As with XRT data, source spectra were binned to a minimum of 20 counts per bin in order to use χ^2 statistics. The PN and MOS spectra were fitted jointly, allowing only the cross normalization to vary between the detectors, which is consistent within $< 5\%$. The two MOS spectra and responses were combined to maximize the signal to noise, after first checking that they were consistent with each other. The average net source count rates obtained over the whole observation are $0.58 \pm 0.01\,\mathrm{counts\,s^{-1}}$ for the PN and $0.20 \pm 0.01\,\mathrm{counts\,s^{-1}}$ per MOS module.

Allowing the absorption column to vary in the spectral fit results in a formally acceptable fit ($\chi^2/\mathrm{dof} = 515/496$). The N_H obtained is $3.1 \pm 0.1 \times 10^{21}\,\mathrm{cm^{-2}}$, while the continuum photon index $= 2.07 \pm 0.04$. The time-averaged, unabsorbed, 0.2–10.0 keV flux obtained for the afterglow is $3.2 \times 10^{-12}\,\mathrm{erg\,cm^{-2}\,s^{-1}}$. These values are consistent with the *Swift* XRT measurement obtained at the time of the *XMM-Newton* observation.

The *XMM-Newton* afterglow spectra were also sliced into three segments of approximately 8 ks in length, in order to search for any spectral evolution within the *XMM-Newton* observation. No change in the continuum parameters was found, all three spectral segments being consistent with photon index = 2.1 and $N_H = 3 \times 10^{21}\,\mathrm{cm^{-2}}$. The spectrum obtained from the PN detector and residuals to an absorbed power-law model (with $\Gamma = 2.08 \pm 0.02$ and $N_H = 3.2 \times 10^{21}\,\mathrm{cm^{-2}}$) are shown in Figure 3.6.

3.1.4.2 Joint *XMM-Newton* /*Swift* Modeling of the Afterglow

The power-law decay index obtained from the *XMM-Newton* observation ($\alpha = 1.4$) appears to be steeper than that obtained from the *Swift* XRT in orbit 2 ($\alpha = 1.0$). In order to compare between the *XMM-Newton* and *Swift* afterglow lightcurves, a combined lightcurve from the *XMM-Newton* and *Swift* observations was produced,

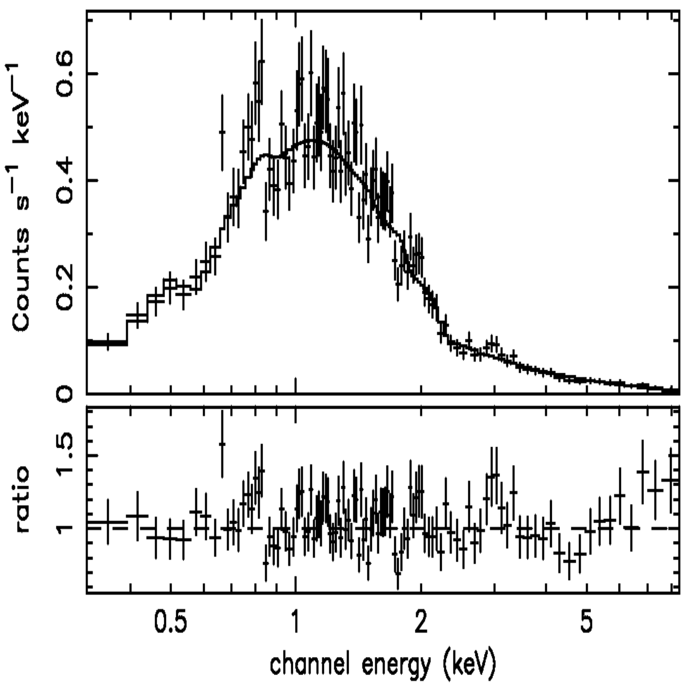

Fig. 3.6 PN spectrum from the first 8 ks of the *XMM-Newton* observation. The top panel shows the PN data (crosses) with best fit model (solid line) overlaid, which consists of an absorbed power-law with photon index = 2.07 and $N_H = 3.2 \times 10^{21}$ cm^{-2}. The bottom panel shows the data/model ratio residuals to this continuum model. A weak excess of counts is seen near 0.8 keV and 3 keV, although if interpreted as emission lines, the detection is not significant.

scaling to the absorbed continuum fluxes measured in the 0.5–10 keV band. The joint *Swift* and *XMM-Newton* lightcurve is shown in Figure 3.7, zoomed to better display the region at which the lightcurve break occurs.

A single power-law decay slope of $\alpha = 1.20 \pm 0.02$ is an extremely poor fit to the lightcurve in this region, with a fit statistic of $\chi^2/\mathrm{dof} = 201.2/65$. Indeed the lightcurve from T_0+4 ks until T_0+1000 ks can be better fitted with a broken power-law. There is a flat decay index of $\alpha = 1.02 \pm 0.07$ at early times and a steeper decay index of $\alpha = 1.45 \pm 0.06$ at later times, with the break in the decay occurring at $T_0 + 25 \pm 3$ ks. The fit statistic is then $\chi^2/\mathrm{dof} = 90.2/59$. The remaining contribution towards the χ^2 originates from two small possible flares present near $T_0+\sim 10$ ks and $T_0+\sim 45$ ks.

3.1.5 MAGIC

The MAGIC Telescope (Mirzoyan & et al. 2005) was able to observe part of the prompt emission phase of GRB 050713A in response to the alert provided by *Swift*. The observation, at energies above 175 GeV, started at T_0+40 s, 20 s after reception of the alert. It overlapped with the prompt emission phase measured by *Swift* and K-W, and lasted for 37 min, until twilight. The observation window covered by MAGIC did not, however, contain the burst onset peak detected at keV-MeV energies, where the *Swift* and K-W spectra were taken. The same region of the sky was observed 48 hours after the burst onset, collecting an additional 49 minutes of data, which was used to determine the background contamination.

The MAGIC (*Major Atmospheric Gamma Imaging Cherenkov*) Telescope is currently the largest single-dish Imaging Air Cherenkov Telescope (IACT) in operation,

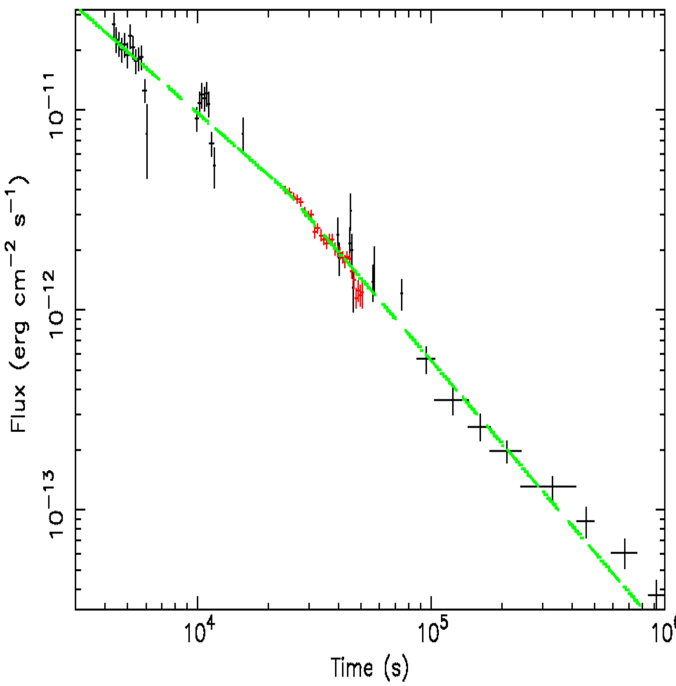

Fig. 3.7 Joint *Swift* XRT and *XMM-Newton* PN lightcurve. *Swift* data are from T_0+4 ks to T_0+1000 ks. *Swift* XRT points are shown in black and *XMM-Newton* as red. The afterglow flux is measured in the 0.5–10 keV band, not correcting for absorption. The solid line plotted to the different segments of data is a broken power-law decay model, outlined in the text. The *XMM-Newton* decay index ($\alpha = 1.45$) is considerably steeper than in the XRT at earlier times ($\alpha = 1.0$), suggesting that a break occurs in the lightcurve decay at around T_0+25 ks.

with the lowest energy threshold (60 GeV at zenith, increasing with zenith angle). In its fast slewing mode, the telescope can be repositioned within ∼30 s. In case of an alert by GCN, an automated procedure takes only a few seconds to terminate any pending observation, validate the incoming signal and start slewing toward the GRB position, as was the case for GRB 050713A.

Using the standard analysis, no significant excess of γ-like air showers from the position of GRB 050713A above 175 GeV was detected (Albert et al. 2006). This holds both for the prompt emission and during the subsequent observation periods. Figure 3.8 shows the number of excess events during the first 37 minutes after the burst, in intervals of 20 s. For comparison, the number of expected background events in the signal region, stable and compatible with statistical fluctuations, is shown. Upper limits to the gamma-ray flux are given in Table 3.1.5. This is the first observation of the GRB prompt emission phase performed by an IACT.

Energy (GeV)	Excess evts. (uplim)	Eff. Area ($\times 10^8$cm^2)	Flux lim (cm^{-2} keV^{-1}s^{-1})	Flux lim (C.U.)
$175 - 225$	8.5	1.7	1.3×10^{-17}	7.6
$225 - 300$	10.4	3.4	3.9×10^{-18}	4.8
$300 - 400$	6.0	5.3	1.6×10^{-18}	3.8
$400 - 1000$	4.3	6.5	2.3×10^{-19}	3.3

Table 3.3 MAGIC upper limit (95% CL) on GRB 050713A between $T_0 + 40$ s and $T_0 + 130$ s. Limits include a systematic uncertainty of 30%. 1 C.U. (*Crab Unit*) = $1.5 \times 10^{-6} \times (E/GeV)^{-2.58}$ ph cm^{-2} s^{-1} GeV^{-1}.

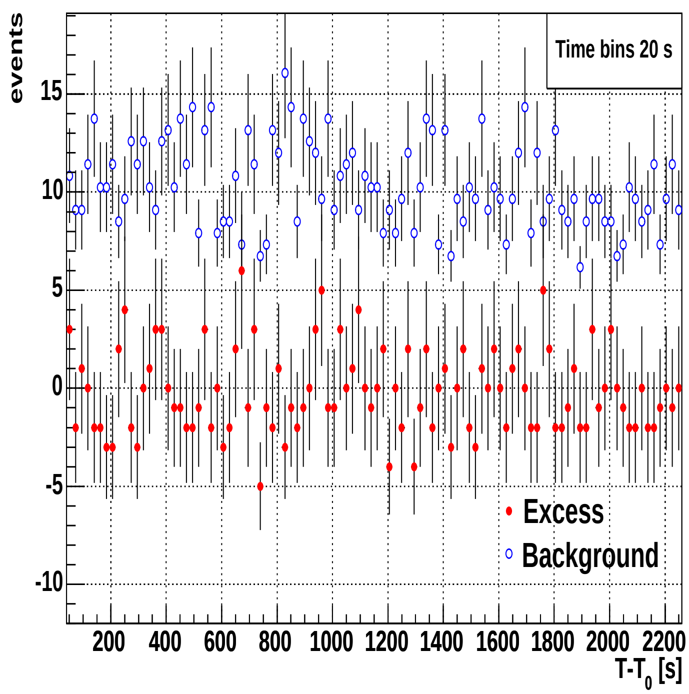

Fig. 3.8 MAGIC Observations. Filled circles: number of excess events for 20 s intervals, in the 37 min window after the burst onset. Open circles: number of background events in the signal region. No significant source signal is detected above the background.

3.1.6 Optical and Other Follow-up Observations

Optical followup observations of GRB 050713A performed by the UVOT and by ground based observatories are summarized in Table 3.4.

Table 3.4. GRB 050713A: Ground Based Optical and Radio Followup.

Observatory	Time	Band	Magnitude/Limit
McDonald Obs, Tex	T_0+22.4 s	unfilt	17.7 (lim)
RAPTOR-S, LANL	T_0+99.3 s	R	18.4 ± 0.18
Liverpool Robotic Telescope, Canary Islands	T_0+180 s	r'	19.2
Swift	T_0+252 s	V	17.98
Swift	T_0+309 s	U	17.81
Swift	T_0+311 s	UVM2	17.13
Swift	T_0+325 s	UVW1	16.85
Swift	T_0+326 s	UVW2	17.08
Swift	T_0+351 s	B	18.08
Red Buttes Obs, Wy	T_0+27m	R	19.4 (lim)
Red Buttes Obs, Wy	T_0+31m	I	18.2 (lim)
Nordic Optical Tel	T_0+47m	R	< DSS limit
Galileo National Telescope, Canary Islands	T_0+48m	I	< DSS limit
ARC Telescope, Apache Point Obs	T_0+53m	J,H,K	detected
Red Buttes Obs, Wy	T_0+93m	R	19.4 (lim)
Red Buttes Obs, Wy	T_0+98m	I	18.7 (lim)
Lulin Telescope, Taiwan	T_0+10.3h	R	22.4 (lim)
VLA, NRAO	T_0+4.3d	8.5 GHz	96 microJan

The earliest optical afterglow measurement comes from the RAPTOR-S robotic telescope at the Los Alamos National Laboratory in Los Alamos, New Mexico at R=18.4 ± 0.18 in a coadded series of 8x10 s images with a midpoint observation time of T_0+99.3 s (Wren et al. 2005). A nearly simultaneous measurement was made by the robotic Liverpool Telescope in a coadded series of 3 ∼2 minute exposures in the r′ band with a midpoint of observation of T_0+3 minutes (Malesani et al. 2005). Later detections below the Digitized Sky Survey limits were reported within the first 60 minutes after the burst trigger in the R band by the Nordic Optical Telescope (T_0+47m), in the I band by the Galileo Italian National Telescope in the Canary Islands and in the infrared J,H, and K bands by the Astronomical Research Consortium Telescope at Apache Point Observatory (T_0+53m).

Due to the bright (V=6.56) star HD204408 which is located just 68 arcseconds from the position of the burst, the UVOT background level at the position of the afterglow is significantly higher than usual, resulting in abnormally poor sensitivity of the instrument in detecting the afterglow of GRB 050713A. Considering this high background, the non-detection of the afterglow by the UVOT is not surprising.

All other reported optical observations of the afterglow position have yielded only upper limits. Most of the upper limits are near in time to the actual detections but at brighter magnitudes and thus do not produce strong constraints on the decay rate of the optical afterglow. The R-band measurement made at T_0+10.3 hours by the Lulin Telescope in Taiwan, however, is at a sufficiently late epoch to place a useful constraint on the optical decay rate. Fitting a simple powerlaw to the two well defined measurements at T_0+99.3 s and T_0+180 s and the upper limit at T_0+10.3 hours yields an upper limit on the power law decay slope of $\alpha \geq 0.5$, as is shown in Figure 3.4.

A radio followup observation made with the VLA reports no detection at T_0+4.3 days.

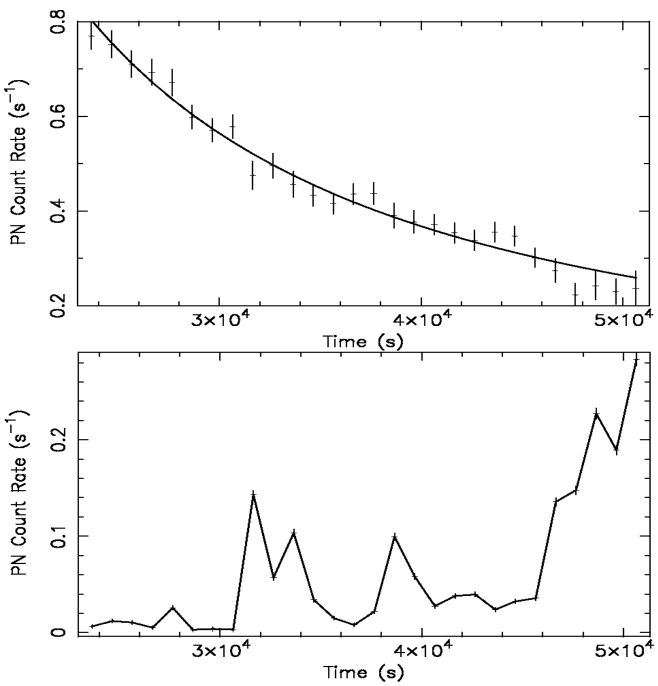

Fig. 3.9 *XMM-Newton* lightcurves for the afterglow of GRB 050713A. The top panel shows the background subtracted afterglow lightcurve for the PN detector. Crosses show the GRB source counts (1σ errors), the solid line shows the best fit decay rate of $t^{-1.45}$. Time is plotted compared to the initial BAT trigger. The bottom panel shows the background lightcurve for the PN, normalized to the size of the source extraction region for comparison.

3.2 Discussion

3.2.1 Multispectral Lightcurve Overview

The K-W light curve in the 18–1160 keV energy range is similar to the *Swift*-BAT light curve (Figure 3.1). The small precursor peak detected by BAT at T_0–70 to T_0–50 s is seen by K-W at statistically significant levels in all three broad, pre-trigger bands: G1 (18–70 keV), G2 (70–300), and G3 (300–1160 keV). The other smaller peaks detected by the BAT after the burst trigger are not seen at statistically significant levels in the K-W data, despite the fact that the peaks at T_0+50 s and at T_0+65 s are more intense in the BAT energy range than the precursor is. The detection by K-W of the precursor but not the later flares is indicative of the harder spectral index seen in the precursor as compared to the later flares (see §3.3 for discussion of separate spectral fits to individual flares).

The XRT lightcurve with BAT data overplotted is shown in Figure 3.4. Both the X-ray and gamma-ray data in the first orbit are dominated by flaring activity, making it difficult to draw a conclusion regarding the underlying powerlaw decay index from this orbit alone. The XRT data beginning at T_0+4 ks (orbit 2) and extending until T_0+40 ks show a significantly flatter powerlaw decay slope of $\alpha = -0.8$, implying that a break in the powerlaw decay has occurred near the end of the first orbit of XRT coverage at $T_0+\sim300$ s and that a period of energy injection occurs from $T_0+\sim300$ s to $T_0+\sim15$ ks. Another break in the lightcurve then occurs near T_0+25 ks to a steeper, "normal", pre-jetbreak decay slope, as shown by the *XMM-Newton* data ($\alpha \sim 1.4$). Support for this notion of the presence of an energy injection phase may be drawn from the harder X-ray spectral slope of the second orbit of XRT data (photon index = 1.9 ± 0.13) compared to the first orbit (photon index = 2.28 ± 0.04), the third orbit (photon index = 2.25 ± 0.23), and the later data (photon index = 2.8 ± 0.6) (Table 3.5). *XMM-Newton* data coverage nicely fills much of the data gap in the XRT coverage between T_0+15 ks and T_0+40 ks and provides high signal to noise data in this regime, producing a confident determination of the lightcurve break.

Table 3.5. Swift and *XMM-Newton* spectral fits pre-break and post-break.

Observatory	photon index	N_H (cm^{-2})	comment
Swift orbit 1	2.28 ± 0.04	$4.8 \pm 0.2 \times 10^{21}$	pre- energy injection phase
Swift orbit 2	1.90 ± 0.13	$3.1 \pm 0.4 \times 10^{21}$	energy injection phase
Swift orbit 3	2.25 ± 0.23	$4.1 \pm 0.7 \times 10^{21}$	flare during energy injection
Swift after orbit 3	2.8 ± 0.6	$5.6 \pm 0.2 \times 10^{21}$	post-break
XMM-Newton	2.1 ± 0.05	$3.0 \pm 0.1 \times 10^{21}$	post-break

The global picture of the lightcurve of this burst is one in which the early data (prior to T_0+12 s) shows a bright plateau in the 15 keV to 1 MeV energy range, consisting of multiple overlapping peaks. At T_0+12 s the emission drops rapidly, consistent with a curvature radiation falloff (Zhang et al. 2006) until subsequent flaring activity begins to be seen in the 0.3–150 keV region with some indication of flux at higher energies from K-W. Due to the rapid rise and decay of the flares, internal shocks from continued central engine activity appears to be the most likely explanation for these flares (Ioka et al. 2005). The earliest ground based optical detections are reported at this time also, suggesting that the flares may also be optically bright. The lack of higher resolution timing information in the optical data, though, admits the possibility that the optical emission may be unassociated with the emission mechanism responsible for the X-ray flares. It is possible that the optical emission is due to synchrotron emission from the reverse shock (RS), though the much higher flux level of the X-ray flare peaks compared to the optical measurements suggests that the X-ray flares themselves are not due to inverse Compton scattering of the optical synchrotron emission of the RS (Kobayashi et al. 2007; Gendre et al. 2007).

Following this prompt emission phase, an energy injection phase begins which dominates the lightcurve until at least T_0+16 ks. During the energy injection phase, continued activity of the central engine adds energy to the afterglow of the burst, either through additional ejection events or through the realization of energy contained in previously ejected outward moving relativistic shells which only collide at later times, producing late time internal shock emission which is then added to the overall decay (Zhang et al. 2006). It may be expected, if the energy injection phase is due to continued central engine activity, that flaring behavior would continue to be observed during this period and, indeed, some evidence for small scale flaring activity during both the second and third orbit of XRT data can be seen, though at a much reduced significance in comparison to the flaring activity of the first orbit. Near T_0+25 ks, the energy injection phase ends, giving way to a steeper decay slope similar to what is often seen in GRBs after the prompt emission phase and prior to the possible onset of a traditional jet-break (Nousek et al. 2006).

3.2.2 Flares

Many flares superimposed on top of the overall decay of GRB 050713A show the typical properties of flares seen in other bursts: that δt/t ~ 0.1 and that the peak flux level is negatively correlated with the time of the flare (Falcone et al. 2006; Barthelmy et al. 2005b). These two properties of flares seen in *Swift* GRB afterglows have been cited as evidence for flares being produced through accretion processes onto the central compact object (Perna et al. 2006), but we offer here that the constancy of the δt/t value of flares may partly be a by-product of the overall decay of the afterglow since the sensitivity of the XRT to flares is naturally degraded as the overall flux level of the afterglow decays, thus *requiring* flares at later times (and hence, lower flux levels) to be longer in duration for enough counts to be collected to produce a significant flare seen above the background. Such a case can be seen in comparing the early time flares in the first orbit of GRB 050713A to the flare seen in the third orbit. During the first orbit, the underlying flux level beneath the flares is poorly determined, but can be assumed to be 10-100 counts s^{-1}. We are dominated in this portion of the lightcurve by the Poissonian error in the flux, which in a 10 second integration will be 10-32 counts, or 3-10% . Thus, for a flare to appear at the 6 sigma level above the background during this portion of the lightcurve, at most a 60% increase in fluence above the normal powerlaw decay is needed, which can be acquired in a few seconds by the introduction of a flare with twice the flux of the underlying afterglow. During the third orbit, however, the underlying afterglow flux level has dropped to ~ 0.1 counts s^{-1}. During a 10 second integration at 0.1 counts s^{-1} the Poisson error alone is 1 count, so for a flare to be detectable at 6 sigma above background at these count levels, the total fluence must be 6 counts, implying an increase in the rate from 0.1 counts s^{-1} to 0.6 counts s^{-1} during the 10 s interval, a 6 fold increase, which has been seen only in the brighter flares. In order to be sensitive to the same 60% increase in flux level as during the first orbit, the flare which occurs at a flux level of 0.1 counts s^{-1} must have a Poission error which is 1/6 of the total counts in the observation, i.e., 36 counts must be collected, which implies an exposure time of at least 180 s if produced by the introduction of a flare with twice the flux of the underlying afterglow. In other words, because the afterglow flux level decays as $t^{-\alpha}$, the exposure time needed to acquire the same fluence level increases as t^{α}. Thus, we see that in moving from the first orbit at T_0+100 s to the third orbit at T_0+10000 s, assuming a typical underlying powerlaw decay of the afterglow of $\alpha \sim 1$, we have greatly decreased the temporal resolution of the XRT to detect flares (from a few seconds to a few hundred seconds). This is not to imply that there is not another more physical cause for the constancy of the δt/t ratio seen in flares, but rather to note that the typical GRB seen by the *Swift* XRT does not provide sufficient flux at times typically greater than a few ks to detect the shorter timescale flares that are so often seen during the first orbit.

In GRB 050713A, a hint of emission above the afterglow powerlaw decay appears in the XRT data at T_0+45 ks, though the statistics are, predictably, poor. This time is overlapped by *XMM-Newton* data, though, so we can look for evidence of a short flare in the *XMM-Newton* data at this time. In Figure 3.9 we show the *XMM-Newton* lightcurve, plotted linearly and zoomed near T_0+45 ks. Though a 1-2 sigma deviation above the background decay is seen at T_0+45 ks, the *XMM-Newton* data appear consistent with a statistical fluctuation rather than a true flare similar to those seen earlier during the burst.

The presence of multiple flares in GRB 050713A argues against "one-shot" emission mechanisms such as synchrotron self-Compton emission in a reverse shock or deceleration of the blastwave (Piro et al. 2005) and it argues in favor of a mechanism which can produce repeated flares, such as late time central engine activity. While it may remain possible that one of the several flares in GRB 050713A is due to the RS or the onset of the afterglow due to external shocks, the steep temporal decays of all the temporally fitted flares coupled with the photon indices of the flares ($1.25 \sim 2.5$; Table 3.6) do not satisfy the closure relations of Sari et al., (1998), Chevalier & Li (1999) and Sari et al., (1999) for propagation of the blast wave into either a wind or constant density ISM. Together these points seem to argue in favor of an internal shock origin for the flares seen in this burst.

segment	**1**	**2**	**3**	**4**	**5**	**6**	**7**	**8**	**9**	**10**
δt (s)	–70 - –49.5	0-8.5	8.5-25	0-16.5	59-68	68-95	100-113	113-150	159-171	171-200
Instr	BAT	and	K-W		BAT		XRT	and	BAT	
powerlaw:N_H	NA	NA	NA	NA	NA	0.56	0.64	0.65	0.59	0.42
powerlaw:Γ	1.45	1.56	1.57	1.55	1.85	2.48	1.72	2.69	2.53	2.58
powerlaw:χ^2_ν	1.19	2.18	1.35	2.62	1.13	1.23	1.28	1.16	0.90	0.94
powerlaw:dof	12	111	91	103	25	75	99	126	23	38
cutoff:N_H	NA	NA	NA	NA	NA	0.57	0.58	0.59	0.59	0.42
cutoff:Γ	1.39	1.29	1.32	1.28	1.71	2.50	1.56	2.27	2.53	2.58
cutoff:E_0	4371	541	390	489	308	9982	41	7.1	9811	9357
cutoff:χ^2	1.23	1.09	1.04	1.14	1.15	1.24	1.18	1.15	0.93	0.96
cutoff:dof	11	110	90	102	24	74	98	125	22	37
Band:N_H	NA	NA	NA	NA	NA	0.48	0.31	0.40	0.42	0.51
Band:α	-1.39	-1.30	-1.39	-1.31	-1.05	-0.95	-0.08	-0.39	-0.58	-1.71
Band:β	-1.45	-9.4	-8.8	-9.37	-2.09	-2.42	-2.42	-2.73	-2.45	-2.64
Band:E_0	172.7	565	496	546	49	1.0	2.15	0.95	1.0	1.0
Band:χ^2_ν	1.23	1.14	1.08	1.23	0.92	1.23	1.02	1.13	0.95	0.96
Band:dof	10	109	89	101	23	73	97	124	21	36
powerlaw+BB:N_H	NA	NA	NA	NA	NA	0.58	0.58	0.43	0.60	0.60
powerlaw+BB:kT	3.61	46.9	26.5	38.6	8.8	7991	1.12	0.40	46.4	1.11
powerlaw+BB:bb_{norm}	0.06	1.88	0.47	1.29	0.14	8720	0.044	0.015	0.097	3.5e-3
powerlaw+BB:Γ	1.24	1.70	1.75	1.68	-0.93	2.53	2.27	2.06	2.57	3.65
powerlaw+BB:pl_{norm}	0.14	16.7	7.32	13.2	4.8e-6	1.32	1.10	0.66	0.59	0.61
powerlaw+BB:χ^2_ν	1.18	1.31	1.03	1.43	1.08	1.20	1.06	1.12	0.79	0.92
powerlaw+BB:dof	10	109	89	101	NA	73	97	124	21	36

Table 3.6 GRB 050713A: Joint Spectral Fits - Data are grouped into segments to separate times which may show different spectra. Segments 1-4 contain BAT and K-W data and are segmented to separate prompt emission from the rapid decay. Segment 5 contains BAT data only and segments 6-10 contain XRT and BAT data. These are segmented to separate the rise and decay of each flare. We attempt fits to each segment using 4 models: 1) an absorbed powerlaw 2) an absorbed cutoff 3) an absorbed Band function and 4) an absorbed blackbody plus powerlaw. In segments where a particular model was inapplicable or the fit did not converge, NA is entered.

3.2.3 Joint Spectral Fitting

Due to the relatively narrow spectral response function of the BAT (15–150 keV for mask-tagged events) and the XRT (0.3–10 keV), a spectral fit to data from only one of the two high energy instruments on *Swift* is usually not able to discriminate between higher order spectral models. Analysts and authors are usually limited to fitting the data with a power-law or possibly the Band function (Band et al. 1993) in cases of high signal to noise ratio. In GRB 050713A we have a rare case of simultaneous detection between BAT and XRT (0.3–150 keV) and also between BAT and K-W (15 keV–14 MeV). Taking advantage of the data overlap where appropriate, considering the relative flux levels in the three instruments, we have jointly fitted spectral datasets between the two pairs of instruments. During the precursor and from T_0+0 to T_0+16.5 s, we perform joint fitting between BAT and K-W data. From T_0+16.5 to T_0+78 s we have only BAT data. From T_0+78 to T_0+116 s and during the onset of the flare at T_0+160 we perform joint fitting between XRT and BAT. We have grouped the data into segments (as shown in Table 3.6) in order to temporally separate data which we expect may show significantly different spectral parameters. Segments 1-4 contain BAT and K-W data and are segmented to separate the precursor from the prompt emission and the prompt emission from the rapid decay phase. Segment 5 contains BAT data only and segments 6-10 contain XRT and BAT data. These are segmented to distinguish the 3 flares which have overlapping data and also to separate the rise of each flare from the decay of each flare. We attempt fits to each of these segments using 4 different spectral models: 1) an absorbed powerlaw 2) an absorbed cutoff powerlaw 3) an absorbed Band function and 4) an absorbed blackbody plus powerlaw.

3.2.3.1 Segment 1: precursor (T_0–65 to T_0–55 s)

The precursor is the most poorly sampled of all the regions. Both the BAT data and KW data (KW has only 3-channel data at this time since the instrument had not yet triggered into its burst follow-up mode) show a rising slope of the νF_ν spectrum. The peak of the spectrum is not observed but we can place a lower limit on the peak energy of the spectrum for this segment by looking at the cutoff powerlaw fit which shows a 90% lower limit of 252 keV (note that the Band function parameter E_0 is unconstrained). It is interesting to note that a powerlaw plus blackbody is a reasonable fit to this segment in the context of models suggesting a thermal signature associated with the breakout of the jet cocoon from the photosphere, but the addition of the blackbody component is not strictly required over the simple absorbed powerlaw, which is found to be an adequate fit in this case. Of all the segments fit, the precursor appears to have the hardest spectrum since it *i)* shows the steepest spectral index in the powerlaw fits, *ii)* is the only segment with $\beta > -2$ in the Band function fits and *iii)* is the only segment with a combination of a very flat spectral index and high turnover energy in the cutoff powerlaw model. This is contrary to the typical reported observation that precursors tend to be softer than the burst prompt emission (Lazzati 2005).

3.2.3.2 Segment 2: prompt emission plateau (T_0+0 to T_0+8.5 s)

The plateau of the prompt emission is best fit by an exponentially cutoff powerlaw model with photon index = 1.29 and E_{cutoff} = 541 keV. A Band function fit to this segment is also reasonable (though not required) and reaffirms the turnover energy of the spectrum with E_0=565 keV. A simple powerlaw is an unacceptable fit to this segment, as is the normal situation for prompt emission spectra. A powerlaw plus blackbody is also a poor fit to the prompt emission segment. Next to the precursor, the prompt plateau has the second hardest spectrum of all the segments fit.

3.2.3.3 Segment 3: rapid decay (T_0+8.5 to T_0+25 s)

As with the other data segments which contain K-W data, the rapid decay segment is poorly fit by a simple powerlaw and is better fit by a cutoff powerlaw, Band function or powerlaw plus blackbody model. The photon index of the cutoff powerlaw in segment 3 is quite similar to that in the prompt plateau, but the cutoff energy is somewhat lower (390 keV compared to 541 keV in the plateau), suggesting that the highest energy flux is "shutting off" during the rapid decay phase. A Band function fit also shows similar values of α and β between the two segments with a decaying value of E_0 (496 keV in this segment compared to 565 keV in the previous). A powerlaw plus blackbody fit suggests a hard spectral index (0.75) with a soft X-ray thermal component (kT = 26.5 keV).

3.2.3.4 Segment 4: plateau + rapid decay (T_0+0 to T_0+16.5 s)

This segment is an extension of the prompt segment to slightly later times, encompassing slightly more data. The cutoff powerlaw is the best fit, with photon indices similar to segment 2 and E_{cutoff} between that in segments 2 and 3. A Band function fit is also reasonable in this segment, indicating α and β similar to segments 2 and 3 with E_0 between the two, as expected. The powerlaw and powerlaw plus blackbody are unacceptable.

3.2.3.5 Segment 5: rise of T_0+60 s flare (T_0+59 to T_0+68 s)

This segment contains only BAT data and is included for completeness, though the narrowness of the BAT spectral response limits the ability to distinguish between models. A simple powerlaw is an adequate fit with photon index of 1.85. N_H is unconstrained. The powerlaw plus blackbody model produces a good fit to this segment, but does so with a very flat spectral index (∼-2) which is difficult to understand in the context of the other segments which show much steeper spectral indices of ∼+2. Therefore we consider the powerlaw plus blackbody model inapplicable to this segment. A Band function and cutoff powerlaw are both adequate fits to this segment and suggest a significant softening of the spectrum. The cutoff powerlaw shows E_{cutoff} unconstrained but a softer spectral index than the preceding segments while the Band function places an upper limit of E_0=363 keV, below the measured values of the previous segments.

3.2.3.6 Segment 6: decay of T_0+60 s flare (T_0+68 to T_0+95 s)

Only in this segment, the data time ranges are mismatched between XRT and BAT (due to XRT observations beginning towards the end of the flare decay). Rather than ignore this flare or consider only the later part of the flare decay where XRT and BAT data coverage overlap, we have chosen to fit the entire BAT time range from T_0+68 to T_0+95 s together with the T_0+79 to T_0+95 s XRT data (note that the Image Mode data taken at T_0+73 s are highly piled up and cannot be used spectrally) for consistency with our treatment of the other flares. A simple powerlaw is a good fit to this segment, yielding $N_H = 5.6 \times 10^{21} \mathrm{cm}^{-2}$ and a photon index of 2.48, significantly softer than the rise of the flare, as expected. The Band function fit is also acceptable and places an upper limit of E_0=2.32 keV, again suggesting a much softer spectrum than the flare onset, as expected. The cutoff powerlaw and the powerlaw plus blackbody models are adequate fits according to χ^2, but since the cutoff energy and blackbody energy are unconstrained we do not consider them further.

3.2.3.7 Segment 7: rise of T_0+100 s flare (T_0+100 to T_0+113 s)

In the rise of the brightest flare seen in XRT, both an absorbed powerlaw plus blackbody model and an absorbed Band function model are significantly better fits (F-test probability of 2×10^{-3} and 3×10^{-4} respectively) than a simple absorbed powerlaw. The powerlaw plus blackbody indicates $N_H = 5.8 \times 10^{21} \mathrm{cm}^{-2}$ and a relatively soft photon index of 2.27 with a blackbody temperature of kT= 1.12 keV. The absorbed Band function indicates $N_H = 5.8 \times 10^{21} \mathrm{cm}^{-2}$ and low and high energy photon indices of $\alpha = -0.08$ and $\beta = -2.42$, respectively, with E_0=2.15 keV. These two models are somewhat degenerate in this dataset, with both models producing a roll over in flux at low (below 0.5 keV) and high (above 50 keV) energies.

3.2.3.8 Segment 8: decay of T_0+100 s flare (T_0+113 to T_0+150 s)

The decay portion of this flare is well fit by a simple absorbed powerlaw with $N_H = 6.5 \times 10^{21} cm^{-2}$ and photon index of 2.69. We note, however, that an absorbed Band function, absorbed cutoff powerlaw and absorbed powerlaw plus blackbody are equally good fits to the data. The Band function fit shows α and β consistent with the previous segment but with E_0 shifted significantly lower, with an upper limit of E_0=1.12 keV. The cutoff powerlaw and powerlaw plus blackbody models are consistent with a spectrum peaking in the soft X-ray as well.

3.2.3.9 Segment 9: rise of T_0+160 s flare (T_0+159 to T_0+171 s)

The rise of the last flare with overlapping data is well fit by a simple absorbed powerlaw with $N_H = 5.9 \times 10^{21} cm^{-2}$ and photon index = 2.53, however the absorbed powerlaw plus blackbody is, strictly, a better fit according to the F-test, though only at about the $90 - 95\%$ confidence level (F-test probability = 0.07), with $N_H = 6.0 \times 10^{21} cm^{-2}$, kT=46 keV and photon index of 2.57. We note that the value of kT is actually unconstrained on the high end, and so is actually only a lower limit of kT $>$ 23.4 keV. The cutoff powerlaw returns an unconstrained value of E_{cutoff}, making it an unpreferred model. The Band function fit is acceptable and has α and β consistent with previous segments and $E_0 < 2.37$ keV, consistent with a slightly higher energy than the previous segment.

3.2.3.10 Segment 10: decay of T_0+160 s flare (T_0+171 to T_0+200 s)

The decay of this flare is well fit by an absorbed powerlaw with $N_H = 4.2 \times 10^{21} cm^{-2}$ and photon index of 2.58. As with segment 9, the absorbed powerlaw plus blackbody is also an acceptable fit with $N_H = 6.0 \times 10^{21} cm^{-2}$, kT=1.1 keV and photon index of 3.65. Also similar to segment 9, the cutoff powerlaw returns an unconstrained value of E_{cutoff}, making it an unpreferred model while the Band function fit is acceptable and has α and β consistent with previous segments and shows $E_0 < 1.24$, consistent with a decrease from the previous segment. It should be noted that the BAT flux is very near the noise level in this segment and really provides only an upper limit on the spectral fitting process in the higher energy region.

3.2.4 Broadband SED

We have produced the broadband SED (spectral energy distribution) of the afterglow of GRB 050713A over the time range from T_0+20 s to T_0+300 s (Figure 3.10). This time range includes detections of the burst afterglow in the optical from the RAPTOR-S and Liverpool telescopes (corrected for the galactic extinction in this direction of A_R=1.04 (Schlegel et al. 1998)) and in the X-ray from *Swift* BAT and XRT. It also includes upper limits in the gamma-ray energy range from K-W (whose detectable emission ends at $T_0+\sim$10 s) and in the GeV energy range from MAGIC. A similar SED has been addressed by the MAGIC collaboration in their paper regarding the MAGIC flux upper limit (Albert et al. 2006) in which they note that the SED composed of data from *Swift* and MAGIC (0.2 keV to 400GeV) is fit by a Band function at low energy and that the MAGIC data are consistent with a single unbroken powerlaw extending from E_{peak}

(at $\sim$ 400 keV) to the MAGIC limits up to 500 GeV. We confirm this result, citing a best fit photon index for a single powerlaw fit from 400 keV to 500 GeV of $\Gamma = 2.1 \pm 0.1$ and a reduced $\chi_r^2 = 1.66$ for 63 dof. We further note that in performing our fit to the MAGIC data, we have treated the MAGIC upper limits as data points during our fit, thus our photon index or 2.1 is only a lower limit on the true photon index of a powerlaw that would fit the true flux level at GeV energies. Our results are, therefore, consistent with the analysis of the Albert et. al., in which they show that their data are consistent with a powerlaw photon index of 2.5 from 400 keV to 500 GeV.

We add that a Band function fit remains consistent with the data when we also consider the contemporaneous optical detections. Neither a cutoff powerlaw nor powerlaw plus blackbody model are acceptable fits to the broadband SED. Figure 3.10 shows the best fit to the entire SED using an absorbed powerlaw (dotted) and absorbed Band function. The spectral parameters and fit characteristics for each of these fits are shown in Table 3.7. We have not corrected for the attenuation of flux above 10GeV due to photon-photon interactions with the infrared background (de Jager & Stecker 2002; Kneiske et al. 2004; Primack et al. 2005). Our spectral fitting results will remain valid independent of this effect, however, due to the constraints placed on the fit by the K-W limiting flux measurement from 20 keV to 14 MeV.

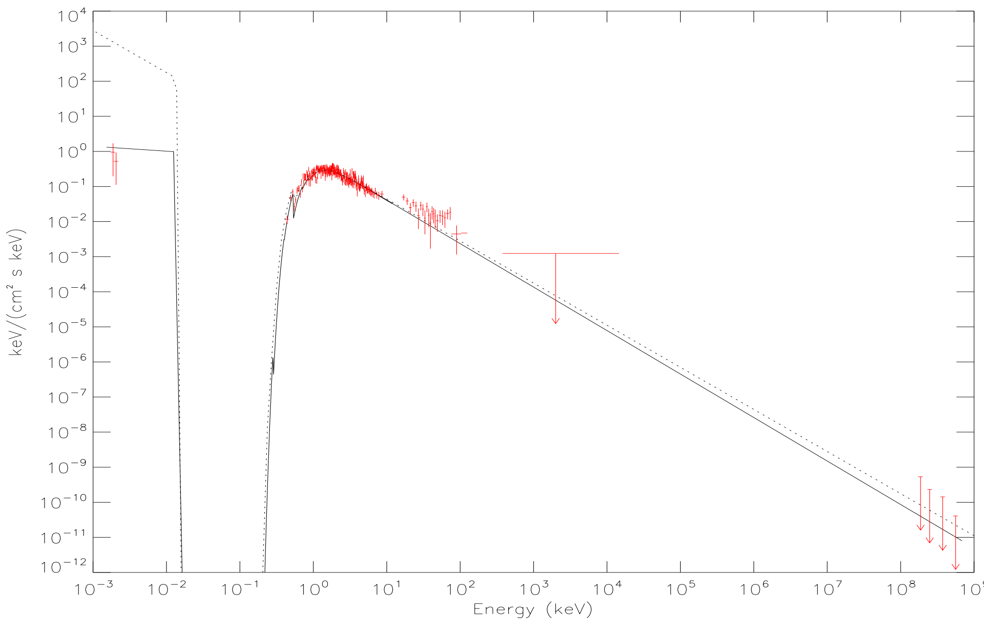

Fig. 3.10 Combined multi-platform SED of the early afterglow of GRB 050713A from T_0+20 s to T_0+300 s. Optical data are from RAPTOR-S at LANL and the Liverpool robotic telescope, soft X-ray (0.2–10 keV) data are from *Swift* XRT, hard X-ray (15–150 keV) data are from *Swift* BAT and gamma-ray upper limits are from Konus-Wind (0.5–14 MeV) and MAGIC (175–500GeV). The two lines plotted over the data represent the models discussed as proposed fits to the SED in the text. The absorbed Band function (solid) is an acceptable fit while the simple absorbed powerlaw (dotted) does not appear reconcilable with the data. The results suggest that the GRB flare emission is characterized by a single mechanism well represented by a smoothly broken powerlaw (ie, the Band function), or that a more complex, possibly multi-component emission mechanism is required to explain the complete SED.

Model:Param	Value
powerlaw:N_H	4.3×10^{21} cm^{-2}
powerlaw:Γ	2.14
powerlaw:χ^2_ν	10 (65 dof)
Band:N_H	$4.2 \pm 0.3 \times 10^{21}$ cm^{-2}
Band:α	-1.24 ± 0.10
Band:β	-2.24 ± 0.02
Band:E_{peak}	2.0 ± 0.4 keV
Band:χ^2_ν	1.19 (63 dof)

Table 3.7 GRB 050713A: SED Fit Data - A broadband SED (R-band optical data points to 500GeV upper limits) has been created and we show the result of fits of an absorbed powerlaw and an absorbed Band function. Only the Band function is an acceptable fit to the entire SED.

3.3 Conclusions

3.3.1 Summary

GRB 050713A is one of the rare bursts observed simultaneously in soft X-rays (XRT), hard X-rays (BAT) and gamma-rays (K-W). The broad spectral coverage of these simultaneous measurements has allowed us to fit the early prompt emission, rapid decay, and several flares in the early emission with several different spectral models. In general we find a cutoff powerlaw model to be a good fit to segments with data extending into the MeV range, thus able to constrain the high energy component of the model. For data segments with 0.3–150 keV coverage (BAT and XRT data) we find that a simple absorbed powerlaw is often an adequate fit to the data, though an absorbed powerlaw plus blackbody or absorbed Band function model seems to sometimes be a marginally better fit during periods of flaring activity.

The lightcurve structure of GRB 050713A is quite typical of many GRBs that have been observed by *Swift* . It has an early section showing steep decay slopes of $\alpha > 5$

and bright flares extending until T_0+~1 ks, followed by a break to a flatter section with decay slope $\alpha \sim$ 1.0 lasting until T_0+~25 ks, followed by a break to a steeper slope of $\alpha = 1.45$. The temporal properties of the flares seen in GRB 050713A, beginning as early as T_0+80 s and as late as T_0+10 ks argue for internal shocks as the likely emission mechanism rather than some other process associated with the external shock. Evidence for this is that all flares are found to have steep powerlaw rise and decay slopes and $0.1 < \delta t/t < 1$ (Burrows et al. 2005b; Ioka et al. 2005), the presence of multiple flares which argues against one-shot mechanisms such as the onset of the afterglow (Piro et al) and the failure of the flares to fit the closure relations associated with the external shock in a wind or constant density ISM.

We have temporally separated the early, flaring portion of the burst into 10 segments and attempted to fit each segment using 4 different spectral models: 1) an absorbed powerlaw 2) an absorbed cutoff powerlaw 3) an absorbed Band function and 4) an absorbed blackbody plus powerlaw. In all segments where at least two instruments provide significant, simultaneous levels of emission, and hence the spectral data span more than 2 decades in energy, we find that at least one of the higher order spectral models is acceptable and, in several cases, is a better fit to the data than a simple absorbed powerlaw. This suggests that the spectral shape of GRB flares, while consistent with a simple absorbed powerlaw when viewed through any particular narrow spectral window, is intrinsically fit, in the broadband, by a model with attenuated flux above (and possibly below) some threshold energy. It has long been known that GRB prompt emission is better fit by spectral models with a high (and sometimes low) energy cutoff than by a simple absorbed powerlaw (Band et al. 1993; Ryde 2005b). This has been interpreted as evidence of spectral breaks associated with the cooling frequency of the electron population (on the high energy end) and with the synchrotron self-absorption frequency (on the low energy end). The indication that GRB flares are fit by a similar spectral model suggests that similar emission mechanisms may be responsible for the production of flares and of the prompt emission itself, namely internal shocks produced as a result of central engine activity.

Finally, we have created a broadband SED of the flaring region of GRB 050713A from 0.002 keV to 500GeV at times from T_0+20 s to T_0+300 s. We find that the SED is inconsistent with a single absorbed powerlaw and is best fit by an absorbed Band function. This overall SED again implies that GRB flares are best fit by a spectral model similar to that of the prompt emission itself and thus suggests a common mechanism for the emission from the prompt phase and from flares.

3.3.2 GRB 050713A as an X-ray Flaring Case Study

Through our segmented spectral analysis of the prompt emission and early X-ray afterglow phases of this burst we see several interesting features of X-ray flares. We have examined three X-ray flares occurring in rapid succession during this burst, beginning at observer times $T_0+\sim59$, $T_0+\sim100$ and $T_0+\sim159$ s after the burst trigger as well as a smaller flare occurring at $T_0+\sim9700$ s. All three early time flares are well sampled by both the XRT and BAT, except during the onset of the first flare which is observed by the BAT only. Within each of these early flares, we see evidence of a relatively hard spectrum during the flare onset followed by a softer spectrum during the flare decay. This behavior is shown in the Band function model fits as an evolution in

E_{PEAK} where the 90% upper limit of E_{PEAK} moves from 345 to 2.5, 6.0 to 1.8 and 3.4 to 0.4 keV, respectively, from the onset to the decay of each of the three successive early flares. This hard to soft evolution is a well-known characteristic of GRB prompt emission (Golenetskii et al. 1983; Norris et al. 1986) and is seen also during the prompt emission phase of GRB 050713A, arguing in favor of a common origin for the prompt emission pulses and these early X-ray flares. The evolution of the late time, low-level X-ray flare is less clear; there is some evidence that the flare may actually appear harder at later times, but given that the flare has a low contrast level compared to the underlying afterglow, we cannot rule out the possibility that this behavior is due to uncertainty in assigning the relative flux level between the flare and UAD. Note that this issue is not of concern in the early time flares where the contrast level is much higher between flare and afterglow, making the uncertainty due to the relative flux level between the two components insignificant.

For the three early time flares, we also notice that the peak energy of each successive flare onset segment and the peak energy of each successive flare decay segment is progressively lower implying also that the spectrum of each successive entire flare is characterized by a spectrum with a lower peak energy than the last. It is unclear if the pattern continues with the late time flare due to uncertainties introduced by the low flux level as discussed above. The peak energy of the first flare in the series is somewhat more difficult to determine accurately since we have only BAT observations during the first half of the flare, while XRT observes only the decaying portion. If we fit a Band function to the BAT data alone, we find $E_{PEAK} \sim 21.0$ keV. We can also fit a power-law to the BAT-only data and then use the relation between Γ and E_{PEAK} (Sakamoto et al. 2007) to find E_{PEAK} = 48 keV. Finally, if we consider the BAT data together with XRT data (available only during the flare decay) we find E_{PEAK} = 1.2 keV. We can be fairly certain that the fit of E_{PEAK} = 1.2 keV is a lower limit since the XRT data comes from the decay of the flare only, therefore omitting the hard emission likely to have occurred during the flare onset. We also note that the spectrum in the BAT energy range is extremely flat, making the measurement of α, and therefore E_{PEAK} very poorly constrained (α, in fact, is effectively unconstrained). The situation of a flat BAT spectrum with poorly constrained E_{PEAK}, however, is exactly the situation in which the Sakamoto et al relation is expected to be used. We, therefore, adopt E_{PEAK}=48 keV as our measure of the peak energy of this flare.

If we fit a powerlaw in time to the E_{PEAK} values of the three early flares in our data, we find a powerlaw relationship $E_{PEAK} \propto t^{-5.1\pm0.8}$. Krimm et al. (2007) have followed a similar procedure in their analysis of GRB 060714 by fitting a powerlaw in time to 5 early flares observed in the BAT and XRT and find a consistent result to ours with $E_{PEAK} \propto t^{-5.81\pm0.68}$. We have also fit a powerlaw in time to the fluence of these 3 early flares, finding a relationship $S \propto t^{-2.4\pm0.8}$. We note that this is also consistent with a similar relation between E_{ISO} and flare time found by Krimm et al in the early flaring behavior of GRB 060714, $E_{ISO} \propto t^{-1.72\pm0.46}$. The presence of these trends in the early flaring behavior of these two bursts supports theories of flare production which naturally invoke decaying energetics such as the fallback model proposed by Perna et al. (2006). At the same time, however, it is clear that these relations cannot hold for all X-ray flares observed by *Swift* since they imply peak energies in the sub-mm and fluences of 10^{-10} ergs cm^{-2} at times of $T_0 + \sim 1000$ s, times at which we regularly observe X-ray flares with fluences much higher than this, such as the flare in GRB 050713A seen in the X-ray at $T_0+\sim$10000 s with S$\sim 10^{-8}$ ergs cm^{-2}.

The implication, then, is that if the relations which appear to hold for the early flares in GRB 050713A and GRB 060714 are ubiquitous, the mechanism responsible for the production of these early flares cannot also be responsible for such late flares as that seen in the third *Swift* orbit of GRB 050713A or numerous other late flares such as that seen in GRB 050502B beginning at $T_0+\sim$40ks (Falcone et al. 2006). This encourages us to undertake a broad survey of all the flares observed by *Swift* in order to characterize them both temporally and spectrally and to try to determine whether they are all consistent with a single emission mechanism (as seems to be argued against by our reasoning above) or, to the contrary, whether we can identify distinguishing characteristics among the flares in the *Swift* archive which appear to identify them with a particular proposed emission mechanism from the literature. We will begin this search in Chapter 4 with a survey of all X-ray flares observed during the first year of *Swift* operations.

Chapter 4

Flares Study I: The first year of Swift data

(published as Falcone et al. (2007), ApJ, 671, 1921)

4.1 The Sample

The sample of flares in this analysis was chosen from the first ~ 12 months of *Swift* data (actually slightly more than twelve months in calendar time but slightly less than 12 months of time during which *Swift* was under normal operations) running from the start of automated slewing on January 17, 2005 to January 24, 2006. All bursts in this time period were inspected for any hint of deviation from the *Swift* canonical GRB decay profile (Zhang et al. 2006; Nousek et al. 2006; O'Brien et al. 2006). After culling bursts without any suggestion of flaring, the remaining burst lightcurves were fit with a temporal powerlaw to represent the non-flaring segment(s) of the afterglow (the underlying afterglow decay (UAD), referred to in the text by the subscript "UAD"). After fitting a powerlaw decay to the quiescent part of the afterglow decay, two separate powerlaws were then fit to the data to represent any possible flares superposed atop the afterglow, one for the rising leg and one for the decaying leg of the potential flare. The start and stop times of each potential flare (hereafter t_{start} and t_{stop} respectively) were then defined as the intersection of the UAD powerlaw with flare rising and decaying powerlaws respectively (see Chapter 2 for further details of the flare temporal fitting method). Any potential flares meeting the criteria of S/N > 3 were added to the sample where S/N is the signal to noise ratio of the flare with respect to the UAD afterglow defined as:

$$S/N = \frac{N_{TOTAL} - N_{UAD}}{\sqrt{N_{TOTAL} + N_{UAD}}} \tag{4.1}$$

where N_{TOTAL} is the total number of photons arriving between t_{start} and t_{stop} and N_{UAD} is the number of photons expected from the UAD during the duration of the flare.

From a surveyed sample of 110 bursts, 33 bursts were found to contain at least one flare of 3-σ significance. Many bursts showed 2 or more flares resulting in a total of 77 flares in our sample. We have attempted to be as complete as possible in this analysis, including all excesses above the UAD afterglow meeting our 3 σ criteria to avoid, as much as possible, introducing flux-based selection biasing. One difficulty that arises when including all flares in our sample is that several of the flares are overlapping in time, making the unique identification of start times or stop times or both, as defined above, quite difficult. The definition of start and stop times in such cases where flares are overlapping and the subsequent flux and fluence corrections undertaken to account for the "missing" data in these cases will be treated in greater detail in due course in the text. X-ray lightcurves of each burst analyzed in this chapter are found in Appendix A.

4.2 Temporal Analysis

We note that there is a companion work by Chincarini et al. (2007) to the analysis presented in this chapter which presents a separate temporal analysis of the flares from the same time period ($\sim$ first year of data). The definition of flare temporal parameters in the companion work is slightly different than here; in the companion work flares are fit to a Gaussian profile superposed atop the underlying temporal powerlaw decay of the afterglow. The duration and peak time of the flares are then defined by the widths and peaks of the Gaussians in contrast to the intersecting powerlaws method used in the analysis of this chapter and as discussed in Chapter 2. The sample in the companion work is, in fact, slightly different from the one in our analysis presented here, but this is due to the fact that fewer photons are required to perform a meaningful temporal analysis on a particular flare than are required to perform a meaningful spectral analysis. The samples are largely overlapping, however, and, furthermore, the values of the temporal parameters for common flares in the two samples are quite similar despite being derived through these different techniques, lending confidence to the temporal parameter designations of both methods. Table 4.1 shows the values of t_{start}, t_{stop} and S/N for each flare in our sample along with the time of peak XRT flux of each flare, t_{peak}.

In some cases, as alluded to in the previous section, the time range used for extraction of the flare did not include the entire flare. This may be due to the lightcurve data itself being incomplete during a portion of the flare (due to observing gaps) or to flares overlapping one another. In such cases, correction factors are applied to account for the missing flux and the uncertainty in the measured spectral parameters and flux values are augmented accordingly (and conservatively). Table 4.2 shows the time segments used for data extraction of the flares as well as the underlying afterglow. In some cases the afterglow was selected from a single contiguous data segment while in other cases it was selected from several separate segments to improve the statistics of the afterglow spectrum.

Table 4.1: The Flare Sample

GRB	**Flare**	t_{start} **(s)**	t_{stop} **(s)**	t_{peak} **(s)**	**S/N**
GRB050219a	1	118	453	120	18.5
GRB050406	1	139	361	205	11.3
GRB050421	1	136	165	156	3.4
GRB050502b	1	410	1045	695	145.7
GRB050502b	2	19958	48591	29896	7.2
GRB050502b	3	50457	178280	75355	18.4
GRB050607	1	94	255	145	10.3
GRB050607	2	255	640	312	25.2
GRB050712	1	88	564	252	31.0
GRB050712	2	302	435	339	12.9
GRB050712	3	415	590	478	8.9
GRB050712	4	788	952	888	3.8
GRB050713a	1	101	155	0	11.7
GRB050713a	2	155	210	0	3.2
GRB050714b	1	285	832	374	19.2
GRB050716	1	155	211	177	11.2
GRB050716	2	315	483	385	13.2
GRB050724	1	78	230	120	102.6
GRB050724	2	63	342	261	33.7
GRB050724	3	13406	402320	55783	19.7

Continued on Next Page…

Table 4.1 – Continued

GRB	**Flare**	t_{start} **(s)**	t_{stop} **(s)**	t_{peak} **(s)**	**S/N**
GRB050726	1	151	195	162	3.0
GRB050726	2	219	324	274	12.2
GRB050730	1	210	280	228	20.6
GRB050730	2	323	611	435	51.9
GRB050730	3	611	795	678	33.7
GRB050730	4	9654	12578	10319	33.2
GRB050802	1	312	457	435	3.8
GRB050803	1	513	879	753	5.8
GRB050803	2	889	1516	1116	4.3
GRB050803	3	4455	5703	5367	5.8
GRB050803	4	7345	27698	22669	14.2
GRB050803	5	7646	13093	11613	14.0
GRB050803	6	17240	27698	18873	5.1
GRB050814	1	1133	1974	1350	3.0
GRB050814	2	1633	2577	2138	6.1
GRB050819	1	56	253	174	11.5
GRB050819	2	9094	36722	19733	6.2
GRB050820a	1	200	382	234	66.6
GRB050822	1	106	190	143	21.3
GRB050822	2	212	276	240	8.4
GRB050822	3	390	758	433	50.9

Continued on Next Page…

Table 4.1 – Continued

GRB	**Flare**	t_{start} **(s)**	t_{stop} **(s)**	t_{peak} **(s)**	**S/N**
GRB050904	1	343	570	463	41.6
GRB050904	2	857	1141	953	3.0
GRB050904	3	1149	1343	1235	4.2
GRB050904	4	5085	9001	6765	23.0
GRB050904	5	16153	24866	17329	22.1
GRB050904	6	18383	38613	24156	19.5
GRB050904	7	25618	30978	29392	21.6
GRB050908	1	129	306	145	7.3
GRB050908	2	339	944	404	14.0
GRB050915a	1	55	170	111	14.3
GRB050916	1	16755	32357	18898	20.1
GRB050922b	1	357	435	377	12.1
GRB050922b	2	476	560	497	5.6
GRB050922b	3	630	1541	827	39.4
GRB051006	1	115	148	132	9.6
GRB051006	2	132	201	162	7.5
GRB051006	3	330	749	495	7.5
GRB051016b	1	374	1940	483	3.1
GRB051117a	1	2	4322	157	117.6
GRB051117a	2	134	2794	380	124.1
GRB051117a	3	292	1313	628	70.4

Continued on Next Page...

Table 4.1 – Continued

GRB	**Flare**	t_{start} **(s)**	t_{stop} **(s)**	t_{peak} **(s)**	**S/N**
GRB051117a	4	574	2695	926	78.6
GRB051117a	5	642	1820	1097	71.0
GRB051117a	6	1237	3119	1335	95.3
GRB051117a	7	659	3126	1535	85.8
GRB051210	1	115	152	132	4.4
GRB051227	1	86	245	120	16.7
GRB060108	1	193	429	285	2.1
GRB060108	2	4951	37986	10471	6.1
GRB060109	1	4305	6740	4810	5.0
GRB060111a	1	27	196	110	51.5
GRB060111a	2	109	203	171	38.6
GRB060111a	3	215	433	312	107.4
GRB060115	1	331	680	406	8.7
GRB060124	1	283	644	574	222.6
GRB060124	2	644	1007	694	179.8

Table 4.2: The time intervals used for spectral extraction of flares and the time intervals used for the extraction of underlying light curve spectra for each flare are tabulated. In many cases, the underlying spectra was constrained with one time interval with sufficient photons to obtain spectral parameters, and thus there are no entries in the last four columns. In some cases, statistics were maximized by using multiple time intervals for the underlying portion. In a few instances there are dashes for all underlying time intervals, indicating that the canonical value for the underlying spectral index was used, as described in the text.

		Flares			**Underlying**				
GRB	Flare	t_{begin} (s)	t_{end} (s)	$^{(1)}t_{begin}$ (s)	$^{(1)}t_{end}$ (s)	$^{(2)}t_{begin}$ (s)	$^{(2)}t_{end}$ (s)	$^{(3)}t_{begin}$ (s)	$^{(3)}t_{end}$ (s)
GRB050219a	1	118	453	670	29603	—	—	—	—
GRB050406	1	139	361	1447	919330	—	—	—	—

Continued on Next Page...

Table 4.2 – Continued

		Flares		**Underlying**					
GRB	Flare	t_{begin} (s)	t_{end} (s)	$^{(1)}t_{begin}$ (s)	$^{(1)}t_{end}$ (s)	$^{(2)}t_{begin}$ (s)	$^{(2)}t_{end}$ (s)	$^{(3)}t_{begin}$ (s)	$^{(3)}t_{end}$ (s)
GRB050421	1	136	165	167	488	—	—	—	—
GRB050502b	1	410	1045	5384	20369	161890	299820	—	—
GRB050502b	2	19958	48591	57	355	1545	19958	178280	264880
GRB050502b	3	50457	178280	57	355	1545	19958	178280	264880
GRB050607	1	94	255	92	94	685	20997	—	—
GRB050607	2	255	640	92	94	685	20997	—	—
GRB050712	1	88	299	5157	105060	—	—	—	—
GRB050712	2	302	435	5151	77682	—	—	—	—
GRB050712	3	415	590	5074	63858	—	—	—	—
GRB050712	4	788	952	5074	63858	—	—	—	—
GRB050713a	1	101	155	3541	399630	—	—	—	—
GRB050713a	2	155	210	3541	399630	—	—	—	—

Continued on Next Page…

Table 4.2 – Continued

		Flares		Underlying					
GRB	Flare	t_{begin} (s)	t_{end} (s)	$^{(1)}t_{begin}$ (s)	$^{(1)}t_{end}$ (s)	$^{(2)}t_{begin}$ (s)	$^{(2)}t_{end}$ (s)	$^{(3)}t_{begin}$ (s)	$^{(3)}t_{end}$ (s)
GRB050714b	1	285	542	3639	139690	—	—	—	—
GRB050716	1	155	211	105	155	211	331	—	—
GRB050716	2	315	483	211	331	—	—	—	—
GRB050724	1	78	230	433	27350	—	—	—	—
GRB050724	2	222	342	433	27350	—	—	—	—
GRB050724	3	13406	402320	433	27350	—	—	—	—
GRB050726	1	151	195	324	12646	—	—	—	—
GRB050726	2	219	324	324	8358	—	—	—	—
GRB050730	1	210	280	132	210	280	313	—	—
GRB050730	2	323	611	—	—	—	—	—	—
GRB050730	3	611	795	—	—	—	—	—	—
GRB050730	4	9654	12578	4366	6863	26422	99149	—	—

Continued on Next Page...

Table 4.2 – Continued

		Flares		Underlying					
GRB	Flare	t_{begin} (s)	t_{end} (s)	$^{(1)}t_{begin}$ (s)	$^{(1)}t_{end}$ (s)	$^{(2)}t_{begin}$ (s)	$^{(2)}t_{end}$ (s)	$^{(3)}t_{begin}$ (s)	$^{(3)}t_{end}$ (s)
GRB050802	1	312	457	494	2873	—	—	—	—
GRB050803	1	513	879	34808	778510	—	—	—	—
GRB050803	2	889	1516	34808	778510	—	—	—	—
GRB050803	3	4455	5703	34808	778510	—	—	—	—
GRB050803	4	7345	27698	34808	778510	—	—	—	—
GRB050803	5	10396	13093	34808	778510	—	—	—	—
GRB050803	6	17240	27698	34808	778510	—	—	—	—
GRB050814	1	1133	1974	5646	8644	32429	98328	—	—
GRB050814	2	1633	2577	5774	8741	32794	96149	—	—
GRB050819	1	154	193	—	—	—	—	—	—
GRB050819	2	9094	36722	475	7975	36722	55757	—	—
GRB050820a	1	200	258	4811	5099900	—	—	—	—

Continued on Next Page…

Table 4.2 – Continued

		Flares		Underlying					
GRB	Flare	t_{begin} (s)	t_{end} (s)	$^{(1)}t_{begin}$ (s)	$^{(1)}t_{end}$ (s)	$^{(2)}t_{begin}$ (s)	$^{(2)}t_{end}$ (s)	$^{(3)}t_{begin}$ (s)	$^{(3)}t_{end}$ (s)
GRB050822	1	106	190	5692	4932900	—	—	—	—
GRB050822	2	212	276	5911	4795400	—	—	—	—
GRB050822	3	415	616	4714	5628400	—	—	—	—
GRB050904	1	343	570	586	868	—	—	—	—
GRB050904	2	857	1141	588	876	—	—	—	—
GRB050904	3	1149	1343	588	861	—	—	—	—
GRB050904	4	5085	7110	581	865	—	—	—	—
GRB050904	5	16153	18205	586	873	—	—	—	—
GRB050904	6	22221	25379	586	873	—	—	—	—
GRB050904	7	27854	30978	586	873	—	—	—	—
GRB050908	1	129	306	—	—	—	—	—	—
GRB050908	2	339	944	—	—	—	—	—	—

Continued on Next Page. . .

Table 4.2 – Continued

		Flares		Underlying					
GRB	Flare	t_{begin} (s)	t_{end} (s)	$^{(1)}t_{begin}$ (s)	$^{(1)}t_{end}$ (s)	$^{(2)}t_{begin}$ (s)	$^{(2)}t_{end}$ (s)	$^{(3)}t_{begin}$ (s)	$^{(3)}t_{end}$ (s)
GRB050915a	1	55	170	170	7424	—	—	—	—
GRB050916	1	16755	32357	221	13085	—	—	—	—
GRB050922b	1	357	435	348	355	435	476	560	623
GRB050922b	2	476	560	348	355	435	476	560	623
GRB050922b	3	630	1541	348	355	435	476	560	623
GRB051006	1	115	148	—	—	—	—	—	—
GRB051006	2	148	180	—	—	—	—	—	—
GRB051006	3	330	749	—	—	—	—	—	—
GRB051016	1	374	1940	3778	382750	—	—	—	—
GRB051117a	1	113	231	16046	2410600	—	—	—	—
GRB051117a	2	295	571	16046	2410600	—	—	—	—
GRB051117a	3	571	729	16046	2410600	—	—	—	—

Continued on Next Page…

Table 4.2 – Continued

		Flares		Underlying					
GRB	Flare	t_{begin} (s)	t_{end} (s)	$^{(1)}t_{begin}$ (s)	$^{(1)}t_{end}$ (s)	$^{(2)}t_{begin}$ (s)	$^{(2)}t_{end}$ (s)	$^{(3)}t_{begin}$ (s)	$^{(3)}t_{end}$ (s)
GRB051117a	4	817	1044	16046	2410600	—	—	—	—
GRB051117a	5	1044	1237	16046	2410600	—	—	—	—
GRB051117a	6	1237	1466	16046	2410600	—	—	—	—
GRB051117a	7	1466	1737	16046	2410600	—	—	—	—
GRB051210	1	115	152	162	426	—	—	—	—
GRB051227	1	86	245	258	20156	—	—	—	—
GRB060108	1	193	429	—	—	—	—	—	—
GRB060108	2	4951	37986	—	—	—	—	—	—
GRB060109	1	4305	6740	8784	325220	—	—	—	—
GRB060111a	1	75	137	2905	712320	—	—	—	—
GRB060111a	2	145	204	2905	712320	—	—	—	—
GRB060111a	3	215	433	2905	712320	—	—	—	—

Continued on Next Page…

Table 4.2 – Continued

		Flares		**Underlying**					
GRB	Flare	t_{begin} (s)	t_{end} (s)	$^{(1)}t_{begin}$ (s)	$^{(1)}t_{end}$ (s)	$^{(2)}t_{begin}$ (s)	$^{(2)}t_{end}$ (s)	$^{(3)}t_{begin}$ (s)	$^{(3)}t_{end}$ (s)
GRB060115	1	331	680	117	257	—	—	—	—
GRB060124	1	283	644	10605	14232	32067	74305	—	—
GRB060124	2	644	1007	10458	14432	33443	71248	—	—

4.3 Spectral Results

This section details the results from our spectral analysis in which we have fit 4 different spectral models to each of the flares in this sample together with an added absorbed powerlaw component to account for the underlying afterglow (see Chapter 2 for analysis details). There is a wide range of S/N level within the flares in this sample, ranging from flares just over our defined threshold of 3 σ to some, such as the well known giant flare of GRB050502B, which have S/N well over 100. Including flares to as faint a level as possible has the benefit of avoiding (or at least better understanding) flux related bias issues. On the other hand, including the faintest flares in our analysis will introduce samples with poorly constrained parameter values due to the low level of precision of the spectral fits. To combat the latter problem, we define a subset of flares within our overall sample which is composed of only flares which have 15 or more degrees of freedom during a powerlaw fit. We will refer to this subsample as the *Gold* sample.

4.3.1 Spectral Parameters of the Underlying Afterglow Decay

The spectral parameters derived by fitting an absorbed power law model to the underlying afterglow of GRBs within the *Gold* sample are shown in Figure 4.1. The mean of the photon index distribution is 1.9 with a standard deviation of 0.3. This is consistent with the typical photon index for GRB afterglows.

4.3.2 Overall Spectral Parameters of the Flares

The spectral parameters derived by fitting the 4 separate spectral models to each flare in our sample are shown in Figures 4.2-4.5 and Tables 4.3-4.6. Figure 4.2 and

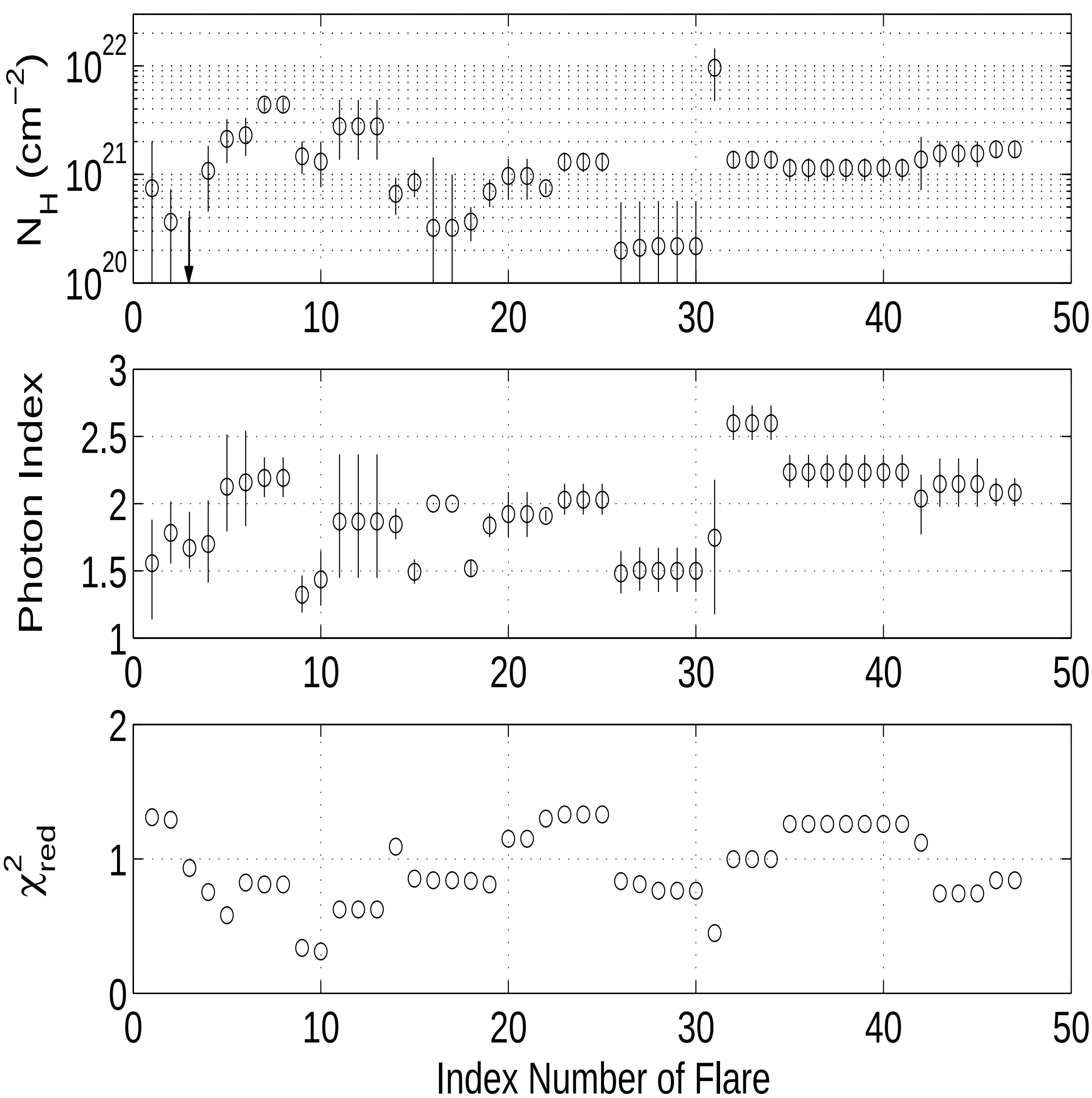

Fig. 4.1 Properties of absorbed power law spectral fits to data from an interval of the lightcurve in which *no flares* were present, for all GRBs with *Gold* flares (i.e. these are the spectral parameters of the underlying light curve). The index number of the flares shown on the x-axis simply refers to the index number for each flare shown in column 1 of Table 4.1.

Table 4.3 show results of powerlaw fits, Figure 4.3 and Table 4.4 show results of the Band function fits, Figure 4.4 and Table 4.5 the cutoff powerlaw fits and Figure 4.5 and Table 4.6 show results of the powerlaw plus blackbody fits (thermal model). All results shown here are for the *Gold* sample only. The index of each flare in the table corresponds to the x-axis value of that flare in the associated figure (e.g., flare #2 in each table is data-point #2 in each figure).

It is clear from the χ^2_ν values in Table 4.2 that a powerlaw provides a satisfactory fit in many cases. We can see from the χ^2_ν values in Tables 3-5, however, that in many cases a more complex model such as the Band function or thermal model appears to provide a superior fit. In order to explore the level of improvement represented by these varying fits, Figure 4.6 shows the histogram of $\Delta\chi^2$ between the powerlaw fits and the Band function fits for the 47 flares in the *Gold* sample (the flares shown in Figures 4.2-4.5 and Tables 4.3-4.6). The mean degrees of freedom in the fits using each model were 130 and 128 respectively.

An improvement in the fit is naturally expected when moving from a lower order model such as a powerlaw to a higher order model such as the Band function. To examine whether the improvement we see is simply a consequence of this expected behavior or whether it indicates that the Band function is actually a better fit to the data, we have created a similar $\Delta\chi^2$ figure comparing artificially generated powerlaw spectra fit with a powerlaw model and with a Band function. To do this, we created 1000 simulated spectra, using the XSPEC *fakeit* command and the appropriate XRT RMFs and ARFs. The simulated spectra were created in Monte Carlo fashion using a photon index drawn from a distribution with mean of 1.9 and standard deviation of 0.3 (the mean and standard deviation of the observed photon index distribution) and were simulated to have a similar number of degrees of freedom as the flares in our observational sample. We then fit these spectra in the same way as we fit our observational sample, first using a powerlaw model, then using a Band function model. The $\Delta\chi^2$ distribution of the simulated powerlaw spectra fit in this way is a representation of the natural improvement in χ^2 expected from simply using a higher order spectral model (ie, not a true improvement in the fit). This distribution is overplotted as a solid curve on the experimental $\Delta\chi^2$ distribution of Figure 4.6 for comparison.

As can be seen in Figure 4.6, the $\Delta\chi^2$ distribution of the Band-powerlaw model fits to our observational flares sample is skewed to positive values more than is the distribution produced from artificial powerlaw spectra, suggesting that the flares in our sample are intrinsically better represented by the Band function than by a simple powerlaw. One way to quantify this notion is to compare the number of flares with a large $\Delta\chi^2$ value in the observational sample and in the simulated sample. In the simulated sample, there are 5 out of 1000 events showing $\Delta\chi^2 > 9.0$, implying that one should expect, purely by chance, 0.23 of the 47 flares in our observational sample to have a $\Delta\chi^2$ larger than 9.0 if our observational sample is composed of flares that are truly best represented by a powerlaw. In fact, our observational sample shows 9 out the 47 flares with $\Delta\chi^2 > 9$. This suggests that it is unlikely that the observed spectra of the flares in our sample are actually drawn from a distribution of powerlaw spectra and makes it clear that at least some cases in our sample are better fit by a Band function than by a powerlaw model. It is worth mentioning, however, that a powerlaw can provide a reasonable fit to many of the flares in this analysis (ie, flares observed at moderate spectral resolution with moderate signal to noise and in the 0.3 to 10.0 keV energy range).

We note here that no compelling evidence was found to prefer either the exponentially cutoff powerlaw model or the powerlaw plus blackbody model in our observational sample. For this reason, for the remainder of this chapter we will discuss further only the results of the powerlaw and Band function fits.

Table 4.3: Properties of power law spectral fits to *Gold* flares

Index	**GRB**	**Flare**	**N**$_H$ ($10^{20} cm^{-2}$)	Γ	χ^2_{red}	**DOF**
1	GRB050219	1	$39.9^{+11.1}_{-9.1}$	$2.67^{+0.41}_{-0.34}$	1.09	38
2	GRB050502	1	$11.7^{+0.7}_{-0.7}$	$2.33^{+0.04}_{-0.04}$	1.41	328
3	GRB050502	3	$10.7^{+5.3}_{-4.5}$	$2.10^{+0.27}_{-0.23}$	0.83	31
4	GRB050607	2	$22.5^{+5.3}_{-4.7}$	$2.40^{+0.23}_{-0.20}$	0.84	33
5	GRB050712	1	$24.6^{+4.7}_{-4.3}$	$2.13^{+0.18}_{-0.17}$	1.57	57
6	GRB050712	2	$20.5^{+8.9}_{-6.9}$	$3.08^{+0.59}_{-0.44}$	1.03	18
7	GRB050713	1	$52.1^{+5.9}_{-5.3}$	$2.19^{+0.11}_{-0.11}$	1.02	188
8	GRB050713	2	$50.7^{+13.8}_{-10.9}$	$3.30^{+0.68}_{-0.51}$	1.19	48
9	GRB050716	1	$24.4^{+66.4}_{-24.4}$	$1.22^{+0.93}_{-0.75}$	0.28	56
10	GRB050716	2	$24.5^{+15.6}_{-10.5}$	$3.38^{+0.93}_{-0.63}$	0.36	55
11	GRB050724	1	$52.1^{+2.0}_{-1.9}$	$1.77^{+0.03}_{-0.03}$	1.05	330
12	GRB050724	2	$55.6^{+4.6}_{-4.3}$	$2.94^{+0.13}_{-0.12}$	0.95	54
13	GRB050724	3	$27.4^{+8.8}_{-6.0}$	$1.61^{+0.15}_{-0.13}$	1.23	22

Continued on Next Page…

Table 4.3 – Continued

Index	**GRB**	**Flare**	**N**$_H$ ($10^{20} cm^{-2}$)	Γ	χ^2_{red}	**DOF**
14	GRB050726	2	$14.6^{+13.9}_{-9.3}$	$2.55^{+0.68}_{-0.50}$	0.93	37
15	GRB050730	1	$11.8^{+3.7}_{-3.3}$	$1.71^{+0.12}_{-0.12}$	1.06	58
16	GRB050730	2	$8.4^{+1.1}_{-1.0}$	$1.66^{+0.05}_{-0.05}$	0.94	187
17	GRB050730	3	$5.9^{+1.3}_{-1.2}$	$1.92^{+0.07}_{-0.07}$	0.93	106
18	GRB050730	4	$13.0^{+3.4}_{-3.0}$	$2.20^{+0.14}_{-0.13}$	0.98	81
19	GRB050802	1	$7.7^{+8.8}_{-6.3}$	$2.13^{+0.46}_{-0.36}$	0.97	30
20	GRB050803	5	$47.9^{+9.0}_{-7.8}$	$2.27^{+0.23}_{-0.21}$	1.41	34
21	GRB050803	6	$87.8^{+28.3}_{-21.7}$	$4.55^{+1.12}_{-0.82}$	1.02	18
22	GRB050820	1	$9.5^{+1.6}_{-1.5}$	$0.82^{+0.04}_{-0.04}$	1.13	202
23	GRB050822	1	$11.1^{+7.6}_{-6.1}$	$1.78^{+0.30}_{-0.27}$	0.44	27
24	GRB050822	2	$19.4^{+4.9}_{-4.3}$	$2.86^{+0.27}_{-0.24}$	1.04	31
25	GRB050822	3	$29.9^{+22.0}_{-14.4}$	$4.36^{+1.45}_{-1.03}$	1.06	18
26	GRB050904	1	$14.6^{+2.6}_{-2.4}$	$1.78^{+0.09}_{-0.09}$	0.98	182
27	GRB050904	4	$8.9^{+2.4}_{-2.2}$	$1.96^{+0.10}_{-0.10}$	1.31	38
28	GRB050904	5	$12.0^{+3.3}_{-3.0}$	$1.96^{+0.14}_{-0.13}$	0.93	26
29	GRB050904	6	$4.2^{+2.5}_{-2.2}$	$1.81^{+0.13}_{-0.12}$	1.00	22
30	GRB050904	7	$7.5^{+2.5}_{-2.2}$	$1.85^{+0.12}_{-0.11}$	0.86	24
31	GRB050916	1	$99.4^{+32.6}_{-26.9}$	$1.70^{+0.31}_{-0.30}$	0.47	20
32	GRB050922	1	$47.9^{+16.4}_{-12.6}$	$3.94^{+0.78}_{-0.58}$	1.01	99
33	GRB050922	2	$20.3^{+18.3}_{-12.0}$	$2.66^{+0.86}_{-0.60}$	0.92	45

Continued on Next Page…

Table 4.3 – Continued

Index	**GRB**	**Flare**	**N**$_H$ ($10^{20} cm^{-2}$)	Γ	χ^2_{red}	**DOF**
34	GRB050922	3	$14.6^{+2.4}_{-2.2}$	$2.36^{+0.10}_{-0.10}$	0.82	116
35	GRB051117	1	$16.7^{+1.1}_{-1.1}$	$1.88^{+0.04}_{-0.04}$	1.11	342
36	GRB051117	2	$16.8^{+1.0}_{-0.9}$	$2.23^{+0.04}_{-0.04}$	1.04	318
37	GRB051117	3	$13.5^{+1.5}_{-1.4}$	$2.26^{+0.07}_{-0.07}$	0.98	181
38	GRB051117	4	$14.4^{+1.4}_{-1.3}$	$2.13^{+0.06}_{-0.06}$	1.04	226
39	GRB051117	5	$14.1^{+1.5}_{-1.5}$	$2.51^{+0.08}_{-0.08}$	1.24	184
40	GRB051117	6	$16.0^{+1.2}_{-1.1}$	$2.22^{+0.05}_{-0.05}$	1.03	265
41	GRB051117	7	$12.5^{+1.2}_{-1.2}$	$2.25^{+0.06}_{-0.06}$	1.11	223
42	GRB051227	1	$29.9^{+9.1}_{-7.1}$	$1.53^{+0.15}_{-0.14}$	0.93	24
43	GRB060111	1	$38.5^{+3.9}_{-3.6}$	$2.89^{+0.14}_{-0.13}$	0.98	118
44	GRB060111	2	$31.1^{+4.1}_{-3.7}$	$2.86^{+0.18}_{-0.17}$	0.95	76
45	GRB060111	3	$26.5^{+1.4}_{-1.4}$	$2.27^{+0.05}_{-0.05}$	1.00	297
46	GRB060124	1	$18.4^{+0.5}_{-0.5}$	$1.21^{+0.01}_{-0.01}$	0.98	681
47	GRB060124	2	$16.4^{+0.5}_{-0.5}$	$1.67^{+0.02}_{-0.02}$	1.11	536

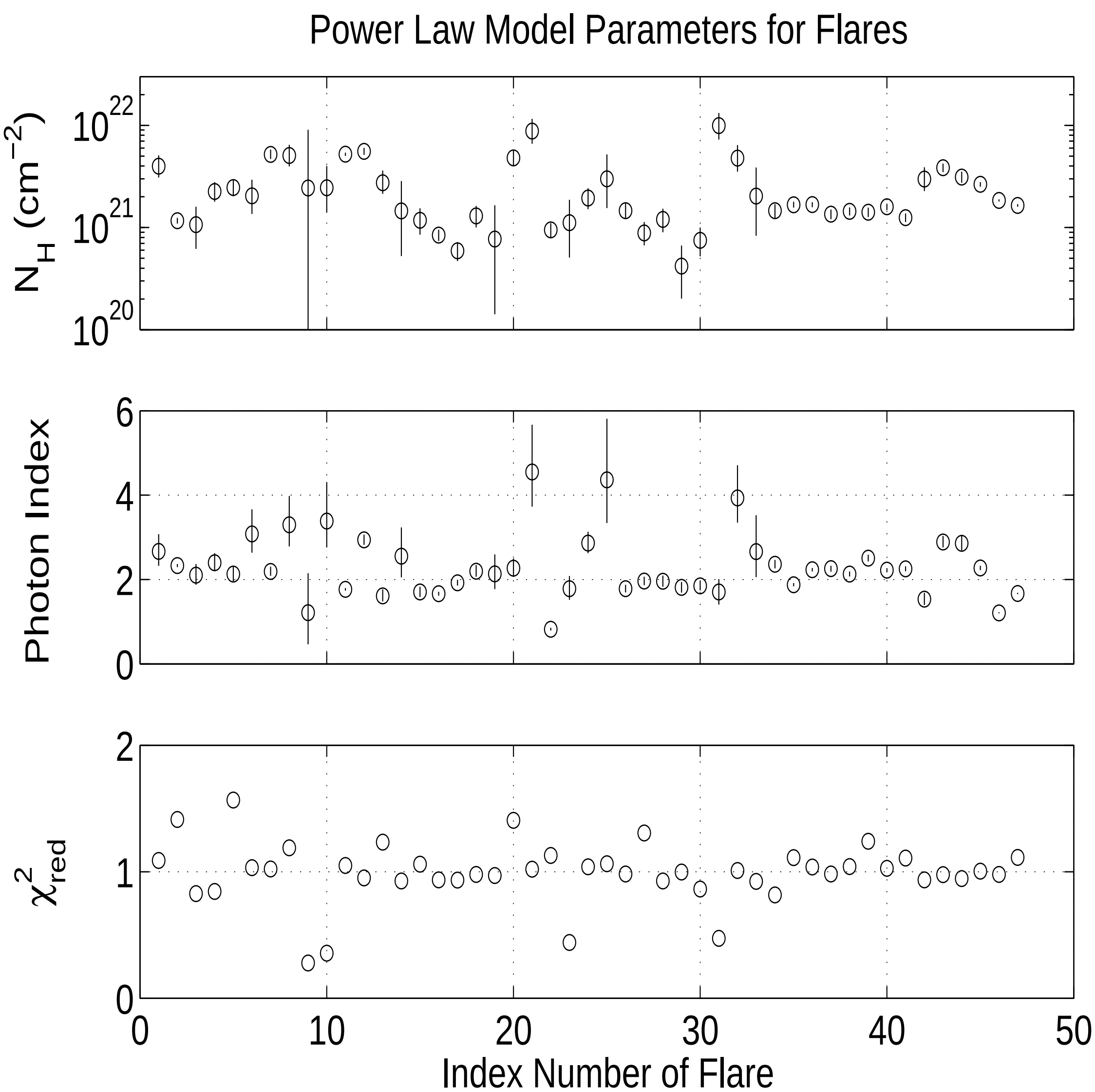

Fig. 4.2 Properties of power law spectral fits to flare data for all *Gold* flares. The index number of the flares shown on the x-axis simply refers to the index number for each flare shown in column 1 of Table 4.3. The top panel corresponds to the fit for the neutral Hydrogen column density (N_H), the second panel corresponds to the photon index (Γ_{flare}), and the bottom panel is the reduced χ^2 for each fit.

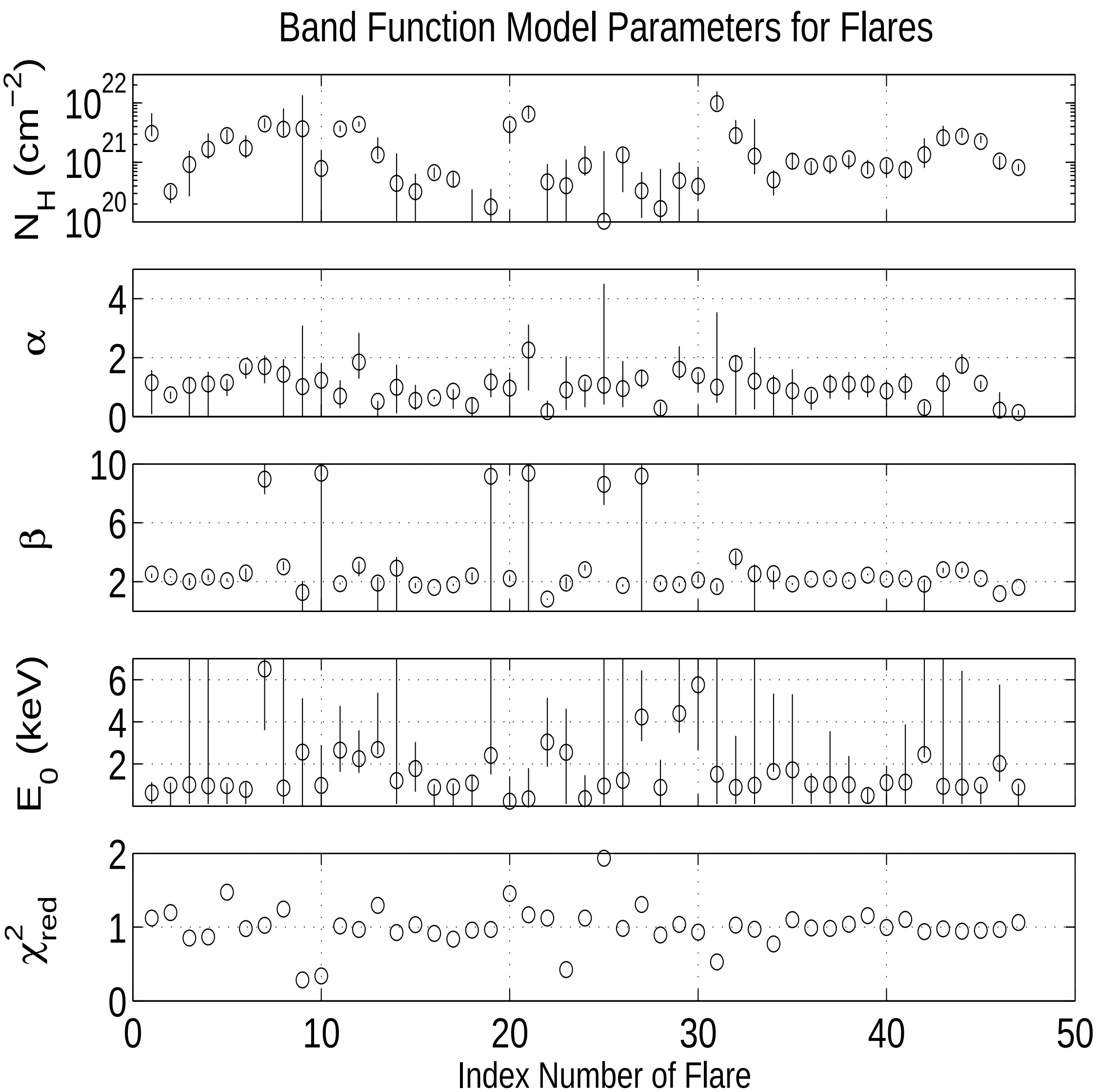

Fig. 4.3 Properties of Band function spectral fits to flare data for all *Gold* flares. The index number of the flares shown on the x-axis simply refers to the index number for each flare shown in column 1 of Table 4.2. The top panel corresponds to the fit for the neutral Hydrogen column density (N_H), the second panel corresponds to the low energy photon index (α), and the third panel corresponds to the high energy photon index (β). The fourth panel is the e-folding energy (E_0), which is related to the peak spectral energy by the relation $E_{peak} = (2 + \alpha)E_0$. The bottom panel is the reduced χ^2 for the fits.

Table 4.4: Properties of Band function spectral fits to *Gold* flares

Index	**GRB**	**Flare**	**N**$_H$ ($10^{20} cm^{-2}$)	α	β	**E**$_{peak}$ (keV)	χ^2_{red}	**DOF**
1	GRB050219	1	$30.8^{+36.3}_{-3.3}$	$1.15^{+0.43}_{-1.07}$	$2.52^{+0.04}_{-0.27}$	$0.6^{+0.5}_{-0.5}$	1.12	36
2	GRB050502	1	$3.3^{+0.9}_{-1.2}$	$0.74^{+0.11}_{-0.14}$	$2.33^{+0.04}_{-0.05}$	$1.0^{+0.1}_{-1.0}$	1.20	326
3	GRB050502	3	$9.2^{+6.5}_{-6.5}$	$1.06^{+0.25}_{-1.24}$	$2.01^{+0.24}_{-0.26}$	$1.0^{+999.0}_{-0.9}$	0.85	29
4	GRB050607	2	$16.7^{+13.9}_{-5.2}$	$1.11^{+0.41}_{-2.52}$	$2.31^{+0.18}_{-0.21}$	$1.0^{+66.8}_{-0.9}$	0.87	31
5	GRB050712	1	$28.2^{+8.0}_{-6.3}$	$1.16^{+0.11}_{-0.46}$	$2.08^{+0.16}_{-0.09}$	$1.0^{+0.1}_{-0.9}$	1.47	55
6	GRB050712	2	$17.2^{+11.3}_{-5.5}$	$1.70^{+0.11}_{-0.42}$	$2.60^{+0.30}_{-0.45}$	$0.8^{+0.3}_{-0.7}$	0.98	16
7	GRB050713	1	$44.1^{+10.8}_{-6.7}$	$1.69^{+0.38}_{-0.57}$	$8.97^{+6.87}_{-1.03}$	$6.5^{+21.9}_{-2.9}$	1.02	186
8	GRB050713	2	$36.1^{+44.7}_{-8.3}$	$1.44^{+0.51}_{-1.58}$	$3.02^{+0.34}_{-0.23}$	$0.9^{+42.8}_{-0.8}$	1.24	46
9	GRB050716	1	$36.7^{+97.4}_{-36.7}$	$1.02^{+2.07}_{-8.74}$	$1.28^{+0.79}_{-1.28}$	$2.6^{+2.6}_{-2.6}$	0.28	54
10	GRB050716	2	$7.9^{+7.9}_{-7.4}$	$1.23^{+0.59}_{-1.40}$	$9.37^{+19.37}_{-9.37}$	$1.0^{+1.9}_{-1.0}$	0.34	53
11	GRB050724	1	$36.5^{+5.1}_{-3.3}$	$0.69^{+0.53}_{-0.42}$	$1.87^{+0.06}_{-0.07}$	$2.7^{+2.1}_{-1.0}$	1.01	328
12	GRB050724	2	$43.6^{+5.5}_{-3.6}$	$1.85^{+0.99}_{-0.56}$	$3.11^{+0.27}_{-0.74}$	$2.3^{+1.4}_{-0.7}$	0.97	52
13	GRB050724	3	$13.4^{+13.0}_{-2.1}$	$0.51^{+0.02}_{-1.15}$	$1.91^{+0.40}_{-1.91}$	$2.7^{+2.7}_{-0.2}$	1.30	20
14	GRB050726	2	$4.4^{+9.7}_{-4.4}$	$0.99^{+0.77}_{-0.88}$	$2.92^{+0.77}_{-7.08}$	$1.2^{+999}_{-1.1}$	0.92	35
15	GRB050730	1	$3.2^{+3.2}_{-3.2}$	$0.55^{+0.52}_{-0.33}$	$1.77^{+0.16}_{-0.20}$	$1.8^{+1.3}_{-1.1}$	1.03	57
16	GRB050730	2	$6.7^{+1.5}_{-1.4}$	$0.63^{+0.03}_{-0.05}$	$1.61^{+0.05}_{-0.03}$	$0.9^{+0.1}_{-0.9}$	0.91	185
17	GRB050730	3	$5.2^{+1.6}_{-1.4}$	$0.86^{+0.07}_{-0.59}$	$1.80^{+0.07}_{-0.08}$	$0.9^{+0.2}_{-0.9}$	0.84	104
18	GRB050730	4	$0.9^{+2.6}_{-0.9}$	$0.38^{+0.24}_{-0.96}$	$2.40^{+0.24}_{-0.32}$	$1.1^{+0.4}_{-1.1}$	0.96	79
19	GRB050802	1	$1.8^{+1.8}_{-1.8}$	$1.17^{+0.45}_{-0.52}$	$9.16^{+19.16}_{-9.16}$	$2.4^{+5.6}_{-0.9}$	0.97	29

Continued on Next Page…

Table 4.4 – Continued

Index	**GRB**	**Flare**	$\mathbf{N}_H$ ($10^{20} cm^{-2}$)	α	β	$\mathbf{E}_{peak}$ (keV)	χ^2_{red}	**DOF**
20	GRB050803	5	$43.1^{+7.1}_{-22.4}$	$0.97^{+0.52}_{-1.41}$	$2.23^{+0.18}_{-0.19}$	$0.2^{+1.2}_{-0.2}$	1.45	32
21	GRB050803	6	$64.8^{+24.6}_{-10.8}$	$2.26^{+0.86}_{-1.37}$	$9.37^{+19.37}_{-9.37}$	$0.3^{+1.5}_{-0.3}$	1.17	16
22	GRB050820	1	$4.7^{+4.7}_{-4.7}$	$0.17^{+0.37}_{-0.19}$	$0.82^{+0.04}_{-0.04}$	$3.0^{+2.1}_{-1.2}$	1.12	201
23	GRB050822	1	$4.0^{+7.2}_{-4.0}$	$0.90^{+1.14}_{-0.69}$	$1.91^{+0.40}_{-0.39}$	$2.6^{+2.1}_{-2.5}$	0.42	25
24	GRB050822	2	$8.9^{+10.1}_{-2.9}$	$1.14^{+0.13}_{-0.82}$	$2.82^{+0.33}_{-0.07}$	$0.4^{+1.1}_{-0.4}$	1.12	29
25	GRB050822	3	$1.0^{+14.4}_{-8.5}$	$1.06^{+3.45}_{-0.65}$	$8.61^{+1.39}_{-1.39}$	$0.9^{+11.9}_{-0.8}$	1.93	16
26	GRB050904	1	$13.4^{+3.9}_{-10.2}$	$0.95^{+0.94}_{-0.63}$	$1.75^{+0.09}_{-0.09}$	$1.2^{+14.5}_{-1.2}$	0.98	180
27	GRB050904	4	$3.3^{+3.6}_{-2.1}$	$1.30^{+0.26}_{-0.35}$	$9.18^{+7.00}_{-9.18}$	$4.2^{+2.2}_{-1.1}$	1.30	36
28	GRB050904	5	$1.7^{+6.1}_{-1.4}$	$0.29^{+0.19}_{-0.71}$	$1.89^{+0.13}_{-0.14}$	$0.9^{+1.3}_{-0.9}$	0.89	24
29	GRB050904	6	$5.0^{+5.0}_{-5.0}$	$1.60^{+0.78}_{-0.36}$	$1.81^{+0.13}_{-0.14}$	$4.4^{+11.0}_{-0.9}$	1.04	21
30	GRB050904	7	$4.0^{+4.5}_{-1.7}$	$1.39^{+0.12}_{-0.56}$	$2.12^{+0.38}_{-0.18}$	$5.8^{+5.8}_{-3.1}$	0.93	22
31	GRB050916	1	$97.2^{+60.1}_{-20.6}$	$1.00^{+2.53}_{-0.54}$	$1.68^{+0.22}_{-0.33}$	$1.5^{+999}_{-1.4}$	0.53	18
32	GRB050922	1	$28.2^{+23.2}_{-6.9}$	$1.80^{+0.29}_{-1.75}$	$3.68^{+0.43}_{-0.84}$	$0.9^{+2.4}_{-0.8}$	1.03	97
33	GRB050922	2	$12.7^{+40.5}_{-6.3}$	$1.20^{+1.14}_{-0.96}$	$2.54^{+0.64}_{-7.46}$	$1.0^{+999.0}_{-0.9}$	0.97	43
34	GRB050922	3	$5.1^{+2.3}_{-2.3}$	$1.04^{+0.36}_{-1.01}$	$2.55^{+0.19}_{-1.07}$	$1.6^{+3.7}_{-0.0}$	0.77	114
35	GRB051117	1	$10.4^{+4.0}_{-2.7}$	$0.87^{+0.73}_{-0.82}$	$1.86^{+0.07}_{-0.07}$	$1.7^{+3.6}_{-1.6}$	1.10	340
36	GRB051117	2	$8.5^{+2.0}_{-2.0}$	$0.72^{+0.19}_{-0.49}$	$2.18^{+0.04}_{-0.03}$	$1.0^{+0.5}_{-0.9}$	0.99	316
37	GRB051117	3	$9.4^{+2.6}_{-3.0}$	$1.10^{+0.33}_{-0.49}$	$2.21^{+0.06}_{-0.07}$	$1.0^{+2.5}_{-0.9}$	0.98	179
38	GRB051117	4	$11.5^{+1.7}_{-3.9}$	$1.10^{+0.41}_{-0.53}$	$2.08^{+0.06}_{-0.06}$	$1.0^{+1.4}_{-0.9}$	1.04	224
39	GRB051117	5	$7.4^{+3.5}_{-1.2}$	$1.09^{+0.34}_{-0.44}$	$2.44^{+0.10}_{-0.02}$	$0.5^{+0.3}_{-0.4}$	1.15	182

Continued on Next Page…

Table 4.4 – Continued

Index	**GRB**	**Flare**	**N$_H$** ($10^{20} cm^{-2}$)	α	β	**E$_{peak}$** (keV)	χ^2_{red}	**DOF**
40	GRB051117	6	$8.8^{+2.3}_{-3.3}$	$0.87^{+0.36}_{-0.50}$	$2.17^{+0.05}_{-0.05}$	$1.1^{+0.8}_{-1.0}$	0.99	263
41	GRB051117	7	$7.5^{+3.2}_{-2.4}$	$1.09^{+0.38}_{-0.52}$	$2.21^{+0.06}_{-0.07}$	$1.1^{+2.7}_{-1.0}$	1.10	221
42	GRB051227	1	$13.5^{+12.0}_{-5.4}$	$0.30^{+0.20}_{-1.02}$	$1.83^{+0.33}_{-1.83}$	$2.5^{+6.5}_{-0.1}$	0.94	22
43	GRB060111	1	$25.8^{+15.4}_{-6.2}$	$1.12^{+0.38}_{-1.79}$	$2.82^{+0.14}_{-0.22}$	$0.9^{+13.5}_{-0.8}$	0.98	116
44	GRB060111	2	$27.2^{+7.5}_{-1.3}$	$1.73^{+0.39}_{-0.26}$	$2.78^{+0.17}_{-0.15}$	$0.9^{+5.5}_{-0.8}$	0.94	74
45	GRB060111	3	$22.5^{+5.6}_{-1.4}$	$1.13^{+0.09}_{-0.19}$	$2.22^{+0.04}_{-0.05}$	$1.0^{+0.0}_{-0.9}$	0.96	295
46	GRB060124	1	$10.5^{+2.2}_{-3.1}$	$0.22^{+0.61}_{-0.62}$	$1.20^{+0.02}_{-0.02}$	$2.0^{+3.8}_{-0.8}$	0.97	679
47	GRB060124	2	$8.2^{+1.2}_{-1.0}$	$0.14^{+0.07}_{-0.09}$	$1.61^{+0.01}_{-0.01}$	$0.9^{+0.2}_{-0.9}$	1.06	534

Table 4.5: Properties of exponentially cutoff power law spectral fits to *Gold* flares

Index	**GRB**	**Flare**	**N$_H$** ($10^{20} cm^{-2}$)	Γ	E_{cut} **(keV)**	χ^2_{red}	**DOF**
1	GRB050219	1	$40.2^{+10.6}_{-10.2}$	$2.68^{+0.37}_{-0.68}$	999	1.12	37
2	GRB050502	1	$8.7^{+1.3}_{-1.2}$	$1.97^{+0.14}_{-0.14}$	$7.2^{+4.4}_{-2.0}$	1.36	327

Continued on Next Page…

Table 4.5 – Continued

Index	**GRB**	**Flare**	**N$_H$** ($10^{20}cm^{-2}$)	Γ	**E$_{cut}$** (**keV**)	χ^2_{red}	**DOF**
3	GRB050502	3	$10.8^{+5.3}_{-5.5}$	$2.11^{+0.24}_{-0.29}$	999	0.86	30
4	GRB050607	2	$22.5^{+5.2}_{-8.4}$	$2.40^{+0.11}_{-0.83}$	999	0.87	32
5	GRB050712	1	$23.9^{+5.3}_{-3.8}$	$2.10^{+0.18}_{-0.16}$	999	1.60	56
6	GRB050712	2	$20.2^{+9.0}_{-7.8}$	$3.06^{+0.55}_{-0.95}$	999	1.09	17
7	GRB050713	1	$46.2^{+9.4}_{-8.6}$	$1.82^{+0.43}_{-0.49}$	$8.8^{+999}_{-6.1}$	1.02	187
8	GRB050713	2	$50.4^{+13.9}_{-10.9}$	$3.29^{+0.65}_{-0.98}$	999	1.21	47
9	GRB050716	1	$23.6^{+66.7}_{-23.6}$	$1.18^{+0.95}_{-1.86}$	$128.0^{+128.0}_{-128.0}$	0.28	55
10	GRB050716	2	$2.3^{+16.4}_{-2.3}$	$0.02^{+2.36}_{-0.66}$	$0.6^{+1.5}_{-0.2}$	0.32	54
11	GRB050724	1	$44.7^{+3.1}_{-3.0}$	$1.37^{+0.14}_{-0.14}$	$8.7^{+4.6}_{-2.2}$	1.03	329
12	GRB050724	2	$48.1^{+9.3}_{-8.9}$	$2.32^{+0.67}_{-0.70}$	$4.3^{+4.3}_{-2.3}$	0.95	53
13	GRB050724	3	$18.0^{+13.1}_{-10.5}$	$0.94^{+0.74}_{-0.71}$	$4.8^{+62.5}_{-2.6}$	1.25	21
14	GRB050726	2	$1.6^{+19.7}_{-1.6}$	$0.63^{+2.25}_{-0.80}$	$1.1^{+498.9}_{-0.4}$	0.90	36
15	GRB050730	1	$10.7^{+4.6}_{-6.3}$	$1.61^{+0.21}_{-0.55}$	$32.2^{+32.2}_{-27.6}$	1.08	57
16	GRB050730	2	$8.4^{+1.0}_{-0.5}$	$1.66^{+0.05}_{-0.05}$	999	0.94	186
17	GRB050730	3	$5.8^{+0.9}_{-1.1}$	$1.91^{+0.08}_{-0.04}$	999	0.94	105
18	GRB050730	4	$7.7^{+6.0}_{-5.0}$	$1.58^{+0.62}_{-0.62}$	$4.1^{+235.8}_{-2.1}$	0.98	80
19	GRB050802	1	$1.8^{+1.8}_{-1.8}$	$1.17^{+0.53}_{-0.64}$	$2.4^{+7.0}_{-1.2}$	0.93	30
20	GRB050803	5	$46.9^{+10.0}_{-6.8}$	$2.23^{+0.24}_{-0.18}$	999	1.45	33
21	GRB050803	6	$83.5^{+32.5}_{-41.3}$	$4.14^{+1.50}_{-3.99}$	$5.9^{+5.9}_{-5.4}$	1.08	17
22	GRB050820	1	$8.0^{+3.4}_{-2.4}$	$0.72^{+0.12}_{-0.14}$	$33.6^{+33.6}_{-19.2}$	1.13	201

Continued on Next Page…

Table 4.5 – Continued

Index	**GRB**	**Flare**	**N$_H$** ($10^{20} cm^{-2}$)	Γ	**E$_{cut}$** (**keV**)	χ^2_{red}	**DOF**
23	GRB050822	1	$4.0^{+13.0}_{-4.0}$	$0.99^{+1.02}_{-0.72}$	$3.3^{+999}_{-1.7}$	0.42	26
24	GRB050822	2	$19.3^{+4.8}_{-8.7}$	$2.86^{+0.26}_{-1.05}$	$275.2^{+999}_{-273.1}$	1.07	30
25	GRB050822	3	$13.2^{+14.8}_{-6.0}$	$1.42^{+1.54}_{-0.35}$	$0.5^{+0.1}_{-0.3}$	0.75	17
26	GRB050904	1	$14.4^{+2.8}_{-2.3}$	$1.77^{+0.09}_{-0.15}$	$496.7^{+999}_{-488.3}$	0.99	181
27	GRB050904	4	$3.9^{+3.6}_{-3.0}$	$1.37^{+0.37}_{-0.35}$	$4.7^{+7.3}_{-1.8}$	1.27	37
28	GRB050904	5	$11.8^{+3.5}_{-6.0}$	$1.93^{+0.08}_{-0.56}$	120.8^{+999}_{-999}	0.96	25
29	GRB050904	6	$4.2^{+2.4}_{-2.5}$	$1.81^{+0.12}_{-0.27}$	$495.6^{+999}_{-485.9}$	1.05	21
30	GRB050904	7	$5.5^{+4.0}_{-3.7}$	$1.59^{+0.34}_{-0.43}$	$10.6^{+10.6}_{-6.7}$	0.89	23
31	GRB050916	1	$94.8^{+36.9}_{-40.9}$	$1.58^{+0.41}_{-1.32}$	$37.7^{+999}_{-35.0}$	0.50	19
32	GRB050922	1	$47.7^{+16.4}_{-24.8}$	$3.92^{+0.75}_{-3.04}$	204.3^{+999}_{-999}	1.02	98
33	GRB050922	2	$19.5^{+18.7}_{-19.5}$	$2.57^{+0.92}_{-3.05}$	25.2^{+999}_{-999}	0.94	44
34	GRB050922	3	$9.1^{+4.1}_{-3.6}$	$1.72^{+0.43}_{-0.41}$	$4.1^{+7.7}_{-1.6}$	0.77	115
35	GRB051117	1	$16.2^{+1.6}_{-1.9}$	$1.83^{+0.08}_{-0.16}$	$62.7^{+999}_{-47.9}$	1.11	341
36	GRB051117	2	$16.4^{+1.3}_{-1.7}$	$2.19^{+0.07}_{-0.15}$	$70.7^{+999}_{-56.2}$	1.04	317
37	GRB051117	3	$13.4^{+1.6}_{-1.8}$	$2.25^{+0.07}_{-0.18}$	999	0.99	180
38	GRB051117	4	$14.3^{+1.4}_{-0.7}$	$2.12^{+0.07}_{-0.12}$	999	1.05	225
39	GRB051117	5	$14.0^{+1.7}_{-1.3}$	$2.50^{+0.08}_{-0.10}$	999	1.25	183
40	GRB051117	6	$13.6^{+2.0}_{-1.9}$	$1.97^{+0.19}_{-0.19}$	$11.2^{+33.1}_{-4.9}$	1.01	264
41	GRB051117	7	$12.4^{+1.2}_{-2.0}$	$2.25^{+0.06}_{-0.21}$	$497.6^{+999}_{-485.7}$	1.11	222
42	GRB051227	1	$17.7^{+11.9}_{-10.2}$	$0.73^{+0.63}_{-0.62}$	$4.2^{+13.4}_{-1.9}$	0.90	23

Continued on Next Page…

Table 4.5 – Continued

Index	GRB	Flare	N_H $(10^{20} cm^{-2})$	Γ	E_{cut} (keV)	χ^2_{red}	DOF
43	GRB060111	1	$38.0^{+4.3}_{-7.4}$	$2.84^{+0.18}_{-0.62}$	$59.9^{+999}_{-55.9}$	0.98	117
44	GRB060111	2	$31.2^{+4.0}_{-4.0}$	$2.86^{+0.17}_{-0.30}$	$499.9^{+999}_{-490.9}$	0.96	75
45	GRB060111	3	$26.5^{+1.3}_{-0.7}$	$2.27^{+0.04}_{-0.06}$	$500.0^{+999}_{-441.5}$	1.01	296
46	GRB060124	1	$17.4^{+0.8}_{-0.8}$	$1.14^{+0.05}_{-0.05}$	$48.5^{+106.7}_{-19.1}$	0.98	680
47	GRB060124	2	$16.4^{+0.5}_{-0.4}$	$1.66^{+0.02}_{-0.02}$	$499.9^{+999}_{-364.8}$	1.12	535

Table 4.6: Properties of blackbody plus power law spectral fits to *Gold* flares

Index	GRB	Flare	N_H $(10^{20} cm^{-2})$	Γ	kT (keV)	χ^2_{red}	DOF
1	GRB050219	1	$56.8^{+55.9}_{-29.1}$	$2.34^{+0.75}_{-0.81}$	$0.1^{+0.1}_{-0.1}$	0.96	36
2	GRB050502	1	$6.4^{+1.3}_{-1.5}$	$2.06^{+0.08}_{-0.10}$	$0.3^{+0.0}_{-0.0}$	1.29	326
3	GRB050502	3	$9.5^{+31.6}_{-9.4}$	$1.86^{+2.12}_{-0.36}$	$0.2^{+0.6}_{-0.2}$	0.84	29
4	GRB050607	2	$26.0^{+25.1}_{-7.8}$	$2.70^{+1.98}_{-0.88}$	$1.1^{+0.9}_{-1.0}$	0.89	31
5	GRB050712	1	$31.2^{+27.6}_{-2.5}$	$2.52^{+1.84}_{-0.10}$	$32.4^{+167.6}_{-31.3}$	1.52	55

Continued on Next Page…

Table 4.6 – Continued

Index	**GRB**	**Flare**	**N**$_H$ ($10^{20} cm^{-2}$)	Γ	**kT** (**keV**)	χ^2_{red}	**DOF**
6	GRB050712	2	$19.5^{+10.3}_{-5.7}$	$3.04^{+0.63}_{-0.39}$	$0.0^{+200.0}_{-0.0}$	1.16	16
7	GRB050713	1	$41.6^{+11.4}_{-11.7}$	$1.93^{+0.34}_{-0.42}$	$0.5^{+0.5}_{-0.1}$	1.01	186
8	GRB050713	2	$117.6^{+63.7}_{-54.1}$	$3.71^{+1.49}_{-1.03}$	$0.1^{+0.0}_{-0.0}$	1.03	46
9	GRB050716	1	$31.3^{+255.4}_{-31.3}$	$1.56^{+8.36}_{-1.56}$	$7.2^{+7.2}_{-7.2}$	0.29	54
10	GRB050716	2	$11.2^{+11.2}_{-11.2}$	$3.29^{+2.98}_{-0.78}$	$0.3^{+0.1}_{-0.1}$	0.34	54
11	GRB050724	1	$41.7^{+3.8}_{-3.9}$	$1.58^{+0.09}_{-0.11}$	$0.7^{+0.1}_{-0.1}$	1.01	328
12	GRB050724	2	$46.2^{+11.5}_{-13.4}$	$2.69^{+0.47}_{-0.57}$	$0.4^{+0.3}_{-0.1}$	0.96	52
13	GRB050724	3	$14.8^{+14.9}_{-14.8}$	$1.31^{+0.25}_{-1.32}$	$0.7^{+0.5}_{-0.2}$	1.29	20
14	GRB050726	2	$2.3^{+17.5}_{-2.3}$	$2.03^{+3.13}_{-1.19}$	$0.4^{+0.3}_{-0.1}$	0.90	35
15	GRB050730	1	$3.2^{+3.2}_{-3.2}$	$1.29^{+0.12}_{-0.15}$	$0.4^{+0.1}_{-0.1}$	1.00	57
16	GRB050730	2	$12.6^{+2.7}_{-2.3}$	$2.00^{+0.21}_{-0.18}$	$2.8^{+22.1}_{-0.8}$	0.90	185
17	GRB050730	3	$9.6^{+3.0}_{-2.5}$	$2.28^{+0.27}_{-0.22}$	$2.1^{+3.1}_{-0.6}$	0.91	104
18	GRB050730	4	$3.1^{+4.9}_{-3.1}$	$1.75^{+0.32}_{-0.35}$	$0.4^{+0.1}_{-0.1}$	0.95	79
19	GRB050802	1	$6.2^{+29.3}_{-6.2}$	$2.45^{+1.69}_{-0.78}$	$0.7^{+0.5}_{-0.2}$	1.00	28
20	GRB050803	5	$40.0^{+32.8}_{-12.9}$	$0.71^{+0.46}_{-0.69}$	$0.3^{+0.1}_{-0.1}$	1.16	32
21	GRB050803	6	$198.7^{+90.1}_{-87.5}$	$5.44^{+2.29}_{-1.41}$	$0.1^{+0.0}_{-0.0}$	0.98	16
22	GRB050820	1	$11.1^{+2.1}_{-1.8}$	$0.84^{+0.04}_{-0.04}$	$0.0^{+0.0}_{-0.0}$	1.12	200
23	GRB050822	1	$2.3^{+2.3}_{-2.3}$	$1.32^{+0.30}_{-0.41}$	$0.4^{+0.2}_{-0.1}$	0.39	26
24	GRB050822	2	$19.2^{+11.9}_{-14.1}$	$2.75^{+0.42}_{-0.08}$	$0.1^{+0.1}_{-0.1}$	1.09	29
25	GRB050822	3	$34.3^{+29.0}_{-3.0}$	$4.57^{+1.71}_{-0.51}$	$0.0^{+0.0}_{-0.0}$	0.94	16

Continued on Next Page…

Table 4.6 – Continued

Index	**GRB**	**Flare**	**N$_H$** ($10^{20} cm^{-2}$)	Γ	**kT** (**keV**)	χ^2_{red}	**DOF**
26	GRB050904	1	$14.8^{+2.5}_{-2.5}$	$1.79^{+0.09}_{-0.07}$	$0.0^{+0.5}_{-0.0}$	0.99	180
27	GRB050904	4	$10.4^{+5.0}_{-3.9}$	$2.29^{+0.43}_{-0.27}$	$1.0^{+0.2}_{-0.2}$	1.29	36
28	GRB050904	5	$5.2^{+6.5}_{-4.2}$	$1.50^{+0.34}_{-0.46}$	$0.3^{+0.1}_{-0.1}$	0.90	24
29	GRB050904	6	$6.0^{+2.6}_{-2.9}$	$1.97^{+0.27}_{-0.22}$	$31.0^{+31.0}_{-31.0}$	1.06	20
30	GRB050904	7	$7.6^{+2.3}_{-3.5}$	$1.96^{+0.20}_{-0.24}$	$0.9^{+0.9}_{-0.9}$	0.91	22
31	GRB050916	1	$84.1^{+56.8}_{-52.3}$	$1.38^{+1.37}_{-2.69}$	$0.5^{+199.4}_{-0.5}$	0.49	18
32	GRB050922	1	$17.3^{+74.6}_{-12.9}$	$1.86^{+1.93}_{-2.11}$	$0.2^{+0.1}_{-0.2}$	0.99	97
33	GRB050922	2	$20.0^{+22.5}_{-11.3}$	$2.65^{+1.27}_{-0.27}$	$199.3^{+0.7}_{-199.3}$	0.97	43
34	GRB050922	3	$11.5^{+4.0}_{-4.3}$	$2.30^{+0.24}_{-0.23}$	$0.5^{+0.2}_{-0.1}$	0.77	114
35	GRB051117	1	$14.3^{+2.6}_{-2.5}$	$1.77^{+0.11}_{-0.12}$	$0.4^{+0.3}_{-0.1}$	1.11	340
36	GRB051117	2	$13.2^{+1.9}_{-2.4}$	$2.06^{+0.09}_{-0.13}$	$0.3^{+0.0}_{-0.0}$	1.01	316
37	GRB051117	3	$11.6^{+3.8}_{-3.0}$	$2.14^{+0.16}_{-0.18}$	$0.3^{+0.2}_{-0.2}$	0.99	179
38	GRB051117	4	$11.8^{+4.7}_{-3.1}$	$1.99^{+0.33}_{-0.12}$	$0.3^{+199.7}_{-0.3}$	1.04	224
39	GRB051117	5	$8.4^{+2.9}_{-2.7}$	$2.04^{+0.17}_{-0.18}$	$0.2^{+0.0}_{-0.0}$	1.08	182
40	GRB051117	6	$15.1^{+2.0}_{-2.7}$	$2.20^{+0.12}_{-0.13}$	$0.5^{+0.3}_{-0.5}$	1.03	263
41	GRB051117	7	$10.6^{+2.5}_{-2.9}$	$2.16^{+0.12}_{-0.17}$	$0.3^{+0.1}_{-0.3}$	1.11	221
42	GRB051227	1	$16.3^{+19.4}_{-12.8}$	$1.24^{+0.94}_{-0.67}$	$0.7^{+0.7}_{-0.2}$	0.95	22
43	GRB060111	1	$35.7^{+26.1}_{-11.5}$	$2.77^{+0.56}_{-0.50}$	$0.3^{+1.0}_{-0.3}$	0.99	116
44	GRB060111	2	$45.0^{+18.2}_{-13.9}$	$2.86^{+0.30}_{-0.28}$	$0.1^{+0.0}_{-0.0}$	0.87	74
45	GRB060111	3	$30.5^{+5.7}_{-4.2}$	$2.18^{+0.09}_{-0.09}$	$0.1^{+0.0}_{-0.0}$	0.93	295

Continued on Next Page…

Table 4.6 – Continued

Index	**GRB**	**Flare**	**N$_H$** ($10^{20} cm^{-2}$)	Γ	**kT** **(keV)**	χ^2_{red}	**DOF**
46	GRB060124	1	$19.4^{+0.4}_{-0.5}$	$1.22^{+0.01}_{-0.01}$	$0.0^{+0.0}_{-0.0}$	0.95	679
47	GRB060124	2	$13.6^{+1.2}_{-1.2}$	$1.53^{+0.05}_{-0.05}$	$0.4^{+0.0}_{-0.0}$	1.10	534

4.4 Fluence of Flares

The flare fluence values to be discussed here are defined as the flux of the flare in the 0.2-10 keV band, integrated from the flare t_{start} to the flare t_{stop} minus the flux of the underlying afterglow in the 0.2-10 keV band, integrated from the flare t_{start} to the flare t_{stop}. We stress the point, here, that the fluxes reported are, therefore, a measure of the *additional* fluence contributed to the GRB afterglow from the flare, rather than the *total* fluence of the GRB afterglow summed during the flare interval, as had often been reported in early flares analyses. This is important to note since, particularly in the cases of flares with low contrast with respect to the underlying afterglow, the subtracted component can prove to be a significant fraction of the total fluence beneath the afterglow lightcurve, thus leading to overestimates of the true flare fluence if not properly accounted for. Table 4.7 shows the fluence values for the powerlaw fits and Band function fits to our entire flares sample (ie, not only the *Gold* flares). Some of

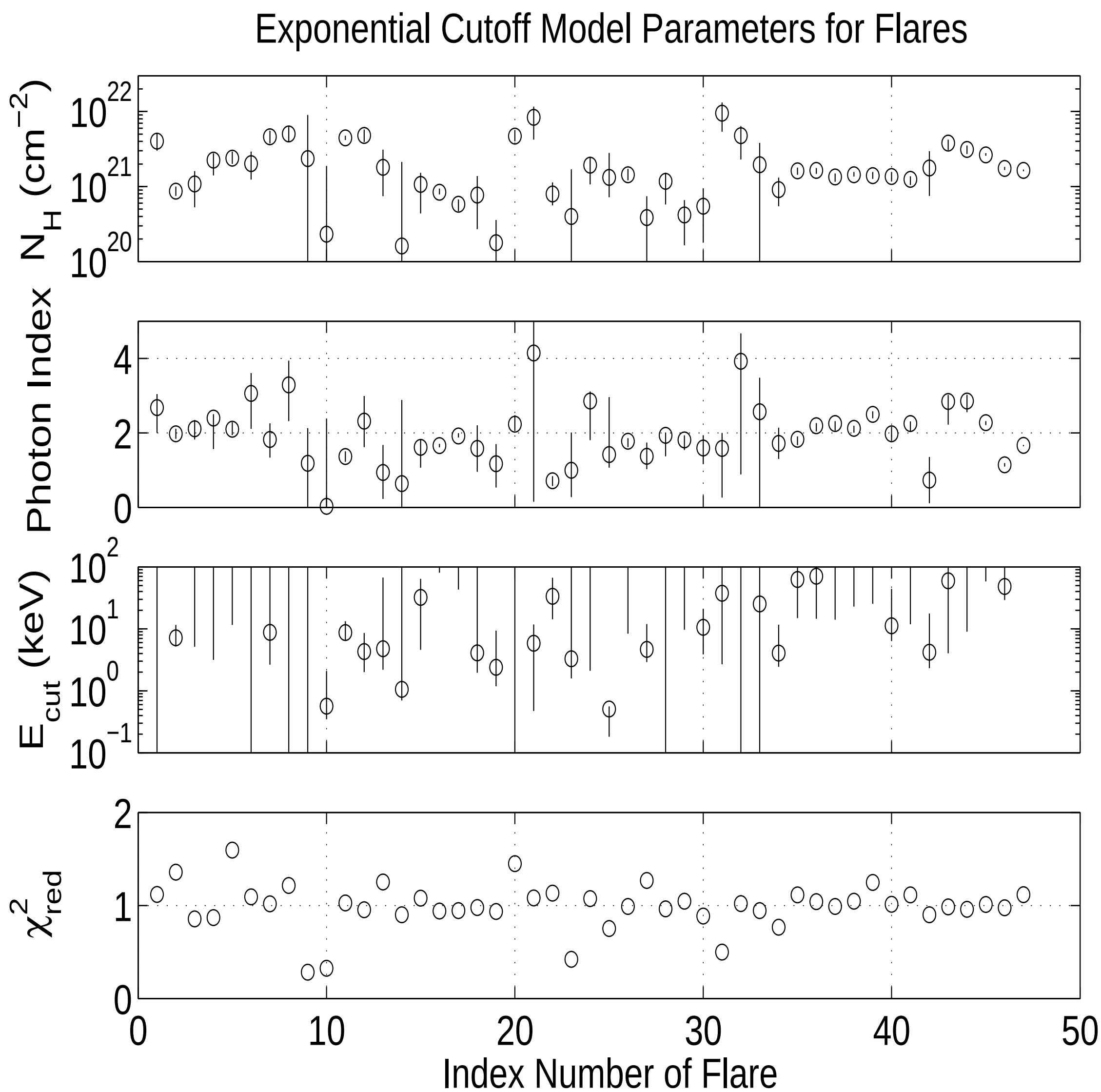

Fig. 4.4 Properties of exponentially cutoff power law model spectral fits to flare data for all *Gold* flares. The index number of the flares shown on the x-axis simply refers to the index number for each flare shown in column 1 of Table 4.3. Many flares did not provide enough data in this energy band to lead to convergence for the cutoff energy, which is clear from the fact that panel 3 has many data points not shown off the top of the plot (these were set to the 500 keV fitting limit and their lower error bars extend into the plot).

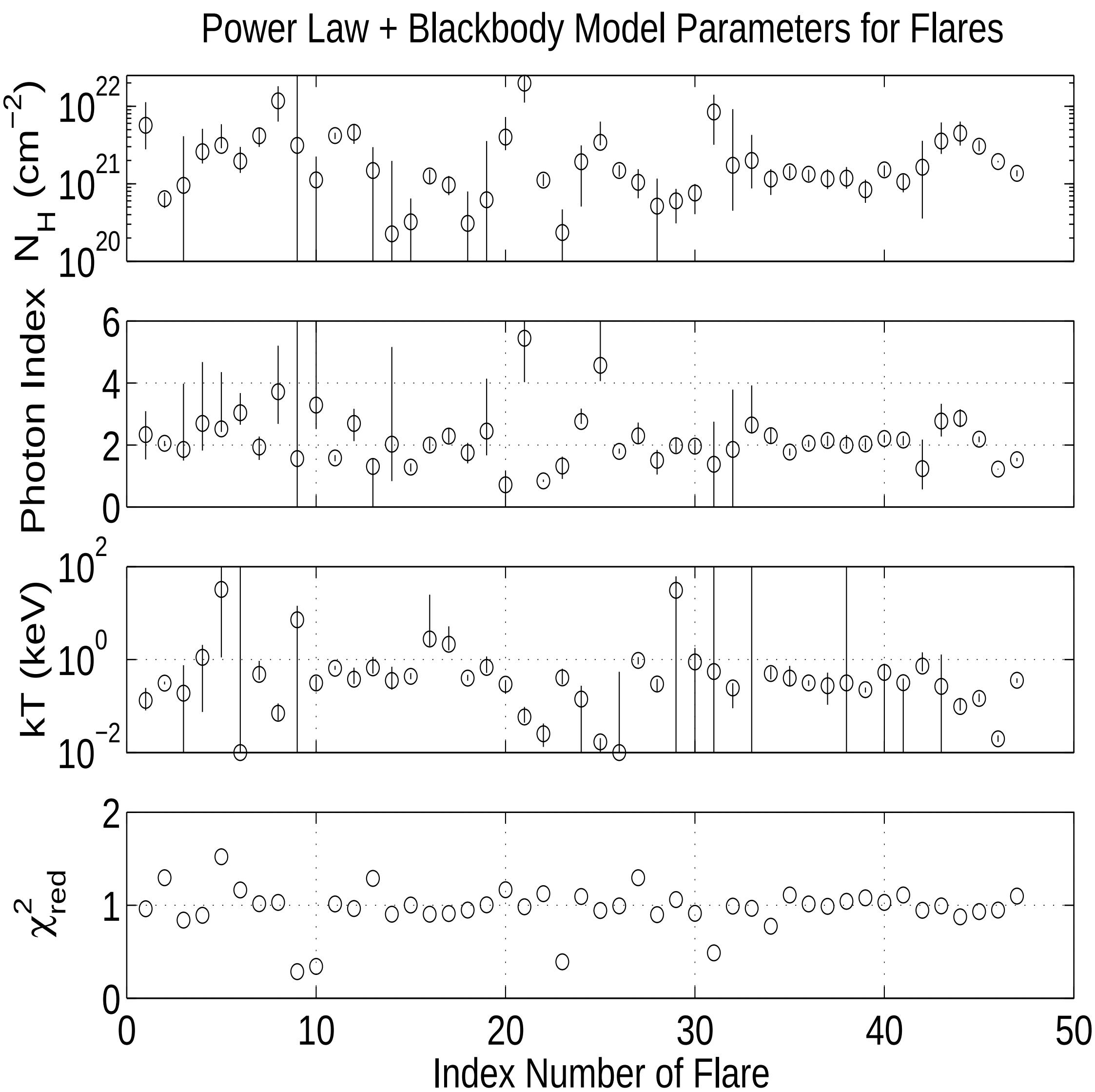

Fig. 4.5 Properties of blackbody plus power law model spectral fits to flare data for all *Gold* flares. The index number of the flares shown on the x-axis simply refers to the index number for each flare shown in column 1 of Table 4.4.

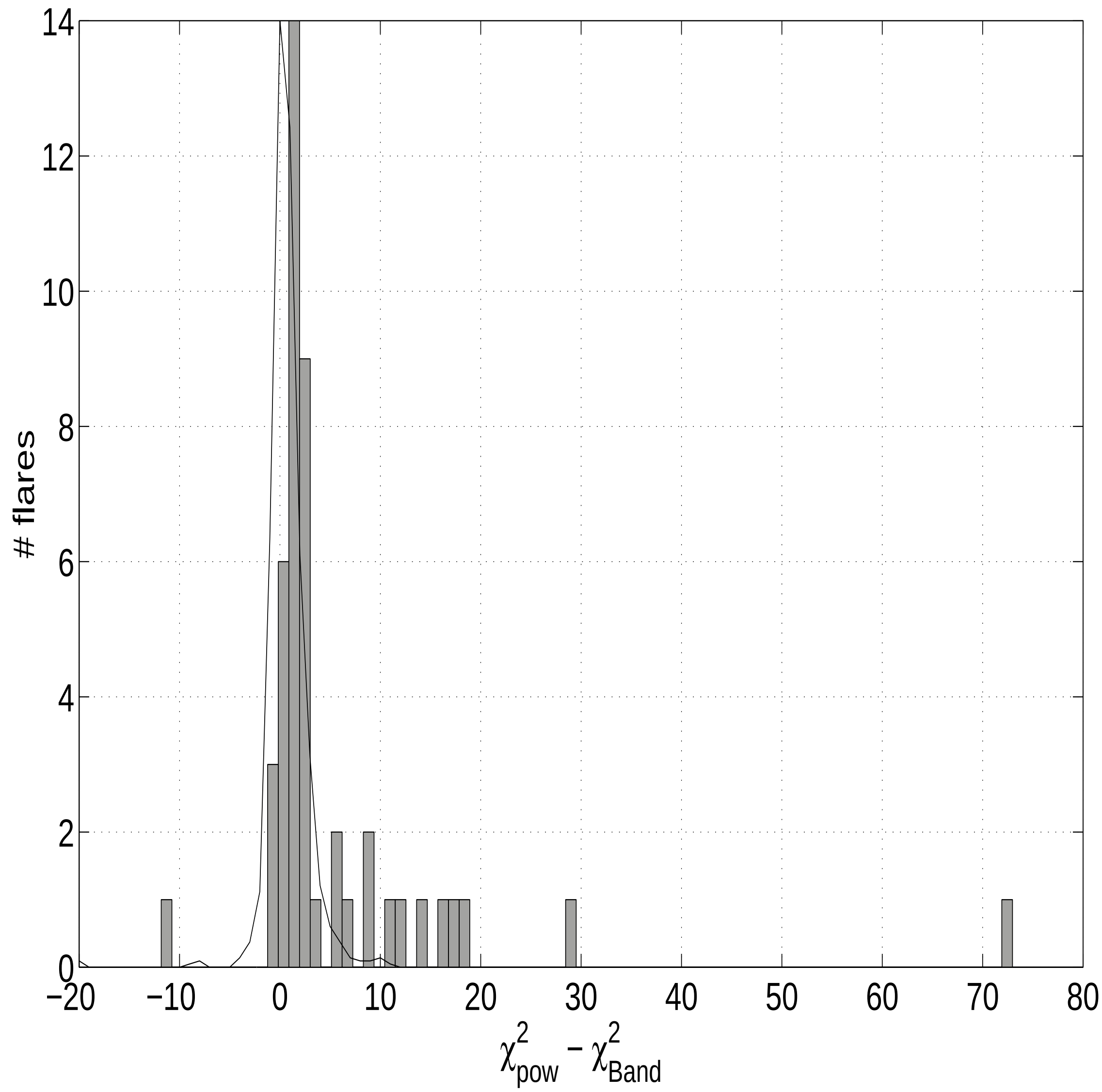

Fig. 4.6 Histogram of $\Delta\chi^2$ between the power law fits and Band function fits for all *Gold* flares. The histogram represents the real data, while the overlayed line represents the distribution of simulated power law spectra subjected to the same fitting procedure.

the flares in the table at lower flux levels have very few degrees of freedom in their spectra, necessarily leading to poorly constrained flux measurements, as reflected in the size of the associated error bars (quoted at 1σ). The reported uncertainties include components due to the uncertainty in the subtracted underlying afterglow contribution as well as components due to uncertainties in the corrections applied to account for "missing" fluence due to incomplete lightcurves.

We have reported the fluence calculations in the observed XRT energy range, 0.2-10 keV. Though this is not necessarily the most widely used energy band for reporting GRB fluences (often GRB fluences are reported in bands more appropriate to the higher energies of the prompt emission such as 1keV-10MeV), it is an appropriate way to report the flare fluences since the bulk of the energy of X-ray flares appears to be emitted in the X-ray band (hence the name). This is supported by the Band function fits detailed previously, for which well constrained fits generally report peak energy values in the νF_ν spectrum in the range 0.2-10 keV. It is further supported by the fact that X-ray flares were initially discovered as an X-ray phenomenon and generally do not show strong accompanying emission at higher (BAT) or lower (UVOT or ground based optical) frequencies. To determine quantitatively whether it is reasonable and informative to quote the flare fluences in this energy band, we have extrapolated a Band function model defined by the median spectral parameters of the *Gold* sample flares and calculated the fluence occurring outside this energy range. The *Gold* flares which had a reasonable spectral fit to the Band function have median parameter values α=1.06, β=2.21 and E_0=1.02keV where α is the spectral index of the low energy powerlaw of the Band function, β is the spectral index of the high energy powerlaw and E_0 is the folding energy of the spectrum. Extrapolating this model to the 0.2-150 keV band more typical of the fluences reported from prompt emission in the BAT, we find that only 1.4% would be added to the fluence from the 0.2-10 keV band. This is insignificant in comparison to the other uncertainties in the fluence and thus we feel justified in reporting fluence values in the native band.

Figure 4.7 shows the distribution of flare fluences (UAD removed) for the powerlaw fits and for the Band function fits. The lefthand panels show all flares in our sample (upper powerlaw; lower Band) while the righthand panels show the *Gold* sample flares (upper powerlaw; lower Band). The mean 0.2-10 keV unabsorbed fluence derived from the Band function fits is 2.4x10^{-7} erg cm^{-2}. There is no evidence of bimodality (multimodality) in the distributions as might be expected if the flares in this sample were produced by two (several) different underlying physical processes.

Table 4.7: Fluences of Flares

GRB	**Flare**	**Fluence** ($erg\ cm^{-2}$)	χ^2_{red}	**DOF**	**Fluence** ($erg\ cm^{-2}$)	χ^2_{red}	**DOF**
GRB050219	1	$0.70^{+999.00}_{-999.00}$	1.09	38	$0.38^{+0.37}_{-0.38}$	1.12	36
GRB050406	1	$0.21^{+0.02}_{-0.07}$	1.78	7	$0.18^{+0.16}_{-2.02}$	2.43	6
GRB050421	1	$0.21^{+0.17}_{-999.00}$	0.53	10	$0.28^{+0.27}_{-0.27}$	0.64	8
GRB050502	1	$12.99^{+0.19}_{-0.20}$	1.41	328	$8.30^{+8.30}_{-0.44}$	1.20	326
GRB050502	2	$0.24^{+0.17}_{-0.07}$	1.21	8	$0.16^{+0.14}_{-0.16}$	1.54	6
GRB050502	3	$0.90^{+0.11}_{-999.00}$	0.83	31	$0.81^{+0.79}_{-0.31}$	0.85	29

Continued on Next Page...

Table 4.7 – Continued

GRB	**Flare**	**Fluence** ($erg\ cm^{-2}$)	χ^2_{red}	**DOF**	**Fluence** ($erg\ cm^{-2}$)	χ^2_{red}	**DOF**
GRB050607	1	$0.20^{+999.00}_{-999.00}$	0.73	9	$0.20^{+0.14}_{-1.12}$	0.83	7
GRB050607	2	$1.09^{+999.00}_{-999.00}$	0.84	33	$0.76^{+0.76}_{-0.35}$	0.87	31
GRB050712	1	$1.51^{+999.00}_{-999.00}$	1.57	57	$1.57^{+3.26}_{-2.93}$	1.47	55
GRB050712	2	$0.40^{+999.00}_{-999.00}$	1.03	18	$0.26^{+0.99}_{-2.44}$	0.98	16
GRB050712	3	$0.35^{+999.00}_{-999.00}$	0.73	10	$0.18^{+0.18}_{-0.09}$	0.86	8
GRB050712	4	—	—	—	—	—	—
GRB050713	1	$3.14^{+999.00}_{-999.00}$	1.02	188	$2.38^{+1.76}_{-5.87}$	1.02	186
GRB050713	2	$1.55^{+999.00}_{-999.00}$	1.19	48	$0.46^{+999.00}_{-686.82}$	1.24	46
GRB050714	1	$1790.20^{+2150.30}_{-2105.80}$	1.68	15	$0.42^{+0.61}_{-32.55}$	6.28	13
GRB050716	1	$0.19^{+0.17}_{-0.07}$	0.28	56	$0.22^{+999.00}_{-999.00}$	0.28	54
GRB050716	2	$0.07^{+0.47}_{-0.69}$	0.36	55	$0.02^{+0.06}_{-0.06}$	0.34	53
GRB050724	1	$0.81^{+0.01}_{-0.01}$	1.05	330	$2.11^{+1.08}_{-1.08}$	1.01	328
GRB050724	2	$0.31^{+0.27}_{-0.27}$	0.95	54	$0.32^{+0.48}_{-0.48}$	0.97	52
GRB050724	3	$1.29^{+0.27}_{-3.04}$	1.23	22	$1.28^{+0.15}_{-0.23}$	1.30	20
GRB050726	1	$0.14^{+999.00}_{-999.00}$	0.73	12	$0.05^{+999.00}_{-999.00}$	0.94	10
GRB050726	2	$0.26^{+999.00}_{-999.00}$	0.93	37	$0.14^{+999.00}_{-999.00}$	0.92	35
GRB050730	1	$0.47^{+0.46}_{-0.54}$	1.06	58	$0.35^{+0.17}_{-0.17}$	1.03	57
GRB050730	2	$2.15^{+0.36}_{-0.36}$	0.94	187	$1.78^{+0.29}_{-0.29}$	0.91	185
GRB050730	3	$1.03^{+0.30}_{-0.30}$	0.93	106	$0.75^{+0.22}_{-0.22}$	0.84	104
GRB050730	4	$1.73^{+1.72}_{-1.69}$	0.98	81	$1.06^{+1.25}_{-1.26}$	0.96	79

Continued on Next Page…

Table 4.7 – Continued

GRB	Flare	Fluence ($erg\ cm^{-2}$)	χ^2_{red}	DOF	Fluence ($erg\ cm^{-2}$)	χ^2_{red}	DOF
GRB050802	1	$0.20^{+0.33}_{-0.31}$	0.97	30	$0.02^{+0.07}_{-0.07}$	0.97	29
GRB050803	1	$0.30^{+999.00}_{-999.00}$	0.79	13	$0.20^{+0.12}_{-0.10}$	0.93	11
GRB050803	2	$2.97^{+999.00}_{-999.00}$	1.10	14	$0.30^{+999.00}_{-999.00}$	1.28	12
GRB050803	3	$0.38^{+0.03}_{-999.00}$	1.34	13	$0.28^{+0.28}_{-0.06}$	1.52	11
GRB050803	4	$418.24^{+999.00}_{-999.00}$	1.20	10	$0.05^{+999.00}_{-999.00}$	1.58	8
GRB050803	5	$0.20^{+2.65}_{-2.65}$	1.41	34	$0.10^{+1.21}_{-1.21}$	1.45	32
GRB050803	6	$0.29^{+0.89}_{-0.88}$	1.02	18	$999.00^{+999.00}_{-999.00}$	1.17	16
GRB050814	1	$0.04^{+999.00}_{-999.00}$	0.29	2	$0.02^{+999.00}_{-999.00}$	999.00	999
GRB050814	2	$0.05^{+999.00}_{-999.00}$	0.92	6	$0.04^{+0.02}_{-999.00}$	1.32	4
GRB050819	1	$0.19^{+2.76}_{-2.76}$	0.50	6	$0.18^{+2.25}_{-2.39}$	0.75	5
GRB050819	2	$0.10^{+0.09}_{-0.13}$	1.66	2	$999.00^{+999.00}_{-999.00}$	999.00	999
GRB050820	1	$6.89^{+108.96}_{-108.96}$	1.13	202	$6.81^{+106.91}_{-106.91}$	1.12	201
GRB050822	1	$0.29^{+0.03}_{-0.04}$	0.44	27	$0.24^{+0.24}_{-0.01}$	0.42	25
GRB050822	2	$0.95^{+0.08}_{-0.09}$	1.04	31	$0.42^{+8.48}_{-999.00}$	1.12	29
GRB050822	3	$2.22^{+41.92}_{-41.92}$	1.06	18	$0.17^{+2.10}_{-2.10}$	1.93	16
GRB050904	1	$2.51^{+999.00}_{-999.00}$	0.98	182	$2.38^{+2.24}_{-0.17}$	0.98	180
GRB050904	2	$0.27^{+999.00}_{-999.00}$	0.86	11	$0.16^{+0.08}_{-0.05}$	1.03	9
GRB050904	3	$0.11^{+999.00}_{-999.00}$	1.38	6	$0.10^{+0.08}_{-1.70}$	2.06	4
GRB050904	4	$0.88^{+14.49}_{-14.57}$	1.31	38	$0.85^{+13.91}_{-13.91}$	1.30	36
GRB050904	5	$0.95^{+22.64}_{-22.69}$	0.93	26	$1.07^{+27.60}_{-27.60}$	0.89	24

Continued on Next Page. . .

Table 4.7 – Continued

GRB	**Flare**	**Fluence** $(erg\ cm^{-2})$	χ^2_{red}	**DOF**	**Fluence** $(erg\ cm^{-2})$	χ^2_{red}	**DOF**
GRB050904	6	$0.60^{+17.74}_{-17.99}$	1.00	22	$0.57^{+15.73}_{-15.73}$	1.04	21
GRB050904	7	$0.40^{+7.53}_{-7.78}$	0.86	24	$0.41^{+7.25}_{-7.25}$	0.93	22
GRB050908	1	$0.26^{+999.00}_{-0.10}$	1.22	5	$0.09^{+0.08}_{-1.95}$	1.79	4
GRB050908	2	$0.23^{+0.03}_{-0.04}$	0.56	14	$0.20^{+0.17}_{-0.97}$	0.85	13
GRB050915	1	$0.41^{+999.00}_{-999.00}$	0.84	16	$0.27^{+0.27}_{-999.00}$	0.93	14
GRB050916	1	$1.30^{+0.70}_{-999.00}$	0.47	20	$1.22^{+0.04}_{-0.04}$	0.53	18
GRB050922	1	$4.80^{+999.00}_{-999.00}$	1.01	99	$0.74^{+999.00}_{-25.18}$	1.03	97
GRB050922	2	$0.30^{+999.00}_{-999.00}$	0.92	45	$0.17^{+999.00}_{-999.00}$	0.97	43
GRB050922	3	$4.57^{+999.00}_{-999.00}$	0.82	116	$2.78^{+2.75}_{-999.00}$	0.77	114
GRB051006	1	$0.35^{+0.35}_{-0.04}$	0.86	6	$0.21^{+0.20}_{-999.00}$	1.59	4
GRB051006	2	$0.11^{+1.92}_{-1.92}$	2.04	3	$0.11^{+1.87}_{-1.87}$	6.11	1
GRB051006	3	$0.30^{+0.14}_{-999.00}$	0.75	8	$0.24^{+0.24}_{-0.24}$	0.98	6
GRB051016	1	$0.18^{+0.14}_{-999.00}$	1.48	1	$999.00^{+999.00}_{-999.00}$	999.00	999
GRB051117	1	$20.60^{+23.04}_{-23.04}$	1.11	342	$19.08^{+22.70}_{-19.05}$	1.10	340
GRB051117	2	$14.24^{+35.16}_{-35.16}$	1.04	318	$11.01^{+25.35}_{-24.04}$	0.99	316
GRB051117	3	$4.83^{+56.05}_{-56.05}$	0.98	181	$4.20^{+43.98}_{-43.88}$	0.98	179
GRB051117	4	$7.20^{+72.04}_{-72.04}$	1.04	226	$6.60^{+61.60}_{-61.41}$	1.04	224
GRB051117	5	$4.91^{+44.67}_{-44.67}$	1.24	184	$3.66^{+28.55}_{-29.01}$	1.15	182
GRB051117	6	$10.15^{+86.29}_{-86.29}$	1.03	265	$8.22^{+61.79}_{-61.45}$	0.99	263
GRB051117	7	$8.40^{+244.17}_{-244.17}$	1.11	223	$7.31^{+184.67}_{-184.60}$	1.10	221

Continued on Next Page…

Table 4.7 – Continued

GRB	**Flare**	**Fluence** ($erg\ cm^{-2}$)	χ^2_{red}	**DOF**	**Fluence** ($erg\ cm^{-2}$)	χ^2_{red}	**DOF**
GRB051210	1	$1.00^{+999.00}_{-999.00}$	1.75	7	$0.05^{+0.02}_{-0.02}$	3.51	4
GRB051227	1	$0.28^{+0.05}_{-0.05}$	0.93	24	$0.20^{+0.02}_{-0.03}$	0.94	22
GRB060108	1	$0.02^{+999.00}_{-999.00}$	0.29	2	$999.00^{+999.00}_{-999.00}$	999.00	999
GRB060108	2	$0.70^{+0.50}_{-999.00}$	0.60	7	$0.46^{+0.34}_{-999.00}$	0.80	5
GRB060109	1	$0.19^{+0.13}_{-999.00}$	0.76	16	$0.32^{+0.30}_{-0.28}$	0.66	14
GRB060111	1	$4.65^{+999.00}_{-999.00}$	0.98	118	$2.15^{+4.52}_{-999.00}$	0.98	116
GRB060111	2	$2.05^{+999.00}_{-999.00}$	0.95	76	$1.39^{+4.13}_{-999.00}$	0.94	74
GRB060111	3	$9.15^{+999.00}_{-999.00}$	1.00	297	$7.20^{+7.20}_{-1.46}$	0.96	295
GRB060115	1	$0.20^{+999.00}_{-999.00}$	1.06	15	$0.20^{+0.15}_{-999.00}$	0.86	13
GRB060124	1	$27.13^{+0.39}_{-0.39}$	0.98	681	$33.73^{+0.47}_{-0.48}$	0.97	679
GRB060124	2	$12.40^{+0.27}_{-0.26}$	1.11	536	$16.80^{+0.35}_{-0.36}$	1.06	534

4.5 Flare Fluence versus Prompt Fluence

Figure 4.8 shows the distribution of prompt fluences measured by the *Swift* BAT in the 15-150 keV energy band for the 33 GRBs in our sample. The mean prompt fluence is 2x10^{-6} erg cm^{-2} with a standard deviation of 2.5x10^{-6} erg cm^{-2}. Recall that the flare fluence, measured in the 0.2-10 keV energy range of the XRT where the

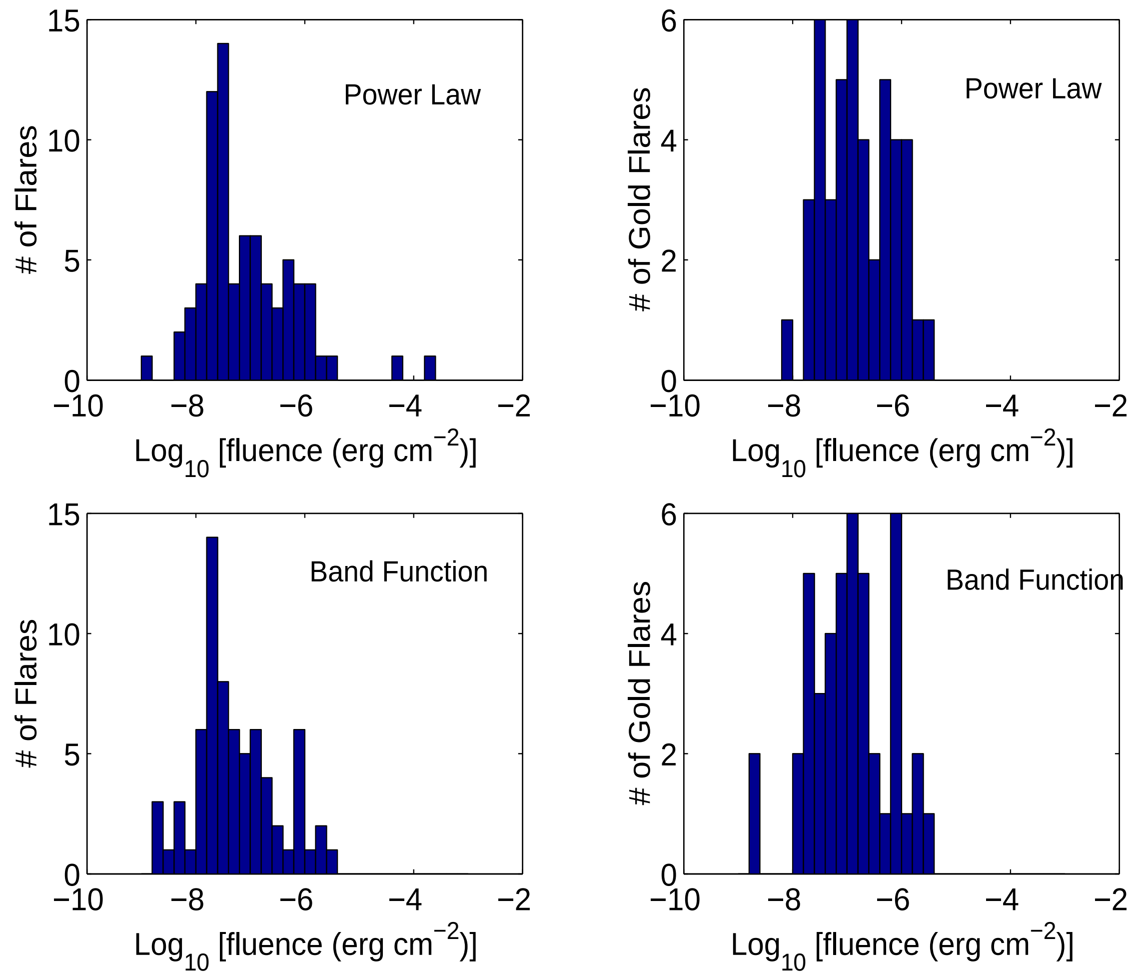

Fig. 4.7 Unabsorbed 0.2–10 keV fluence distribution of flares. The two panels on the left are for all flares that had a convergent spectral fit. The two panels on the right are for *Gold* flares that have > 15 DOF in the spectral fit and $\chi^2_{red} < 1.5$. Fluence derived from both power law fits (top) and Band function fits (bottom) are shown.

flare flux peaks, is approximately a factor of 10 lower than this ($2.4\text{x}10^{-7}$ erg cm^{-2}; see previous section). The distributions of prompt fluence and flare fluence do, however, overlap, with at least one X-ray flare containing as much fluence as the prompt burst which preceded it (the well known GRB050502B). In Figure 4.9 we plot the flare fluence in its native 0.2-10 keV energy band versus the prompt fluence in its native 15-150 keV energy band. We have chosen to investigate the relationship between these two quantities in these non-bolometric measures because of the uncertainties in the fitted parameters of the broadband model fits to the data and the associated uncertainties in fluence that would be introduced if we were to extrapolate far outside the observed energy band. Furthermore, as was demonstrated in the previous section, extrapolating the flare energy range (0.2-10 keV) up to the prompt energy range (15-150 keV) adds only a negligible contribution to the flare fluence. Therefore it is most appropriate to examine the relationship between prompt burst fluence and flare fluence in the observed bands as we show in Figure 4.9. We note, however, that the behavior of the flares as well as of the prompt burst emission at energies below the XRT energy range (ie, in the optical to UV energy range) is somewhat less well quantified, and could potentially add a significant amount of fluence to either the flares or prompt events. We will return to this subject in Chapter 5 when we examine flares in a multiwavelength context. We conclude by noting that no correlation is seen between the prompt burst fluence and the fluence of associated later X-ray flares in the burst to within the limits of the uncertainties of the data.

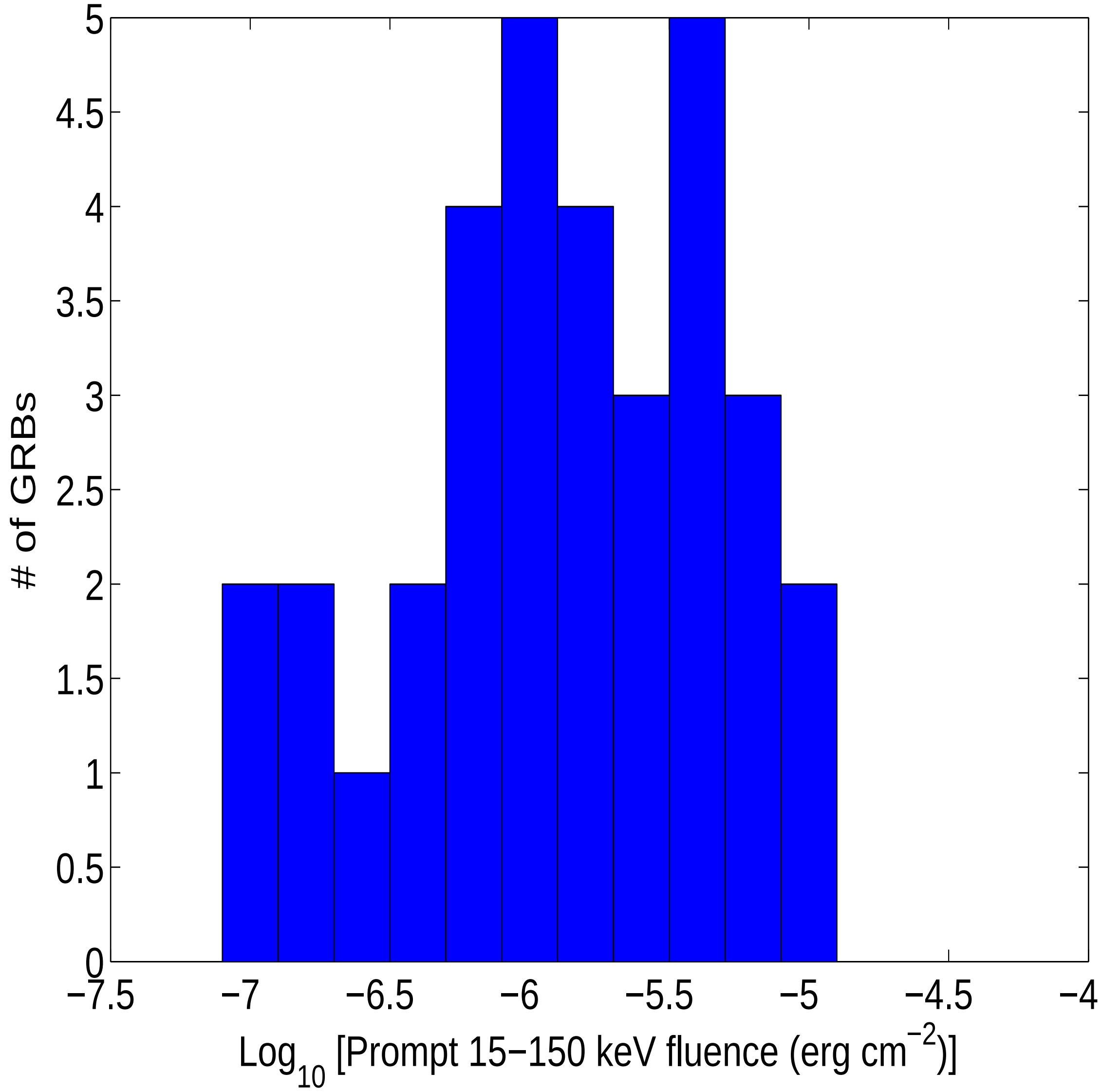

Fig. 4.8 Prompt emission 15–150 keV fluence distribution of GRBs that are in this sample of flaring GRBs.

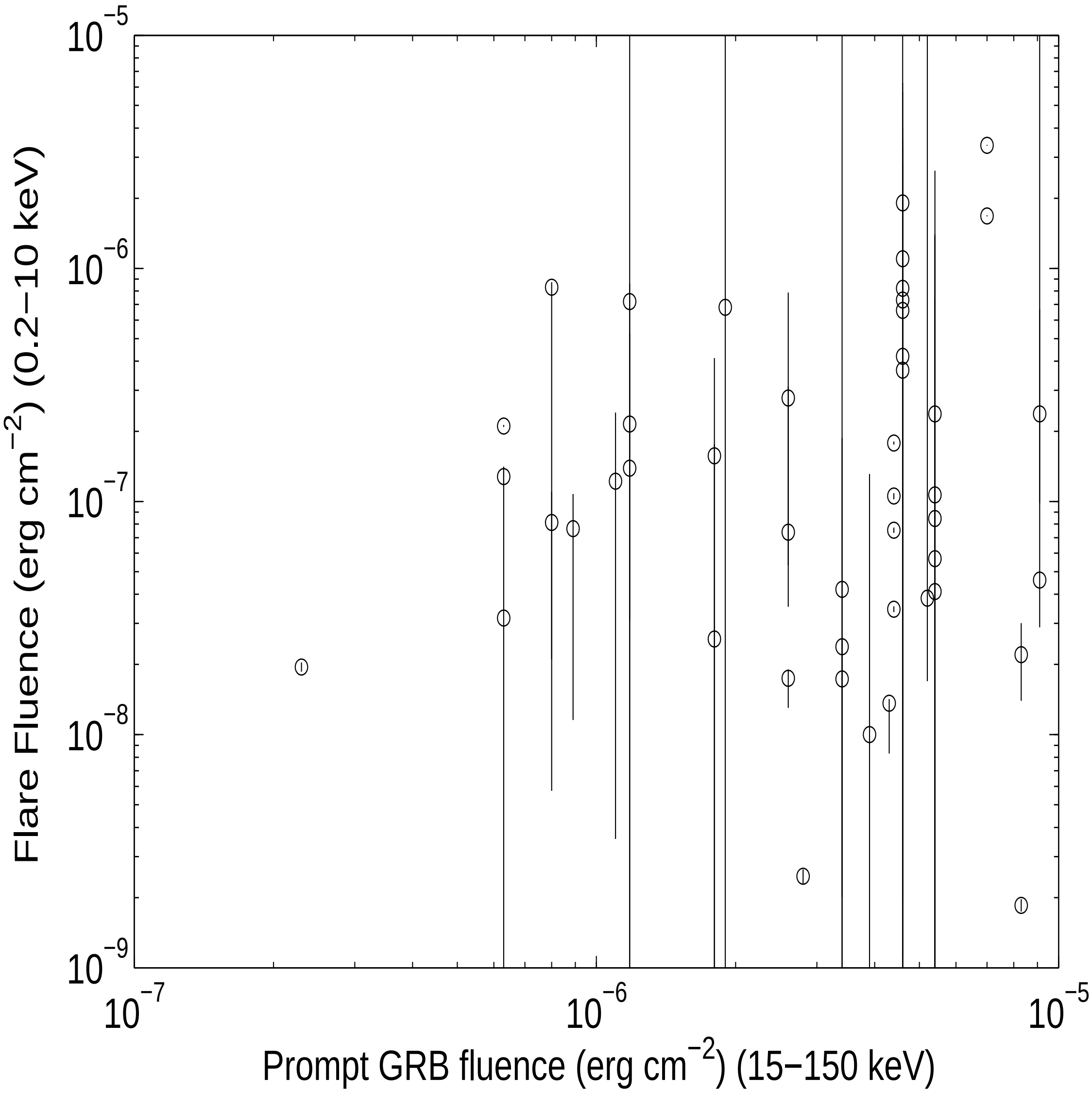

Fig. 4.9 Flare fluence in the 0.2–10 keV band (derived using a Band function) plotted as a function of the prompt GRB fluence in the 15–150 keV band.

4.6 Flare Properties versus Underlying Afterglow Properties

Previous studies of X-ray flares in GRBs have argued for flares being due to central engine activity rather than a process associated with the long-lived afterglow based on rapid temporal variability (steep rising and steep decaying), the presence of multiple flares within individual bursts and spectral variability within flares (among other arguments). Chincarini et al further strengthen this argument with their temporal analysis companion paper to this work, showing overall rapid rises and rapid decays to the sample of flares treated here. We add further to this argument here by presenting a comparison between the photon index of powerlaw fits to the underlying afterglow spectra and the photon index of powerlaw fits to the associated flares. Though we have recently argued for fitting the flares using the Band function, we revert to using the powerlaw model here for consistency with the fits to the underlying afterglow since a Band function is not warranted (and is, indeed, difficult to constrain) for the afterglow spectra. Figure 4.10 shows the photon index for each spectrum plotted against index number with separate symbols representing the flare and associated afterglow spectrum. We see that the flare powerlaw fits have a wider distribution than the associated afterglows, suggesting a different, more varied and dynamic process at work in the flares than in the afterglows.

4.7 Temporal Evolution of Flare Properties

Several authors have investigated evolution within individual X-ray flares as well as flare to flare evolution within individual GRBs with bright flares. Spectral evolution within flares and from flare to flare has been noted in GRB050406 (Romano et al. 2006),

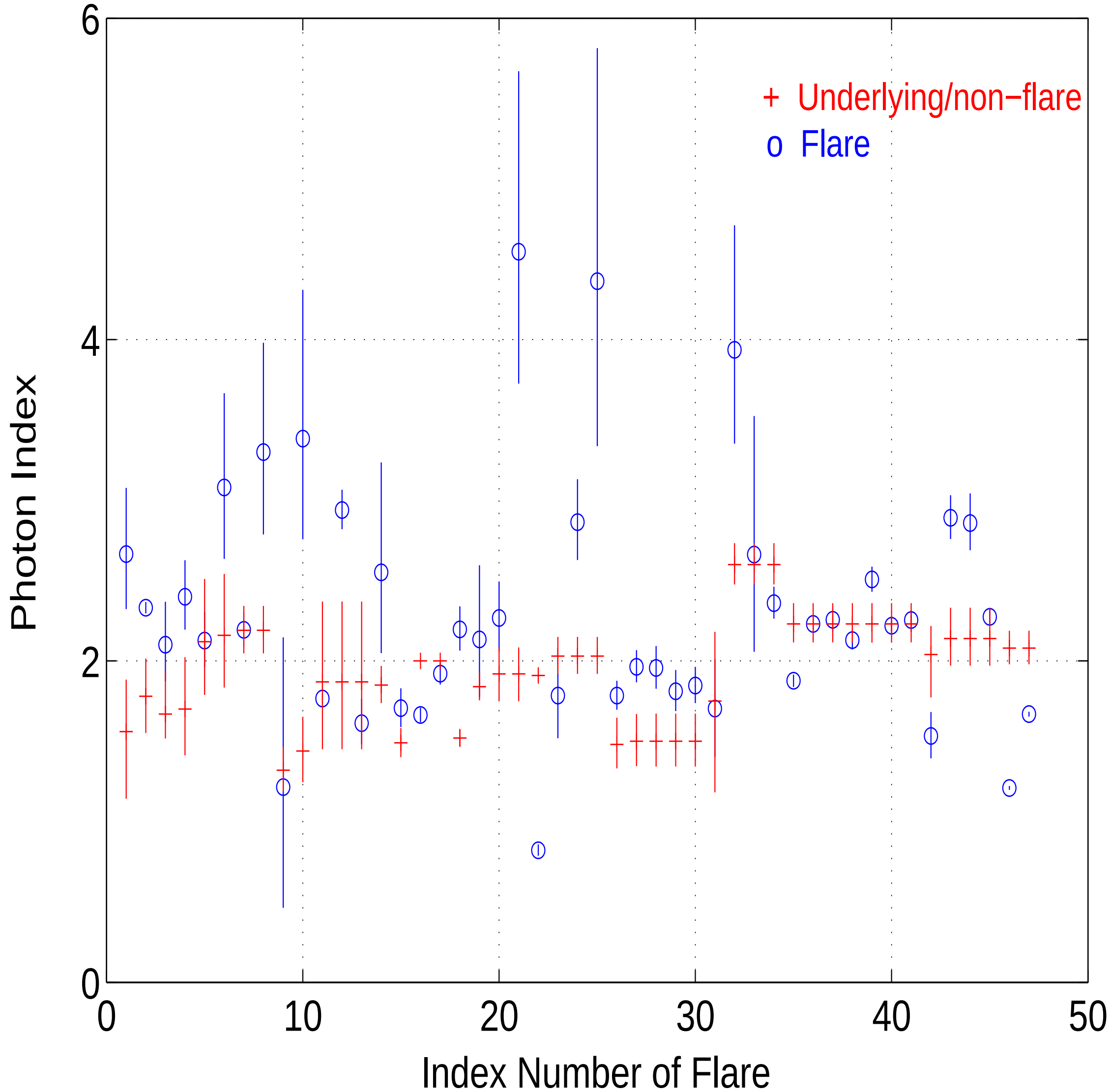

Fig. 4.10 Comparison of the power law spectral photon indices for the underlying afterglows and for the flares

GRB050502B (Falcone et al. 2006), GRB050607 (Pagani et al. 2006), GRB050713A (Morris et al. (2007) and Chapter 3), GRB050822 (Godet et al. 2007) and GRB060714 (Krimm et al. 2007) among others. The general trend noted within individual flares is that of a soft (prior to the onset of the flare) to hard (at $\sim$ the peak flux of the flare) back to soft (as the flare decays) evolution, possibly also seen with a spectral lag of the soft emission with respect to the hard emission (ie, the hardness ratio rises slightly in advance of the rise of the flux lightcurve). Krimm et al and Butler and Kocevski (Butler & Kocevski 2007) have investigated flare to flare evolution in detail and have found some evidence of a general trend for successive flares to occur at progressively lower values of E_{PEAK}.

We have not separated the flares in this chapter temporally, thus we are unable to discuss the nature of the intra-flare evolution here (we will return to this subject in Chapter 5), but we are able to discuss the relationship between the overall onset time of the flares in our sample and associated spectral parameters of the flares. In Figure 4.11, we plot E_{PEAK} versus rest frame time of the onset of the flare for all the flares in bursts in our *Gold* sample for which we have measured redshifts. The data in the figure are scaled in no way to try to correct for differences from burst to burst that surely must exist and effect the timing and relationship between subsequent flares. As a result, this figure investigates only whether there is a general relationship between the rest-frame onset time of a flare and the characteristic peak energy of the flare.

The lower limits on E_{PEAK} in the figure represent Band function fits in which the value $\beta > -2$. In such cases, the standard relation $E_{PEAK} = E_0 \times (2 + \alpha)$ is not valid and the implication of such a flat high energy powerlaw segment in the Band function is that the peak energy is above the observing band. Thus, while the narrowness of the XRT energy range often limits us from determining an accurate measurement of E_{PEAK}, we are, nevertheless, able to measure useful lower limits in those cases. The red datapoints in the figure represent flares from the short burst GRB050724. The green datapoint represents a flare from GRB050802, which is highly unusual in its lightcurve profile, and may be best considered separately. Likewise, the blue datapoint represents the prompt emission pulse of GRB060124, which may also be best considered separately. The remaining black datapoints appear suggestive of a relationship, due primarily to the presence of a cluster of lower limits at early flare restframe times. There are clear outliers, however, to any potential powerlaw fit to the data, most obviously, the two lower limit points at $T_0+\sim$2000 and 3000 s which represent two of the late flares from GRB050904. A "best-guess" powerlaw fit to the data implies a relation (again, with significant outliers) of $E_{PEAK} \propto T_{rest}^{\sim -2}$, clearly different from the relation of $E_{PEAK} \propto T_{rest}^{\sim -5}$ found in Chapter 3 during our investigation of the series of flares seen in GRB050713A and by Krimm et al in their investigation of GRB060714. These differing results are not necessarily at odds, however, since the inherent differences in possibly unappreciated scaling relationships between the bursts in our sample may well mask the underlying relationship between flares within each burst in our sample.

We can investigate whether each individual burst displays a similar proportionality between E_{PEAK} and time, only with different offsets, by plotting E_{PEAK} vs restframe time for each of the individual bursts in our sample which display multiple flares. This is shown in Figure 4.12, in which we have also overplotted dashed lines corresponding to $\mathrm{E}_{PEAK} \propto T_{rest}^{-5}$ with varying proportionality constants. While we see several cases in this figure in which the flares do appear to be consistent with a relation similar to that seen in Chapter 3 (individual cases such as GRB050712, GRB050713a expectedly, GRB050716 and possibly GRB050803), it is certainly clear that there are cases where such a relation is violated by the data (GRB050502b, GRB050724, GRB050904). This would seem to suggest that a relation such as that seen in Chapter 3 and by Krimm et al is not ubiquitous among flares and may suggest that multiple flare emission mechanisms are required to explain the observations.

Figure 4.13 shows flare fluence (in the 0.2-10 keV band) versus rest frame flare onset time. We again restrict ourselves to plotting only flares from bursts in our *Gold* sample with measured redshifts. Here, however, no significant relationship is seen. Also as in the previous figure, it is possible that an underlying relationship exists from flare to flare within each individual burst which is being masked by uncorrected scaling relations that exist between the bursts. We investigate this possibility as we did previously for the E_{PEAK} versus time relation, by plotting the relation for each burst individually in Figure 4.14. The lines overplotted in Figure 4.14 represent the proportionality found between fluence and time in the Chapter 3 study of GRB050713A, S $\propto t^{-1.7}$. As in the case of our investigation of E_{PEAK} versus time above, some bursts appear possibly consistent with a decaying fluence with time as seen in GRB050713a, but there are clear cases in which such a relation does not hold throughout the burst. These cases clearly present difficulty for any model seeking to explain flares through a mechanism in which such a trend is predicted.

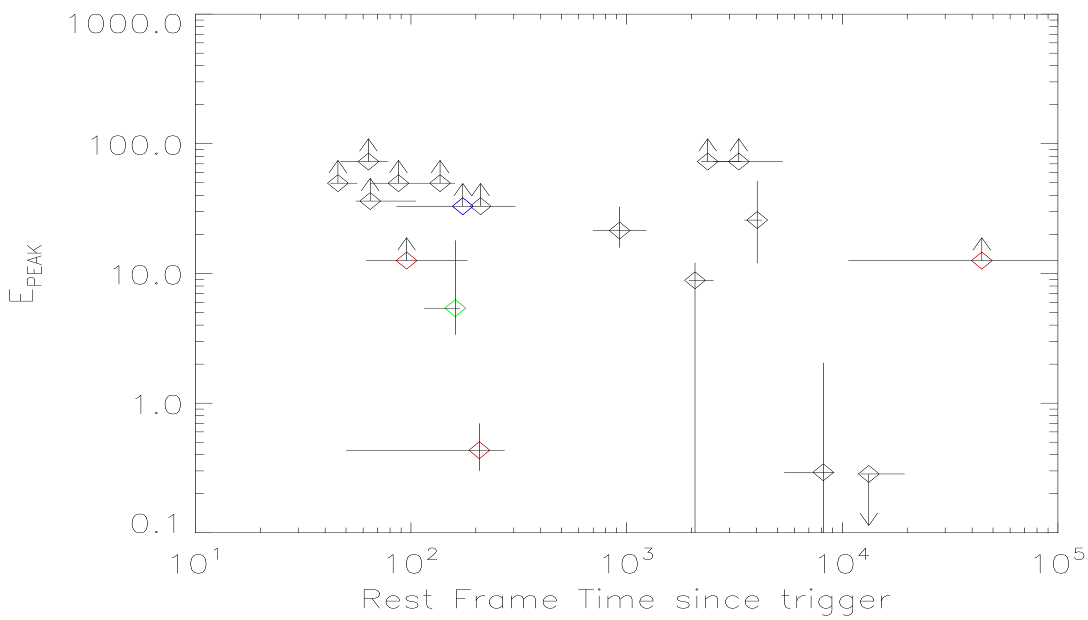

Fig. 4.11 Redshift corrected peak energy of *Gold* flares as a function of rest frame flare time relative to the trigger time, T_0. This plot contains all flares irrespective of (and unscaled for) prompt emission E_{peak}.

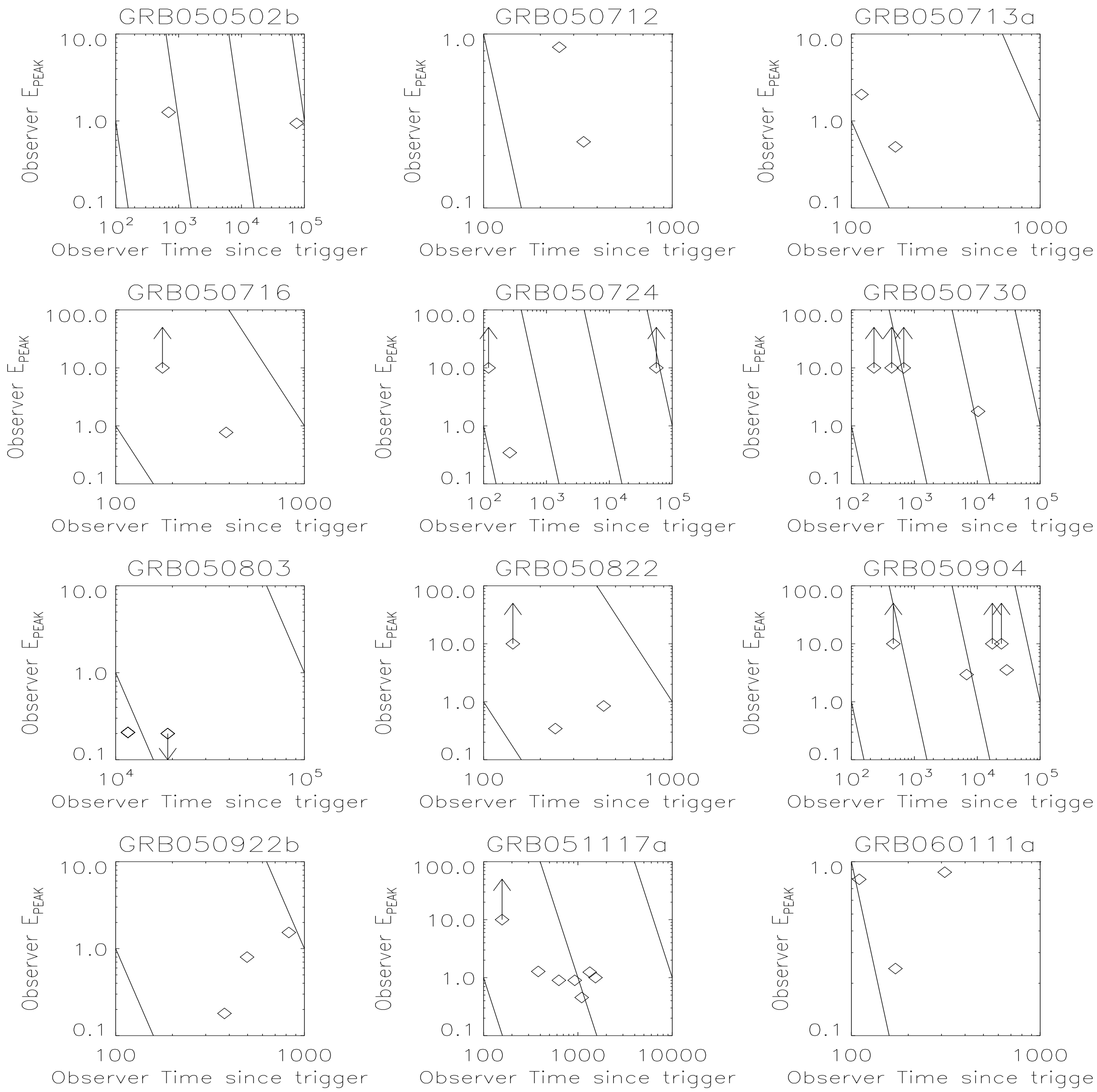

Fig. 4.12 Peak energy of *Gold* flares as a function of time relative to the trigger time T_0. This plot contains all flares irrespective of (and unscaled for) prompt emission E_{peak}. Lines corresponding to the relation $\mathrm{E}_{PEAK} \propto T_{rest}^{-5}$, found in our earlier study of a series of flares in GRB050713a and also found by Krimm et al. (2007), are overplotted with varying proportionality constants for comparison.

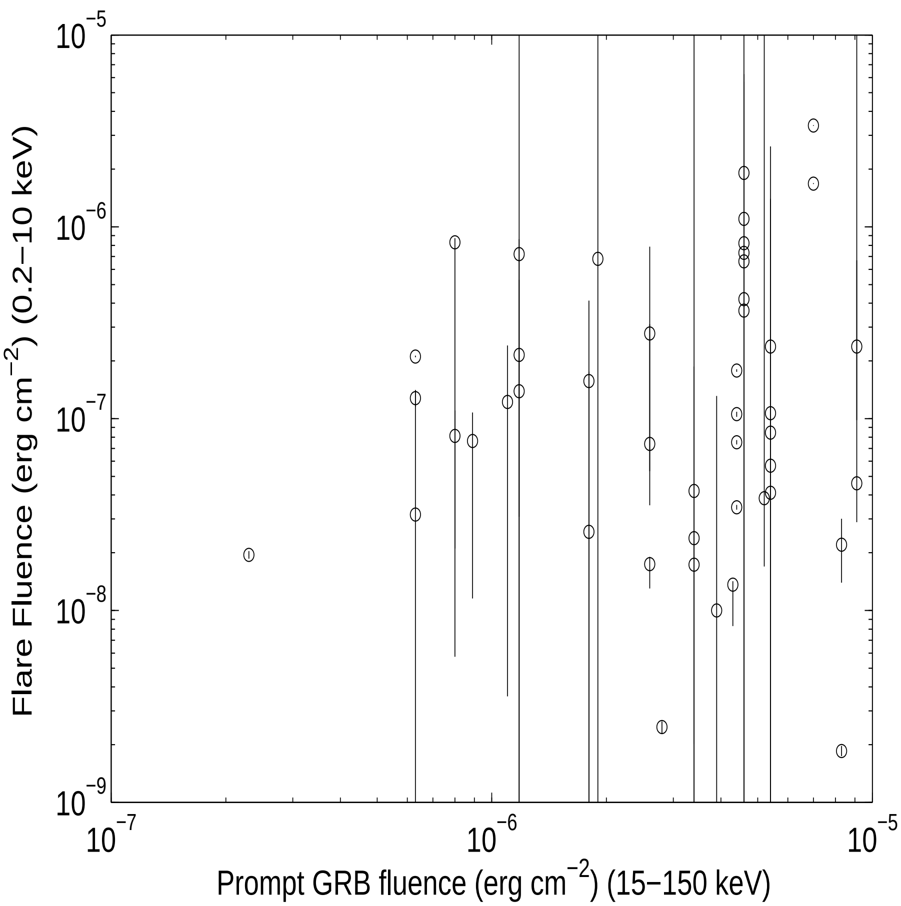

Fig. 4.13 Fluence for *Gold* flares as a function of flare time relative to the trigger time T_0. Fluence is k-corrected and is calculated in the 0.2 keV to 10 MeV band. This plot contains all flares irrespective of (and unscaled for) prompt emission properties.

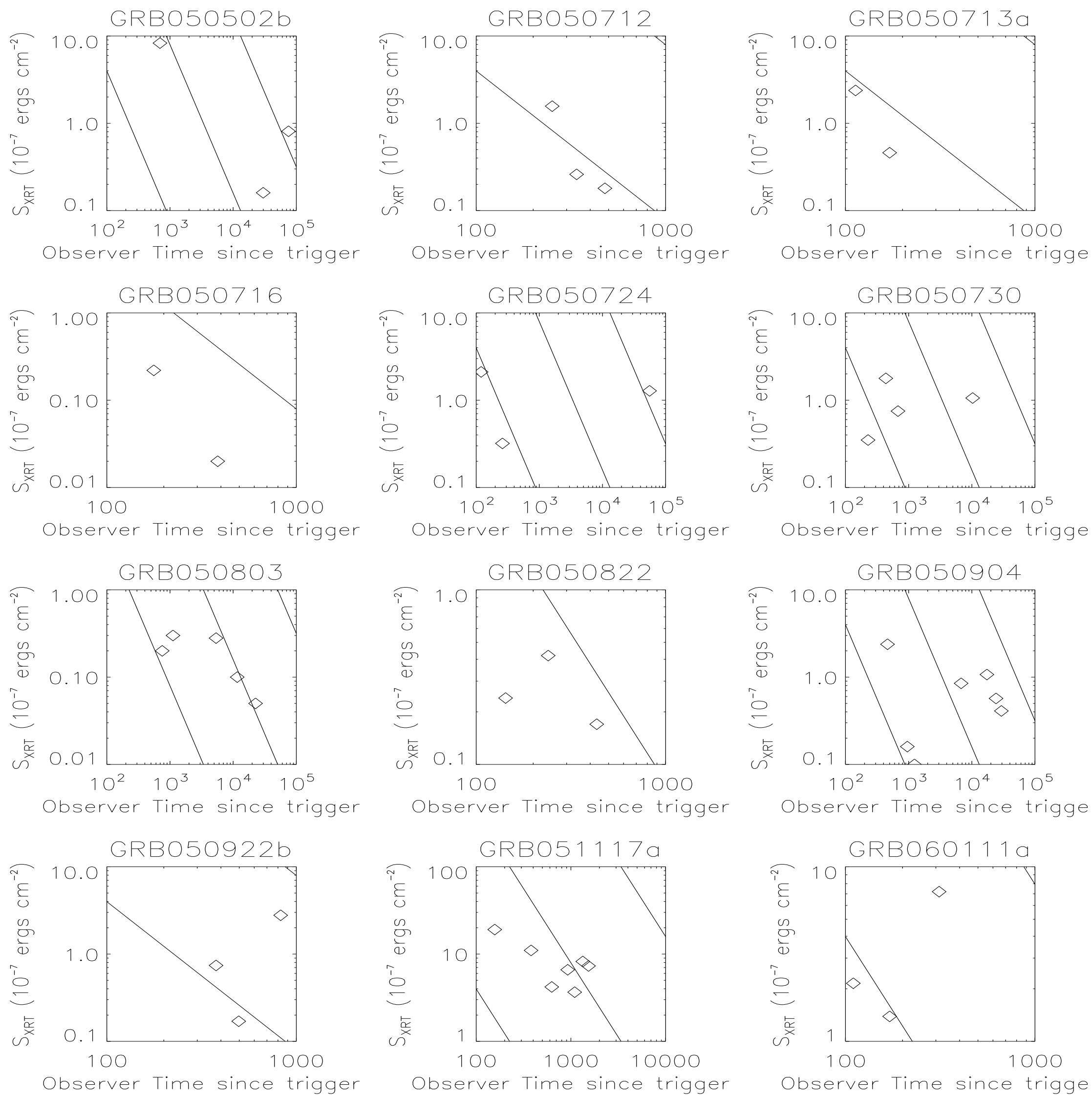

Fig. 4.14 Fluence for *Gold* flares as a function of rest frame flare time relative to the trigger time T_0. Values are k-corrected and calculated in the 0.2 keV to 10 MeV band. This plot contains all flares irrespective of (and unscaled for) prompt emission properties. Overplotted lines represent the proportionality found between fluence and time in Chapter 3, $S \propto t^{-1.7}$

4.8 E_{PEAK} versus E_{ISO}

It seems clear that the spectra of X-ray flares usually peak in the X-ray band, as evidenced by the fact that they were discovered as a *Swift* XRT phenomenon and have subsequently been observed primarily by the XRT, usually without strong emission in the neighboring energy bands of the UVOT and BAT. Though this statement slightly exaggerates the prevalence of X-ray flares in the XRT energy range since the limiting sensitivity of the XRT is lower than that of the BAT ($\sim 10^{-13}$ erg cm^{-2} s^{-1} vs. $\sim 10^{-8}$ erg cm^{-2} s^{-1}, respectively) and since there are other mitigating factors which may conspire to extinguish flux levels in the UVOT energy range, it has, nevertheless, been shown through high quality spectral fits to some individual flares (Falcone et al. 2006; Morris et al. 2007; Krimm et al. 2007) that X-ray flares usually do, indeed, have peak energy in the XRT bandpass. The precise determination of E_{PEAK} for flares is a topic of considerable importance since prompt GRB emission has shown evidence of an empirical relationship between the peak energy of the spectrum and the total energy in the ejecta, as well as the observed timescales of the emission (Ghirlanda et al. 2005; Amati 2006; Liang & Zhang 2006; Firmani et al. 2006; Thompson et al. 2007). Unfortunately, the narrowness of the bandwidth of this study (0.3-10.0 keV) combined with only moderate signal to noise level leaves E_{PEAK} somewhat poorly constrained in most flares in our sample. Given the considerable interest in this topic, however, we have proceeded to explore the E_{PEAK} - E_{ISO} relationship in our flares sample despite this limited precision. E_{PEAK} is defined as the peak energy of the νF_{ν} spectrum and is calculated from the e-folding energy parameter from the Band function fits to our flares as $E_{PEAK} = E_0$

(2+α) where E_0 is the e-folding energy and α is the spectral index of the low energy powerlaw segment of the Band model. E_{ISO} is the isotropic equivalent energy of the flare and measures the energy contained in the ejecta which produced the flare. We calculate E_{ISO} in the 0.2-10 keV energy range, assuming a Band function fit to the spectrum, and k-correct this value to the more standard energy range of 0.2keV - 10.0MeV as discussed by Bloom et al. (2001b). E_{ISO} is calculated as:

$$E_{ISO} = k \times \frac{4\pi d_{lum}^2}{(1+z)} \times [S_{obs}] \tag{4.2}$$

where S_{obs} is the unabsorbed observed fluence in the 0.2-10 keV band, z is the redshift, k is the correction factor to translate from the 0.2-10 keV to 0.2keV-10.0MeV energy band and d_{lum} is the luminosity distance calculated using a flat Λ dominated universe with Ω_M=0.31, Ω_Λ=0.69 and H_0 = 70 km s^{-1} Mpc^{-1}.

Figure 4.15 shows E_{ISO}, calculated as described, plotted versus (1+z)$\times E_{PEAK}$ for the flares in our *Gold* sample that have a measured redshift. Unfortunately, jet breaks in *Swift* GRBs have been rather difficult to identify and the paucity of confident jet breaks in the GRBs in our sample means that we cannot calculate the beaming-corrected energy E_γ. Thus we cannot explore the tighter E_{PEAK}-E_γ relationship reported for GRB prompt emission by Ghirlanda et al. (2005).

The redshift corrected E_{PEAK} values in Figure 4.15 seem to clearly indicate that X-ray flares are characterized by lower peak energy values than are typically seen in the prompt emission of GRBs. The relatively large uncertainties on these values of E_{PEAK}, however, make it unclear whether there is as strong a relationship between E_{PEAK} and

E_{ISO} seen in flares as is seen in the prompt emission. The hint of a relationship evident in Figure 4.15 is intriguing, however, and we will return to this subject in Chapter 5 with improved uncertainty in E_{PEAK}, achieved by expanding our spectral fitting band outside the XRT energy range.

4.9 Redshift Distribution

This sample contains 14 GRBs with measured redshifts. The redshift distribution is shown in Figure 4.16. The mean redshift for these 14 GRBs is $z=2.6 \pm 1.7$, which is consistent with the mean redshift of all *Swift* GRBs, reported to be between 2.5 and 2.8 (Burrows & The XRT Team 2006; Jakobsson et al. 2006b). Thus within this somewhat limited sample of measurements, flaring GRBs do not appear to show a radically different redshift distribution than their non-flaring counterparts. We note, however, that the uncertainty in the measured mean redshift of this small sample of flaring GRBs leaves open the possibility that the redshift distributions of flaring and non-flaring GRBs may differ and we refer the reader to Appendix C for a more detailed investigation of the redshift distribution of flaring versus non-flaring GRBs, performed using a larger sample of *Swift* GRBs.

4.10 Discussion

Based on the analysis of the first $\sim$ one year of *Swift* data, we see that X-ray flares are produced frequently and at late times. From 110 GRBs in the timeframe surveyed, we have found 33 GRBs to contain flares. Some bursts display multiple flares with two bursts displaying as many as seven distinct flares, and a total of 77 flares found

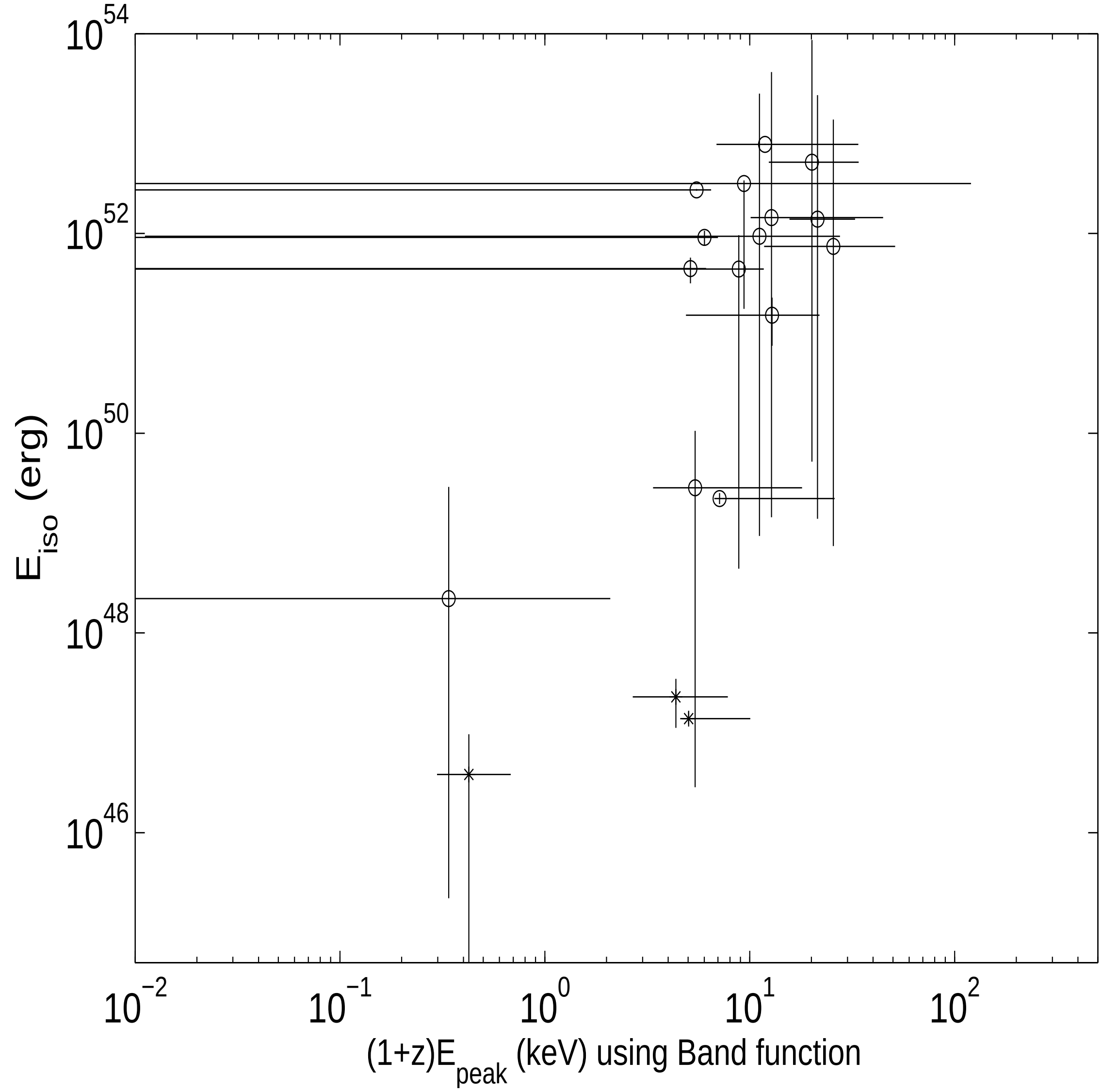

Fig. 4.15 Exploration of Band function fit for E_{peak} relationship with E_{iso} for flare emission. E_{iso} has been k corrected into the co-moving 0.2 keV to 10.0 MeV band. Only the fluence from the flare itself (i.e. underlying afterglow emission subtracted) was included in the calculation of E_{iso}. The three data points with the lowest E_{iso}, plotted as x symbols, are from flares associated with a short burst.

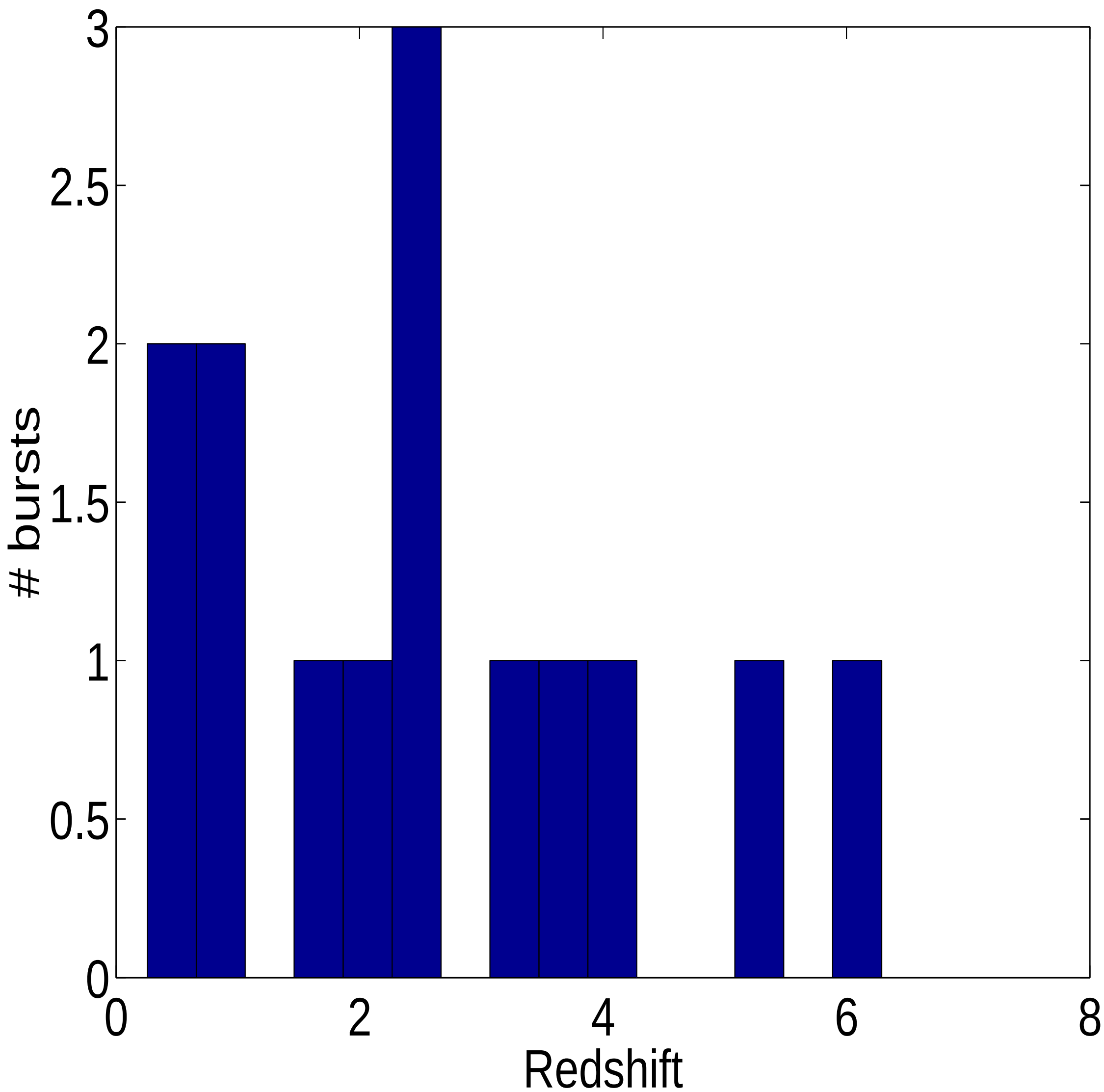

Fig. 4.16 Redshift distribution of GRBs with flares.

in the 33 burst sample. Each flare has been treated as a separate event and the resulting ensemble of parameters resulting from the spectral fits have been presented. This work, together with the companion work by Chincarini et al. (2007) provide the first systematic studies of the spectral (this work) and temporal (Chincarini et al) properties of a large set of flares. This work is also the first to separately treat and account for the spectral component underlying the flare which results from the GRB afterglow. This component can be an important factor in both the spectral fit and the resulting flux and fluence measurements of the flares when the afterglow is a significant fraction of the fluence of the flare.

Several spectral models were fit to each flare, including a powerlaw (similar to the model often characterizing the late time GRB X-ray afterglow) and a Band function (similar to the model most often used to characterize the GRB prompt gamma-ray and hard X-ray emission). Some flares were adequately fit by the simpler powerlaw model while some flares showed significantly improved fits by applying the Band function. We have shown that the improvement seen in the fit by applying the Band function is significant above the natural improvement in the fit that would be expected by using a model with a larger number of free parameters and it is unlikely that the entire sample of flares was drawn from a distribution of powerlaw spectra. We note here that the curvature implied by the improvement to the fits from using the Band function may be due to intrinsic curvature in the underlying emission mechanism but may also be due to evolution of a flat spectral model (such as a powerlaw) within the time region over which our individual flares are summed (we have treated each flare in its entirety in this study, ie without temporal separation). Such spectral evolution has been noted in prompt GRB emission by several authors (Golenetskii et al. 1983; Norris et al. 1986) and has been noted in flares by authors analyzing individual flaring bursts (Morris et al. (2007), also Chapter 3, Godet et al. (2007), Krimm et al. (2007)). We will return to this issue in Chapter 5 where we will temporally separate some brighter flares observed by *Swift* to investigate spectral evolution within a sample of flares. Nevertheless, the results of this analysis are similar to the results found for prompt emission from GRBs (Kaneko et al. 2006; Band et al. 1993), in which powerlaws sometimes provided a reasonable fit to prompt emission while the Band function provided a better fit to the overall sample.

We have also shown that the spectral indices of the flare spectra (if fit by a powerlaw) are often different from the spectral indices of the underlying afterglow (also fit by a powerlaw) and that the distributions from which these spectra are drawn are different from one another. In cases in which the underlying afterglow shows a different spectrum from the flare, this argues in favor of separate emission mechanisms for the two components. When combined with the $\Delta T/T \lesssim 1$ result from the companion work of Chincarini et al along with previous studies of individual bursts (Burrows et al. 2007; Falcone et al. 2006), this argues for flares as a product of late internal engine activity in the context of the standard GRB fireball model. These internal shocks may be due to shells of material ejected at early times which interact only much later or may be due to shells of material directly ejected at late times. We will return to discuss this topic in Chapter 5, but based on the inefficiency of the former process it seems most likely that the flares are due to shells ejected at very late times, comparable to the time of the flare occurrence.

We have calculated the average redshift value of the GRBs in our sample (among those with reliable redshift determinations) and find that the value is consistent with the average *Swift* redshift value. While the uncertainty on this value does not allow us to rule out the possibility that the flaring redshift distribution and the non-flaring redshift distribution may differ, it does imply that there is not a drastic difference in the redshift distributions of the two kinds of bursts (though see Appendix C for a detailed treatment). Together with individual analyses of flaring GRBs with measured redshifts showing bright flares at late rest-frame times, this implies that the large fluences sometimes seen in X-ray flares (e.g., in GRB050502B) must be able to be produced at late times and with peak energies in the X-ray band by any acceptable model for the production mechanism of X-ray flares. We will return to discuss the individual models proposed to explain flares and their ability or inability to explain the observations in Chapters 5 and 6.

Finally, we have also attempted, in this work, to explore the E_{PEAK} - E_{ISO} relationship for flares, in an effort to see if the Amati relationship (Amati 2006) is present in flares as well as in the prompt emission data in which it was originally noted. Unfortunately, the limitations of our sample (too few bursts with high signal to noise and measured redshifts) leads to uncertainties in the relation that are too large to conclusively determine whether the relationship is present or not (Figure 4.15). Although a relationship may exist and there is an intriguing hint of a correlation in this data sample which is similar to that reported by Amati for GRB prompt emission, more accurate measurements, particularly of the E_{PEAK} parameter, are required to make an accurate assessment of the validity of the relation with respect to flares.

Chapter 5

Flares Study II: A Broadband Window on Flares

We have seen, in the previous chapter, that much can be learned about the properties of GRB flares through an exhaustive survey of all flares viewed through the XRT energy window, in regards to timing and overall energetics. We have also learned, though, that the narrowness of the XRT energy window leaves much ambiguity regarding some key physical parameters describing the flares, in particular, the spectrum peak energy and neutral hydrogen column. To gain insight into the true nature of the spectral characteristics of GRB X-ray flares, it is apparent that an approach which uses the broader SED available by incorporating BAT and UVOT data would be helpful. Furthermore, the previous chapter showed us that spectral interpretation of faint flares is muddied by systematic uncertainties introduced by the underlying GRB afterglow. In order to make progress in the detailed understanding of GRB flares, then, it would seem fruitful to investigate the broadband SED of only the brightest X-ray flares seen to date, taking care to appreciate and account for systematic effects which may be caused by the introduction of data from each successive instrument from the XRT, to the BAT and finally the UVOT. In this chapter, we have defined a sample of only the brightest flares from the first 2 years of the *Swift* mission, which are well separated from one another so as not to suffer significantly from superposition contamination. We analyzed this sample of flares in a method similar to that of the sample in the previous chapter (methods as described in Chapter 2).

In this chapter, we detail the primary results from this multi-wavelength approach to the analysis of X-ray flares in GRBs. The chapter is organized as follows: in §5.1 we discuss the spectral fitting goodness-of-fit results. §5.2 presents the underlying afterglow properties of our sample of flares in comparison to the flares themselves. §5.3 presents the global spectral properties of the sample of flares. In §5.4 we discuss trends seen in bursts with multiple flares. In §5.5 we discuss the evolution of individual flares in a time-separated analysis. In §5.6 we discuss the flares in our sample in the context of the models proposed for the production of flares and categorize the flares in our sample according to criteria associated with each mechanism. Finally in §5.7 we discuss the implications of our analysis for the likely production mechanisms.

The complete gallery of XRT lightcurves from this flares sample is contained in Appendix B. These figures can be compared with the XRT lightcurve gallery from Chapter 4 (included as Appendix A) to qualitatively contrast the overall observational characteristics of the two samples. Hardness ratios accompany each lightcurve in Appendix B, supplying some simple spectral information.

5.1 Spectral results: Model Fit Comparison

The results from the spectral analysis on a whole-flare basis are summarized in Table 5.1 below.

Table 5.1: Flare χ^2

GRB	tstart (s)	PL	Band	PL+BB	BknPL
GRB 050502B	136719100.690	434.843	369.368	361.713	406.732
GRB 050502B	136770631.470	26.391	23.575	22.508	22.389
GRB 050904	147491812.740	203.493	192.847	192.331	191.871
GRB 060204B	160756776.680	44.958	39.777	40.093	39.680
GRB 060204B	160756567.590	203.638	166.286	176.296	164.929
GRB 060418	167022484.340	355.370	341.505	333.794	341.415
GRB 060418	167026926.010	94.033	73.807	44.145	94.033
GRB 060526	170353947.290	692.150	337.319	373.454	345.239
GRB 060526	170354000.030	331.336	279.337	277.924	297.698
GRB 060607A	171350024.600	142.064	138.776	138.607	137.151
GRB 060607A	171350136.610	255.396	226.417	232.643	226.500
GRB 060714	174582844.620	222.103	152.602	164.624	159.000
GRB 060714	174582883.600	118.689	108.903	109.698	107.569
GRB 060814	177289459.410	812.303	740.620	745.246	715.355
GRB 060904B	179029990.130	640.501	520.222	630.116	545.318
GRB 060929	181252979.040	301.141	270.202	275.881	272.651
GRB 061121	185815415.910	378.040	278.988	162.199	347.653
GRB 070107	189864569.110	218.175	217.546	213.938	215.153
GRB 070107	189865547.230	13.958	13.358	12.130	11.802
GRB 070318	195895938.980	134.239	156.654	126.855	124.671

The χ^2 value of the fit of a proposed spectrum to the observed data is a commonly used measure of the goodness-of-fit of the proposed spectrum to the data, and the difference in χ^2 between competing models can be used as a discriminator between models. We use this approach to compare the results of fitting the proposed spectral models to our flare SEDs. We need to use caution with this method in comparing models with differing numbers of free parameters since χ^2 values will naturally improve with the addition of more free parameters, as noted in the previous chapter. As a general rule of thumb, data which are equally well fit at approximately the 3-σ level by two models which differ by 1 in the number of free parameters in the models will yield χ^2 values which differ by about 1. To quantitatively examine the improvement in the fit from one model to another while taking into account the expected improvement from the addition of free parameters and random variation, we have, as in the previous chapter, run a Monte Carlo simulation in which we generate simulated data from the simpler of two spectral models that we wish to test, then attempt to fit the simulated data using both the simpler model (the one used to generate the data) and a more complex model. The number of counts in our Monte Carlo spectra are tuned to match the average counts found in our experimental data, ~ 4000 counts. Our first test compares fits using a simple absorbed powerlaw to fits using an absorbed Band function. In our second test, we compare fits using an absorbed Band function to fits using an absorbed powerlaw plus blackbody. To gauge the improvement in the spectral fitting process produced by the introduction of increasingly larger spectral windows (first XRT data alone, then XRT and

BAT together, and finally UVOT, XRT and BAT data together), we perform identical Monte Carlo simulations over the XRT band alone, the XRT and BAT band together and finally over the UVOT, XRT and BAT bands together.

Figure 5.1 shows the results of the spectral fits to our experimental data. The three panel figure shows the difference in χ^2 value between the absorbed powerlaw fit and absorbed powerlaw plus blackbody fit (top panel), the difference in χ^2 between the absorbed powerlaw fit and absorbed Band function fit (middle panel) and the difference in χ^2 between the absorbed Band function fit and absorbed powerlaw plus blackbody fit (bottom panel). In each panel, the 3 progressively broader energy windows are represented by different colors with red representing the XRT spectral window alone, blue representing the XRT and BAT spectral window together and black representing UVOT, XRT and BAT together. The different traces are also plotted in differing linestyles (solid red, dashed blue and dotted black) to help the readability of the figure where the histograms overlap.

Figure 5.2 shows the results of the spectral fits to the Monte Carlo simulated data. The three panel figure is formatted similarly to Figure 5.1 for the experimental data, with Powerlaw (PL) minus Powerlaw plus blackbody (PL+BB) in the top panel, Powerlaw minus Band in the middle panel and Band minus Powerlaw plus blackbody in the bottom panel. Unlike in Figure 5.1, here we show only the simulated results using data from all three instruments, though simulations were also run using only the XRT and the XRT-BAT energy ranges.

Turning our attention first to Figure 5.1 (the experimental results), we see the obvious advantage to performing this kind of spectral analysis in progressively broader spectral windows. The red histogram shows that in the XRT energy window alone, we have some ability to distinguish between spectral models, but a large fraction of the spectral results fall into the lowest $\Delta\chi^2$ bin in both the PL versus PL+BB (11/21) and PL versus Band (11/21) panels. Moving to the XRT-BAT energy window, the fraction in the lowest bin decreases for both the PL versus PL+BB (7/21) and PL versus Band (8/21) and decreases still further when we move to the complete UVOT-XRT-BAT spectral window (3/21 PL versus PL+BB and 2/21 PL versus Band). The experimental results imply that the Band function spectral model is generally found to be a more appropriate fit to these flaring data than a simple absorbed powerlaw, and that this implication becomes stronger as we observe the spectra through an increasingly broader energy range, as should be expected.

Comparing our experimental results to the Monte Carlo simulated results in Figure 5.2 we gain insight into what fraction of the improved fits may be attributed to random variation and what fraction can be confidently attributed to a better intrinsic spectral model. In the Monte Carlo results we do not see the strong tendency for an increase in the $\Delta\chi^2$ as we move to the broader energy band which is expected since the spread in $\Delta\chi^2$ seen in the Monte Carlo data should be due to random variance rather than due to revelation of a poorly fitting spectral model as in the actual data results.

The trivia of which model fits the data best is of little physical importance of course, particularly when the best fitting model is a purely empirical creation, specifically crafted to fit the observed data (as is the Band function) rather than a model grounded in physics which fortuitously happens to fit the observations. In the latter case, the fitted parameter values would offer direct information regarding the underlying physics of the emission process. In our case, however (the former), we are left to draw conclusions about the underlying physics based on the benchmark parameters fitted by the model, though those benchmark parameters themselves are not directly indicative of any particular physics. Therefore, the result from the analysis above showing that the Band function is generally a better fit to the X-ray flare spectra than a simple absorbed powerlaw is only interesting if we additionally consider the reasons for the improvement in fit. The mere fact that the Band function generally fits better than an absorbed powerlaw may be somewhat naively taken as evidence for these X-ray flares to be associated with GRB central engine activity rather than to be associated with the GRB afterglow, but once again, this result is only particularly interesting if we understand its implications.

A simple absorbed powerlaw is often a good approximation to the GRB afterglow fit because at times appropriate to the afterglow, the forward shock (hereafter, FS) cooling break is presumed to have evolved below the observing band and no new e^{-} are being injected into the fireball. This means that the afterglow, as observed in the soft X-ray band, possibly even in the UV (depending on the exact time since the onset of the afterglow) is produced by the synchrotron cooling of the FS e^{-} and is, therefore, expected to have a characteristic powerlaw shape set by the distribution of thermal Lorentz factors of the e^{-} (a powerlaw distribution with slope generally taken to be $2 < \mathrm{p} < 2.5$). The fact that a simple absorbed powerlaw does not fit the spectra of the flares implies that a break is required somewhere between the UV and hard X-ray to explain the emission process.

Through inspection of the SED fits that we have produced to our X-ray flares sample, we find that the break to the spectrum is generally required due to a deficit in the UV region of the spectrum (as described by a simple absorbed powerlaw fit to the data). There are two general reasons why such a UV deficit may be introduced. Firstly, a UV deficit (again, as fit by an absorbed powerlaw) would be seen if the peak of the νF_ν spectrum was to move from below the low-energy edge of the UVOT observing window into the region between the UV and X-ray (approximately the 10-100eV range) in our spectra. This would imply the injection of newly shocked e^- to the afterglow or the addition of a new "hot" synchrotron component, with newly shocked e^- on top of the continuing "cold" afterglow emission. In either case, the implication is an additional input of energy to the GRB above what was seen prior to the flare. A second possible reason for a break between the UV and X-ray range is a poorly understood dust reddening component. The effects of dust reddening in GRBs have been a topic of considerable recent interest (Schady et al. 2007; Jakobsson et al. 2006a) due, in large part, to the fact that the *Swift* UVOT has seen far fewer GRB afterglows than expected (Roming et al. 2006). As discussed in Chapter 2, throughout this work we have used a generalization of the analysis by Schady et al. (2007), leading us to use the same fixed dust to gas ratio for all bursts in our sample. If this dust to gas ratio is inappropriate for our burst sample (note that the Schady et al analysis was, by necessity, performed on a low-redshift GRB sample while our flaring bursts sample is, if anything, biased towards larger redshifts (see Appendix C)) or if the dust to gas ratio is not constant throughout a burst or from burst to burst, this assumption will clearly introduce a measure of uncertainty into our analysis. In favor of the utility of the single dust to gas ratio value used in this analysis, though, we note that fits to the underlying afterglow spectra in this analysis have generally been quite reasonable. If the global dust to gas ratio used here were inaccurate, we would expect that the fits to the underlying powerlaw would not be well fit by a simple absorbed powerlaw (owing to a deficiency in the UV, as we see when fitting flares). In fact, however, the late time afterglow is generally well fit by a simple absorbed powerlaw, the result one should expect if the dust to gas ratio is accurate and the break seen in flare spectra is actually due to the e^{-} injection or cooling break, both of which are likely to have shifted below the UVOT observing range at the epoch where the underlying afterglow is measured. Thus, the solid fitting results produced in fitting the late time underlying powerlaw afterglow component (generally fit using UVOT and XRT data) give us confidence in using the same dust to gas assumption in fitting the spectra of the flares sample. Throughout this work we will proceed under the assumption that the spectral break we find in the flares is due to the presence of physically evolving injection or cooling breaks rather than a systematic effect of an inaccurate reddening measurement.

5.2 Underlying Afterglow Properties

Fits to the underlying afterglow component of the flares are generally well modeled by a simple absorbed powerlaw. As noted in Chapter 2, however, we also fit an absorbed broken powerlaw to the underlying afterglow decay (hereafter, UAD) data for comparison. If an F-test comparison showed the broken powerlaw fit to be superior to the simple powerlaw at 3-σ significance, the broken powerlaw was used instead. This criteria was met in 6 of 20 of our flares (4 bursts) as shown in Figure 5.3. In cases where a broken powerlaw fit to the underlying afterglow component was preferred, the break is required to better fit the upper limits of the UVOT measurements during the afterglow.

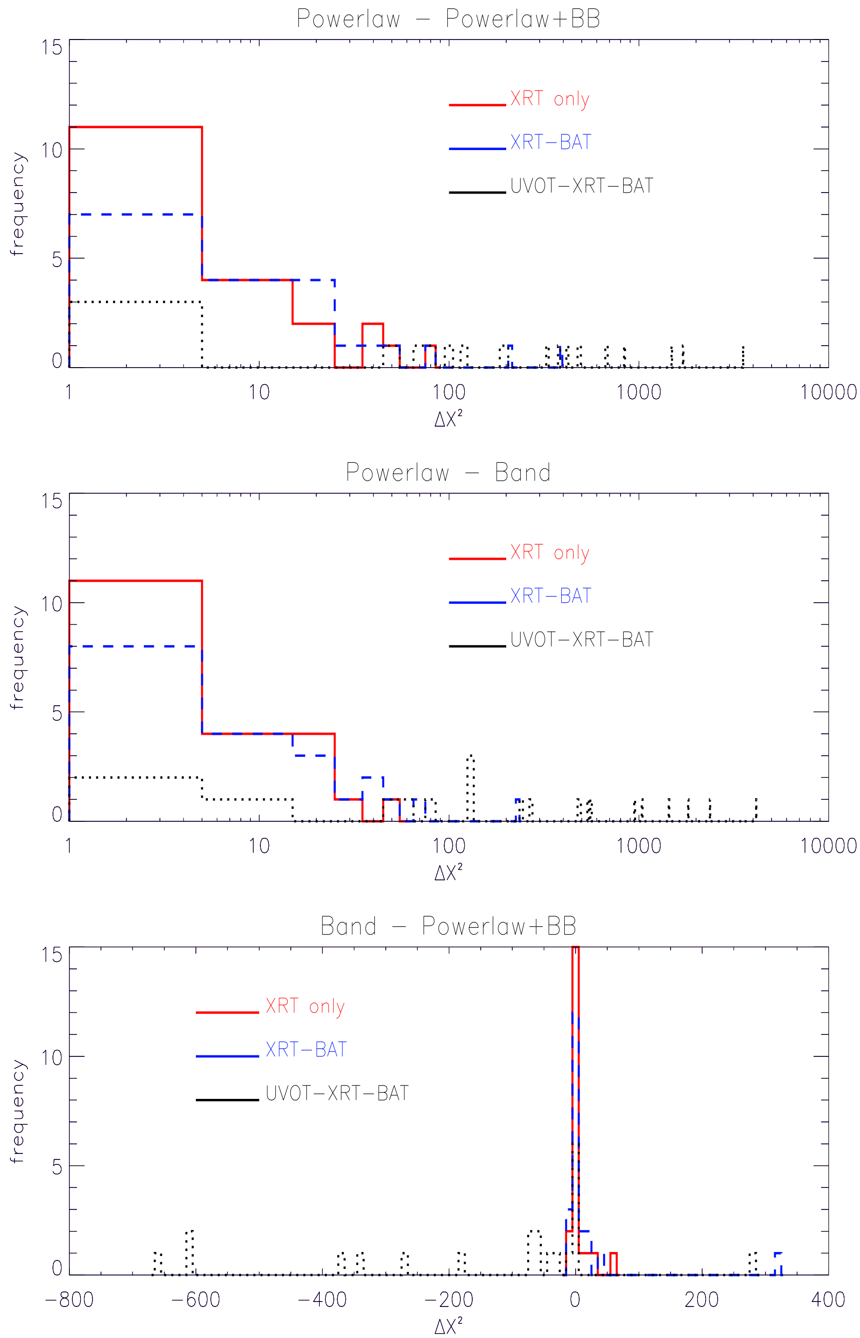

Fig. 5.1 Flare Fits $\Delta\chi^2$. This figure details the goodness-of-fit of a thermal model in comparison to a simple powerlaw (top panel), a Band function to a simple powerlaw model (middle panel) and a thermal model in comparison to a Band function (lower panel). Within each panel, the results of spectral fits performed on XRT data alone are shown in red, fits to XRT-BAT together are shown in blue and fits to the entire UVOT-XRT-BAT dataset are shown in black. $\Delta\chi^2$ clearly shifts to larger values in all panels, showing that fitting in broader bandpasses improves our ability to discern between models. Upper and middle panels are plotted logarithmically in X since there are no values below zero in these panels. The lower panel has both positive and negative values and is therefore plotted linearly in X.

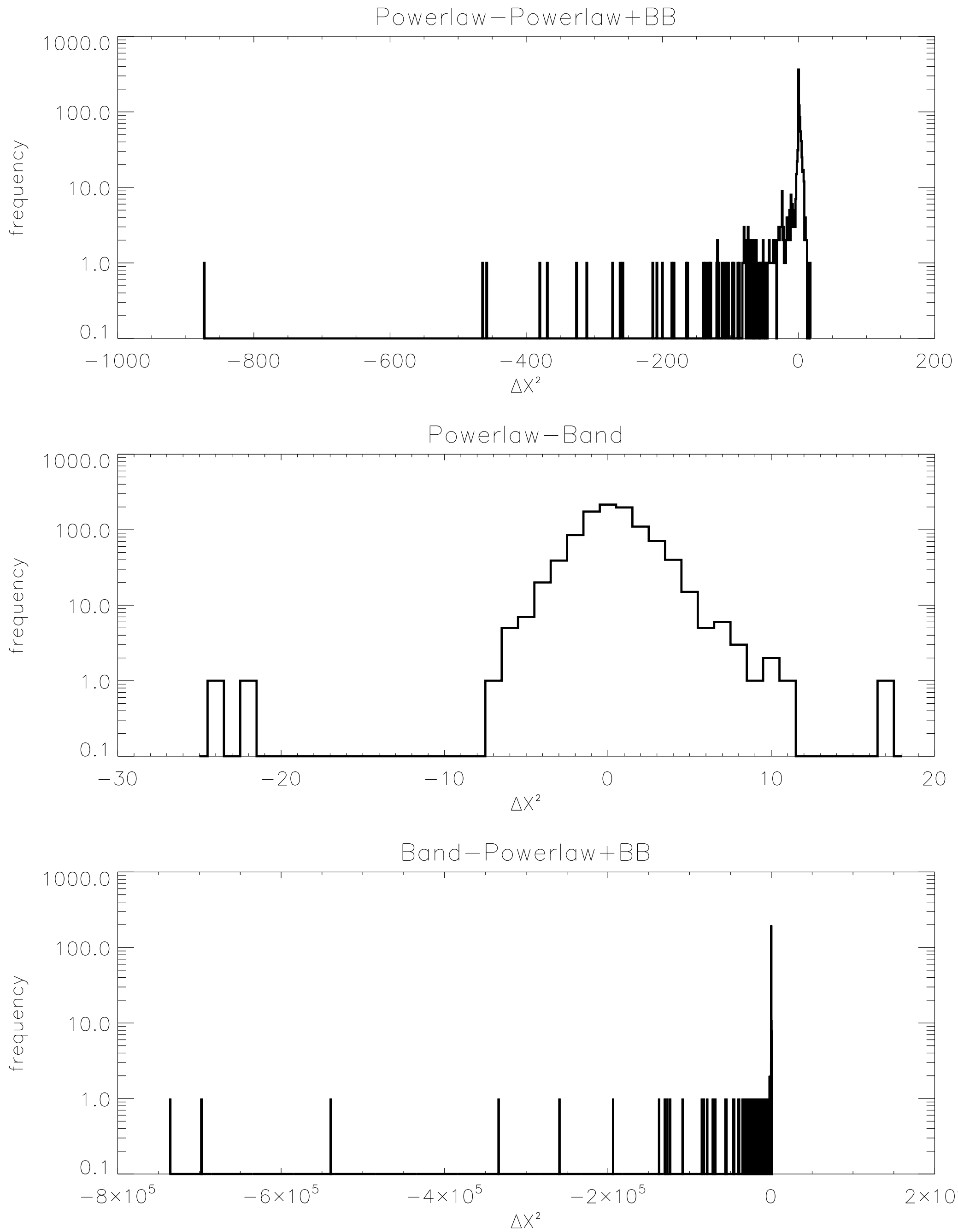

Fig. 5.2 Simulated Flare Fits. This figure shows the results of a false-positive detection simulation done to test the likelihood of incorrectly finding a superior fit to a higher order spectral model using data which are due to a process inherently described by a lower order spectral model. In the top panel, fake spectra were generated using a powerlaw model, then fit with both a powerlaw and a thermal model; the $\Delta\chi^2$ results are shown. In the middle panel, fake data are produced from a powerlaw model and are fit using a powerlaw and a Band function. In the lower panel, fake spectra are generated using a Band function and are fit using a Band function and also using a thermal model.

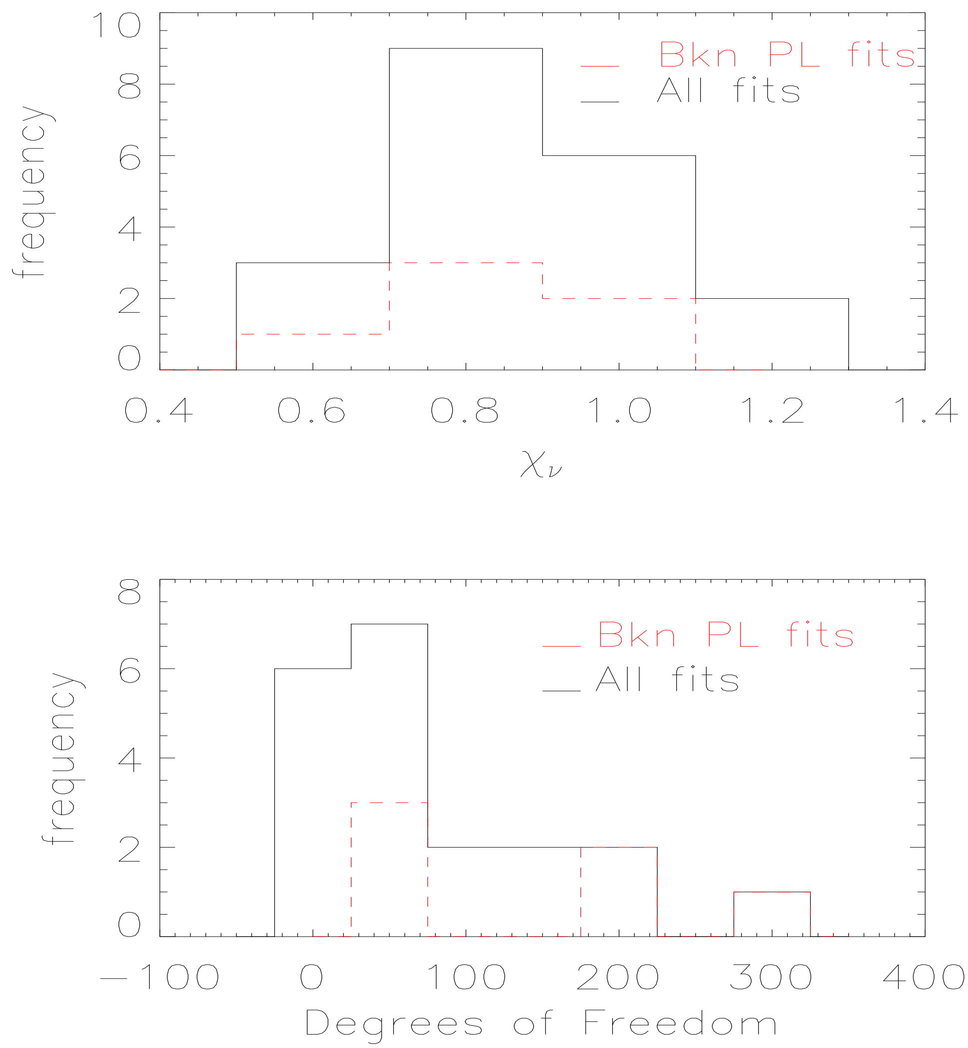

Fig. 5.3 Underlying Afterglow Fits. The upper panel shows results of reduced χ^2 while the lower panel shows total degrees of freedom in each fit. In both panels, the complete sample is shown by the solid line while the subsample of values for flares refit using a broken powerlaw are showed by the dashed line.

There are two possible reasons why a break may be needed to fit the UVOT limits in these 6 flares: either because a physical break in the spectrum exists, or because we have poorly accounted for extinction in the UVOT band as defined by our linking of the N_H to dust reddening, as has been discussed in the Chapter 2 and §5.1. I believe the former to be the case on the following grounds. First, most of our UADs show a reasonable fit using a single-slope power-law fit, suggesting that both the cooling break ν_c and characteristic electron energy break ν_m are below the red end of the UVOT observing range at these times and, furthermore, that the N_H to dust ratio used in the fitting is consistent with these simple powerlaw fits (see §5.1). In the case of the 4 bursts in which a broken powerlaw fit is preferred, all are calculated using afterglow data prior to T+10ks in the observer frame. Under the assumption that ν_c was near the XRT energy bandpass during the early afterglow observations, it is not unreasonable to believe that ν_c has not yet dropped below the bottom of the UVOT observing range when the afterglow data are collected for this subset of afterglows. Even in the few cases where a broken powerlaw fit is preferred, the improvement to the fit is not overwhelming (just above 3-σ). Considering, therefore, that our tying of the dust reddening to N_H generally produces reasonable fits to the simple absorbed powerlaw fit that one would expect for this observing band at later times of the GRB afterglow, and that the only cases in which a broken powerlaw fit is preferred are both a) marginal improvements and b) potentially explained on the physical grounds of needing a cooling break, it seems that the dust-gas ratio we have used is a reasonable approximation to use in our fits to the afterglow and, by extension, in our fits to the flares themselves.

The mean spectral index of the simple powerlaw fits to the underlying afterglows is $\beta = 0.87^{0.33}_{0.33}$ while the mean break energy, high energy spectral index and low energy spectral index of the broken powerlaw fits are $1.7^{0.45}_{0.45}$ keV, $0.11^{0.65}_{0.59}$ and $0.80^{0.46}_{0.42}$ respectively. These values of the spectral index (the high energy spectral index in the case of the broken powerlaw fits) are in good agreement with values seen for the underlying afterglow components from Chapter 4 (in which we were analyzing XRT data alone and did not have an additional reddening component) and, moreover, with typical X-ray afterglow spectral indices of the late-time afterglow phase in the literature.

One of the distinguishing characteristics which we will use to help determine the likely emission mechanism of the flares in our sample is the flux contrast level of the flare with respect to the underlying afterglow beneath it. Figure 5.4 shows a histogram of the ratio of the time averaged flux levels of the flares in our sample (ie, the flare fluence divided by duration) to the time averaged flux level of the afterglow beneath the flares. As can be seen in the figure, the flares in our sample are often 10-100 times brighter than the underlying afterglow in a time averaged sense, though a few flares are seen at a ratio as low as 2. Concentrating mostly on bright flares in this sample has the advantage of isolating the flare spectral parameters from the underlying afterglow parameters throughout most of the analysis, though it may necessarily introduce some bias against identifying and categorizing the faintest flares in the *Swift* database, a discussion of which is left until later.

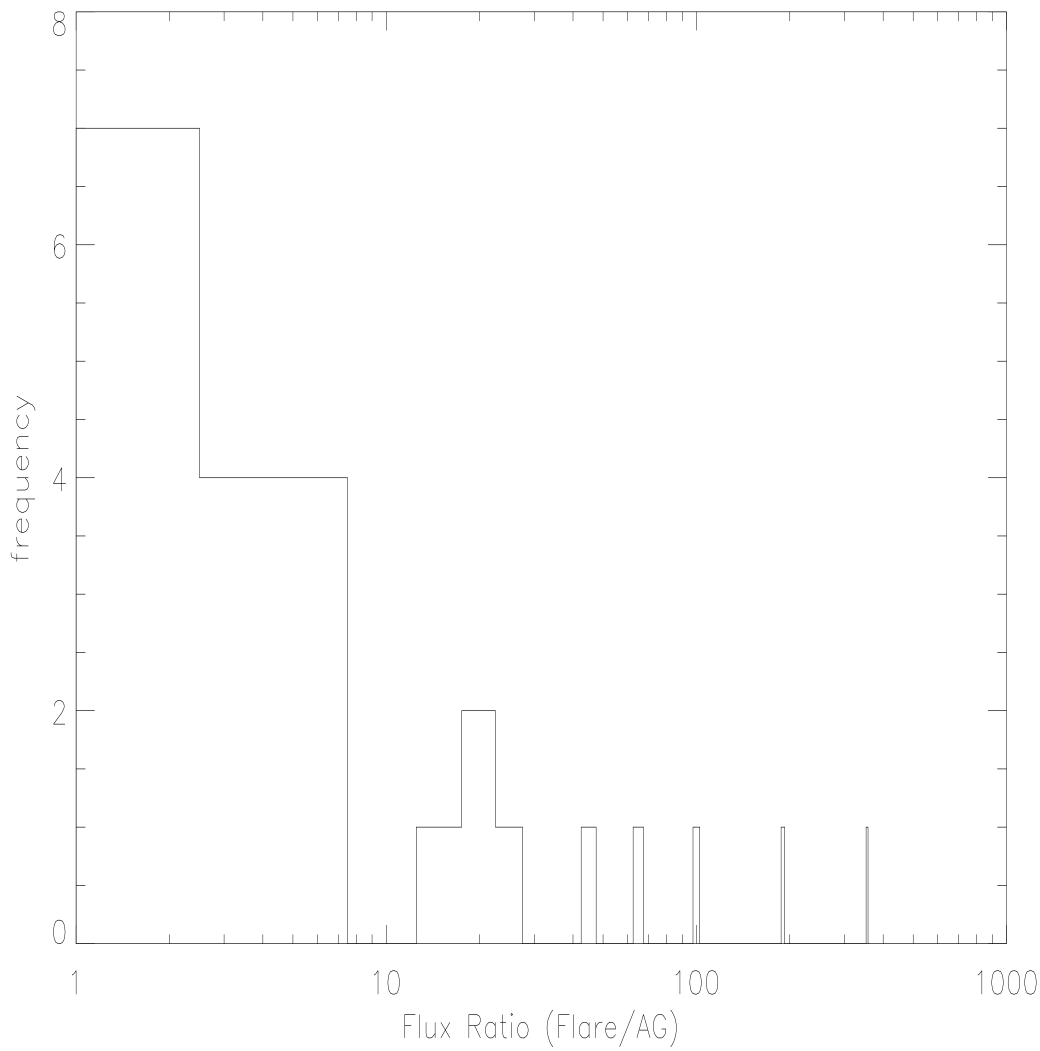

Fig. 5.4 Ratio of time averaged flux of flares and afterglow. Flares in our sample and the underlying afterglow flux generally differ by about an order of magnitude, though it can be seen that we include a small number of flares in this sample at relatively low flux levels. These flares are included in the sample because they are well isolated making them useful as clean flare samples.

5.3 Flare Global Properties

5.3.1 Band Function: α - β

The $\alpha - \beta$ distribution from fits to the Band function is shown in Figure 5.5. The means and standard deviations of the total populations of αs and βs are -1.2 $\pm$ 0.55 and -3.0 $\pm$ 2.4 respectively. While the mean values of these parameters are within the expected range for a spectrum fit by a Band function with the peak of the νF_ν spectrum within the observed data window, there are a number of individual flares for which this is not true. Specifically, there are 4 flares for which we measure $\beta > -2$, indicating that the peak energy of the spectrum is outside the observed energy range, and that the Band function parameter E_0 is actually a lower limit on the true peak of the spectrum, indicating, instead, the lower boundary of the high energy powerlaw component of the spectrum (Preece et al. 2000). This is not a completely surprising result considering the relatively low energy window to which our SEDs are biased by the use of the highly sensitive XRT instrument in the 0.2-10 keV energy range while the BAT and UVOT are relatively less sensitive in their respective energy ranges (due, in the case of the BAT, to inherently lower sensitivity and possibly due, in the UVOT, to the mitigating effects of excessive dust and gas in the GRB host (Roming et al. 2006)).

It has been argued, however, on both observational (Chapter 3 and Krimm et al. (2007)) and theoretical (King et al. 2005) grounds that there is a general trend for successive pulses or flares within a GRB to exhibit progressively lower peak energy. If this is true, we would expect that flares in our sample for which $\beta > -2$ may precede flares with $\beta < -2$ but not the reverse. There are 4 cases in our flares sample in which

$(\beta - \sigma_\beta) > -2$ and in 3 of those 4 cases the flare is found in a burst with multiple flares. In 2 of those 3 cases, the flare with the larger (ie, less negative) value of β is, indeed, followed by at least one later flare with $\beta < -2$ and, hence, a peak energy measurement within or below the observed energy range. The 1 case in which the flare with $\beta > -2$ follows a flare with $\beta < -2$ is GRB 050502B. This is a well chronicled GRB (Falcone et al. 2006) which shows a very large flare at early time (starting at T+350s) generally attributed to central engine activity and one or two flares with much later start time (starting at T+50ks) which are possibly explained by central engine activity but also possibly explained by other scenarios such as interaction of the external blastwave with the circumburst environment or re-energization (Falcone et al. 2006). If the second flare (in our analysis we have analyzed the 'bump' beginning at T+50ks and lasting for $\sim$ 100ks) is due to a process unassociated with the central engine activity that is strongly believed to be responsible for the first giant flare in this GRB, there is no reason to expect the generalization that E_{peak} decays with time to hold with respect to this sequence of flares. Thus, the observation that the peak energy of the late time flare in GRB 050502B appears to be above the observed energy range (0.002-10 keV in this case since BAT event data for this late time flare are not available) may suggest that the late time flares in this burst are not due to central engine activity. We will return to this discussion later during a closer examination of all bursts in our sample with multiple flares.

We overplot the $\alpha - \beta$ distribution of a broad sample of BAT bursts (blue dots - all bursts up to GRB 070809) in Figure 5.5 for comparison to the flares. The distributions show general similarities, though there is a clear tendency for the high energy spectral index to be well constrained in the flares data more often than in the prompt emission data. Values of $\beta \sim -2$ are typically seen in these fits when the high energy end of the spectrum is well populated whereas β tends to go to extremely steep values ($\lesssim -8$) when the region above the break energy is poorly populated. Thus, we can understand the apparently better constrained values of the high energy spectral index β as indicative of the movement of the characteristic peak energy of the emission from within or often above (leading to the poorly constrained βs) the BAT energy range during the prompt phase, to well within the XRT-BAT energy range during the flaring emission.

5.3.2 Band Function: E_{peak} and N_H

If we contrast the E_{peak} - N_H distribution of the flares in our sample with the Γ - N_H distribution from fits of a simple absorbed powerlaw, we find a trend to lower N_H values when fit using the Band function than with an absorbed powerlaw.

This is a trend noted by Butler & Kocevski (2007) that we also see in our work. We reiterate at this point that a separate neutral hydrogen column is included in the fit to account for the galactic absorption component, meaning that the values of the N_H parameter noted here are measures of the GRB-local gas (and dust). The mean value of the N_H measured by fitting an absorbed powerlaw model is 6.5×10^{21} with a standard deviation of 7.8×10^{20} while the mean value of N_H measured by fitting an absorbed Band function is 1.8×10^{20} with standard deviation of 1.6×10^{20}. The reason for the difference between the N_H values measured using the Band function and those measured using a simple absorbed powerlaw is that there is a parameter degeneracy in using a simple absorbed powerlaw to fit data which are dominated by emission (or at least dominated by events observed) in the soft X-ray band. The degeneracy is “due”

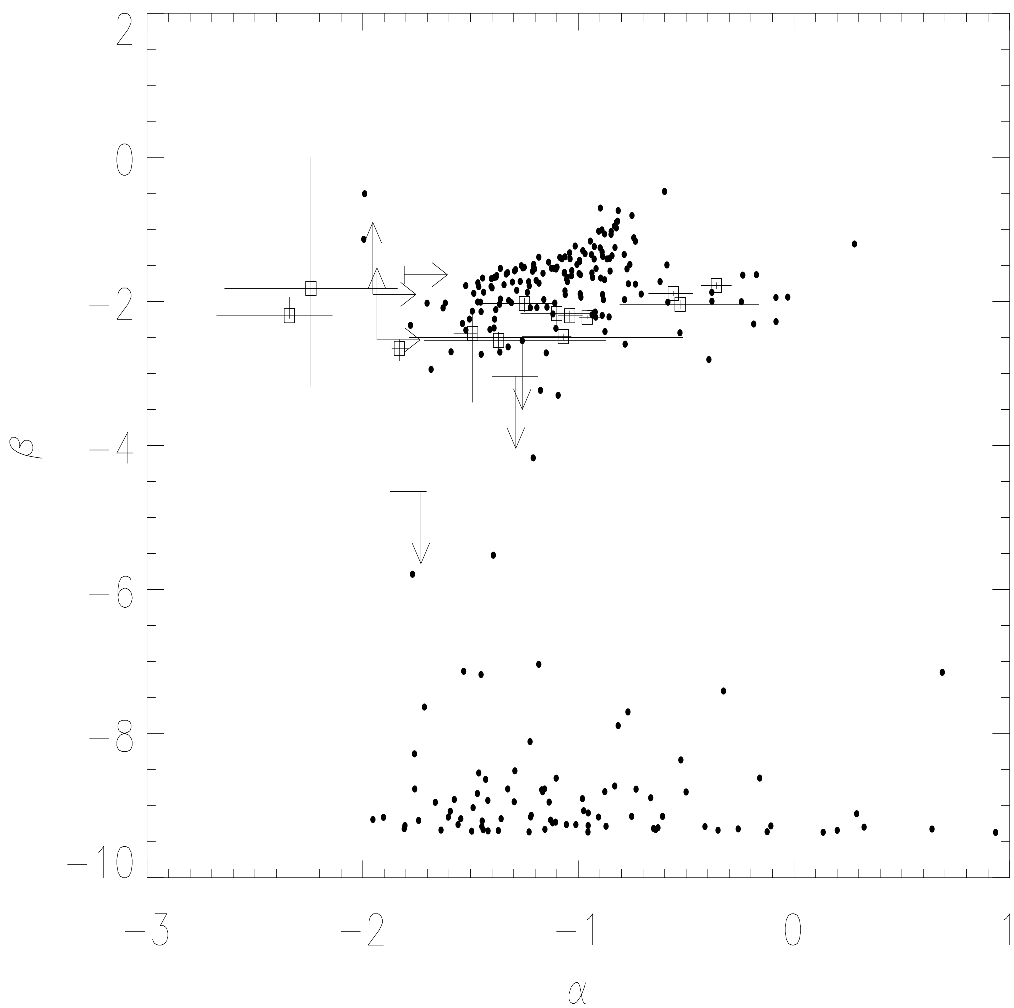

Fig. 5.5 Flares $\alpha-\beta$ plane. The distribution of the low energy spectral index α and high energy spectral index β from a fit of our flares to the Band function is shown (boxes). For comparison, values of α and β from the complete set of BAT-detected GRBs are shown as dots. The BAT data show two distinct populations, one at $\beta \sim -2$ and another at $\beta \sim -10$. The latter is due to extremely soft bursts with little high energy flux where the Band function becomes approximately a cutoff powerlaw. Two X-ray flares in our sample are found at $\beta \sim -10$ but the vast majority are found with well-defined values of β. In general, the flares spectral parameters seem to agree well with the parameters of the typical prompt GRB emission, albeit at lower values of E_{PEAK} (see later discussion).

to the effect of metal absorption (colloquially known as N_H absorption though this is a misnomer as the absorption is actually due to the presence of heavier metals, for which N_H is only a tracer) in the energy range between $\sim$ 0.1 and 2.0 keV in the observer frame. The result of this degeneracy is that the N_H parameter and the spectral index of the fit "share" the work of accounting for a soft deficit (or excess), leading to generally overestimated values of N_H and overestimated (in the sense of being too steep) spectral indices.

Introducing the Band function and fitting also to BAT and UVOT data helps to remove this degeneracy. With E_{PEAK} generally in the 1.0-50.0 keV range, the Band function upper spectral index is generally ignorant of the effects of N_H absorption (since it begins at the energy break, generally near or above the end of the largest effects of N_H at $\sim$ 2 keV) and, furthermore, is constrained by the BAT data so effects from absorption, when present, are minimized. On the other hand, the low energy spectral index will be susceptible to effects of absorption. Fitting also to UVOT data at the low spectral energy end, however, helps to constrain the low end index, though we again admit that reddening effects may be important in this part of the spectrum, and while we have earlier shown that our dust-gas correction seems to be acceptable, this is a caveat that should be noted.

The result of using the Band function together with data from the BAT and UVOT as well as XRT, is a model with low and high energy spectral indices that are well constrained and independent of the N_H measurement to as high a degree as can be achieved within the *Swift* dataset. It seems reasonable, then, to take the N_H measurements from this method as more reliable than those from using other spectral models.

Several authors have noted N_H excesses or variable N_H values during X-ray flares which appear to decay to values only slightly above the galactic value at later times in the afterglow (Starling et al. 2005; Campana et al. 2007) and have invoked this change in N_H as evidence of ionization or recombination activity or both during flares.

Our analysis shows that the N_H values derived from fitting the Band function to the entire UVOT-BAT dataset yield values of N_H during flaring periods which are consistent with the N_H values seen during the later afterglow phase of the burst (measured at the time of the underlying afterglow measurements in our analysis). Figure 5.6 compares N_H values in the flares to the N_H values of the afterglows and shows that the overall distributions are roughly similar. The K-S test of these two distributions shows them to be consistent (77% probability). Table 5.2 shows the time regions and N_H values for each burst in our sample as well as the background segment together with a fit to the ostensible decay of N_H through the burst, assumed simply to follow a powerlaw trend. In Figure 5.9 we show the N_H vs rest frame time behavior of our flare sample. A powerlaw fit to the complete sample is consistent with no change in N_H with time or a slight decay of N_H with time. The uncertainty in the data leaves open the possibility that the N_H may be either increasing or decreasing, though we can impose the limits that N_H appears not to increase faster than $t^{0.1}$ or decrease faster than $t^{-0.1}$. While this may seem a narrow range, it leaves open the potential to either increase or decrease the N_H by a factor of 2 in the first 1000 s of the burst and by a factor of 3 in the first day (rest frame). We will return to discuss the implications of these limits for dust and gas models around GRBs later in the discussion (see Chapter 6).

Table 5.2. Flare N_H in Time

GRB	T (s)	N_H ($\times 10^{22} cm^{-2}$)	T (s)	N_H ($\times 10^{22} cm^{-2}$)	T (s)	N_H ($\times 10^{22} cm^{-2}$)	T (s)	N_H ($\times 10^{22} cm^{-2}$)	fit
050502B	314	1.8e-4	26675	0.159	3279	1.e-5	3311	5.5e-4	1.5
050904	27.6	3.2	61.0	5e-4	-	-	-	-	-11.0
060204B	34.8	2.19	86.8	2.75	935	1.68	906	1.99	-0.1
060418	65.25	0.63	337.6	0.0069	1933	0.46	3587	0.00038	-1.1
060526	62.3	1.17	95.6	1e-5	396.4	0.53	396.4	0.44	2.0
060607A	28.6	1e-5	71.1	1e-5	1080	0.144	1080	0.150	2.9
060714	38.1	1.61	54.81	0.69	803	0.48	803	1.32	-0.1
060814	48.7	0.72	130.6	0.87	-	-	-	-	0.2
060904B	128.5	0.64	2780	1e-5	-	-	-	-	-3.6
060929	175.1	1.15	35126	1e-5	-	-	-	-	-2.2
061121	33.4	0.19	352.6	0.57	-	-	-	-	0.5
070107	112.2	1e-5	403.6	0.111	9769	1.42	9769	1.62	2.2
070318	188.0	0.37	718.5	0.74	-	-	-	-	0.5

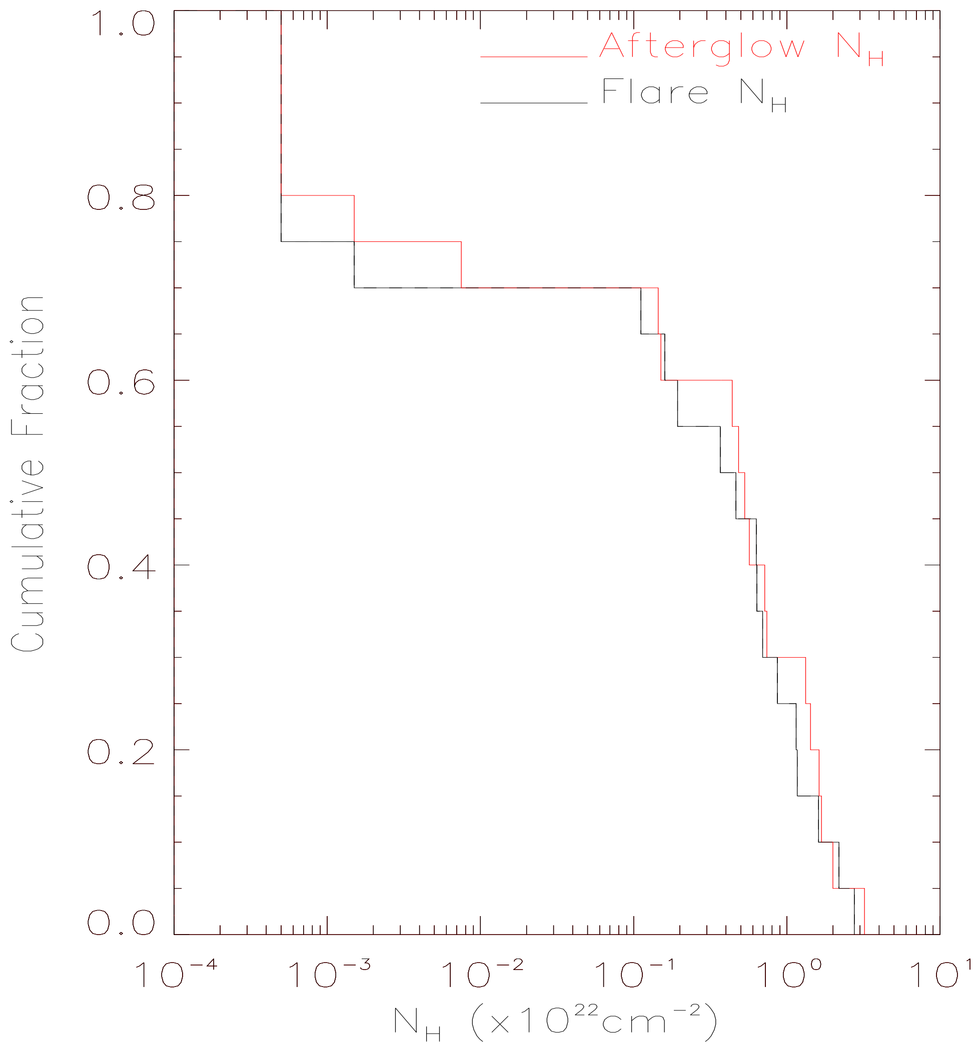

Fig. 5.6 Time averaged N_H of the flares and afterglow. The distribution of N_H column density of our flares sample and that of the associated afterglow measurements is shown in the form of cumulative histograms. Both the flares and the afterglow segments are considered in a time-averaged sense here. While N_H of the afterglows appears to be generally slightly larger than N_H of the flares, a K-S test confirms the consistency of these two distributions (77% probability). Thus, we see no significant difference between the N_H level in the flares and the associated afterglows occurring at later times. This implies that there is no significant ionization of the circumburst medium occurring on the timescale of minutes to days after the burst (though we can not rule out that some initial flash ionization may have occurred in the first seconds of the burst prior to XRT observations).

5.3.3 Band Function: E_{peak} vs α and E_{peak} vs β

Figures 5.7 and 5.8 show the E_{PEAK} vs α and E_{PEAK} vs β distribution of our flares sample. For comparison, BAT prompt data are overplotted in each figure as solid datapoints. The open datapoints are the same BAT data, but substituting E_{PEAK} as determined from a fit of the Band function with E_{PEAK} as derived using the powerlaw relation between the true E_{PEAK} of the νF_{ν} spectrum and the photon index of a power-law fit to the spectrum in the BAT band (Sakamoto et al. 2007). The open datapoints, therefore, may give a better representation of the true E_{PEAK} distribution of the prompt data, while the solid datapoints have the advantage of comparing parameters produced in the same fit. We show both values for completeness. Correlations have been noted in previous studies of X-ray flares between the E_{PEAK} and α parameter (Butler & Kocevski 2007), however such trends are not apparent in our results shown here.

5.4 Bursts with Multiple Flares

We now discuss systematic trends seen in bursts displaying multiple flares. If X-ray flares are similar to prompt emission pulses, then almost all bursts have multiple "flares" and much work in the literature regarding the evolution of prompt pulses should be applicable to late time X-ray flares as well. We can investigate whether the multiflare bursts in our sample agree with or disagree with these predicted trends. This will lead us to another potential characteristic to test in our flare survey to come at the end of this chapter.

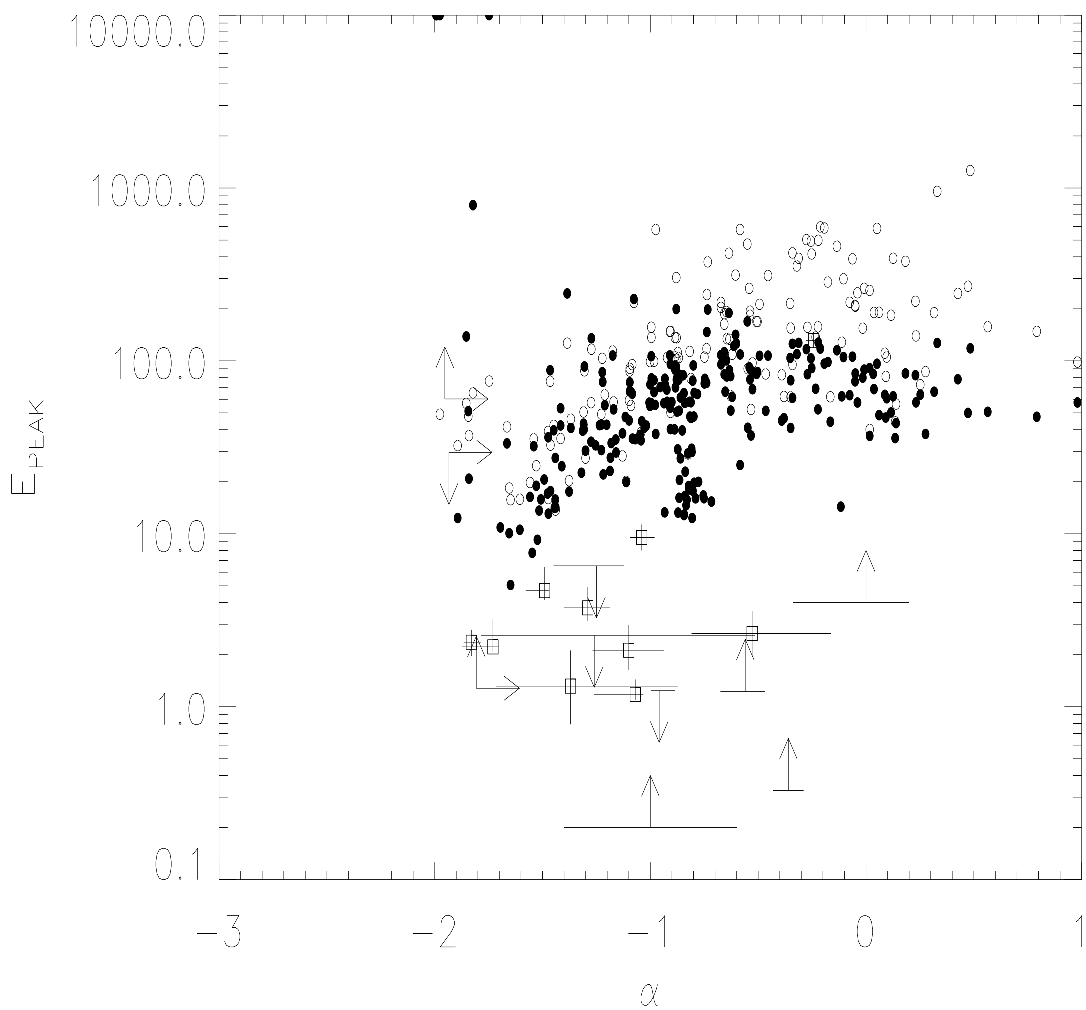

Fig. 5.7 Flares and prompt α vs E_{PEAK}. The $\alpha - E_{PEAK}$ distribution of the flares is shown as squares with the BAT prompt data overplotted as filled circles. The open datapoints are the same BAT data, but substituting E_{PEAK} as determined from a fit of the Band function with E_{PEAK} as derived using the the powerlaw relation between the true E_{PEAK} of the νF_{ν} spectrum and the photon index of a powerlaw fit to the spectrum in the BAT band (Sakamoto et al. 2007)

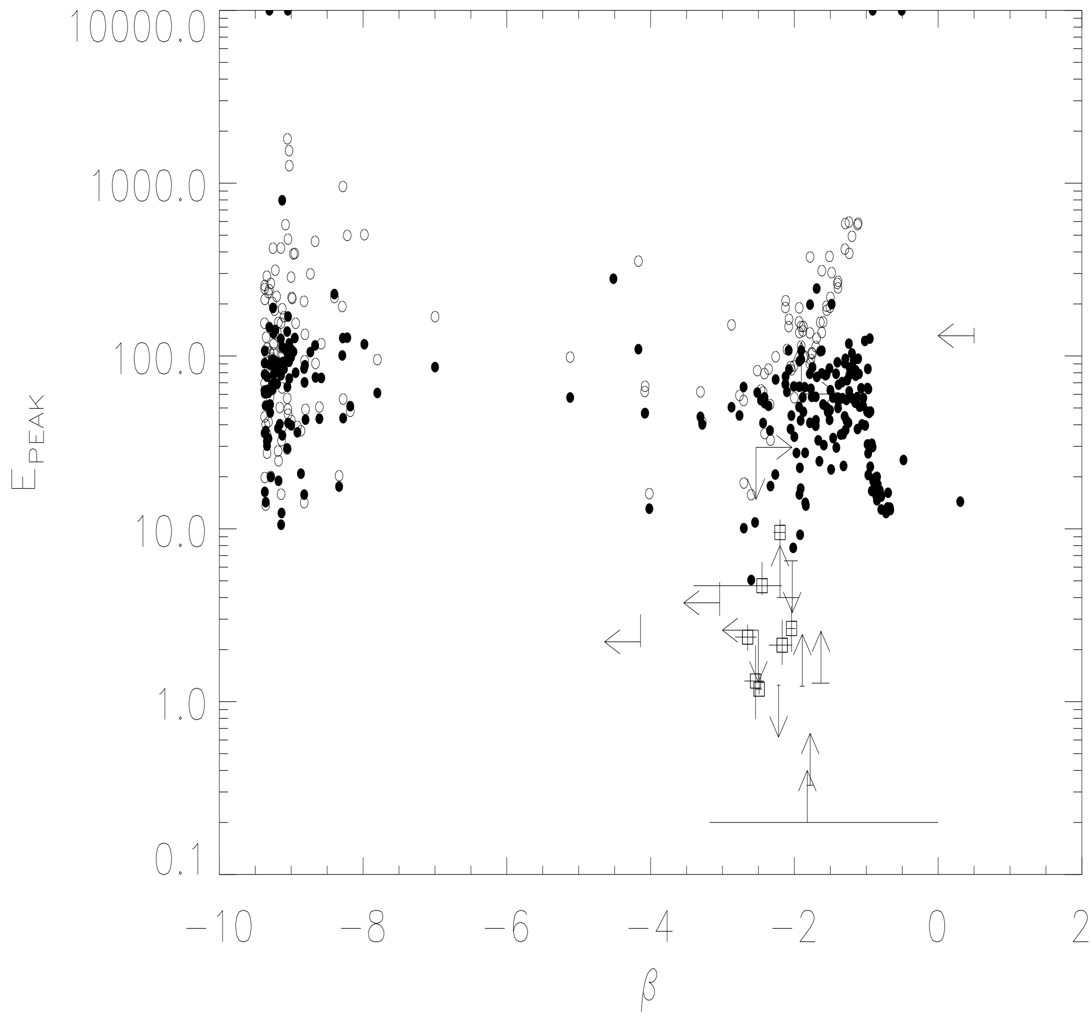

Fig. 5.8 Flares and prompt β vs E$_{PEAK}$. The $\beta - E_{PEAK}$ distribution of the flares is shown with the BAT prompt data overplotted as filled circles. The open datapoints are the same BAT data, but substituting E$_{PEAK}$ as determined from a fit of the Band function with E$_{PEAK}$ as derived using the the powerlaw relation between the true E$_{PEAK}$ of the νF$_\nu$ spectrum and the photon index of a powerlaw fit to the spectrum in the BAT band (Sakamoto et al. 2007)

There are 7 bursts in our sample with multiple flares. The means and standard deviations of α, β, E_0 and the resultant E_{PEAK} of the "first" flares and "second" flares are shown separately in Table 5.3.

Table 5.3. Band function fit parameters of bursts with multiple flares.

param	mean_{1st}	σ_{1st}	mean_{2nd}	σ_{2nd}
α	-0.85	0.36	-1.6	0.5
β	-2.3	0.83	-2.3	0.4
E_0	2.98	3.48	12.1	24.6
E_{PEAK}	2.8	3.2	-1.8	9.4

Figures 5.9 and 5.10 show the evolution of N_H and E_{PEAK} from flare to flare in each burst (plotted against rest frame time). In two cases the N_H data show evidence of a decrease larger than the 1-σ uncertainty in N_H (GRB 060526 and GRB 060714) while in the other 5 cases the N_H data are consistent with no change. The E_{PEAK} results from flare to flare are a bit more challenging to interpret due to the complications of searching for E_{PEAK} in what remains a reasonably narrow energy range, particularly for late flares observed at times when BAT data are unavailable. We will thus briefly discuss the E_{PEAK} determination of each burst:

GRB 050502B: The first flare is the well chronicled giant flare of this burst (Falcone et al. 2006) and has a moderately well defined E_{PEAK} determination, despite a lack of BAT data, measured as E_{PEAK}=$1.12^{+0.12}_{-1.08}$ keV. The second flare in this burst is at much later time and lower countrate and is therefore less well constrained. The nominal

E_{PEAK} value is 1.8 keV but β=-1.6 in this fit, suggesting that the true E_{PEAK} value may be above the observing window. Falcone et al also found a spectral hardening at late times during this burst, though they did not attempt to fit a model to the spectrum of the late flare.

GRB 060204B: Both flares are reasonably well fit in this burst with E_{PEAK}=$2.7^{+0.6}_{-0.5}$ keV and E_{PEAK}=$1.3^{+0.9}_{-1.3}$ for the first and second flares respectively.

GRB 060418: The first flare has E_{PEAK}=$1.5^{30}_{1.5}$ while the second has flare has an upper limit of E_{PEAK}=1.1 keV but since both α and β are (similarly) steep at $\alpha \sim \beta \sim$ -2 in this flare, it is likely that the true E_{PEAK} of the second flare is actually at or below the low energy edge of the UVOT observing window ($\sim$ 0.001 keV).

GRB 060526: Both flares are reasonably well fit in this burst with E_{PEAK}=$9.5^{+1.9}_{-1.6}$ keV and E_{PEAK}=$1.2^{+0.3}_{-0.1}$ for the first and second flares respectively.

GRB 060607A: The first flare in this burst has β=-1.8, suggesting that the true E_{PEAK} is beyond the high energy end of the BAT observing range, $E_{PEAK} \gtrsim$ 100 keV. The second flare is well fit with E_{PEAK}=$4.7^{+3.4}_{-1.1}$.

GRB 060714: Both flares are reasonably well fit in this burst with E_{PEAK}=$3.7^{+1.7}_{-0.8}$ keV and E_{PEAK}=$1.3^{+1.3}_{-0.8}$ for the first and second flares respectively.

GRB 070107:The first flare in this burst has β=-1.9, suggesting that the true E_{PEAK} is beyond the high energy end of the BAT observing range, $E_{PEAK} \gtrsim$ 100 keV. The second flare has α and β similarly steep at $\alpha \sim \beta \sim$ -2.3, suggesting that the true E_{PEAK} is actually at or below the low energy edge of the UVOT observing window ($\sim$ 0.001 keV).

In summary, 6/7 of the bursts in question with multiple flares show evidence of a decreasing E_{PEAK} from flare to flare with the sole outlier being GRB 050502B which appears to suggest a significantly harder spectrum for its very late flare at $T_0+\sim 10^5$ s than for the early giant flare. This trend for successive flares within an individual burst to show decreasing E_{PEAK} has been previously noticed by other authors in individual bursts (Krimm et al. 2007; Morris et al. 2007). Our contribution here is to extend this result to a broader sample of bursts with multiple flares, showing that the relation is seen in several cases but may not be universal. We will discuss this subject as well as the late time flare in GRB 050502B and the implications of these results for its nature later.

5.5 Temporal Properties

The overall temporal characteristics of our sample, including measures of $\Delta T/T$ and measures of the onset time of occurrence of the flares are consistent with the results of Chincarini et al. (2007) (and, indeed, several of the same flares are analyzed in both samples though our sample here extends to later dates) and the reader is referred to their work for details of the morphology of the global flares sample. In this section, we will discuss in greater detail the intra-flare temporal evolution properties of our sample.

5.5.1 Band Function: E_{peak} vs time and N_H vs time

We have noted the trend of successive flares within an individual GRB to show decreasing E_{PEAK} and the lack of overwhelming evidence for a decrease of N_H through the entire course of a burst (§5.3.2) or from successive flares within an individual burst

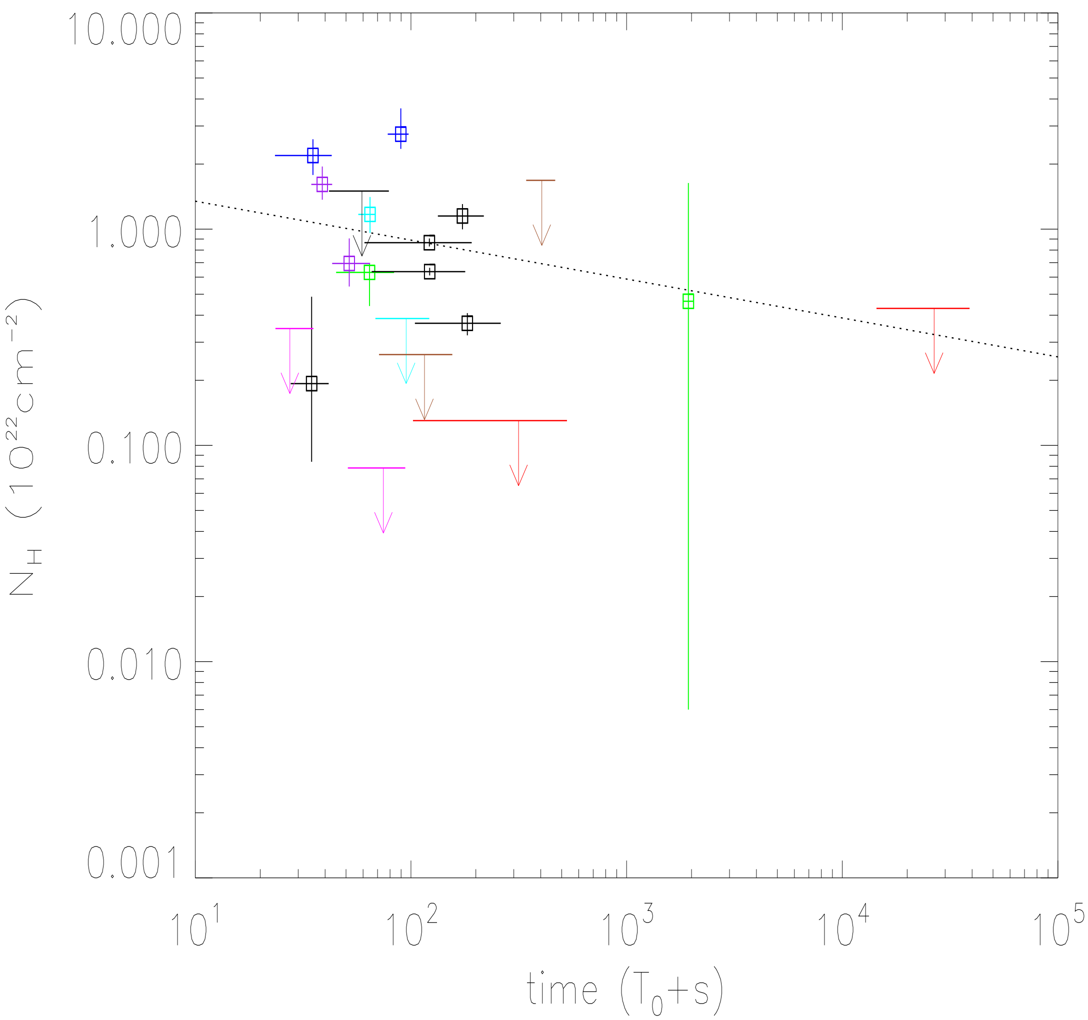

Fig. 5.9 Flare to flare evolution: N_H versus time. The N_H value is plotted against restframe time for all bursts in our sample which have multiple flares. Flares from the same burst are plotted in the same color.

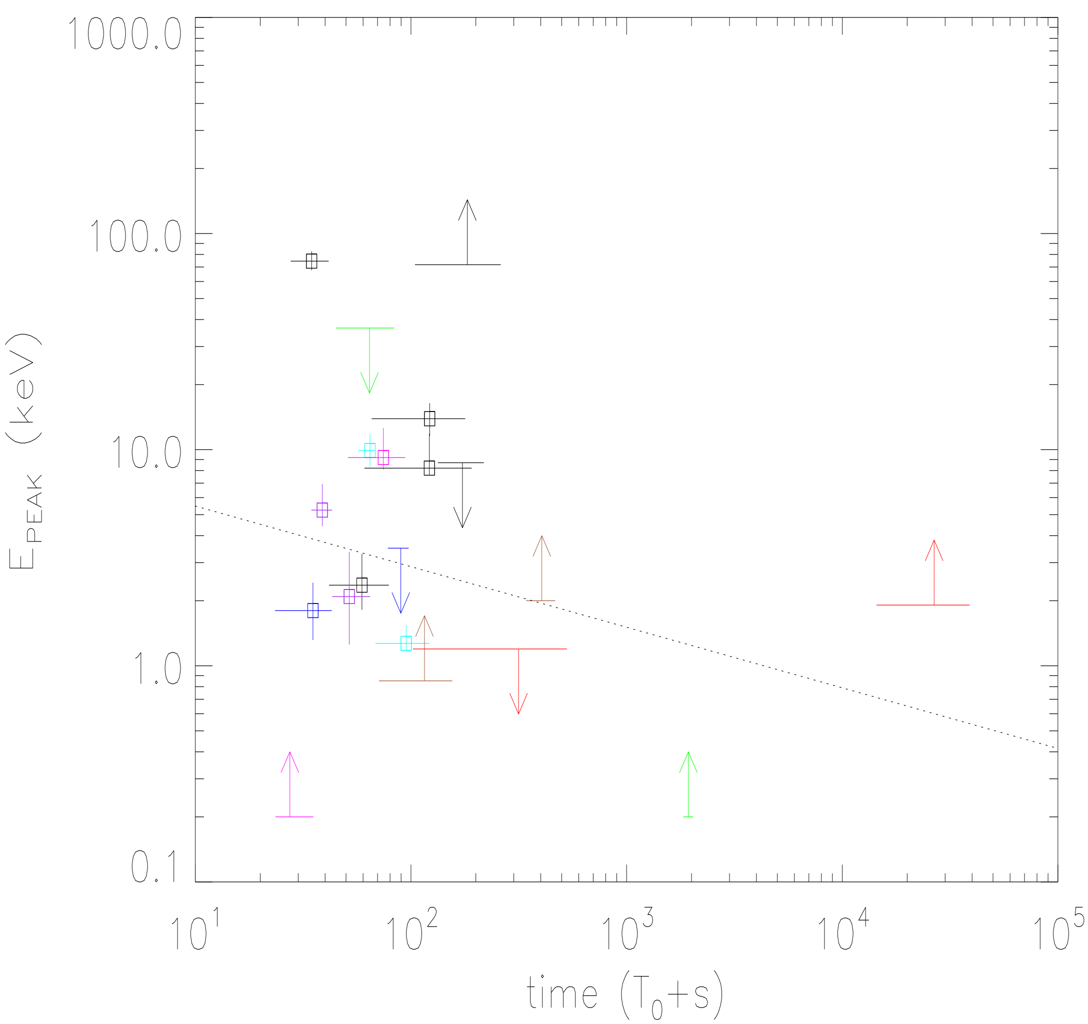

Fig. 5.10 Flare to flare evolution: E_{PEAK} versus time. The E_{PEAK} value is plotted against restframe time for all bursts in our sample which have multiple flares. Flares from the same burst are plotted in the same color.

(§5.4). We now turn our attention to the evolution of the spectral characteristics of flares from onset through peak flux and as they decay back to the quiescent afterglow level.

***E**$_{PEAK}$:*

There is a well known tendency of prompt emission pulses to show a hardness - flux correlation during their evolution (Borgonovo & Ryde 2001; Ryde & Petrosian 2002; Kocevski et al. 2003; Ryde 2005a). Butler and Kocevski have shown that a similar relation appears to exist between hardness and flux for some of the brighter flares (and prompt emission pulses) observed by *Swift* (Butler & Kocevski 2007). We have investigated this relation in the form of an E_{PEAK} - flux correlation in our sample of bursts.

We separate each flare in our sample into segments containing 1000 counts above the background afterglow level in the XRT. This generally allows us to create between 2 and 20 slices from each of our flares with each slice having sufficient S/N to produce reasonably accurate spectral fits (about 40 degrees of freedom). The results of this analysis are shown in Figures 5.11 through 5.13. Figure 5.11 (top panel) shows the entire sample of time slices from all flares, with each flare designated by a separate color. We determine an average E_{PEAK} to flux correlation of $E_{PEAK} \propto f^{\gamma}$ with $\gamma = 0.5 \pm 0.1$, consistent with the results of Butler and Kocevski. We find also, however, that the relation is somewhat more prominent in the post-peak flare emission than pre-peak emission (Figure 5.12), with $\gamma = 0.6 \pm 0.1$ after the time of peak flux compared to $\gamma = 0.4 \pm 0.1$ prior to the time of peak flux. Figure 5.12 shows fits to the data using both a simple linear fit and using a Bayesian mixture of models technique which is more appropriate to fit data with errors in multiple axis and non-detections, as is the case here (Kelly 2007). We have, furthermore, investigated the variation in this relationship from flare to flare in our sample. We find significant spread in the relationship from flare to flare, varying from γ = -0.5 to γ = 0.7. In Figure 5.13 we show the E_{PEAK} versus flux figure separated for the rising and falling legs of the flare with each burst plotted as a separate color to show the nature of the relation in individual flares. The spread in the relationship from flare to flare may be suggestive of multiple mechanisms for flare production.

$\boldsymbol{N_H}$:

We have previously shown our flare sample and the associated measurements of the afterglow measured at later times to be consistent with a constant value of N_H, suggesting that little or no ionization occurs in the X-ray regime on timescales similar to the X-ray afterglow duration (hours to days). Here we investigate whether we find evidence of ionization in the X-ray regime on the much shorter timescales of seconds to minutes associated with individual flares.

Figure 5.11 (bottom panel) shows the general behavior of N_H in our sample, plotted as N_H column density versus flux. If the N_H ionization and recombination timescales are short with respect to the typical duration of flares, we might expect to see an anticorrelation between the flux and N_H column density, since an increase in the flux from the flare would, effectively instantaneously, lead to increased ionization and a lower N_H column. The subsequent decrease in flare flux would, again instantaneously with respect to the temporal resolution of the data, lead to decreased ionization and a higher N_H column. As can be seen in the figure, however, the overall sample is roughly consistent with a slope of zero, suggesting either that there is no ionization activity or that the

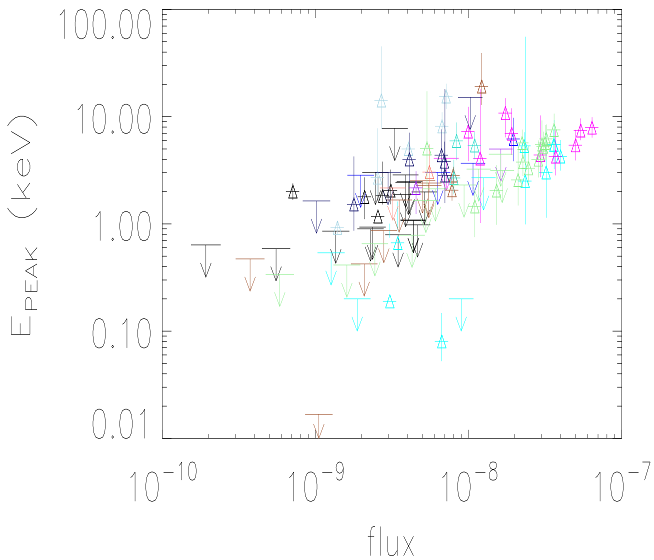

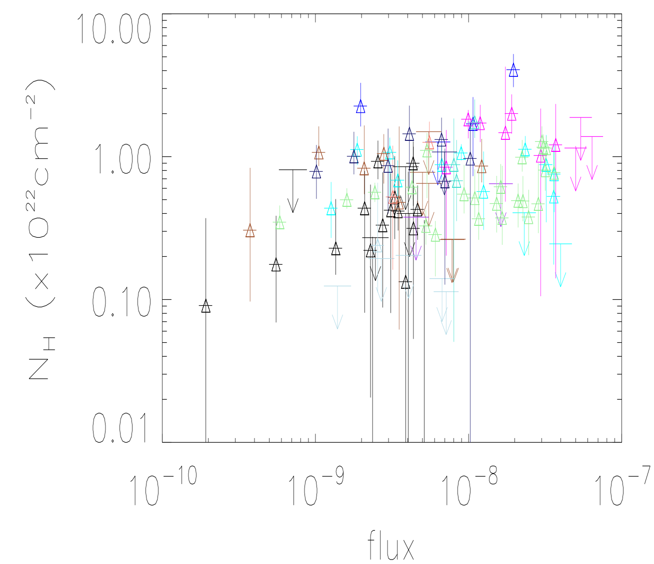

Fig. 5.11 E_{PEAK} and N_H vs Flare Flux. For each time segment of each flare analyzed, we plot peak energy of the νF_ν spectrum for that time segment versus the time averaged flux of the flare during that time segment (upper panel) and the N_H of the spectral fit versus the time averaged flux of the flare during that time segment (lower panel). In each panel, all segments (both before and after the peak flux) of all flares are shown together. Powerlaw fits to the data of each individual flare have been determined using a Bayesian technique employing a mixture model. In the E_{PEAK} vs flux plot, fits are of the form $\log_{10}(\text{flux}) \propto A\log_{10}(E_{PEAK})$ with $0.1 < A < 0.7$ with one fit showing A=-0.5. In the N_H vs flux plot, fits are of the form $\log_{10}(\text{flux}) \propto A\log_{10}(N_H\ )$ with $-0.6 < A < 1.0$.

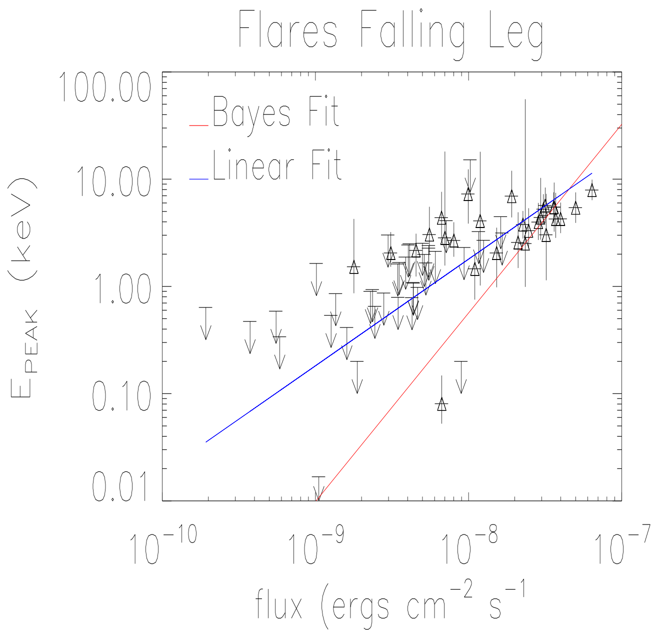

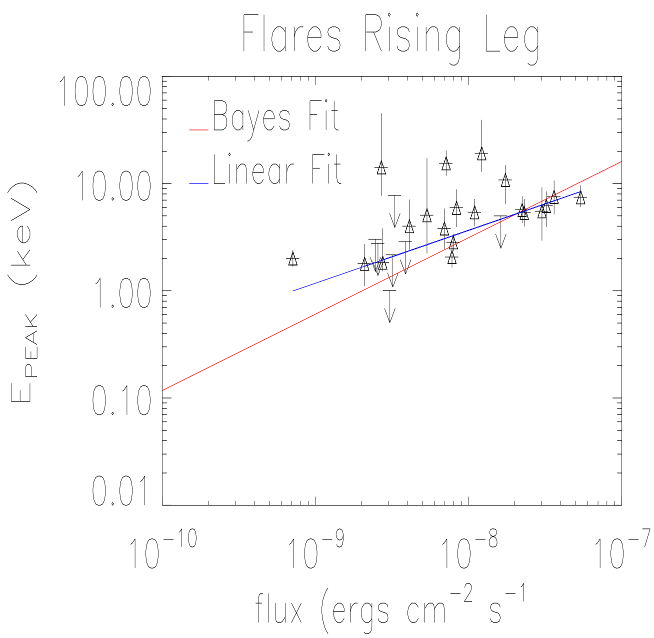

Fig. 5.12 E_{PEAK} vs Flare Flux. For each time segment of each flare analyzed, we plot the peak energy of the νF_ν spectrum for that time segment versus the time averaged flux of the flare during that time segment. Segments contain a minimum of 1000 XRT counts. Different colored points correspond to different flares. The upper panel shows all segments occurring after the time of the flare peak flux while the lower panel shows segments occurring before the flare peak flux. The correlation seen in the data after the peak flux is a representation of the well known curvature relation (Zhang et al. 2006). In brief, the effect is due to the delay in arrival time of photons emitted at large angles from the observer line of sight with respect to photons emitted along the observer line of sight. The correlation appears to be present also in the data prior to the flare peak flux though at a lower significance and different slope. The correlation is $\log_{10}(E_{PEAK}) \propto 0.6*\log_{10}(\text{flux})$ with a correlation coefficient of 0.85 in the post-peak data while it is $\log_{10}(E_{PEAK}) \propto 0.4*\log_{10}(\text{flux})$ with a correlation coefficient of 0.55 in the pre-peak data.

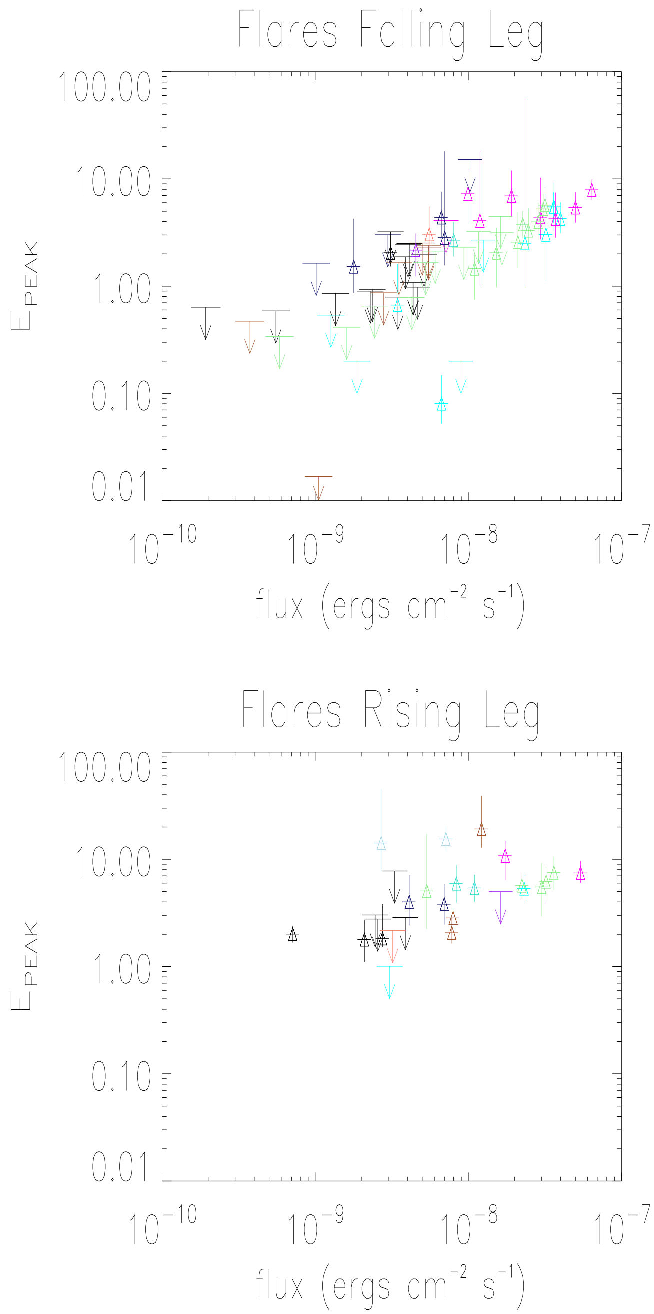

Fig. 5.13 E_{PEAK} vs Flare Flux. For each time segment of each flare analyzed, we plot the peak energy of the νF_{ν} spectrum for that time segment versus the time averaged flux of the flare during that time segment. Segments contain a minimum of 1000 XRT counts. Different colored points correspond to different flares. The upper panel shows all segments occurring after the time of the flare peak flux while the lower panel shows segments occurring before the flare peak flux. Each flare is represented by a separate color to allow comparison of the relation on a flare by flare basis.

timescales are much longer than the typical duration of X-ray flares. As noted previously, we will return to discuss the implications of the N_H behavior on models of the circumburst environment in Chapter 6.

5.5.2 Restframe E_{iso} vs Restframe Flare Time

Figure 5.14 shows the flare fluence measured in the 0.002 - 150 keV energy range versus time for our flare sample. Both the fluence and time are corrected for redshift using values from the literature (boxpoints) or using a canonical value of z=2.6 in cases where the redshift is undetermined (crosses). From the points using known redshifts alone, an apparent relationship exists between the total fluence and redshifted time with an approximate fit of $S \propto t^{-\Gamma}$ with $\Gamma = 0.5 \pm 0.3$.

5.5.3 Restframe ΔT vs Restframe T

The ΔT-T distribution of our sample is shown in Figure 5.15, where ΔT is the duration of the flare (see Chapter 2 for definition of flare start and stop times) and T is the peak time of the flare. It has been argued by several authors that values of $\Delta T/T << 1$ cannot be achieved through external shock processes (although see Dermer (2007) for a recent refutation of this claim). Our sample shows a clear tendency toward $\Delta T/T < 1$ though a few flares are found near or even above the overplotted line designating $\Delta T/T = 1$. The general sample shows $\Delta T/T_{total} = 0.6 \pm 0.3$; $\Delta T_{rise}/T = 0.1 \pm 0.1$.; $\Delta T_{decay}/T = 0.4 \pm 0.3$, where ΔT_{rise} and ΔT_{decay} are the duration of the rising and falling segment of the flare respectively.

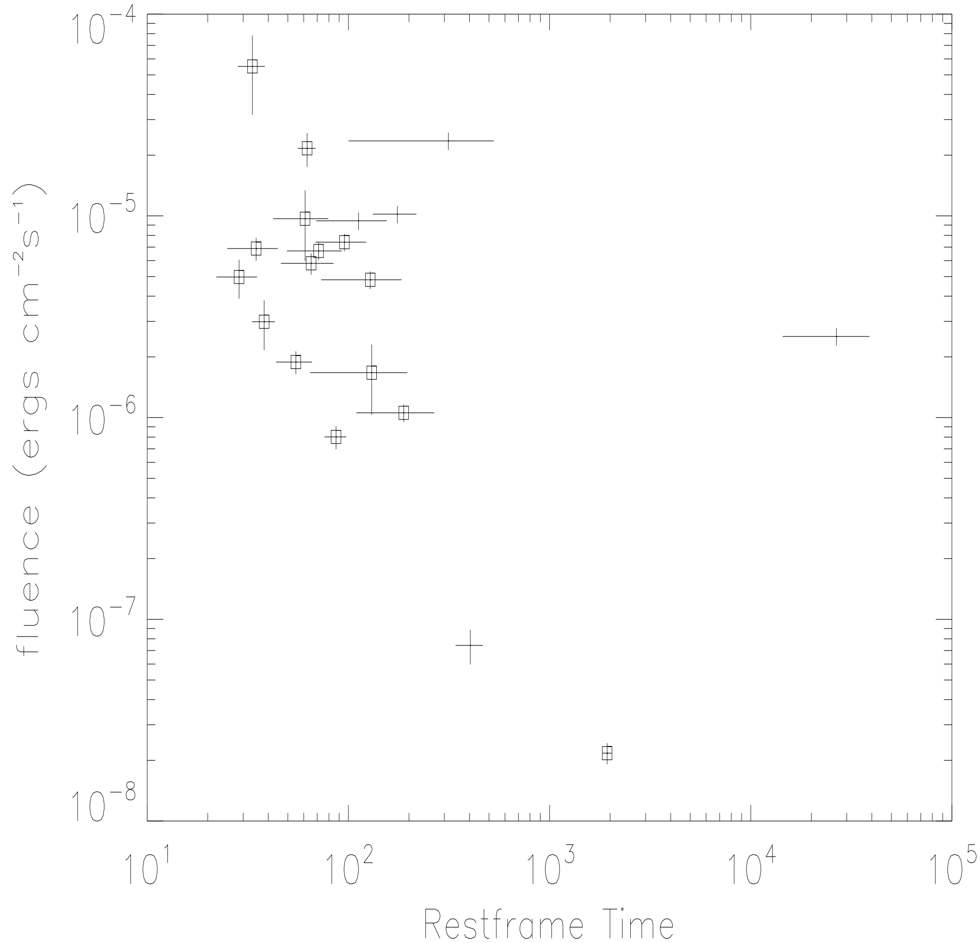

Fig. 5.14 $S_{0.002-150keV}$ vs time. Unabsorbed fluence in the 0.002 to 150 keV energy range is plotted versus restframe time. The fluence is corrected for redshift by multiplying by $(1+z)^2$ in cases where the redshift is known (boxpoints). In cases where the redshift is unknown, the redshift correction is made by assuming the average *Swift* redshift of z=2.6 (crosses).

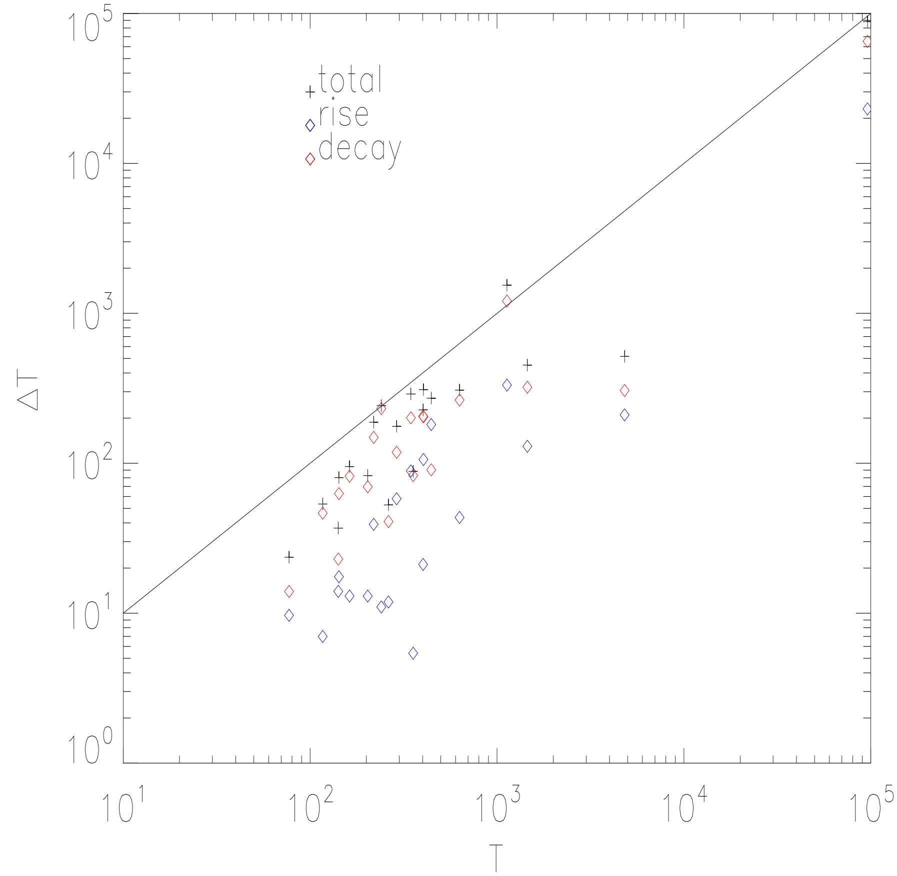

Fig. 5.15 ΔT vs T. For each flare in our sample, we plot ΔT versus T. Crosses show the entire flare while blue symbols show the rise of the flare and red symbols the decay of the flare. The ΔT/T=1 is plotted as a solid line. The flares in our sample seem to generally follow ΔT/T $\sim$ 0.6 (total flare duration). We also clearly see that the flares tend to rise more rapidly than they decay.

5.6 Categorizing Flares by Spectral and Temporal Characteristics

As discussed throughout this work, there are many different mechanisms proposed for the production of late time X-ray flares in GRBs. In this section, we critically analyze each of the flares in our sample to determine whether it contains the necessary characteristics to be the result of each potential production mechanism. We begin with a brief overview of the potential mechanisms we will explore and the characteristics of each that we will test. We then present the results of our flares analysis in tabular and figure form, indicating whether each criterion for each mechanism is met.

5.6.1 Potential Flare Mechanisms

5.6.1.1 External Reverse Shock

As the forward shock blast wave sweeps up an amount of material from the ISM roughly equal to the mass of the blastwave itself, the outgoing shell of material is decelerated at a characteristic time given by

$$t \sim (E/nm_pc^5)^{1/3}\Gamma_0^{-8/3}(\text{thick shell scenario}) \tag{5.1}$$

$$t \sim (3E/(32\pi\Gamma_0^8 nm_pc^5))^{1/3}(\text{thin shell scenario}) \tag{5.2}$$

where E is the energy of the blast wave, n is the circumburst density, Γ_0 is the blast wave Lorentz factor and m_p and c are physical constants (Sari & Piran 1999b). Synchrotron emission from the forward shock plowing into the ISM is generally regarded as the likely radiation mechanism of the long-lived afterglow which begins at this time (Sari & Piran

1999b; Kumar & Panaitescu 2000; Meszaros & Rees 1993). Synchrotron emission is also expected due to the reverse shock which develops at this time and propagates backward into the (as yet) unshocked material of the outgoing shell. Whereas the forward shock emission is a smooth, long-lived component, the RS component is expected to last only as long as the RS takes to cross the thickness of the shell, a time roughly comparable to the onset time of the RS, generally $\sim 10 - 100$ s in the observer frame. As a result, if the RS emission is visible above the FS emission, a flare may be observed at this time.

The RS Lorentz factor is generally smaller than that of the FS, however, and as a result the typical synchrotron frequency of the RS emission is in the optical, at lower energy than that of the FS which is generally found in the X-ray. If one considers Inverse Compton scattering during the RS, however, and tunes the shock parameters just right, Kobayashi et al have shown that a low contrast X-ray flare may be visible above the FS induced afterglow with typical flux levels at the IC peak of a few times the FS afterglow emission (Kobayashi et al. 2007). While higher contrast levels are technically possible for very high ISM densities or very low values of the magnetic energy density parameter η_B, we will consider the result obtained for typical parameter values n = 10 cm^{-3} and $\eta_B \sim 0.01$ and thus set a limiting flux contrast of ~ 6 for the flare to be considered as potentially due to the Reverse Shock mechanism.

We note also that the RS induced component should technically decay as a result of curvature emission and therefore show the characteristic $\alpha = 2 + \beta$ temporal decay profile, but due to the low contrast between a RS flare and the ongoing FS afterglow (which is not constrained to follow curvature), it will be extremely difficult to see the effect of curvature in the decay of a RS flare. Even if one accurately subtracts the underlying emission due to the FS afterglow, the residual bumps and wiggles in the lightcurve will make it difficult to accurately identify the curvature signature. Therefore, we will not require the curvature decay signature to be present to consider RS emission as a mechanism for a flare. Finally, we also note that since the RS does not add energy to the forward shock afterglow, we expect the level of the afterglow prior to the flare to match the level after the flare. Thus, our criteria for flares to be considered potentially due to the reverse shock mechanism are (where italicized criteria are indicative of the process but not required) i) the flare should occur at t $\sim$ t_{dec}; ii) the contrast should be no greater than 6 times the afterglow level; iii) UV-optical emission should be suppressed since we expect X-ray flares only to be prominent through the IC boosting of the nominal synchrotron optical photons; iv) we expect $0.1 \lesssim \Delta T/T \lesssim 1.0$; v) the afterglow level prior to the flare should match the afterglow level after the flare and; *vi)* the flare may be consistent with the curvature relation.

5.6.1.2 Forward Shock Interaction with an Inhomogeneous ISM

As the FS propagates into the ISM, if density inhomogeneities are encountered, the relative increase in the number of synchrotron emitting electrons will produce an increase in the emitted synchrotron flux (Dermer, 2007), assuming $\nu_c > \nu_{obs}$ (Panaitescu and Kumar, 2000). It has been argued that this mechanism is unable to produce the large contrast factors (up to hundreds) (Ioka et al. 2005) and rapid decay temporal structure seen in *Swift* X-ray flares (see, e.g., Zhang et al. (2006); Chincarini et al. (2007)) without invoking unrealistically dense and sharply-bounded clouds of material in the ISM. As described here, interactions with external density clumps are generally considered to be limited to contrast factors of ∼2 (∼6-12 if one invokes off-axis jets and off-axis jets plus multiple simultaneous emitting regions; for simplicity in this work we will allow for the on-axis and off-axis single emitter scenarios only, discussing the multiple emitters scenario only as relevant) (Ioka et al. 2005). Though external clumps can produce rapid rises in flux, presumably as rapid as one desires, given a sufficiently dense cloud and steep density gradient, the decay of a flare produced in this manner is nevertheless expected to be shallow due to the slowing of the shell Lorentz factor Γ as it enters the cloud and the related stretching of the associated observer time given by t $\sim R/2\Gamma$ where R is the radius from the central engine. As a conservative estimate for this study, we will assume a factor of 2 decrease of Γ as the shell interacts with the cloud leading to a factor of 4 stretching of the observer time. A flare decay which might otherwise be expected to follow the curvature relation $\alpha = 2+\beta$ then will be expected to appear as $\alpha \sim (2+\beta)/1.6$.

Recent work by Dermer however (Dermer, 2007), has argued that the flaring behavior seen in *Swift* GRBs can, in fact, be explained by encounters of the FS with density inhomogeneities if the assumption is made that the FS does not undergo significant spreading before encountering the inhomogeneities (a "cold" blastwave model). An interesting morphological feature of this model is a characteristic flat-topped nature to the flare profile roughly at its apex (as the blastwave travels through the dense cloud), followed by a rapid decay in flux (as the blast wave exits the cloud). The duration of this "flat-top" is roughly the duration of the blastwave-cloud interaction and can be calculated as

$$\Delta t \simeq 2t_{z0}\frac{\theta_{cl}}{\Gamma}(1+\theta_i^2) \tag{5.3}$$

where t_{z0} is the observer collision time and θ_{cl} and θ_i are the angle subtended by the cloud and by the viewing angle respectively. Also note that we have assumed here that the blast-wave cloud interaction time is less than the blastwave deceleration time (see Dermer, 2007 for detailed discussion of the model). For typical values of input parameters, flares occurring at observer times of several hundred seconds and lasting for $\Delta T/T \sim 0.1$ are produced. Since the blast wave is decelerated by its interaction with the dense clump of material producing the flare, one should expect a dip in the afterglow level following the flare in comparison to the level prior to the flare.

In both versions of this model a Band function spectrum is expected with the possible additional contribution of an optical reverse shock signature associated with the shell-clump interaction depending on the strength of the magnetic field equipartition energy. For large values of the magnetic field strength parameter an excess in the UV or soft X-ray may be seen (Dermer, 2007).

Our criteria for a flare to potentially be due to interactions with the external medium, then, are divided into criteria for the original cloud model (CM1) and the revised cloud model (CM2). For CM1 our criteria are that i) $\nu_c > \nu_{obs}$ at the time of the flare, ii) the flare must have a contrast factor < 6, iii) the flare must show a decay profile more shallow than predicted by the curvature relation, given by our approximately modified curvature relation $\alpha \sim (2+\beta)/1.6$ (above) and *iv)* the flare may show a UV or soft X-ray excess. For CM2 our criteria are that i) $\nu_c > \nu_{obs}$ at the time of the flare,*ii)* the flare may show a flat topped profile, *iii)* the flare may show a UV or soft X-ray excess.

5.6.1.3 Onset of the Afterglow Phase

As noted in the introduction, X-ray flares are not an entirely new phenomenon to *Swift*. Piro et al have produced several papers (Piro et al. 1998, 2005; Galli & Piro 2006) analyzing flares observed by Beppo-SAX that they have interpreted as the signature of the onset of the FS afterglow emission phase. In this scenario, the observed X-ray flare is due to the rise of the FS afterglow component as it becomes the dominant emission component relative to the decaying tail of the prompt GRB emission. Beginning at the characteristic blastwave deceleration time, as discussed in the External RS model, a flare produced by this mechanism is expected to smoothly transition into the long-lived FS afterglow seen in most GRBs. Thus, if a flare is produced by this mechanism we expect that the spectrum of the flare should be similar to the spectrum of the long-lived afterglow to follow. Furthermore, we expect that the flare decay and the extended afterglow decay should be fit temporally by a single powerlaw, taking T_0 to be either the trigger time of the prompt burst emission (the thin shell case) or to be roughly the onset of the flare (the thick shell case). In the former case, we expect a clear separation between the end of the prompt emission and the flare signaling the AG onset while in the latter case the end of the prompt emission may be mixed with the onset of the AG. Since the flare designates the onset of the afterglow (which can only happen once) we also expect that, at most, only one flare in a given burst may be attributed to this mechanism. Finally, since the flare designates a transition between emission mechanisms (the end of the tail of the prompt emission phase and the start of the afterglow phase), we may also expect the temporal decay before the flare to be different from the temporal decay of the flare (or late afterglow since in this scenario they are the same) and we may expect the spectrum of the emission prior to the flare to differ from the spectrum of the AG afterward.

Our criteria for a flare to be considered as possibly indicative of the AG onset then are also divided into two sets of criteria; in both cases we expect that i) the spectrum of the flare should be similar to the spectrum of the late time afterglow to follow, ii) no more than one flare in a burst may be produced by this mechanism, *iii)* we may expect a change in temporal slope of the afterglow from before the flare to after the flare and *iv)* we may expect a change in the spectrum of the AG from before the flare to after the flare. For the thin shell case additionally v) we expect that the late time AG decay should fit the decay of the flare with T_0 set to the burst trigger while for the thick shell case v) we expect that the late time AG decay should fit the decay of the flare with t_0 reset to correspond to the onset of the flare itself.

5.6.1.4 Energy Injection with the FS at Late Time

Injection of energy into the FS, either via a Poynting flux dominated flow or via a kinetic energy dominated flow may produce a flare signature. In the Poynting flux dominated case, energy is injected directly into the FS without the creation of a RS propagating backward into the flow. In the kinetic energy dominated flow, shells of material ejected from the central engine at late time eventually reach the decelerated FS front at a time given by $R/c\Gamma\gamma+t_e$ where t_e and γ are the emission time and Lorentz factor of the shell and R and Γ are the deceleration radius and Lorentz factor of the FS (Zhang & Mészáros 2002b).

In either form of this scenario, we may expect a contrast factor of up to a few. We also expect that the emission level of the FS afterglow will be energized by the injected energy, so that the AG flux level after the flare will be greater than the projected level predicted by the flare decay rate of the AG prior to the flare. Furthermore, since the FS is energized, the flare and subsequent shift in AG level is expected to be achromatic. A matter dominated flow is expected to produce a more violent (and complex) interaction during the injection, potentially leading to a sharper rise at the onset of the flare. Though the exact parameters governing the steepness of the rise of such a flare are somewhat unclear and as yet have not been treated in full hydrodynamical detail, for purposes of this study we will make the generalization that Poynting flux dominated flares may be characterized by $\alpha \lesssim 0$ while matter dominated flares will be expected to show $\alpha \gtrsim 0$, where α here is used to refer the temporal decay slope of the X-ray lightcurve (thus, $\alpha \lesssim 0$ implies a slowing or stalling or the decay rate without an actual rebrightening, while $\alpha \gtrsim 0$ implies an actual increase in flux level). The flare emission in both the Poynting flux dominated and kinetic energy dominated cases is expected to show characteristically different profiles in the X-ray and optical (Zhang & Mészáros 2002b). While the fidelity of the *Swift* data is unlikely to be high enough to pinpoint the exact shapes expected, we nevertheless expect a UV-optical flare to accompany the X-ray flare. Finally, in the case of the kinetic energy dominated flow, the shells of material which ultimately produce the energy injection flare may, prior to interaction with the FS, interact with other outflowing shells to produce late internal shocks (see below). If *Swift* is viewing the burst during such an episode, a bright flare meeting the IS characteristics (below) will be observed with fluence comparable to the prompt burst itself.

Thus, our criteria for a flare to be considered as possibly indicative of energy injection are i) a contrast factor of a few up to perhaps 10, ii) that the afterglow level after the flare should exceed the level prior to the flare, iii) a UV-Optical flare coincident with the X-ray flare, iv) that the rising slope of the flare should be $\alpha \lesssim 0$ (Poynting dominated) or $\alpha \gtrsim 0$ (KE dominated) and additionally for the KE dominated flow case, *v)* that we may see a bright IS flare preceding the later energy injection flare with energy comparable to the prompt emission itself.

I reiterate here that this mechanism requires an input amount of energy comparable to the energy contained in the initial FS fireball in order for the flare produced to be visible above the AG itself. Therefore, the implication of this model in the production of extremely bright flares seems unlikely due to the large energy budget required. This will be treated in greater detail during the discussion.

5.6.1.5 Early Internal Shocks, Interacting at Late T

Shells of material ejected from the GRB central engine need not interact immediately. If a pair of shells is ejected with only slightly different Lorentz factors (with the trailing shell slightly outpacing the forward shell), the two shells may interact at a much later time, potentially after the central engine has stopped emitting material, given by $t_i = d/(\gamma^2 c)$ where γ is the approximate Lorentz factor of the two shells and $d = \gamma c \delta t$ is the distance between the two shells at the emission time of the latter, with the shell emission separated by a time δt (Zhang & Mészáros 2002b). In this scenario, the efficiency is extremely low, such that the emission level is expected to be below our detection threshold and so we do not consider this mechanism further in this study (Lazzati & Perna 2007).

5.6.1.6 Late Internal Shocks

In the late internal shock mechanism of producing X-ray flares, the central engine becomes active again at times that are possibly well separated from the end of the prompt GRB emission phase. During this late episode of emission from the central engine, shells of material with varying Lorentz factors are emitted (as was the case during the prompt emission phase) and the interaction of these shells of material produces bursts of synchrotron emission (as was the case to produce the prompt burst emission). Since pulses of emission in this mechanism are expected to occur behind the FS (ie, prior to any interaction with the ISM), the emission is expected to decay according to the curvature radiation relation, $\alpha = 2 + \beta$. Furthermore, we have the following proportionality for the peak energy of the spectrum of an IS pulse (in νF_ν):

$$E_p \propto L^{1/2}\Gamma^{-2}\delta t^{-1} \tag{5.4}$$

(Zhang et al. 2006) where E_p is the peak energy of the flare spectrum, L is the luminosity of the flare, Γ is the Lorentz factor of the flare and δt is the characteristic variability timescale. This relation allows us to form a limit for the expected peak energy for flares produced through this mechanism based on the luminosity and duration of the flare and luminosity and the duration and peak energy of the prompt emission:

$$E_{PEAK_{flare}} > E_{PEAK_{prompt}} \frac{L_{flare}^{1/2}}{L_{prompt}^{1/2}} \frac{\delta t_{prompt}}{\delta t_{flare}} \tag{5.5}$$

Furthermore, since this mechanism is the same as that believed to produce the prompt emission, we expect similar spectral characteristics to that seen in the prompt emission, namely that the spectrum is well fit by the Band function and that the flare displays hard to soft spectral evolution.

Thus, our criteria for a flare to be considered as possibly indicative of internal shocks are i) that the decay of the flare is well fit by the curvature relation $\alpha \sim 2 + \beta$, ii) that the peak energy of the flare satisfies the inequality $E_{PEAK_{flare}} > E_{PEAK_{prompt}} \frac{L_{flare}^{1/2}}{L_{prompt}^{1/2}} \frac{\delta t_{prompt}}{\delta t_{flare}}$, iii) that the Band function is as good or better a fit to the spectrum than any of the other potential models we have investigated (PL or thermal model) and iv) that the flare displays a hard to soft spectral evolution.

5.6.2 Characteristics of Flares in our Sample

Having outlined the characteristics that we will consider as required by or indicative of each of the above mentioned flaring mechanisms, we now turn our attention to a discussion of each flare in our sample in the context of these criteria. Tables 5.4-5.7 list, for each of the flares in our sample, whether that flare satisfies, does not satisfy or is indeterminate for each of the characteristics discussed above as potential indicators of the mechanism that produced the emission.

We will now treat each of these mechanisms in some detail in light of the characteristics determined for each flare and the resulting plots in Figure 5.16. The figure shows a plot for each of the six flare mechanisms discussed previously, summarizing the information contained in Tables 5.4 through 5.7 in figure form.

Reverse Shock IC

Table 5.4. Flare Indicator Fractionals1

GRB	$t_{dec_{thin}}$	$t_{dec_{thick}}$	$\frac{F_{flare}}{F_{AG}}$	$\frac{\Delta T}{T}$	$2+\beta$	$\nu_{c_{ISM}}$	$\nu_{c_{Wind}}$	α_{rise}
GRB 050502B	21	7	583	1.1	3.2	1.4	1.6e-3	13
GRB 050502B	21	7	8.8	1.1	2.6	0.14	1.6e-2	2.7
GRB 050904	94	29	4.1	0.6	2.7	0.17	1.3e-2	1.4
GRB 060204B	45	14	40	0.8	3.5	1.1	2e-3	6.9
GRB 060204B	45	14	15.3	0.4	3.7	0.54	4e-3	22
GRB 060418	35	11	17	0.6	4.0	1.2	2e-3	23
GRB 060418	35	11	1.5	0.1	2.8	0.20	1e-2	11
GRB 060526	35	11	336	0.3	3.3	0.91	2.4e-3	36
GRB 060526	35	11	198	0.6	4.2	0.77	2.9e-3	11
GRB 060607A	43	13	18.6	0.6	3.0	1.1	2.1e-3	21
GRB 060607A	43	13	14.7	0.8	3.2	0.71	3.1e-3	7.7
GRB 060714	40	12	114.6	0.9	3.8	1.2	1.9e-3	10
GRB 060714	40	12	108	0.5	3.1	0.93	2.4e-3	19
GRB 060814	27	8	2.4	1.2	3.6	1.9	1.2e-3	8.3
GRB 060904B	11	3.4	297	1.2	4.5	7.0	3e-4	17
GRB 060904B	11	3.4	3.5	0.4	6.3	0.26	8.7e-3	6.4
GRB 060929	26	8	845	0.9	3.2	1.1	2e-3	15
GRB 061121	38	12	100	2.0	2.7	10.	2e-4	2.9
GRB 070107	48	15	12.6	0.9	3.2	0.53	4e-3	5.8
GRB 070107	48	15	2.5	0.3	3.2	0.24	9e-3	8.1
GRB 070318	15	4.6	4.4	1.0	3.1	3.3	7e-4	4.8

Table 5.5. Flare Indicator Fractionals2

GRB	UV def/fl	$\chi^2_{AG_{thin}}$	$\chi^2_{AG_{thick}}$	$E_{ISO_{prompt}}$	$E_{pk_{prompt}} \frac{L_{fl}^{1/2}}{L_{pr}^{1/2}} \frac{\delta t_{pr}}{\delta t_{fl}}$
GRB 050502B	D	32	17.2	2.6e52	0.1
GRB 050502B	ND	0.5	0.5	2.6e52	1e-5
GRB 050904	ND	2.8	6.3	2.2e54	0.6
GRB 060204B	ND	11.3	24.2	2.5e53	1.5
GRB 060204B	ND	6.3	6.5	2.5e53	0.2
GRB 060418	Ex	49	6.8	1.2e53	4.2
GRB 060418	Ex	1.1	0.65	1.2e53	0.02
GRB 060526	Ex	11	2.5	1.2e53	1.1
GRB 060526	D	66	17	1.2e53	0.3
GRB 060607A	Ex	19	10	2.1e53	3.8
GRB 060607A	ND	38	21	2.1e53	0.6
GRB 060714	ND	38	24	1.7e53	1.1
GRB 060714	ND	61	21	1.7e53	1.2
GRB 060814	D	34	13	5.0e52	1.0
GRB 060904B	Ex	22	11	3.6e51	0.4
GRB 060904B	NA	1.7	0.84	3.6e51	3e-6
GRB 060929	ND	14	6.0	4.6e52	0.7
GRB 061121	Ex	94	33	1.4e53	11.0
GRB 070107	Ex	13	7.6	2.9e53	1.0
GRB 070107	ND	1.6	2.9	2.9e53	0.02
GRB 070318	Ex	9.5	1.8	8.5e51	0.2

Table 5.6. Flare Indicators 1

GRB	Time	Curv	H to S	Lum-Hrd Lag	Bump	$E_{ISO_{fl}}$	Fl Γ
GRB 050502B	417	N	Y	Y	Y	1.2×10^{53}	20
GRB 050502B	41000	Y	NA	N	NA	1.2×10^{52}	NA
GRB 050904	309	N	Y	N	NA	1.1×10^{50}	NA
GRB 060204B	74	Y	Y	Y	NA	3.7×10^{52}	NA
GRB 060204B	281	N	NA	Y	NA	6.8×10^{51}	NA
GRB 060418	113	N	Y	N	Y?	1.7×10^{52}	29
GRB 060418	4573	N	S-H	N	N	2.2×10^{51}	NA
GRB 060526	212	N	Y	Y	M	1.2×10^{53}	NA
GRB 060526	292	N	Y	N	M	5.1×10^{52}	NA
GRB 060607A	85	N	Y	N	N	2.6×10^{52}	NA
GRB 060607A	188	Y	Y	N	N	4×10^{52}	NA
GRB 060714	84	Y	Y	N	N	1.8×10^{52}	NA
GRB 060714	138	N	Y	N	N	1.3×10^{52}	NA
GRB 060814	119	N	Y	Y	N	3.8×10^{51}	NA
GRB 060904B	116	Y	Y	Y	Y	8.3×10^{51}	9
GRB 060904B	86843	N	NA	NA	NA	5.8×10^{48}	NA
GRB 060929	342	N	Y	Y	M	5.0×10^{52}	NA
GRB 061121	65	Y	Y	N	N	1.0×10^{53}	NA
GRB 070107	249	Y	Y	N	Y	4.8×10^{52}	NA
GRB 070107	1228	N	NA	N	Y	2.4×10^{51}	NA
GRB 070318	215	N	N	Y	N	1.3×10^{51}	NA

Table 5.7. Flare Indicators 2

GRB	flat	AG_{amp}	α_{rise}	$flare_{prior}$	$\Delta\alpha$	$\Delta\chi^2_{Band-PL}$	$\Delta\chi^2_{Band-BB}$	AG=Fl
GRB 050502B	N	NA	12.9	NA	NA	65.6	-7.7	Y
GRB 050502B	N	Y	2.7	Y	NA	2.8	-1.1	N
GRB 050904	N	N	1.4	NA	N	10.6	-0.5	Y
GRB 060204B	N	NA	6.9	NA	NA	5.2	0.3	Y
GRB 060204B	N	N	21.8	Y	N	37.3	10.0	Y
GRB 060418	N	Y	22.2	NA	Y	13.9	-7.7	Y
GRB 060418	N	N	11.1	Y	N	20.2	-29.7	Y
GRB 060526	N	N	36.5	NA	NA	354.8	36.1	Y
GRB 060526	Y	N	10.9	Y	NA	52.0	-1.4	Y
GRB 060607A	N	N	21.4	NA	N	3.3	-0.2	Y
GRB 060607A	N	N	7.7	Y	N	29.0	6.2	Y
GRB 060714	N	NA	10.0	Y	NA	69.5	12.0	Y
GRB 060714	N	NA	19.0	Y	NA	9.8	0.8	Y
GRB 060814	N	Y	8.2	NA	Y	71.6	4.6	Y
GRB 060904B	N	NA	17.4	NA	NA	120.3	109.9	Y
GRB 060904B	N	N	6.4	Y	N	NA	NA	Y
GRB 060929	N	N	15.1	NA	NA	30.9	5.7	Y
GRB 061121	N	N	3.4	N	NA	99.1	-116.8	Y
GRB 070107	N	NA	6.2	NA	NA	0.6	-3.6	Y
GRB 070107	N	N	8.4	Y	N	0.6	-1.2	Y
GRB 070318	N	Y	4.8	NA	Y	-22.4	-29.8	Y

The first panel treats the Reverse Shock Inverse Compton mechanism. Recall that among the criteria for this mechanism to be plausible was that the contrast between the flare and afterglow be $\lesssim 6$ and also that the flare occur at t $\sim$ t$_{dec}$ where t$_{dec}$ is the blast wave deceleration time, measured either in a Wind or ISM model. These two parameters form the plotting plane in this panel, with a region shaded blue representing the nominally allowed region, though I note, as will be true in all panels, that the allowed regions are not as sharply edge-defined as this binary representation may make them appear, and some data points slightly outside the nominally allowed regions may be considered as potentially allowable. We further identify datapoints within this plane as meeting or not meeting the other criteria specified above through the addition of color and supplemental symbols to each datapoint, the nominal datapoint in each case being black crosses. Thus, we see that in this first panel, none of the flares in our sample meet all the criteria, both required and supplemental criteria. We also note, however, that one flare (the early flare of GRB 050904) does meet both the deceleration time and contrast criteria and also satisfies the $\Delta T/T$ criterion. While the UV data does not show a deficit, the uncertainties are large and may be consistent with a deficit.

This flare appears to be the only strong candidate in our sample for being due to this mechanism, as the next most likely flares are a factor of several times too bright in contrast or occur a factor of several times too delayed with respect to the deceleration time. We also note that the deceleration time plotted here is calculated for a homogeneous thin shell interaction. The deceleration time due to a thick shell is, generally, about a factor of 3-4 times shorter than that for the thin shell in our sample, meaning that all cases which are excluded due to a too early value of the thin shell deceleration time will be excluded with greater confidence by assuming a thick shell interaction.

Cloud Model I

The second panel in our figure (top, right) shows the results of our analysis on the original form of the clumpy medium interaction model, CM I. In this panel, the figure plane is flare contrast level on the y-axis, as in the previous panel, but now plotted versus the ratio of the cooling frequency to the nominal observing frequency. As our measure of the nominal observing frequency, we use a value corresponding to 3 keV. This value is indicative of the region of the XRT energy range where the typical GRB spectrum and XRT effective area will combine to produce a peak in instrumental flux. The UVOT and BAT wings of our energy range, while useful in constraining our spectral fits, are far less sensitive than the XRT to the sources that we study here and thus we choose this canonical value within the XRT bandpass to represent our observing band.

The requirements for this mechanism to be a likely source of flares are that the contrast level be below ~ 6, that the cooling frequency be above the observing window at the time of the flare and that the flare, being produced by a blast wave that is decelerated upon encountering the density enhancement, will decay more slowly than the curvature relation would otherwise suggest. A UV or soft X-ray excess is possible but not required. We see in this panel, as in the previous, that only 6 of the 21 flares in our sample have a contrast level low enough to be considered as due to this mechanism. Furthermore, among those 6, only two are marginally consistent with the cooling frequency requirement and one of those two is ruled out by our modified curvature relation, leaving only one flare, that from GRB 060814 as a potential candidate for this Cloud Model.

We note here that the ν_c shown in this panel (and the next) is the cooling frequency determined by a homogeneous ISM model. The cooling frequency determined assuming a Wind environment model is generally 1 to 2 orders of magnitude lower at the typical observation time of the flares in our sample, placing it generally in the UV band and thus excluding the Wind environment variation of this model for all our flares.

Cloud Model II

The third panel (middle left) shows the modified version of the density clump interaction model, where we recall that the main modification is in the form of a non-spreading ejecta shell which improves the contrast factor of the mechanism and the rapidity of the potential rise and decay produced. In this modified form the mechanism is, unfortunately, somewhat devoid of highly constraining and testable characteristics, with the only required characteristic being that the cooling frequency be above the observing band. This requirement alone, nevertheless, excludes all but 4 flares in our sample, the aforementioned GRB 060814 which we previously noted fit the original form of the Cloud Model, and, additionally, the first flare of GRB 060904B, the initial prompt emission peak of GRB 061121 and the flare of GRB 070318.

We note that the three flares which are newly allowed by this model all show a UV or soft X-ray excess, which is a potential characteristic of the reverse shock component of the blast wave structure as it enters the density clump. A notable characteristic of this refined cloud model seems to be a distinctive flat-topped, slowly decaying temporal profile to the flares produced in this manner. The shape comes from the rapid enhancement of emission as the steep density gradient is encountered followed by a deceleration of the blastwave within the clump (the source of the flat-topped, slow decay) followed by a rapid decay of the flare as the blastwave exits the clump. Only one of the flares in our sample shows such a temporal structure (the second flare of GRB 060526) and it would seem to be ruled out from having this mechanism as a source due to a low cooling frequency. We further note that one of the flares accepted as potentially due to this mechanism is, in fact, the initial prompt emission pulse of GRB 061121. We have included this prompt pulse in our sample to study the differences between prompt pulses and flares as characterized by our analysis techniques. Its inclusion also serves as a potentially useful test case for, or indicator of the selectivity of each model. The inclusion of GRB 061121 in the list of bursts explainable by the Cloud Model II would seem to suggest either that our testing criteria for this model are not sufficiently selective or that the model is equally capable of explaining prompt emission and X-ray flares. Given the preponderance of other evidence in favor of the internal shock mechanism as the likely mechanism behind GRB prompt emission, it seems inappropriate to consider this model as potentially able to explain prompt emission pulses such as that in GRB 061121 and we therefore must assume that we have not sufficiently constrained this model through selection criteria. The addition of supplemental selection criteria to constrain the adherence of this model to the data is ongoing.

Internal Shocks

The fourth panel (middle right) shows the Internal Shocks selection criteria, presented in the plane of the curvature relation versus an E_{PEAK} limitation. The E_{PEAK} criterion requires that the peak energy of the flare as measured by a fit of the Band function exceeds the lower limit of E_{PEAK} set by the flare luminosity and duration and the prompt burst luminosity, duration and peak energy (see §5.6.1.6 for details). We further require that a flare produced by this mechanism exhibit the typical hard to soft evolution typically seen in prompt emission pulses and that the flare spectra be better fit by the Band function than by a simple absorbed powerlaw. Slightly more than half the flares in our sample (11/21; GRB 050502B-1, GRB 060204B-1, GRB 060204B-2, GRB 060526-1, GRB 060526-2, GRB 060607A-2, GRB 060714-1, GRB 060714-2, GRB 060904B-1, GRB 060929-1, GRB 070107-1) meet all the listed criteria, making this mechanism easily the most well suited to explain the flares in our sample.

AG Onset

Panel five (lower left) shows the Afterglow Onset mechanism criteria, presented in a $\chi^2 - \chi^2$ plane. The χ^2 values refer to the goodness-of-fit of a temporal powerlaw fit to the decay of the flare and the subsequent evolution of the GRB afterglow during the rest of its observation. Recall that in this mechanism, since the flare represents the peak of the afterglow flux and since, furthermore, the afterglow is then expected to decay normally through synchrotron cooling from the peak time forward, a powerlaw should accurately fit the entire evolution of the GRB beginning at the peak time of the flare. The χ^2 measure on the X and on the Y axis differ in the time which is taken as T_0 for the powerlaw fit. The X-axis represents the fit to the thin shell scenario (with T_0 set to the trigger time of the burst) and the Y-axis represents the fit to the thick shell scenario (with T_0 reset to the onset time of the flare). We furthermore indicate flares for which the spectrum is consistent with the spectrum of the AG to follow (as is required) and flares which show a change in the temporal decay slope of the AG decay from before to after the flare (which is not required by but is supportive of the mechanism).

The requirement that the flare spectrum be consistent with the later afterglow spectrum rules out all but one of the flares in our sample from being explained as a result of this mechanism, the second flare of GRB 050502B. This late time flare (occurring at $\sim T + 100ks$) is also consistent with a single powerlaw fit to the decay of the flare extending to the end of the observing window. We note, however, that the data sampling is rather sparse after this flare and therefore the fact that the data are fit well by a simple powerlaw is not too surprising, since the decay is largely dominated by the immediate decay of the flare from its peak flux level. We further note that the temporal fit is consistent with placement of T_0 at either the burst trigger time or the start of the flare itself, and thus is unconstraining in regards to selecting between the thin and thick shell scenario in this model.

Energy Injection

Panel six (lower right) shows the Energy Injection mechanism criteria, presented in the plane of the flare contrast factor versus the index of a powerlaw fit to the rising edge of the flare. We furthermore indicate flares which show an elevation in the afterglow level post-flare (an energization of the afterglow) which is a requirement of this mechanism and we indicate flares which have a detected previous flare (which may have ultimately produced the energy injection seen in the later flare) which is not required by but is suggestive of this mechanism.

Only one flare in our sample, the secondary flare in GRB 050502B fits all of these criteria. If we relax the requirement that the post-flare afterglow be energized, however, the secondary flares seen in GRB 060418, GRB 060904B and GRB 070107 also fall into this category. Relaxing the constraint for a visible energization of the afterglow may, in fact, be a reasonable step considering the lower level of precision in fitting the late time afterglow slopes due to the lower overall signal level at late times.

We note that all flares in our sample have $\alpha > 0$, which is indicative that no flares in the sample are consistent with production by a pure Poynting flow energy injection event. This is, however, not an altogether surprising result given the observational bias in our selection criteria (and moreover in any selection method which hopes to identify a flare with $\alpha < 0$ from an afterglow which is itself evolving with $\alpha < 0$) against identifying flares meeting the $\alpha < 0$ criterion.

5.7 Discussion

We have found the following distribution of flares potentially due to each of our studied mechanisms:

- Reverse Shock IC: 1
- Cloud Model I: 0
- Cloud Model II: 3
- Internal Shocks: 11
- Afterglow Onset: 1
- Energy Injection: 4

Our result generally supports the conclusions of several authors (Burrows et al. 2005b; Falcone et al. 2006; Liang & Zhang 2006; Zhang et al. 2006; Butler & Kocevski

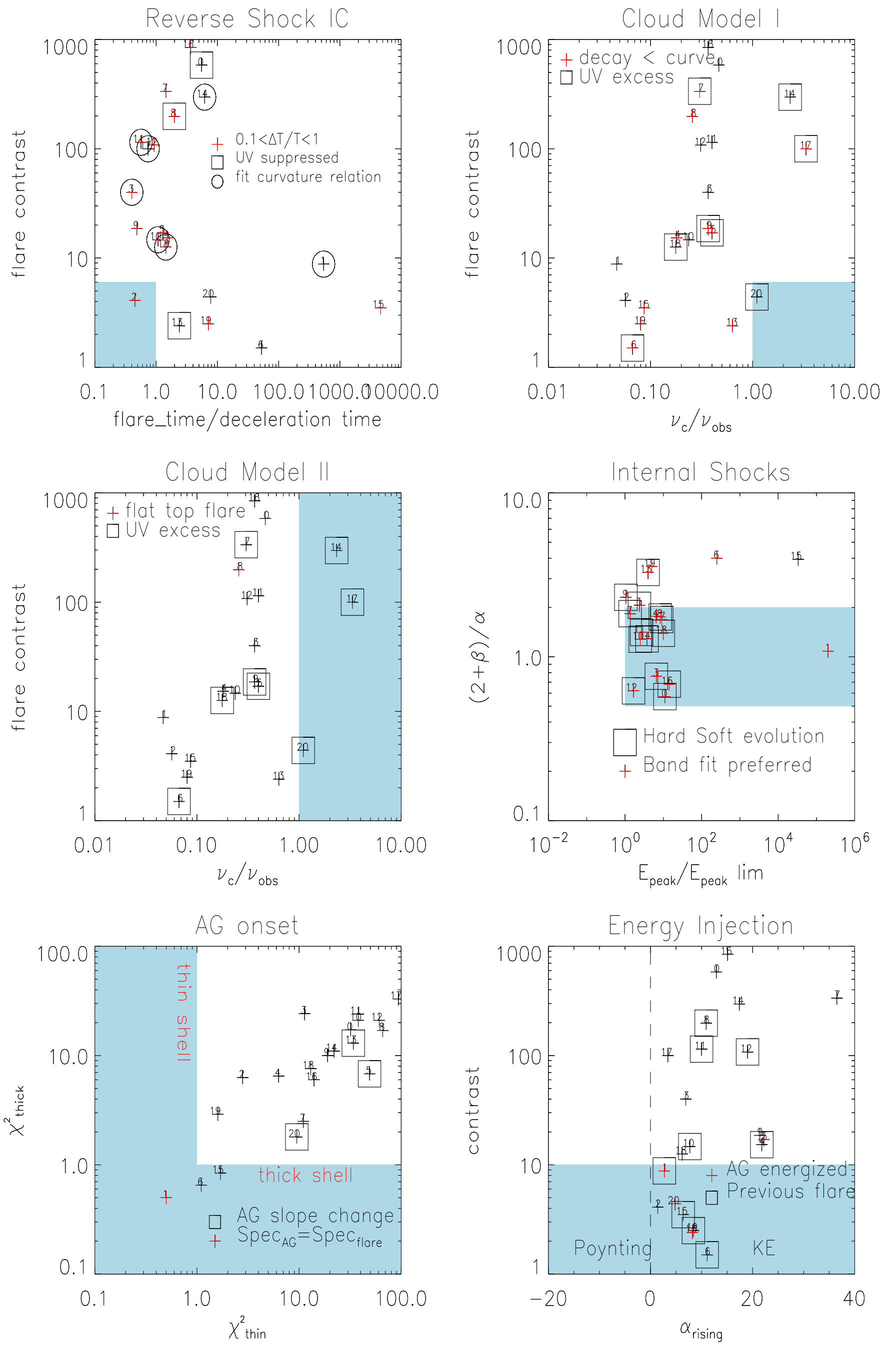

Fig. 5.16 Allowed regions for each flaring mechanism. The six panels in this figure detail the characteristics of the flares in our sample with respect to the expected characteristics of several flaring mechanisms from the literature (see text for details). In general, the Internal Shock mechanism seems to be favored with more than half the flares well within the allowed parameter region and several more only marginally outside. No other mechanism shows more than a few flares within the allowed region, though it is notable that some flares seemingly incompatible with the IS mechanism fall within the allowed regions of other mechanisms. Numbers are overplotted on each symbol to aid in comparison of individual datapoints from model to model.

2007; Morris et al. 2007) that the most likely production mechanism for the majority of X-ray flares seen in *Swift* GRB data is direct synchrotron emission produced in the collision of shells of ejecta emitted at highly relativistic velocities at late times. Our analysis has gone on to show, however, that this mechanism is unlikely to be able to explain all X-ray flares detected by *Swift* and that several other mechanisms are likely required to explain the entire flare taxonomy.

One of the most interesting results of the analysis is the potential indication that several late time, low contrast level flares are consistent with energy injection produced by the interaction of a previous flare with the FS. This is a potential explanation of the secondary flares in GRB 050502B, GRB 060418, GRB 060904B and GRB 070107. Apart from merely helping to explain the structure of the bumps and wiggles in the X-ray lightcurves of these bursts, the combination of these late time flares together with knowledge of the parameters describing the earlier flare which led to the ultimate energy injection can provide another valuable piece of information regarding GRB flares, namely the Lorentz factor.

We have the following relationship between the early flare Lorentz factor and energy, the late flare onset time and the density of the environment

$$\Gamma_{ef} \simeq (\frac{3E_{ef}}{8\pi n m_p c^5})^{1/8} t_{lf}^{-3/8} \tag{5.6}$$

where Γ_{ef} and E_{ef} are the Lorentz factor and isotropic equivalent energy of the early flare, t_{lf} is the onset time of the late flare and n is the particle density of the surrounding medium (Lazzati & Perna 2007). A measured redshift is required to determine E_{ef}. 2

of the 4 bursts in our sample which meet the criteria of this mechanism have measured redshifts, GRB 060418 and GRB 060904B. If we calculate Γ_{ef} using the equation above, we find Γ_{ef} = 29±2 and 8±1 assuming n=1 cm^{-3}. I further note that the quoted uncertainties refer to propagation of only the uncertainties in E_{iso} and the onset time of the late flare, ie, the quoted uncertainties do not account for the unknown true density of the circumburst medium. The uncertainty in this value, which is speculated to range from values of 0.01 cm^{-3} to 10 cm^{-3} easily dominates the uncertainty in these calculated values (29^{+22}_{-8} and 8^{+6}_{-2} respectively). These values of the Lorentz factor are consistent with the value of $\Gamma \lesssim 20$ found by Falcone et al for the early giant flare in GRB 050502B if it is responsible for the late time flare in that burst.

Though we do not have a measured redshift value for the other two bursts fitting this mechanism in our sample, we note that the Lorentz factor equation above is only weakly dependent on the E_{iso} of the early flare and therefore it is not unreasonable to assume a "typical" redshift for the two bursts to calculate E_{iso} and then find the predicted Γ for these two remaining bursts. If we assume the reported *Swift* average GRB redshift of z=2.6 (Jakobsson et al. 2006b), we can expect to, at worst, incorrectly predict E_{iso} by a factor of ~ 8 (roughly a factor of 2 in the value (1+z), assuming z is likely between 0.75 and 6.0, which enters as a square in the luminosity distance calculation and again in the energy redshift correction), leading to an uncertainty of $\sim \pm30\%$ in the calculated value of Γ. Proceeding in this manner we find values of Γ for the early flares GRB 050502B and GRB 070107 of 16±6 and 54±18 respectively. While the value for GRB 050502B is both consistent with the result of Falcone et al and in keeping with the suggestion of the results from GRB 060418 and GRB 060904B that the Lorentz factor of flares is $\Gamma \lesssim 30$, the value from GRB 070107 of $\Gamma \sim 50$ is somewhat higher that the other three.

The reason for the large value of Γ determined in GRB 070107 is the very early time of the supposed late flare due to energy injection. There are other reasons to prefer to explain this flare through a mechanism other than energy injection, however, e.g., a value of $\Delta T/T$ smaller than is typically expected for energy injection ($\Delta T/T \sim 0.3$ compared to values of $\sim$1 which are expected to be more typical of this mechanism). It is interesting, however, that inspection of the X-ray lightcurve of GRB 070107 reveals a low level flare, which falls below the selection criteria level of our original sample, at T+ $\sim$ 70 ks. If we assume this low level, late time flare to be associated with the energy injection event of the large early flare of GRB 070107 instead, the calculated value of the Lorentz factor becomes similar to those in the previous 3 cases at Γ=12$\pm$4. This leads to the interesting suggestion that a sizeable fraction of bright, early X-ray flares in GRBs may have associated energy injection events apparent at later times. A systematic study to identify late time energy injection events associated with bright early time flares is left for future work. Nevertheless, if the 4 cases discussed here do indeed represent instances of early flares produced through the internal shock mechanism injecting energy at later times into the FS afterglow, we can use them to place an observed limit on the Lorentz factor of flares produced through internal shocks. We can assume that the energy injection event which we have identified in each case is the earliest such event in each burst since $\Delta T/T \sim$1 for energy injection flares which implies that at times later than the first *Swift* orbit, any flare occurring through this mechanism would not be short enough to be completely missed due to an orbital observing gap. Furthermore in each case, since there is sufficient fluence in the observed late time flare to make it apparent above the background afterglow level, we can assume that any such flares occurring earlier during the afterglow, when both the afterglow and any flare flux would be higher, would not have been missed due to low signal to noise level. It is possible, of course, that energy injection events at times beyond the late time flares identified here may have been missed due to low flux levels at the end of the observations of a particular burst. This implies that if the Lorentz factor of early IS flares is much lower than $\Gamma_{IS} \lesssim 30$, as suggested here, the associated late energy injection events may occur much later, at much lower flux and therefore be below detection level. We therefore suggest the observed limit $\Gamma_{IS} \lesssim 30$ for the Lorentz factor of X-ray flares as produced through the internal shock mechanism.

Chapter 6

Discussion

In the previous chapters of this thesis, we have presented 3 separate analyses of the GRB flaring phenomenon. In Chapter 3 we studied a series of flares in the individual burst GRB050713A, in Chapter 4 we presented the first spectral survey of a large (77) sample of GRB flares observed in soft X-rays (0.3-10.0 keV), and finally in Chapter 5 we presented a more stringent analysis of a smaller set of bright and isolated flares, as observed from the optical through hard X-ray range (0.002-150 keV). We have noted several characteristics during the presentation of the analyses results relating to the timing and energetics of flares, culminating in the presentation of Figure 5.16 in which we represent the fraction of flares in the sample of Chapter 5 allowed by each of several mechanisms from the literature proposed for the production of flares. In this chapter, we now expand our discussion of the implications of these results in the context of the various proposed mechanisms and in the context of the requirements placed on the GRB central engine. (We will also treat, in this chapter, discussion of observational biases in our analyses, put off from previous chapters.)

6.1 Γ of Flares and Γ of Prompt Emission

One of the intriguing results of our analysis is shown in Figure 6.1 in which data from the multiwavelength flares sample are plotted together with data from the prompt emission phase of a large sample of *Swift* bursts in the plane of E_{PEAK} versus $L^{1/2}/\delta t_v$ where L is luminosity and δt_v is the characteristic variability timescale. Lines are overplotted representing the relationship $E_{PEAK} \propto L/\delta t\Gamma^2$ for various values of Γ/Γ_0 where Γ is the bulk Lorentz factor of the ejecta and Γ_0 is an arbitrary fiducial value of Γ. This relation is appropriate if the flares are due to the internal shock mechanism as discussed in Zhang & Mészáros (2002a). The clustering of the flare data relative to the clustering of the prompt phase data with respect to the direction of the Γ gradient suggests an observable distinction between the Lorentz factor characterizing the prompt emission phase and that characterizing X-ray flares. Note that the figure treats only the relative value of Γ between prompt emission and flares since the absolute value will be a function of variables not able to be investigated in this study, such as the circumburst particle density.

The variability timescale δt_v is the timescale associated with the interaction of a particular shell with the outflow in which the internal shocks develop. In the case of flares, the temporal profiles typically show a single powerlaw rise followed by a single powerlaw decay between t_{start} and t_{stop}. This is, in fact, by definition of our method of flares identification (Chapter 2), but moreover it is generally true of GRB X-ray flares that they often occur separated in time from other flares. This is expressly true for the sample of flares treated in this figure, since in the analysis of Chapter 5 we intentionally chose our flares sample to be composed of bright, well-separated flares in order to provide as "clean" a dataset as possible for our spectral analysis of that chapter. Therefore, in Figure 6.1 we use the flares duration, as found in Chapter 5, as our measure of δt_v for flares and we expect this to be a reasonable estimate of the true value.

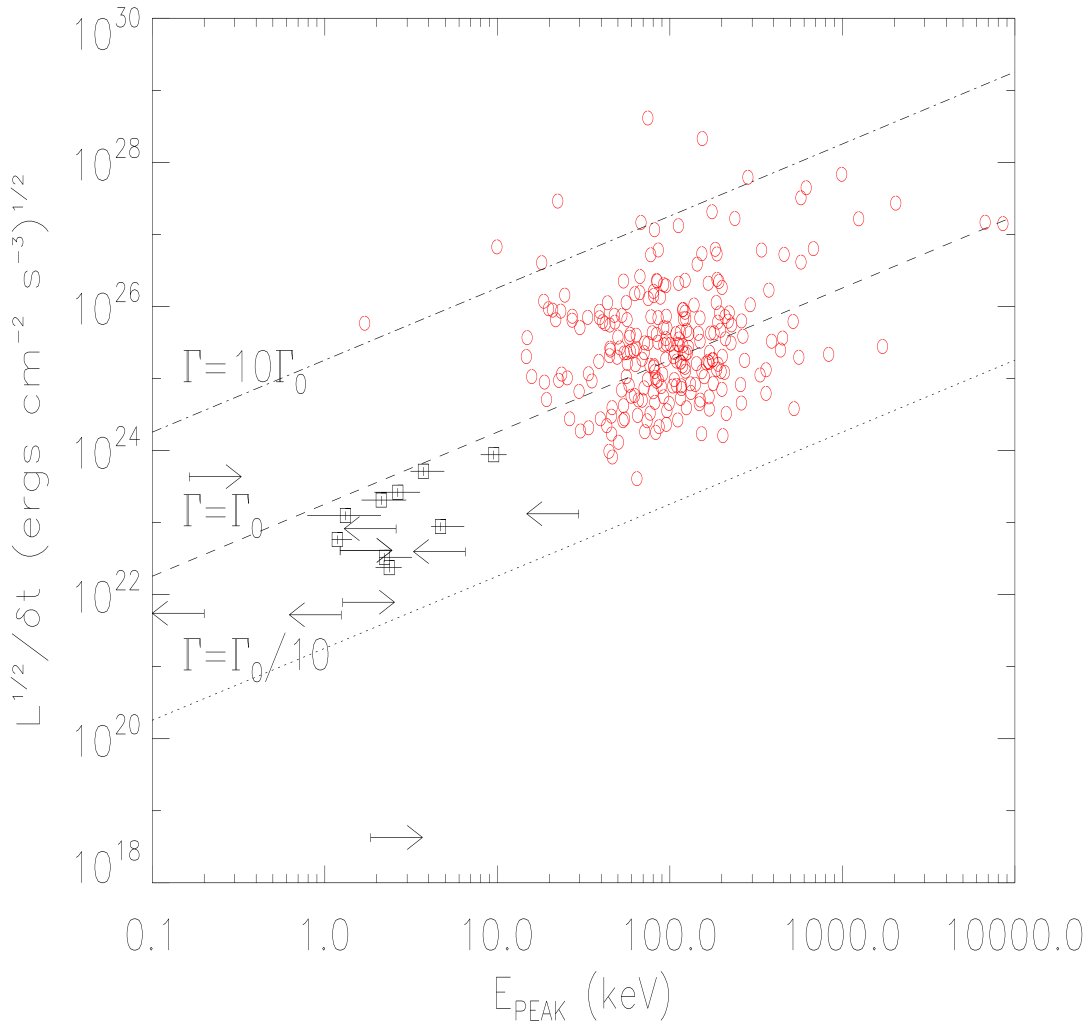

Fig. 6.1 Luminosity-variability measure versus E_{PEAK}. The internal shock model implies $E_{PEAK} \propto L^{1/2}\Gamma^{-2}\delta t^{-1}$ (Zhang & Mészáros 2002a) where δt is a measure of the variability timescale of the emission. Here we show $L^{1/2}\delta t^{-1}$ plotted against E_{PEAK} for the flares in our sample (boxes) with data from the BAT prompt burst sample (points) overlaid for comparison. The diagonal lines correspond to fits to the internal shock relation with Γ=0.1×Γ_0 (dotted), Γ=Γ_0 (dashed) and Γ=10×Γ_0 (dash-dotted). The fact that the prompt data fall between the Γ=Γ_0 and Γ=10×Γ_0 curves while the flares data fall between the Γ=0.1×Γ_0 and Γ=Γ_0 curves suggests that the shells causing late time X-ray flares are ejected with significantly lower Lorentz factor than the shells which produce the prompt emission.

For the prompt emission data in the figure, the measurement of δt_v is less straightforward. Ideally, as with the flares data, we would like to be able to identify individual pulses within the prompt emission phase as we are able to do in the later flares data. Due to the much greater degree of overlap often seen between pulses during the prompt phase, though, this is extremely difficult if not impossible. As a proxy for the true value of δt_v in the case of the prompt data, and chosen in part because of its ready availability, we instead use the value T_{50}, which measures the duration of time over which 50% of the prompt γ-ray emission is emitted. In cases in which the prompt emission is of a Fast Rise Exponential Decay (FRED) profile, T_{50} may be a reasonably accurate measure of the intended timescale and is analogous to the timescale measured for the flares. Unlike flares, however, there are many cases in the plotted prompt data for which pulses are highly overlapping. In these cases T_{50} will be only an upper limit on the true value of δt_v.

With this caveat in mind, let us consider the implications of Figure 6.1. The figure shows that flares occur at characteristically lower peak energy than prompt emission episodes do, though this is in part an instrumental bias since the BAT instrument which is responsible for the triggering of GRB identification is sensitive to energies from 15-350 keV while the XRT, which is the instrument in which late time X-ray flares are generally identified, is sensitive only from 0.2-10 keV. The separation between the flaring and prompt emission data in the Y-axis implies that flares tend to occur at lower luminosity or with longer duration than the prompt emission or both. Taken in this form, together with the relation $E_{PEAK} \propto L/\delta t\Gamma^2$ from Zhang & Mészáros (2002a), these properties combine to suggest a characteristically lower value of Γ for flares than for the GRB prompt emission phase. In fact, the flare data appear to occupy the same region of the figure as the lower portion of the prompt emission data, in the sense of the Γ parameter pseudo-axis, which increases from the lower right corner of the figure towards the upper left of the figure. There appears, however, to be a somewhat abrupt end to the flares distribution, represented in the figure by the, arbitrarily scaled, $\Gamma = \Gamma_0$ dashed line. The one flaring datapoint occurring above this line is associated with a lower limit in E_{PEAK}. Therefore even this datapoint is consistent with being below the $\Gamma = \Gamma_0$ line if the true E_{PEAK} of this flare is $\gtrsim$ 2 keV, which is a reasonable value to expect. The implication is that while the Lorentz factor of some of the "faster" X-ray flares may be comparable to that of the "slower" prompt bursts, the "faster" prompt bursts appear characterized by Lorentz factors of several to ∼10 times larger than the fastest flares.

Furthermore, as cautioned above, the timescale used in the presentation of the prompt bursts data in the figure may be an overestimate of the true value of δt_v. It may therefore be appropriate to consider the red circles in the figure as only lower limits (in the Y-direction) for the prompt emission data, suggesting a greater separation in Γ between the prompt and flaring emission. In fact, several authors have suggested that the true variability timescale (and particularly that of short bursts) may be as small as 0.01ms, perhaps only limited by geometrical arguments of the size of the emitting region such that $r \sim c\delta t_v \sim$ few to a few tens of km and thus $\delta t_v \sim 0.01$ to ∼0.1 ms. If that is true then the prompt data move to even higher values of Γ relative to the flares. It should be noted, however, that small scale perturbations are seen atop X-ray flares as well, suggesting that if we are to use the smallest detectable δt in regards to the prompt emission, we should do so also in regards to the X-ray flares which would push the flares also to higher values of Γ. In choosing to characterize the variability timescale δt_v by the duration of individual pulses we have sought to identify a common physical timescale between the two phenomena, namely the shell interaction time within the internal shock scenario.

The presentation of the data in Figure 6.1 can be considered as a conservative representation of the disparity in Lorentz factor between the prompt phase emission and the later X-ray flares. Such a difference in Γ is expected to exist in the context of the internal shock model for flares and has been investigated in the case of individual flares within individual bursts in previous works. In Falcone et al. (2006), the authors worked backward from the assumption that the late time bump seen in the X-ray lightcurve represented energy injection into the FS due to the early, giant flare catching up to the decelerating blastwave. In Chapter 5, we performed a similar analysis for two of the bursts in our sample which show evidence of a bright X-ray flare followed later in the X-ray lightcurve by a less luminous, but longer duration, "bump". Recall that in those two cases, we found $\Gamma = 29 \pm 2$ (GRB060418) and $\Gamma = 8 \pm 1$ (GRB060904B) for the Lorentz factor of the early bright flares as inferred from their properties as well as the properties of the respective later "bumps". These values for Γ are in good agreement with the value found by Falcone et al. (2006) of $\Gamma \lesssim 20$. Furthermore, if we again consider Figure 6.1 and adopt a value of $\Gamma \sim\ 300$ for the upper dot-dashed line representing the upper end of the Γ distribution of the prompt emission data, we see that the flares data are then bracketed by lines which respectively correspond to $\Gamma = 30$ and $\Gamma = 3$, also in good agreement with both our findings for GRB060418 and GRB060904B and with the Falcone et al results for GRB050502B. We emphasize here that the method of determining Γ in Figure 6.1 is different from that used to infer Γ of an early time flare from properties of the associated later time energy injection signature. In the former case we are tapping the expected relation between the peak energy of the emitted spectrum and the total energy of the emission event (Amati 2006; Ghirlanda et al. 2005) while in the latter case our calculation is based completely on the dynamics of the outward propagation of the IS-producing shells toward the previously decelerated FS blastwave. The fact that these two independent methods appear to agree with one another is an encouraging endorsement of the results of each.

In Figure 6.2 we show the contrast level plotted against total fluence for each of the flares in our sample of Chapter 5. It is worth noting that two of the three flares which show the possible presence of an associated late time flare due to energy injection occur both at high contrast level and at high fluence. Being at high contrast level implies that the afterglow is sufficiently dim that flares, produced either through IS or through energy injection (or any other mechanism for that matter) will be more readily observable than they would be in a burst with a relatively brighter afterglow component. On the other hand, being at high fluence implies that a large enough amount of energy is contained in the initial flare to potentially produce an instrumentally observable energy injection signature at later times. All three flares are seen at high fluence, with a mean fluence of $2.4 \pm 1.3 \times 10^{-6}$ ergs cm^{-2} s^{-1} compared to the overall sample mean of $7.6 \pm 9.2 \times 10^{-7}$ ergs cm^{-2} s^{-1} while two of the flares are also seen among the four flares of highest contrast in our sample.

While two of these three flares are both among those of highest contrast and highest fluence in our sample, there are other flares in our sample which are only slightly

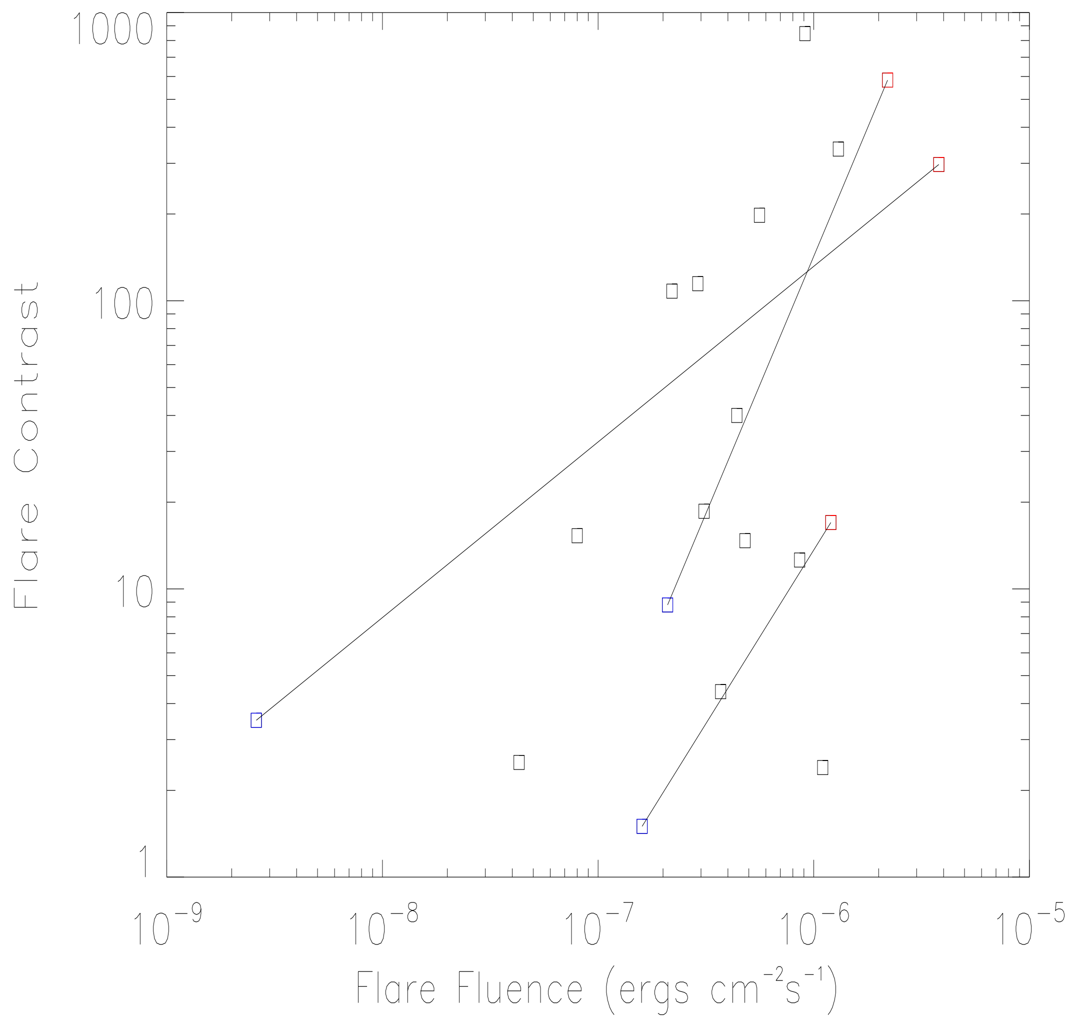

Fig. 6.2 Flare contrast versus flare fluence. Flare contrast level, defined as the flux of the flare divided by the expected flux of the afterglow during the peak of the flare, is plotted against the flare fluence. The contribution of the fluence to the flare due to the underlying afterglow has been subtracted. The 3 flares in our sample which have been discussed in association with later related energy injection events are shown in red. The possible associated energy injection flares are shown in blue with lines connecting associated pairs.

lower in either of these parameters (and several which are of higher contrast than the third flare which is possibly associated with late time energy injection). It is worth asking in these other cases, then, whether our initial flares selection criteria may have missed identification of a late time energy injection event associated with some of these other flares.

Oftentimes, GRB X-ray lightcurves observed by *Swift* are characterized by occasional low level "bumps and wiggles". Thus, in asking whether some of the remaining flares in our sample might be associated with a particular bump or wiggle which may be attributed to an energy injection event, we clearly need to exercise caution. One step that we can take to constrain our search is to assume a common value of Γ for all flares in our sample and to use that value of Γ together with our measured values of E_{ISO} for each flare and a typical assumption about the density of the circumburst medium (n ~ 1 cm^{-3}) to derive the expected observation time of a late time bump due to energy injection associated with each earlier flare using the relation

$$T^{-3/8} = (\Gamma/(3E_{ISO}/(8\pi n\ m_p c^5))^{1/8} \tag{6.1}$$

(Lazzati & Perna 2007) where T is the expected time of the late flare, Γ is the Lorentz factor of the early flare, n is the circumburst density, E_{ISO} is the isotropic equivalent energy of the early flare, m_p is the proton mass and c is the speed of light.

To constrain the value of Γ that we will use, we look first to our own previous analysis of late time flares which are potentially associated with earlier IS flares. We have 3 such flare pairings in GRB05052B, GRB060904B and GRB060418. For an assumed circumburst density of n$\sim$1 cm^{-3} we find a mean and 1-σ error of $\Gamma \sim 20 \pm 10$ for these three bursts. We adopt this mean value plus or minus the 1-σ error, $10 < \Gamma < 30$ as the limiting range of Γ which we will test. This range is consistent with the Γ values bracketing our entire flares distribution as discussed above (see Figure 6.1). It has also been shown that curvature emission timescale arguments of flare data can be used to place lower limits on the combined value $\Gamma\Theta_j$ for flares, where Θ_j is the expected opening angle of the jetted emission (Wu et al. 2007). In their work, Wu et al. (2007) suggest a lower limit on Γ of ~ 10 assuming a value of Θ_j=0.1, in agreement with the lower limit we have adopted here.

In Table 6.1 we calculate lower and upper limiting times for the expected occurrence of an energy injection event into the FS due to all flares in our sample and list these values together with the flare contrast and fluence values plotted in Figure 6.2.

Table 6.1. Predicted time range of energy injection events due to early IS flares.

GRB	Flare #	$T_{inj}(\Gamma_{10})$ (ks)	$T_{inj}(\Gamma_{20})$ (ks)	Contrast	Fluence ergs $cm^{-2}s^{-1}$
050502B	1	152	8	583	2.2×10^{-6}
050502B	2	71	4	8.8	2.1×10^{-7}
050904	1	39	6	4.1	4.1×10^{-7}
060204B	1	103	6	40	4.4×10^{-7}
060204B	2	58	3	15.3	8.0×10^{-8}
060418	1	79	4	17	1.2×10^{-6}
060418	2	40	2	1.5	1.6×10^{-7}
060526	1	152	8	336	1.3×10^{-6}
060526	2	114	6	198	5.6×10^{-7}
060607A	1	91	5	18.6	3.1×10^{-7}
060607A	2	106	6	14.7	4.8×10^{-7}
060714	1	81	4	115	2.9×10^{-7}
060714	2	73	4	108	2.2×10^{-7}
060814	1	48	3	2.4	1.1×10^{-6}
060904B	1	63	3	297	3.8×10^{-6}
060929	1	114	6	845	9.1×10^{-7}

Table 6.1—Continued

GRB	Flare #	$T_{inj}(\Gamma_{10})$ (ks)	$T_{inj}(\Gamma_{20})$ (ks)	Contrast	Fluence ergs $cm^{-2}s^{-1}$
061121	1	143	8	100	1.0×10^{-5}
070107	1	112	6	12.6	8.6×10^{-7}
070107	2	41	2	2.5	4.3×10^{-8}
070318	1	34	2	4.4	3.7×10^{-7}

Lightcurves and hardness ratios of each GRB with vertical lines overplotted representing the expected time of an energy injection event associated with each early flare are shown in Appendix B. A complete investigation of the spectral and temporal evidence of energy injection in each case is left for future work, but inspection of the lightcurves presented in Appendix B, nevertheless, offers some intriguing suggestion of X-ray flux excesses at or close to the times specified in Table 6.1. Besides the previously discussed cases (GRB050502B, GRB060418 and GRB060904B), we see some evidence of excess flux in at least 3 other cases, GRB060526, GRB060714, and GRB070107. There are also cases, however, of highly energetic early flares which are well explained only by the IS mechanism and which do not show obvious evidence of a later energy injection event (GRB060929). If we are to argue in favor of associating some of the late time flares discussed in this thesis (and in GRB afterglows in general) as due to the eventual energy injection signature of earlier IS flares, we must account for the observation that some bright (and thus energetic) IS flares do not show evidence of a later energy injection signature.

A straightforward explanation for this is a value of Γ for some IS flares that is even lower than the lower limit value of 10 suggested previously. Since the onset time of an energy injection flare goes as t $\propto \Gamma^{8/3}$, a small change in Γ results in a large change in the onset time and thus the actual interaction time of energy injection flares associated with these early IS flares may be significantly later than what is listed in Table 6.1. Furthermore, since the luminosity of the energy injection flare is proportional to Γ^2, such slower flares will be inherently fainter and more difficult to detect. We noted previously that Wu et al. (2007) suggest a lower limit of $\Gamma \sim$10 in their analysis. It should be noted, however, that this lower limit estimate is based in part on an assumed value of Θ_j=0.1, taken from observations of GRB afterglows in the literature. Since it remains an open question whether the GRB jet collimation angle varies during the lifetime of the afterglow, it may be possible to invoke a smaller value of this lower limit on Γ by allowing larger values of the jet collimation angle during the time when the late time IS flare shells are ejected.

6.2 Lack of Ionization Due to Flaring

We showed in Chapter 5 that when spectral models which allow intrinsic curvature (the Band function, e.g.) are used to fit GRB X-ray flares, the neutral hydrogen column density is generally consistent with a constant value. This is consistent with the results of Butler & Kocevski (2007), is contrary to earlier reports in the literature of rapidly varying X-ray column densities (Starling et al. 2005; Campana et al. 2007; Gendre et al. 2007) and implies that we do not observe significant ionization of the GRB environment during X-ray flares. There are several potential explanations for such a lack of evolution in the X-ray column density. One possible explanation is that flaring GRBs do not occur in dense molecular clouds, where the column density would be expected to be high, and therefore there is no significant local source of neutral hydrogen (and associated metals) available for ionization by the GRB outflow. This explanation, however, is immediately ruled out by the large constant values of the column density found in these, and indeed in most, GRBs, typically 10^{21}-10^{22} cm^{-2}. It has furthermore been noted that these high column densities, inferred from soft X-ray absorption, are not a product of intervening absorption but rather are evidence of an absorbing column intrinsic to the GRB host environment. The inference is based on comparison of the spectral absorption characteristics of GRBs to those of blazars, another astrophysical source population which samples the high redshift universe. GRBs and blazars show similar excesses of large equivalent width MgII absorbers (with respect to low redshift sources), implying that the two source populations sample similar intervening columns (ie, they lie at similarly large redshift). GRBs, however, generally show soft X-ray absorption column densities of $\sim 10^{22}$ while blazars typically have much lower soft X-ray derived columns of $\sim 10^{20}$ (Watson et al. 2007; Donato et al. 2005; Stocke & Rector 1997). Since the additional inferred N_H column in GRBs seems not to be associated with additional MgII absorption, the implication is that the additional N_H absorption is intrinsic to GRBs or their hosts.

Another possible explanation is that the timescale for ionization of the circumburst medium is longer than the timescale probed by individual flares (T_0+10^2-10^4 s). This scenario also seems unlikely, though, since numerical simulations have been used to show that, for typical GRB luminosities and reasonable circumburst environmental parameters, roughly 40-90% of the column can be expected to be be ionized over a few hundreds of seconds after the burst onset, depending on the circumburst cloud geometry (Lazzati & Perna 2002). We note here that while the N_H data are consistent with no change, the uncertainties do leave open the possibility of a decrease or increase of $\sim \times 2$ within the first 1000s of the onset of flares. While an increase of a factor of 2 due to an increase in ionizing radiation seems unrealistic, the allowed decrease of (up to) a factor of 2 is compatible with simulations of a circumburst environment with a shell geometry, but would appear to rule out a uniform circumburst environment (Lazzati & Perna 2002) (though, see below).

A third possible explanation for the apparent constancy of the N_H column density (and one which, if assumed, invalidates the incompatibility of the uniform medium previously noted), is that flash ionization of the surrounding medium due to the prompt GRB emission may initially ionize the entire available local column, thus leaving no local absorbing medium available for ionization at the later times probed by X-ray flares. This explanation, however, suffers from a similar difficulty as the previous explanation of an inherently low density environment, namely that the large and apparently constant column densities seen in GRBs seem to argue for the presence of a large intervening column. Since this column, as previously discussed, has been shown to likely be associated with the local GRB environment, one would need to introduce a "clumpy" structure to the GRB local environment to explain the observations. In such a scenario, the prompt GRB emission may fully ionize an immediately local pocket of gas surrounding the GRB (to within several to several tens of parsecs) beyond which a void (region of relatively low density) exists. A sufficiently large void would suppress any ionization effects of subsequent flaring emission. Additional clumps or shells of absorbing material beyond such a void, however, would be sufficient to maintain an elevated N_H signature in the GRB spectrum to late times. Such a clumpy or multiply shelled circumburst medium is certainly not unexpected given the likely mass loss profile of massive stars like those expected to produce long GRBs. Unfortunately, the accuracy of soft X-ray data measured to date has not been sufficient to probe the circumburst environment so precisely to allow mapping of the circumburst environment on this scale. Thus, a sufficiently structured medium can presently be invoked to explain any of the collected data. Future observations will hopefully be able to better test predictions of this model.

6.3 Implications of $\Gamma \lesssim 10$ for Flares

The typical bulk Lorentz factor of GRB flares is somewhat poorly constrained. Suggestions are made in the literature both that Γ may be expected to increase with time due to the evacuation of the channel through which the burst ejecta propagate (Burrows et al. 2005b; Zhang et al. 2006) and that Γ may be expected to decrease with time due to lower energetics of later ejections (King et al. 2005; Perna et al. 2006; Proga & Zhang 2006). As noted earlier, some observational indications in the literature have previously suggested measured values of Γ of $\sim$20 (Falcone et al. 2006) and an approximate lower limit on Γ of $\sim$10 (Wu et al. 2007). In this work we have proposed that the overall distribution of flares may be consistent with few $< \Gamma <$ few tens.

We point out here an argument in favor of lower values of Γ based on the geometry of the post burst environment. The FS deceleration is expected to occur at a radius given by

$$R = (E/(n\ m_p c^2))^{1/4}; thick\ shell\ case \tag{6.2}$$

$$R = (3E/(4\pi\gamma_0^2 n\ m_p c^2))^{1/3}; thin\ shell\ case \tag{6.3}$$

where E is the energy of the blast wave, n is the circumburst density, R is the deceleration radius, Γ is the blast wave Lorentz factor and m_p and c are physical constants as before (Sari & Piran 1999b). For typical values of the associated parameters, these equations predict minimum values of the deceleration radius of $\sim 10^{17}$cm. This implies that any fast moving, late emitted shells of ejecta must either interact to produce IS emission prior to reaching this radius or else be absorbed into the forward shock, dissipating energy through the energy injection mechanism. Since we have previously shown that the energy injection mechanism cannot explain the bright, rapid timescale flares often seen in GRB afterglows, it follows that late ejected shells of material must be able to interact at times as late 10 ks or later (the rest frame time of some of the latest flares seen in GRB afterglows) prior to reaching this radius.

For the radius at which IS shells will interact, we have $R_{IS} \simeq \frac{\gamma}{\Delta\gamma}\gamma^2 c\Delta\ t_{ej}$ where γ is the typical Lorentz factor of the interacting shells, $\Delta\gamma$ is the difference in Lorentz factor between the interacting shells, $\Delta\ t_{ej}$ is the elapsed time between the ejection of the two shells of ejecta which will interact and c is the speed of light. We also know that energy constraint arguments imply that $\Delta\gamma \sim \gamma$ in order to prevent the required energy contained within the late time shells from becoming unreasonably large (Krimm et al. (2007); this is essentially the argument against IS emission due to early emitted shells interacting at late times). Thus, if we assume $\Delta\gamma \sim \gamma$, and use equation (3) from

Krimm et al. (2007) to substitute our $\Delta\ t_{ej}$ with their parameter $\Delta\ t_{fl}$ (the observed duration of the flare), we arrive at $R_{IS} \simeq 10^4 s \times \gamma^2 c \lesssim 10^{17}$cm which gives us the limit $\gamma \lesssim 18$.

Of course, this limit is dependent on the exact value of the deceleration radius (dependent as the square root, in fact), for which we have chosen a relatively low estimate in our calculation above, so this upper limit on γ should be considered a lower limit of the value of the true upper limit. Though, since the deceleration radius is dependent on unknown parameters itself (namely the circumburst density and total burst energy, not to mention the Lorentz factor of the prompt burst itself), the possibility of such a low limit on γ should not be dismissed.

Furthermore, the limit above assumes a constant value of γ for all flares, limited by the γ required to produce the latest observed flares. This is clearly a simplification of the more likely situation that γ is a function of the energy reservoir remaining available to produce progressively later emission episodes as a given GRB progresses. Several models in the literature for the ultimate production mechanism of GRB flares (where by "production mechanism" we refer to the process at work within the GRB central engine which extracts energy from the post-prompt central engine and injects it to a jetted outflow, rather than "emission mechanism" as we have discussed earlier throughout this thesis, referring to the method of conversion of bulk kinetic energy of the outflow into radiation energy) seem conducive to such a progressive decrease in the remaining energy reservoir and hence a progressively lower γ for later flares, including fragmentation models (King et al. 2005; Perna et al. 2006) and magnetic regulation of a decreasing mass accretion rate (Proga & Zhang 2006) among others.

A natural expectation of a mechanism invoking a steadily decreasing value of γ is that later flares should be expected to show progressively lower values of E_{peak}. While observation of this effect has been reported for GRB060714 (Krimm et al. (2007), also this work), the effect has not been shown to be ubiquitous throughout all flares, though the lack of a clear signature could be confused due to contamination of the sample from non-IS flares, which are not expected to follow the relation.

6.4 Flare Mechanism Breakdown and Observational Bias

One of the primary goals of this work has been to determine a taxonomy of GRB X-ray flares. The result of this effort for our flare sample of Chapter 5 is shown in Table 6.2.

With more than half the sample (52%) well identified with the IS mechanism and no other mechanism identified with more than 14% of the sample, the primary result is that the late time internal shock mechanism is indicated as the most likely scenario to explain the majority of X-ray flares seen by *Swift*.

A common limitation of several of the mechanisms (though not of IS) and one which generally rules out $\sim 2/3$ of our flares sample (Chapter 5) from consideration is the flare contrast limitation. As discussed previously (see Chapter 5), the RS IC, CM-I and Energy Injection mechanisms all can produce flares only up to a contrast level of several to $\sim$10 times the underlying afterglow flux level. Since the flares sample discussed in Chapter 5 was intentionally selected to contain bright, well-isolated flares (necessary in order to facilitate accurate analysis of several of the characteristics discussed in Chapter 5, such as intra-flare spectral evolution and the temporal characteristics of the flare

GRB	Flare #	RS	FS ClumpsI	FS ClumpsII	AG Onset	Energy Inj	Late IS
050502B	1	N	N	N	N	N	Y
050502B	2	N	N	N	Y	Y	N
050904	1	Y	N	N	N	N	N
060204B	1	N	N	N	N	N	Y
060204B	2	N	N	N	N	N	N
060418	1	N	N	N	N	N	N
060418	2	N	N	N	N	N	N
060526	1	N	N	N	N	N	Y
060526	2	N	N	N	N	N	Y
060607A	1	N	N	N	N	N	N
060607A	2	N	N	N	N	N	Y
060714	1	N	N	N	N	N	Y
060714	2	N	N	N	N	N	Y
060814	1	N	N	N	N	Y	N
060904B	1	N	N	Y	N	N	Y
060929	2	N	N	N	N	N	Y
061121	1	N	N	Y	N	N	Y
070107	1	N	N	N	N	N	Y
070107	2	N	N	N	N	N	N
070318	1	N	N	Y	N	Y	N
Total		1	0	3	1	3	11

Table 6.2 Flares Taxonomy. For each model discussed in Chapter 5, we list whether it can explain each flare in the Flare Sample II based on the criteria expected.

decay), it unavoidably includes some bias against identification of fainter flares. One straightforward way to gain some insight into the degree of this bias is to compare the flux distribution of the flares sample from Chapter 5, which was chosen with an expected flux-bias, to the sample from Chapter 4 in which we explicitly sought to find all apparent flares in the *Swift* archive up to the noted cutoff date (January 24, 2006) and which should, therefore, suffer less from such bias. The comparison of the samples is shown in Figure 6.3. The Chapter 5 sample (black) clearly shows a larger fraction of bursts at higher flux ratios. The fraction of flares in the sample of Chapter 4 at a flux ratio less than 10(6) is 56(47)% while the fraction below the same level in the Chapter 5 sample is 33(28)%. From this alone we might conclude that our sample of Chapter 5 undercounts the faint flares, which are expected to be due to several of the mechanisms explored in this study, by $\sim$ 65-70%. This assumes, however, that the flares sample of Chapter 4 is complete, which certainly should not be expected. If we examine the histogram of flux ratio distributions of Chapter 4, we see that the faintest bin (corresponding to flux ratios between 1.0 and 1.5, where a ratio of 1.0, by definition, is the limit below which flares do not exist) contains no flares. A conservative estimate of the number of flares missed in this lowest bin (and moreover, of the total number of faint flares missed in the Chapter 4 sample) can be obtained by assuming a similar number of flares in the lowest bin as is in the next to lowest bin. This estimates that 17 flares have been missed in this sample, or $\sim$35% of the sample below the flux ratio threshold of 10 which is the relevant level for the previously mentioned flare mechanisms. Combining these two factors, we find a potential bias against finding flares below a flux ratio $\sim$10 of $(0.325^{-1})(0.65^{-1})$ $\sim$5.

While the calculation presented above is not done rigorously, it reminds us to exercise caution in interpreting the results of this analysis, and of those that have come before it, regarding the acceptance or dismissal of particular flare production mechanisms. The intrinsically variable nature of GRB afterglow decays will often make the identification of faint deviations in the lightcurve difficult or ambiguous. Since several mechanisms in the literature are limited to interpreting such faint flares, we should expect to find relatively fewer flares matching the characteristics of these mechanisms than of other mechanisms free of such contrast constraints.

This argument may be particularly salient as regards flares which signal energy injection into the FS of the afterglow. Since these flares are expected to occur at low flux contrast, over long durations and at late times in the afterglow decay when the afterglow decay index α is often poorly constrained, it should not be surprising, even if such flares are a common component of GRB X-ray afterglows, that they are rarely positively identified in the *Swift* archive. It is somewhat interesting to consider the possible statistics of our sample if we attempt to account for the "missing" flares at low contrast level in our sample. If we assume 5$\times$ more flares in our sample below a flux ratio of 10 (presumably the complete true, though partially unobserved, sample as determined from our rough calculation of the bias against low flux flares on the previous page), we can consider a pseudo-sample of 48 flares, 15 of which could be attributed to energy injection, 5 due to AG onset and 5 due to the reverse shock. The remaining mechanisms to which we attributed flares in our sample (Late IS and FS ClumpsII) are not bound by contrast limitations, so we might expect the remaining 23 flares in our "corrected" sample to be split between these mechanisms in the same proportion as seen in the actual sample, namely at a ratio of 11/3, meaning 18 flares due to the Late IS and 5 flares due to FS ClumpsII. Thus, if we imagine a more complete version of the sample presented in Chapter 5, we begin to see much closer agreement between the number of Late IS flares and the number of Energy Injection flares, as should be expected.

6.5 Summary and Conclusions

The IS mechanism has steadily gained support over the last 2 1/2 years as the preferred explanation for late time X-ray flares seen in *Swift*-observed GRBs. Only recently however have broad samples of flares begun to be analyzed with the goal of quantifying the degree to which this preference is warranted. Beginning our discussion with a series of flares observed in a single burst (Chapter 3), then proceeding to discuss the X-ray properties of a large collection of flares (Chapter 4) and finally presenting the first UV through hard X-ray survey of a large collection of flares from multiple bursts, we have made a quantitative presentation of several of the arguments discussed previously in the literature in favor of the IS mechanism.

With more than half the sample (52%) well identified with the IS mechanism and no other mechanism identified with more than 14% of the sample, the primary result is that the late time internal shock mechanism is indicated as the most likely scenario to explain the majority of X-ray flares seen by *Swift*. This notion has been endorsed previously by several authors arguing both on theoretical grounds together with observational generalizations from *Swift* data (Zhang et al. 2006; Lazzati & Perna 2007) and on observational grounds based on analysis of individual or small multiples of flaring GRBs (Burrows et al. 2005b; Falcone et al. 2006; Romano et al. 2006; Butler

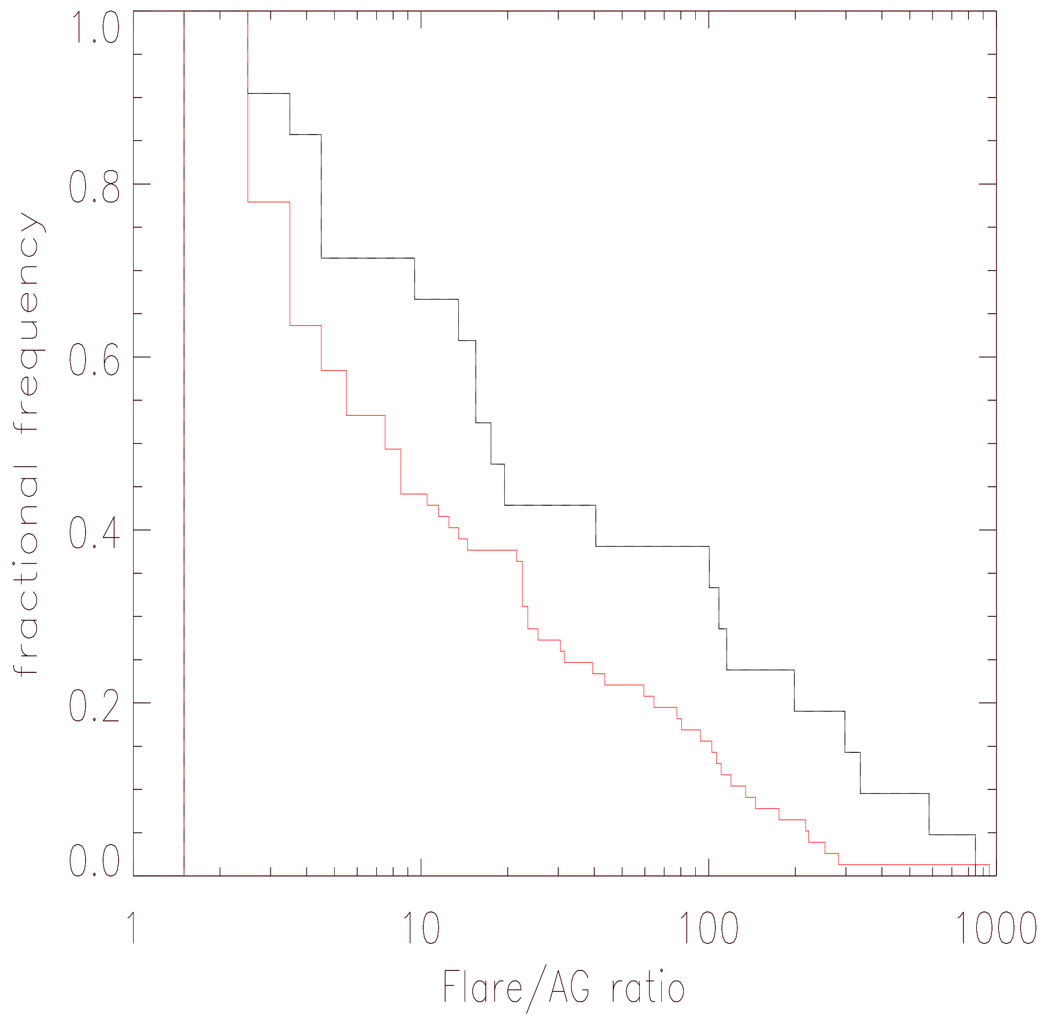

Fig. 6.3 Comparison of Flares Flux Distributions. Cumulative fractional distributions are plotted of the ratio of the peak flux level of the flares to flux level of the underlying afterglow for the flares samples discussed in Chapter 4 (red) and Chapter 5 (black). It can be seen that the sample from Chapter 5 is selected to have a larger fraction of flares that are bright relative to the underlying afterglow as compared to the sample from Chapter 4 which was selected for completeness.

& Kocevski 2007; Chincarini et al. 2007; Krimm et al. 2007; Falcone et al. 2007; Morris et al. 2007). In this work we have expanded on these earlier works in an effort to inventory a large sample of flaring bursts and to categorize the flares present in those bursts according to the allowed emission mechanism responsible for their production.

We have noted that the fractional breakdown of flares attributed to each mechanism presented may under-represent the true importance of those mechanisms expected to produce only faint contrast flares by a factor of several. Even correcting for this bias, however, one arrives at the conclusion that the IS mechanism is the most likely of any mechanism in the literature to account for any individual GRB flare (above or below the *Swift* XRT detection threshold) and we furthermore find that if we make a simplistic correction for the faintness bias of our sample, we find close agreement between the number of late IS flares observed and the number of energy injection events, which should be expected as a natural consequence of early IS flares in the confines of the standard fireball model.

We have discussed the importance of fitting spectral models with intrinsic curvature to X-ray flares, particularly when analyzing flares in the broadband where the observational band is likely to cross one or more of the intrinsic spectral breaks of GRB spectra. We have noted, in agreement with previous work (Butler & Kocevski 2007), that when using such appropriate spectral models, we do not find evidence of evolution of the N_H column density during X-ray flares to within the observational uncertainties. Considering several potential scenarios to explain this observation, we conclude that the large constant N_H values found imply that GRBs are, indeed, associated with local regions of high column density. Furthermore, we find that a clumpy circumburst medium may be compatible with flash ionization of the nearby neutral material by the prompt burst, leaving no neutral material to be ionized by the later flares. We note also, though, that the uncertainties in the data leave open the possibility that X-ray flares are producing ionization below our current detection threshold on a level consistent with a shell-structured circumburst environment. Ionization of a uniform circumburst environment is ruled out by the data.

Finally, we have also investigated the relationship between the Lorentz factor of the prompt burst emission and of late time flares. We find that X-ray flares generally have Lorentz factors about 10% as large as those of the prompt burst emission, though we note also that uncertainties in relating the timescales appropriate to these two phenomena render this value an upper limit, and that the Lorentz factor of flares may be even lower than this relative to the prompt burst phase. For an assumed prompt Γ ~300 this implies Γ_{flares} ~3-30 and agrees with values in the literature (Falcone et al. 2007; Wu et al. 2007) and with values derived in this work from association of early IS flares with later energy injection events in GRB05052B, GRB060418 and GRB060904B. We have furthermore noted that many *Swift* bursts show low level flares ("bumps and wiggles") at delays after IS flares which would be roughly consistent with energy injection events assuming Γ_{flares} ~10. We leave a detailed investigation of this intriguing possibility for future work.

Appendix A

Flare Sample I: XRT Lightcurves

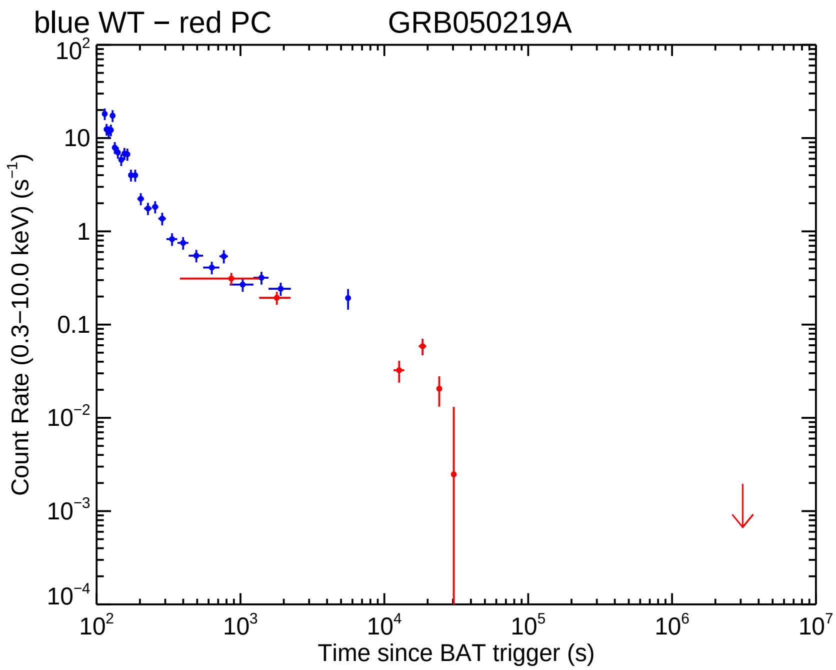

Fig. A.1 GRB050219A

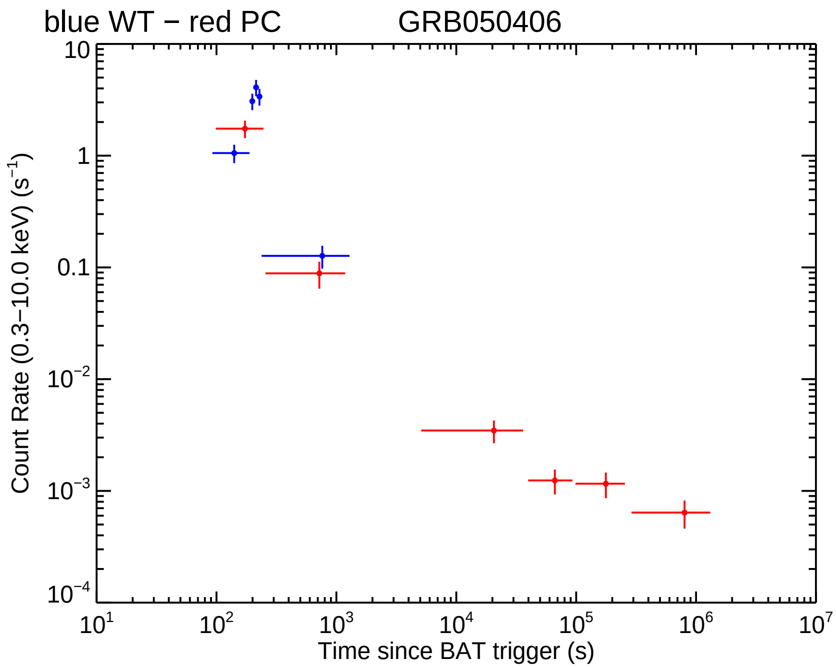

Fig. A.2 GRB050406

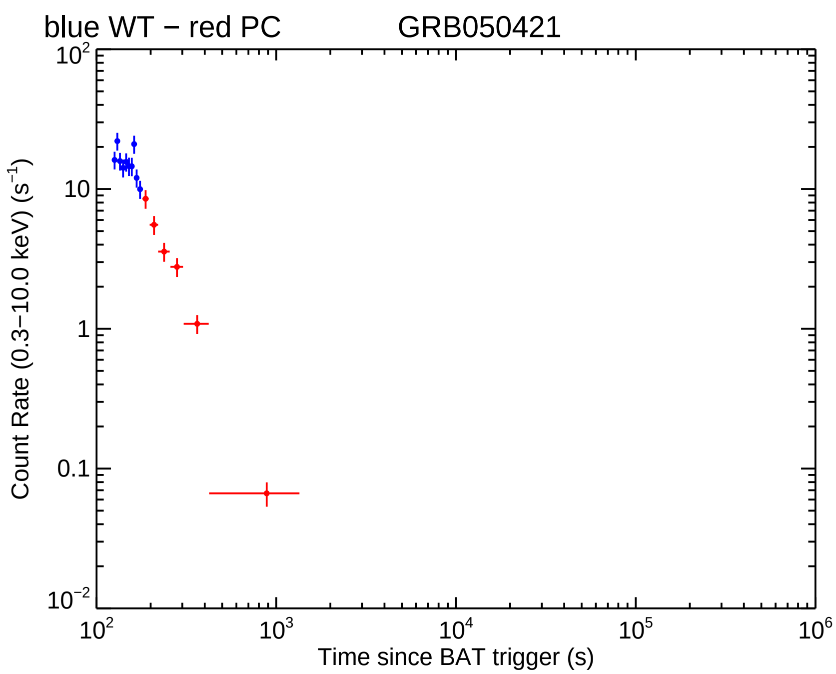

Fig. A.3 GRB050421

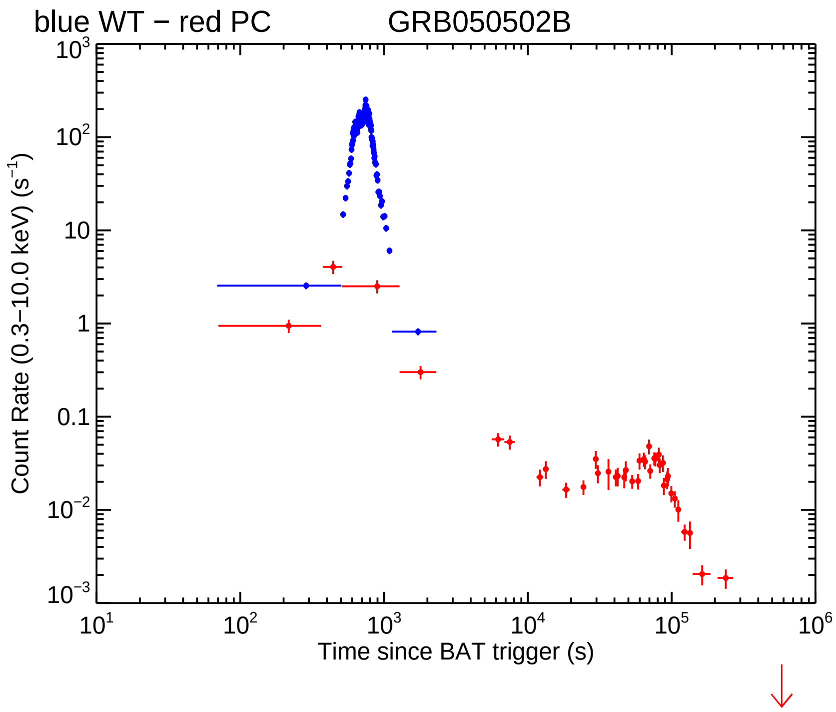

Fig. A.4 GRB050502B

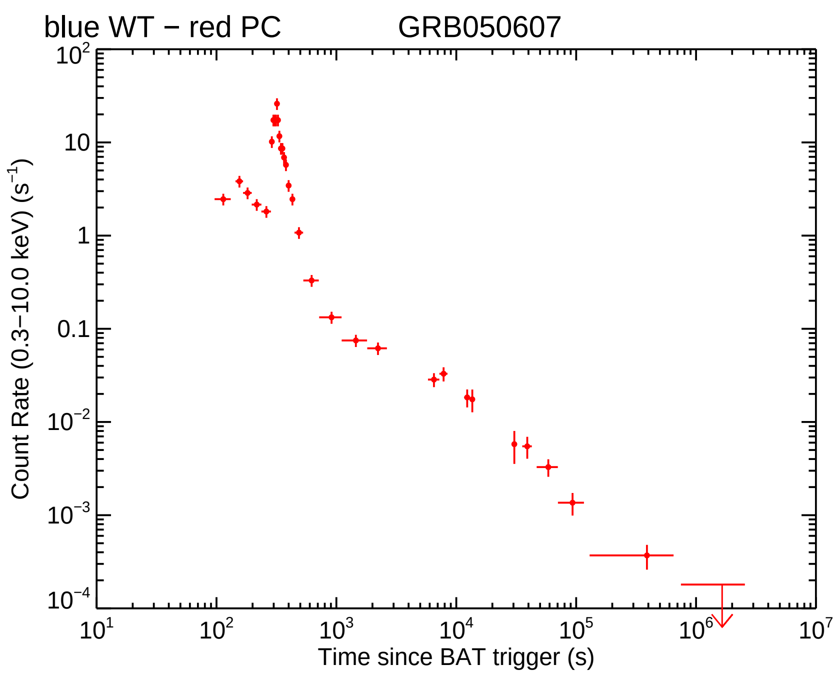

Fig. A.5 GRB050607

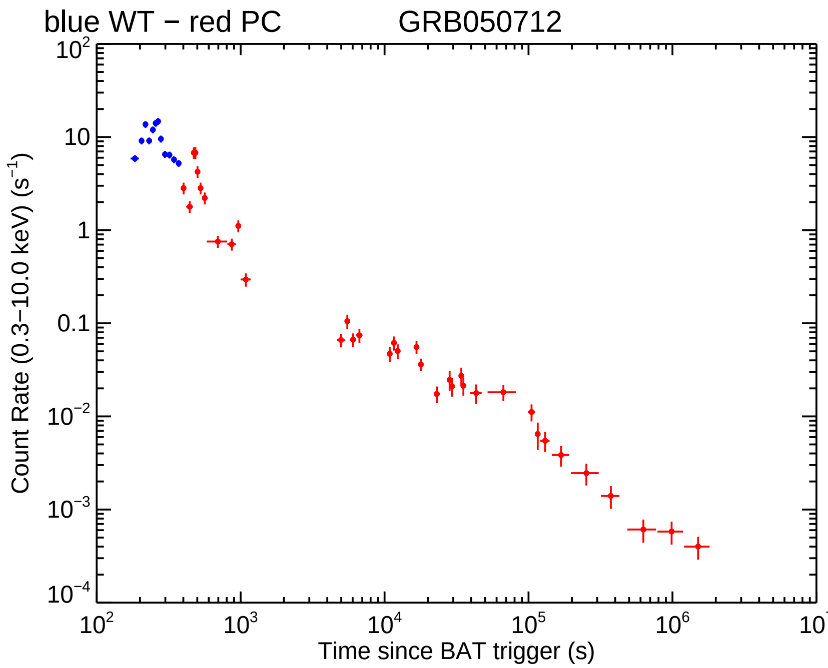

Fig. A.6 GRB050712

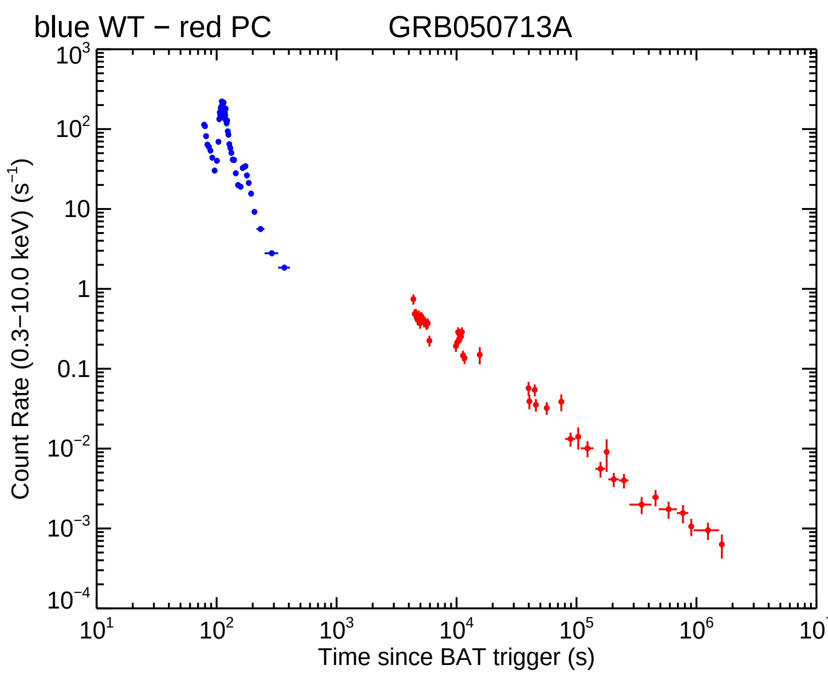

Fig. A.7 GRB050713A

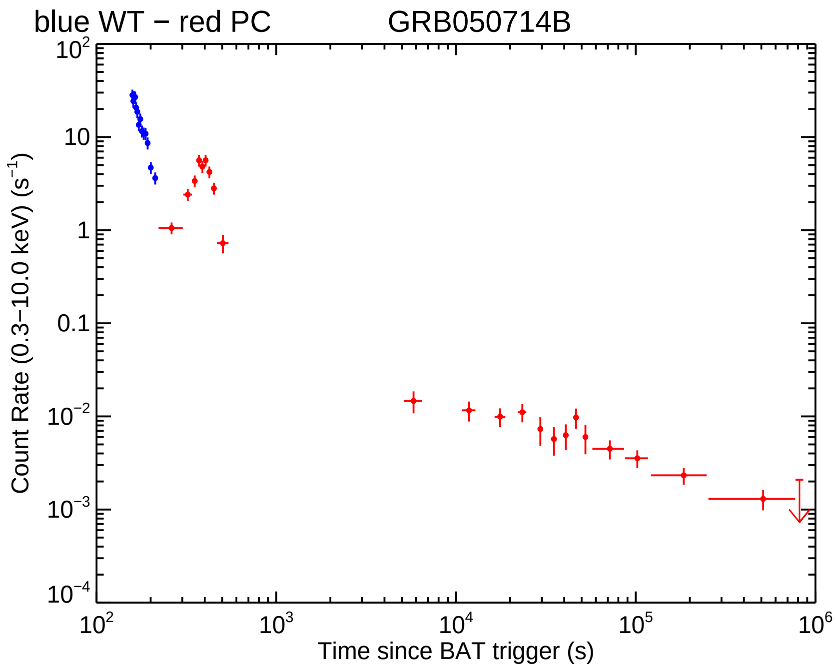

Fig. A.8 GRB050714B

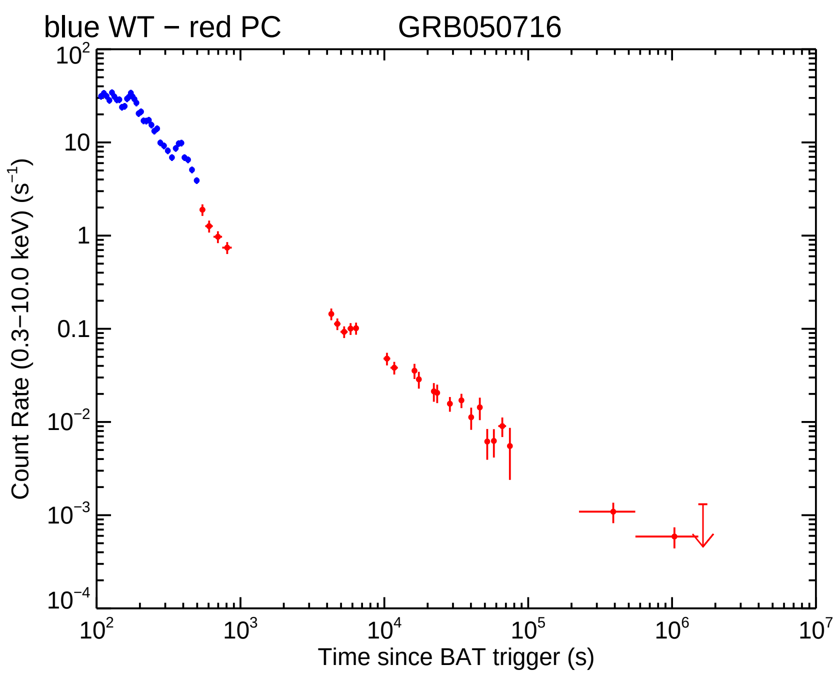

Fig. A.9 GRB050716

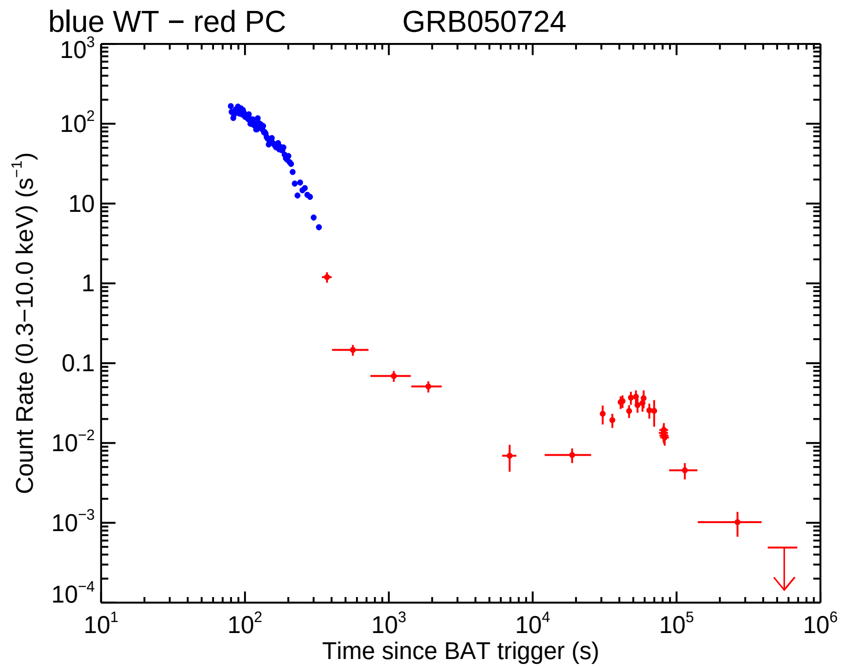

Fig. A.10 GRB050724

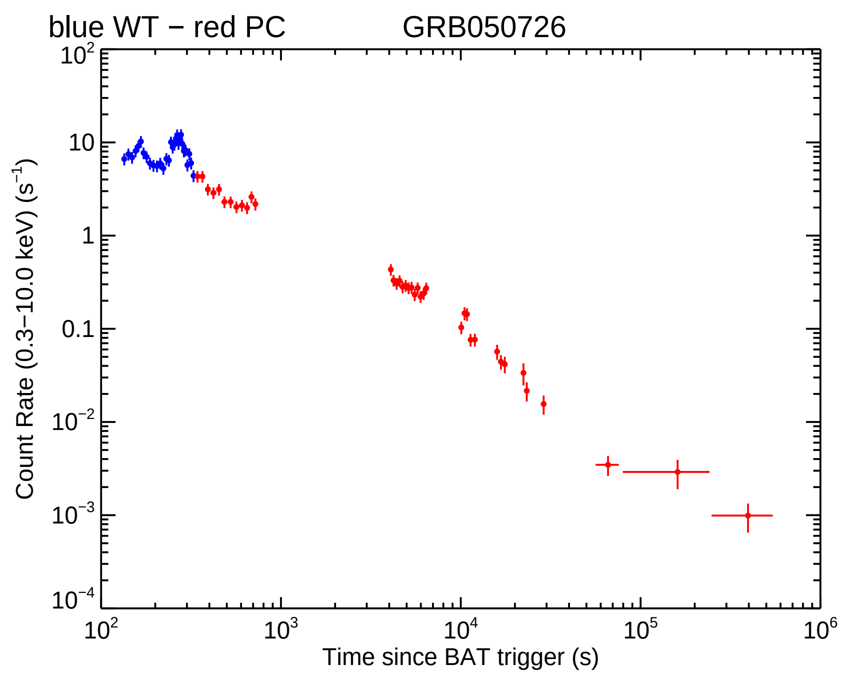

Fig. A.11 GRB050726

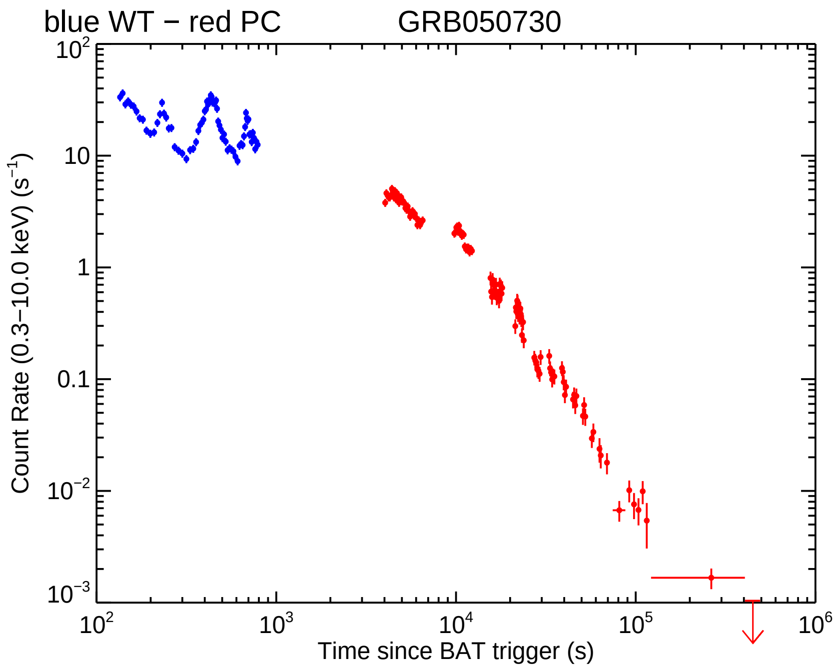

Fig. A.12 GRB050730

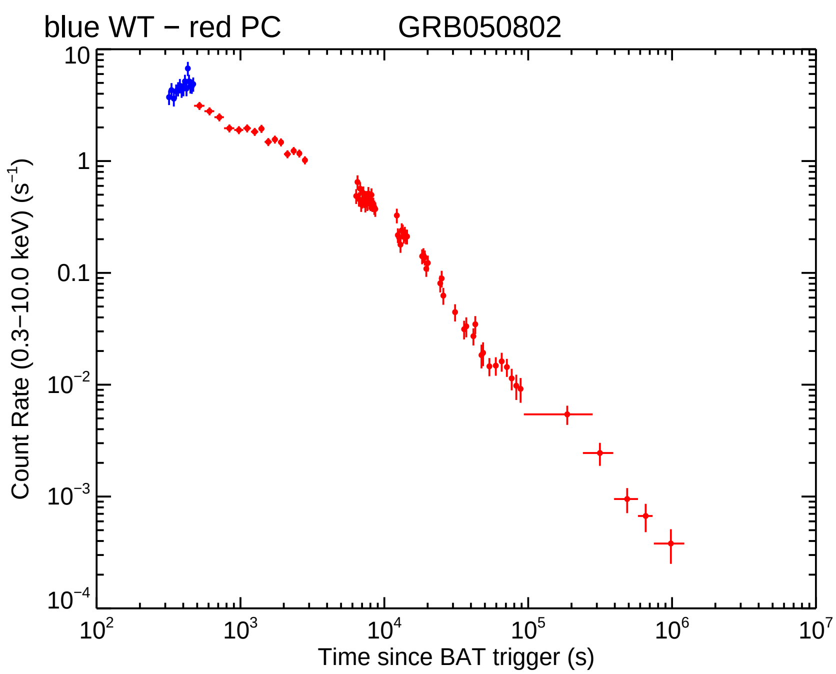

Fig. A.13 GRB050802

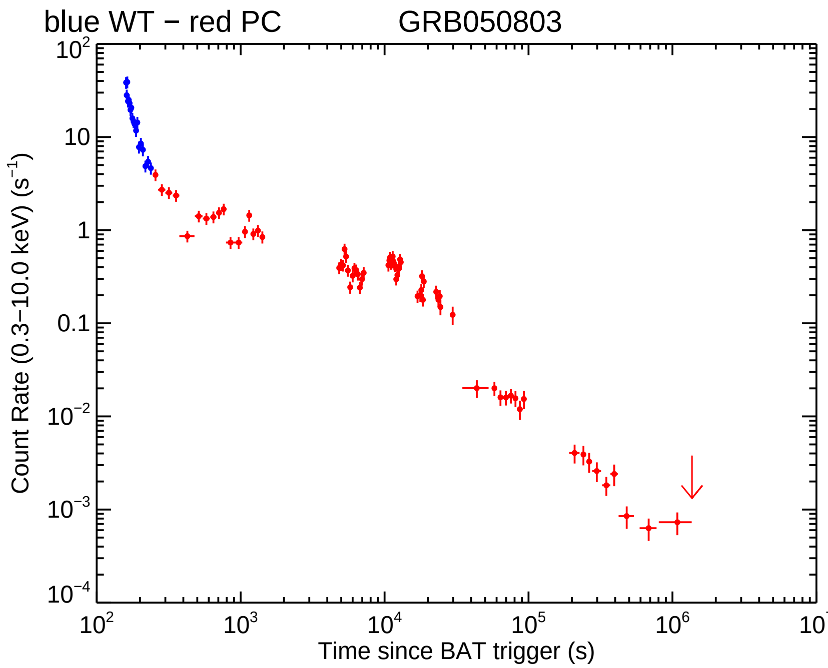

Fig. A.14 GRB050803

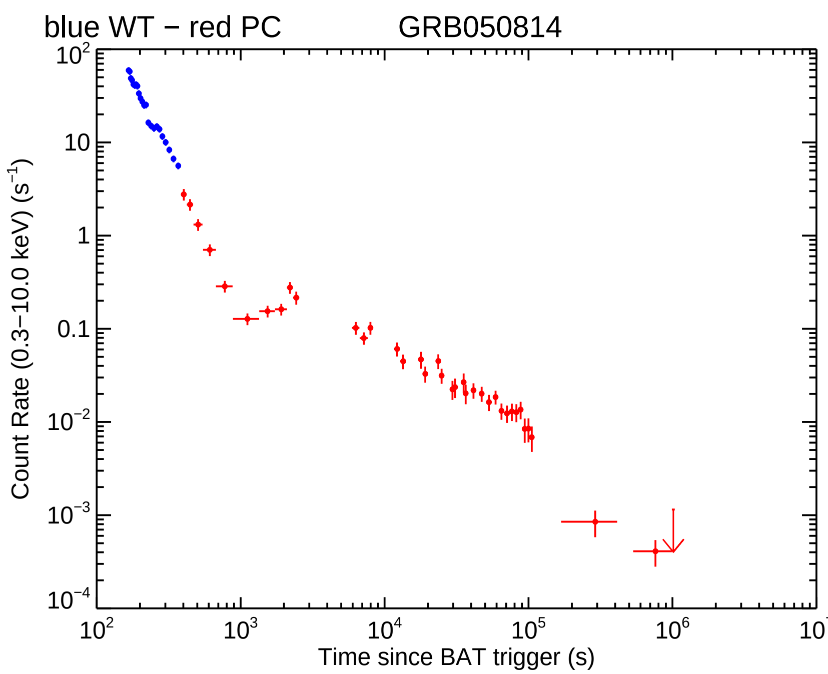

Fig. A.15 GRB050814

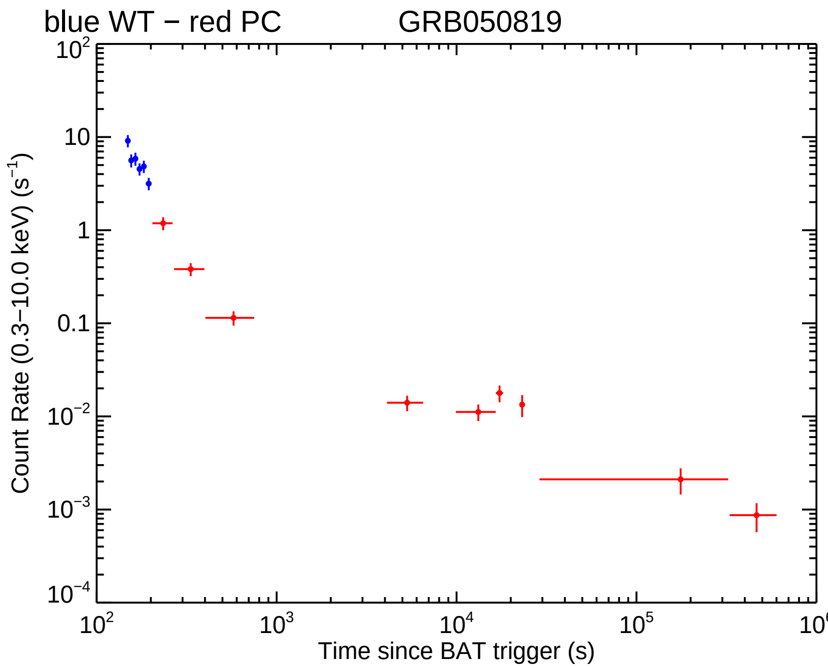

Fig. A.16 GRB050819

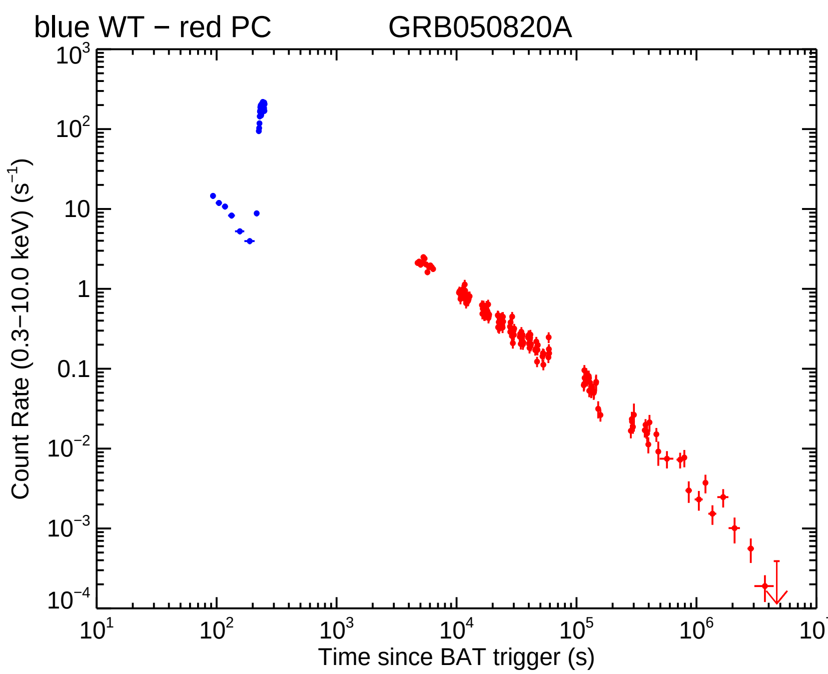

Fig. A.17 GRB050820A

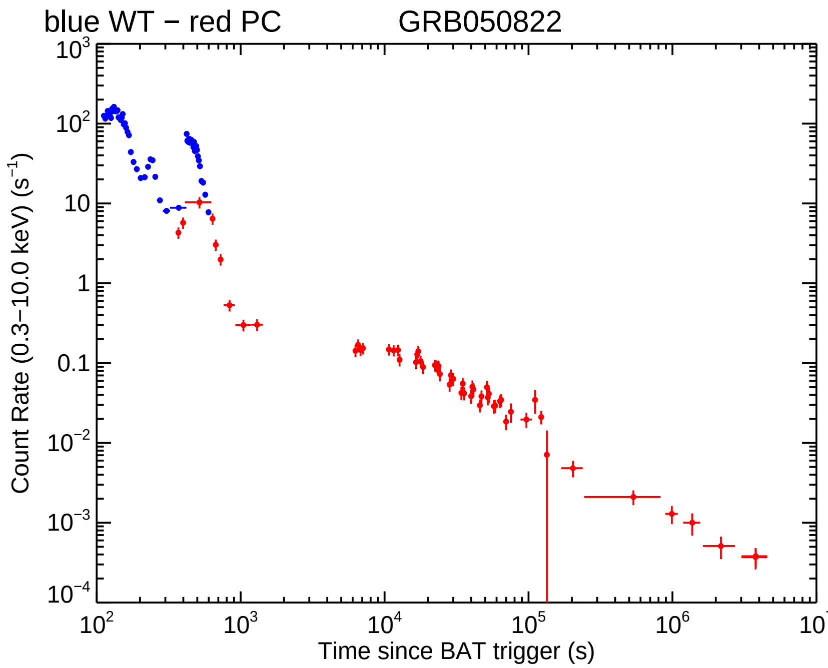

Fig. A.18 GRB050822

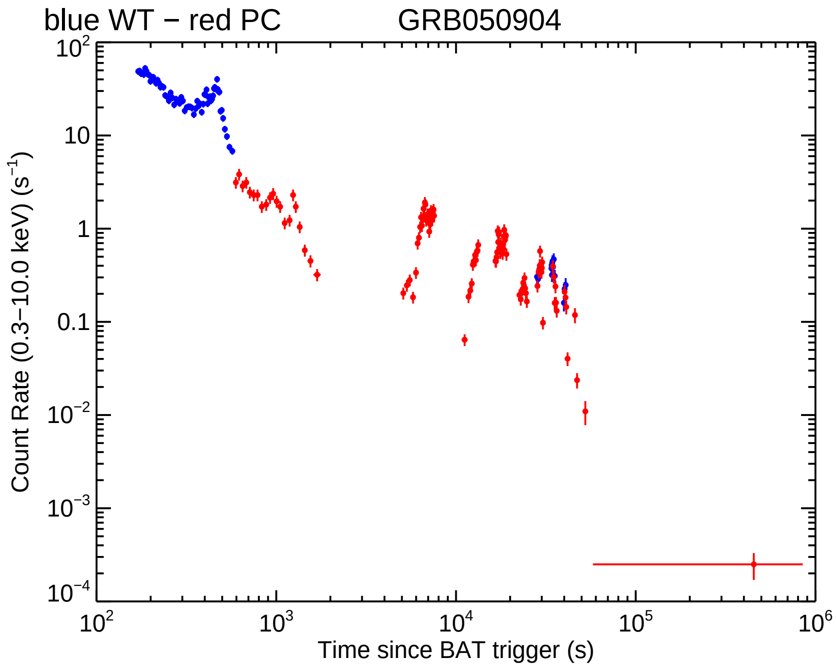

Fig. A.19 GRB050904

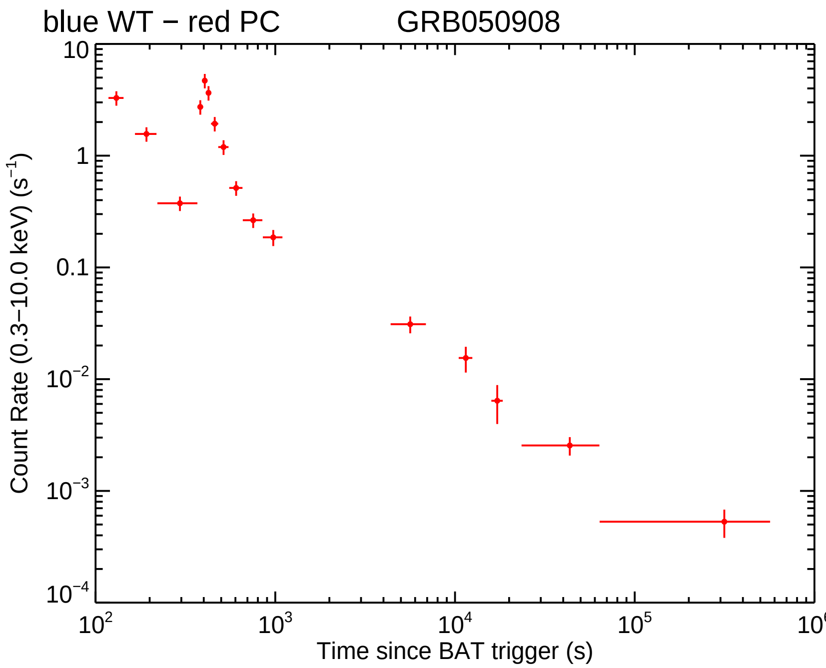

Fig. A.20 GRB050908

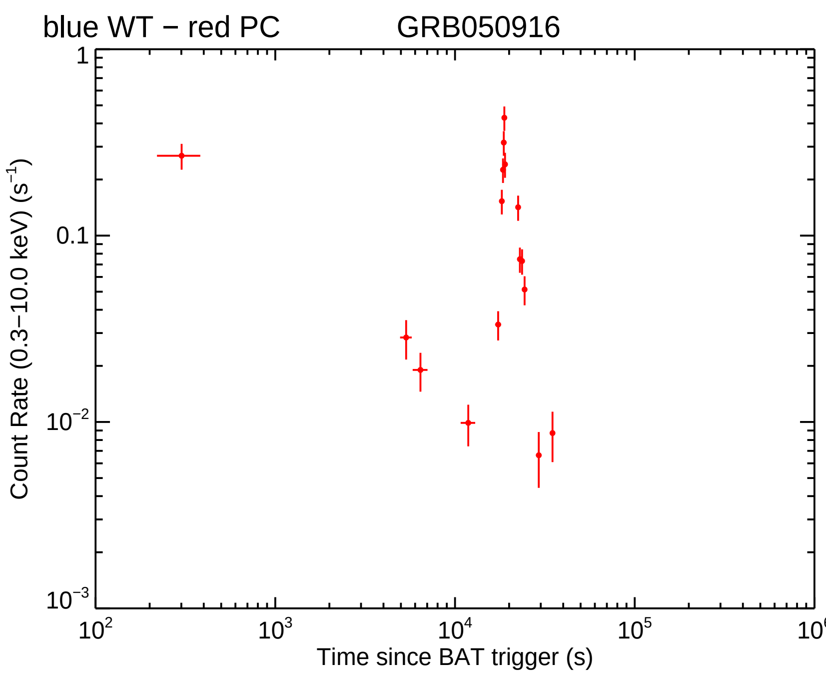

Fig. A.21 GRB050916

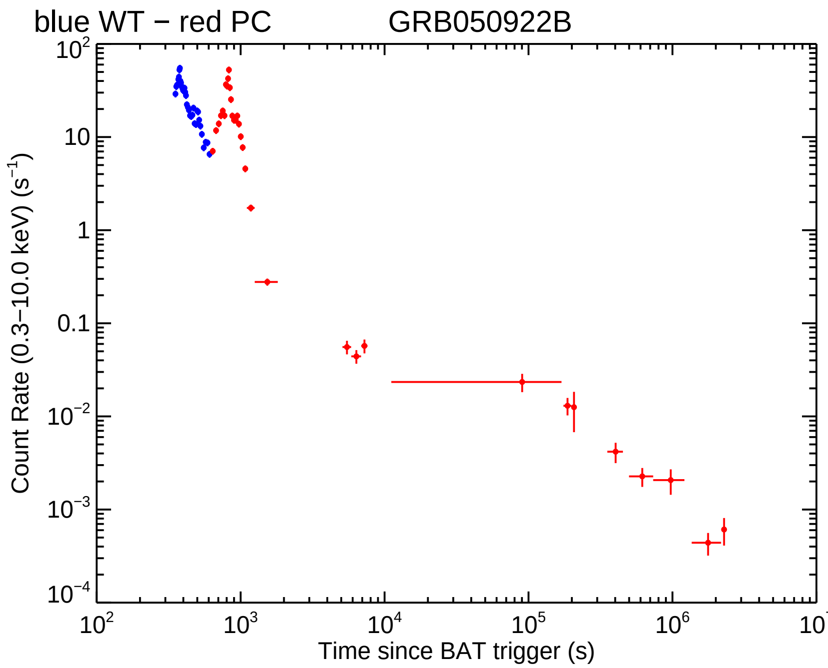

Fig. A.22 GRB050922B

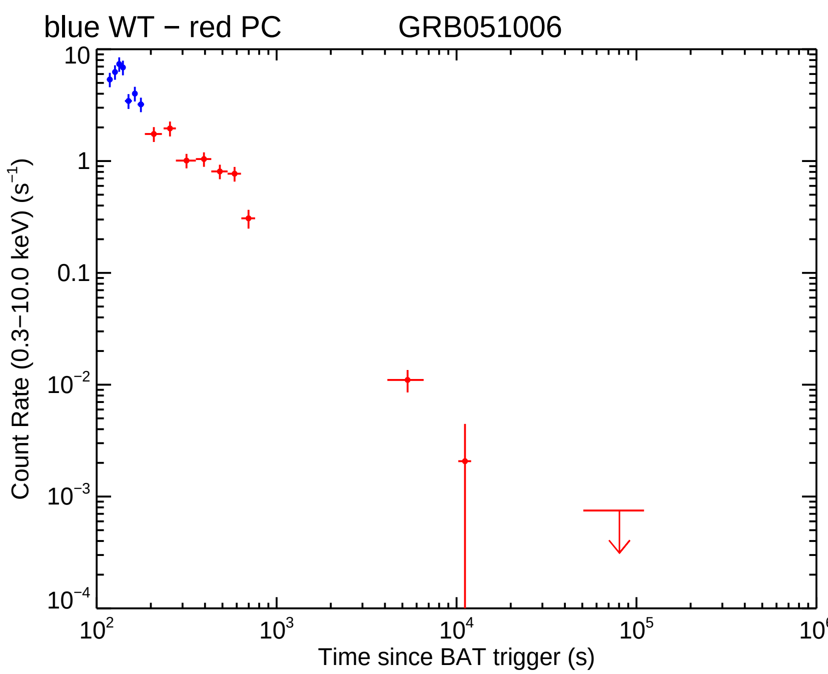

Fig. A.23 GRB051006

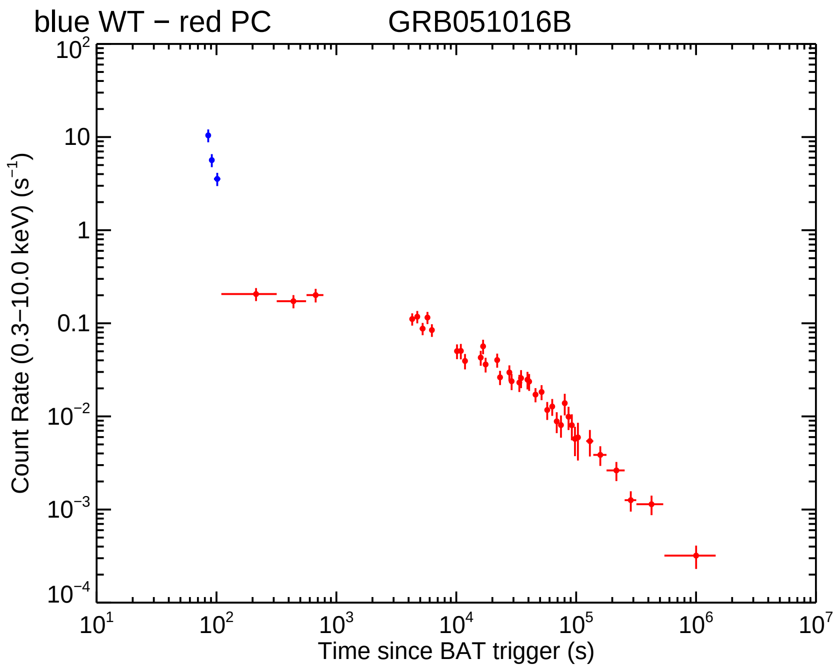

Fig. A.24 GRB051016B

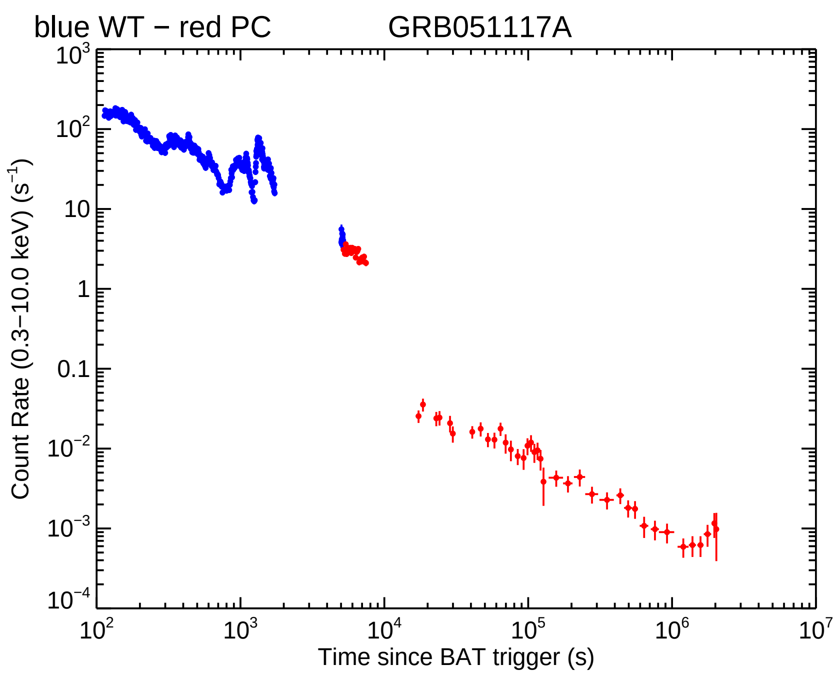

Fig. A.25 GRB051117A

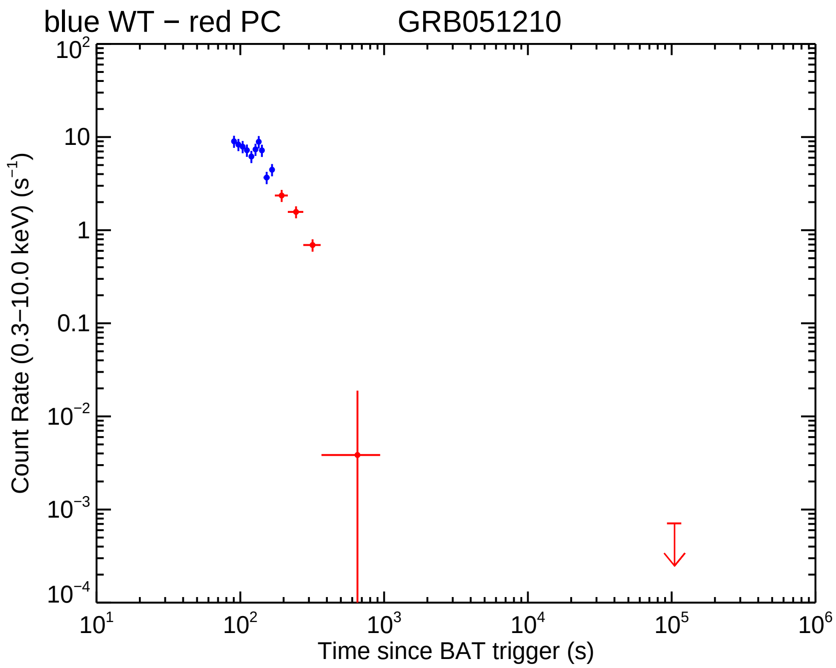

Fig. A.26 GRB051210

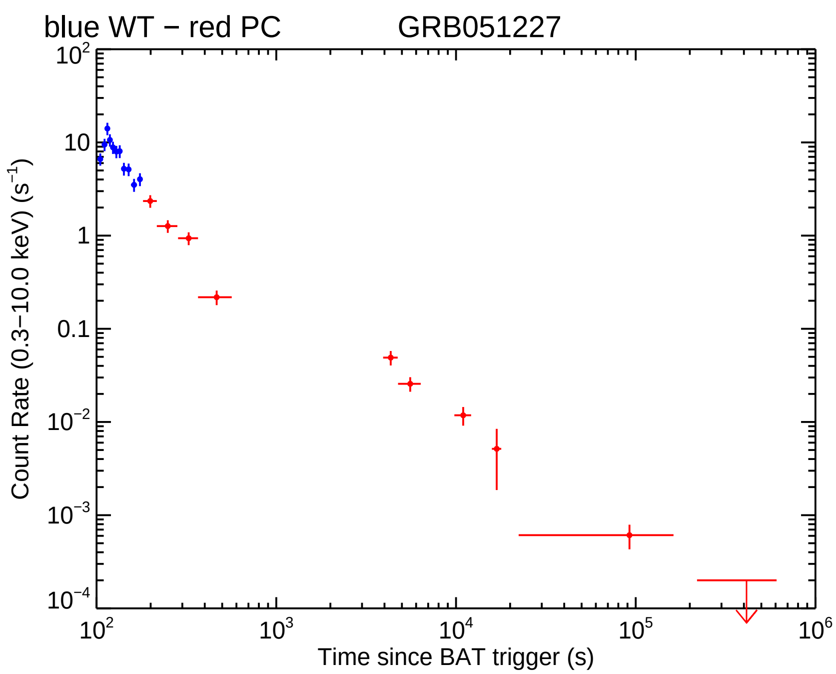

Fig. A.27 GRB051227

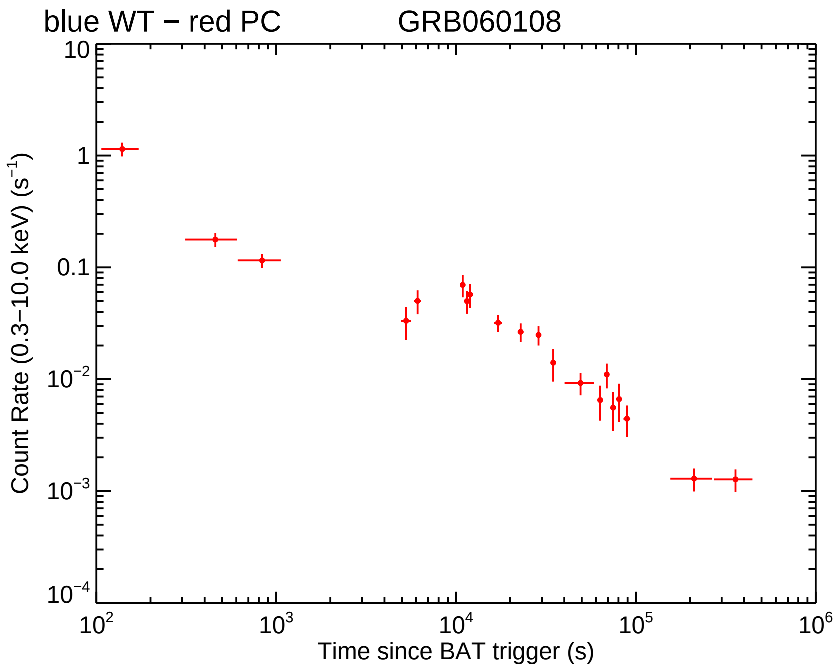

Fig. A.28 GRB060108

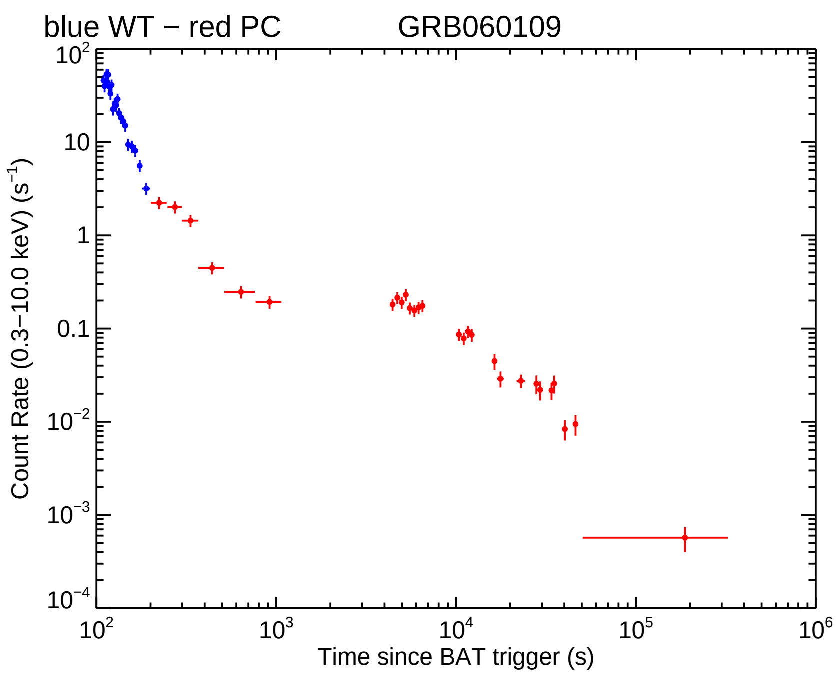

Fig. A.29 GRB060109

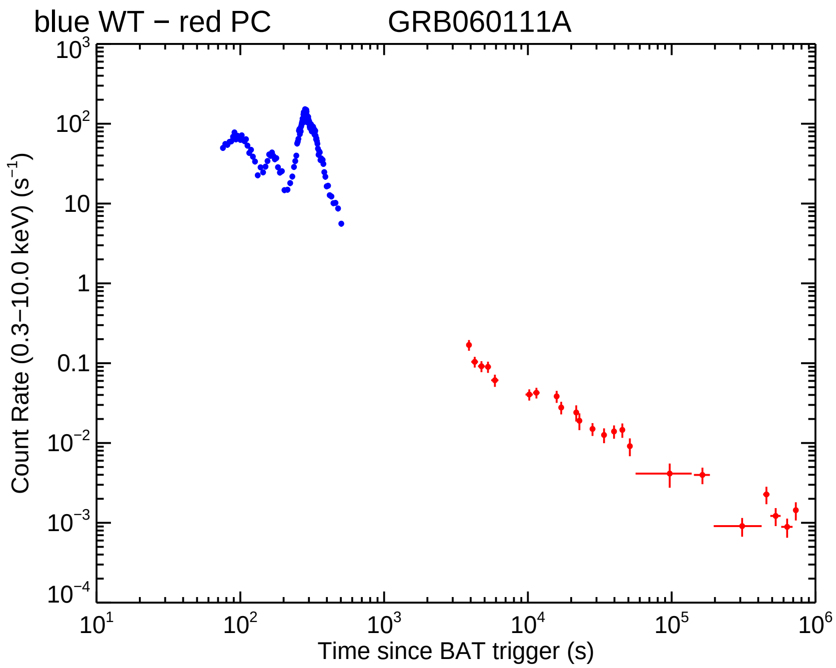

Fig. A.30 GRB060111A

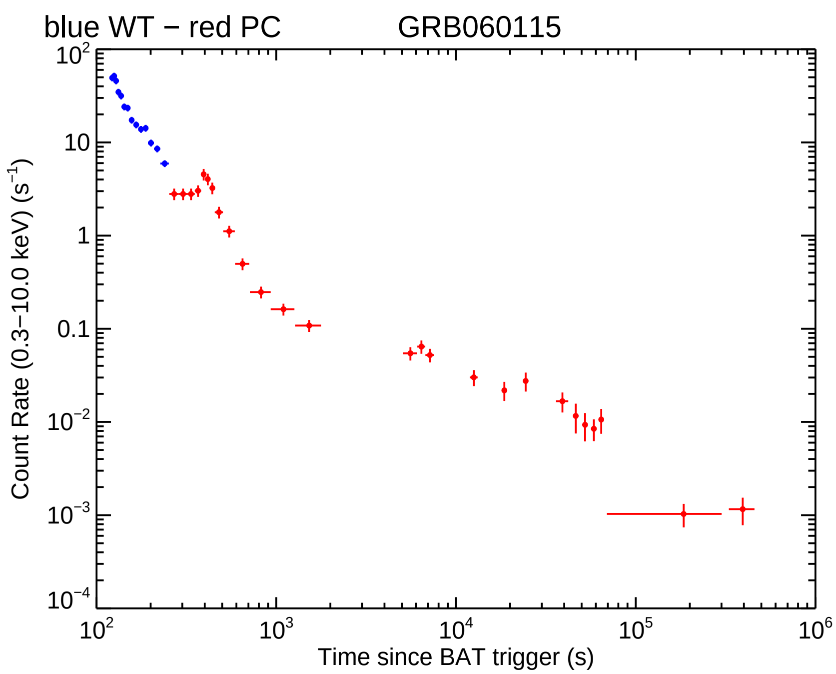

Fig. A.31 GRB060115

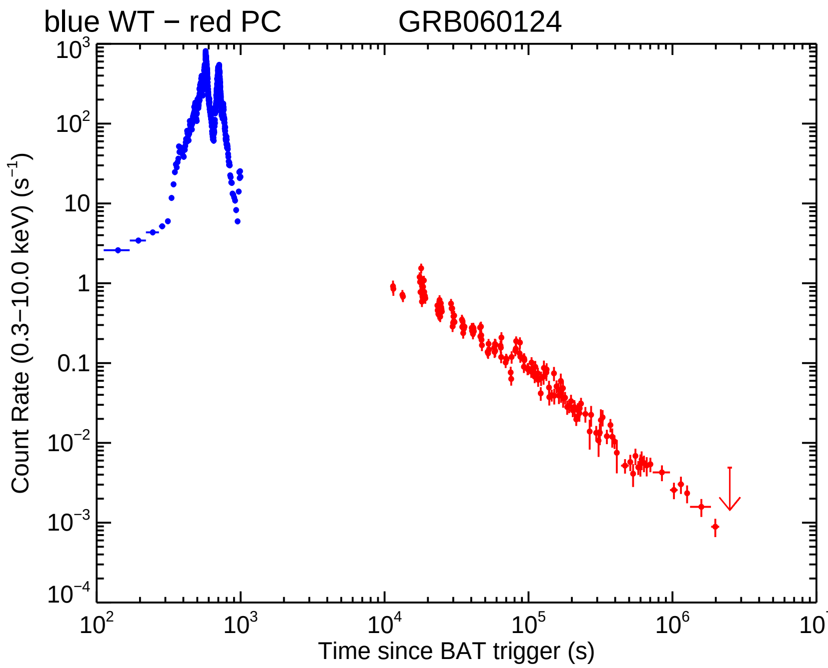

Fig. A.32 GRB060124

Appendix B

Flares Sample II: XRT Lightcurves

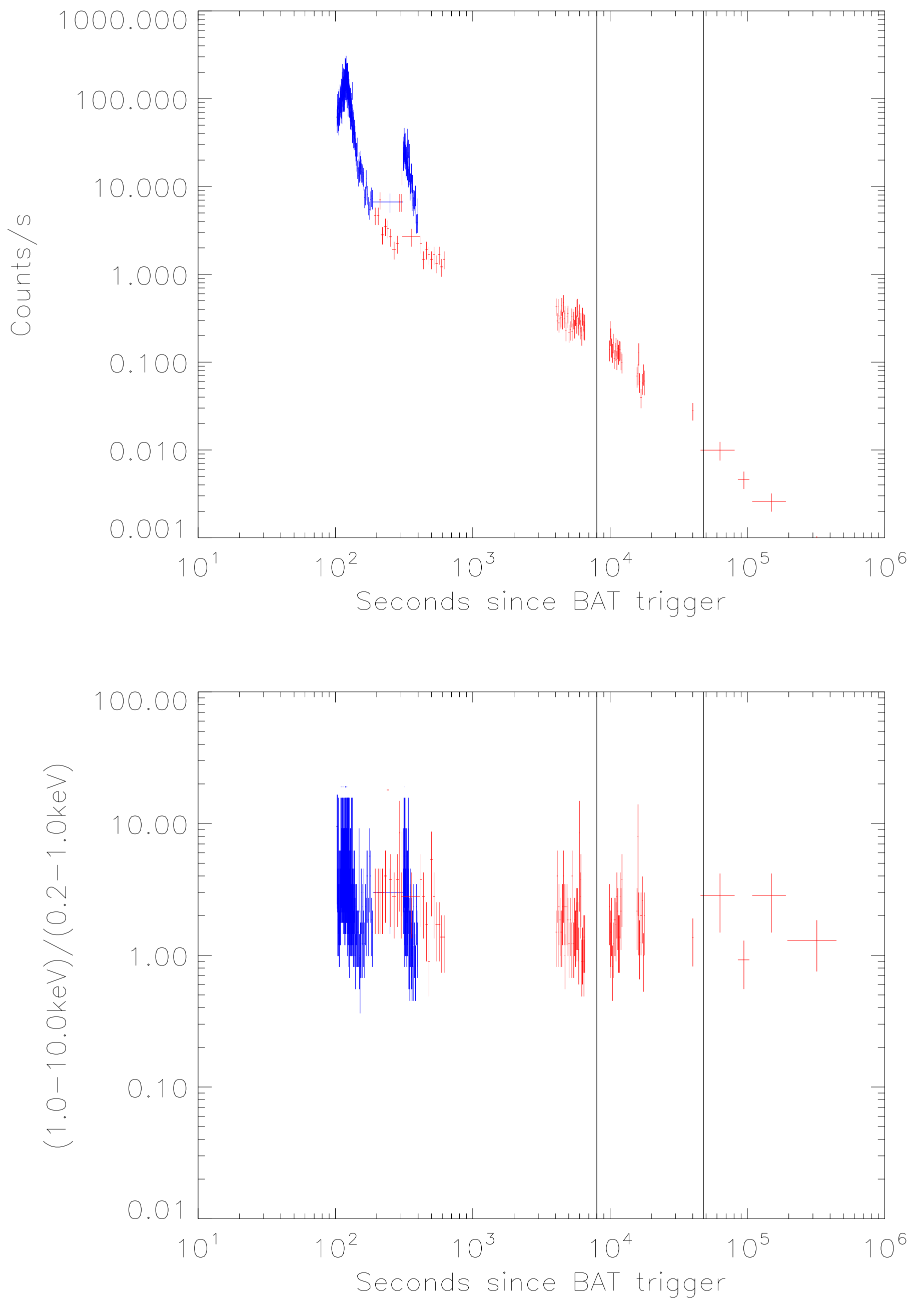

Fig. B.1 GRB060204B

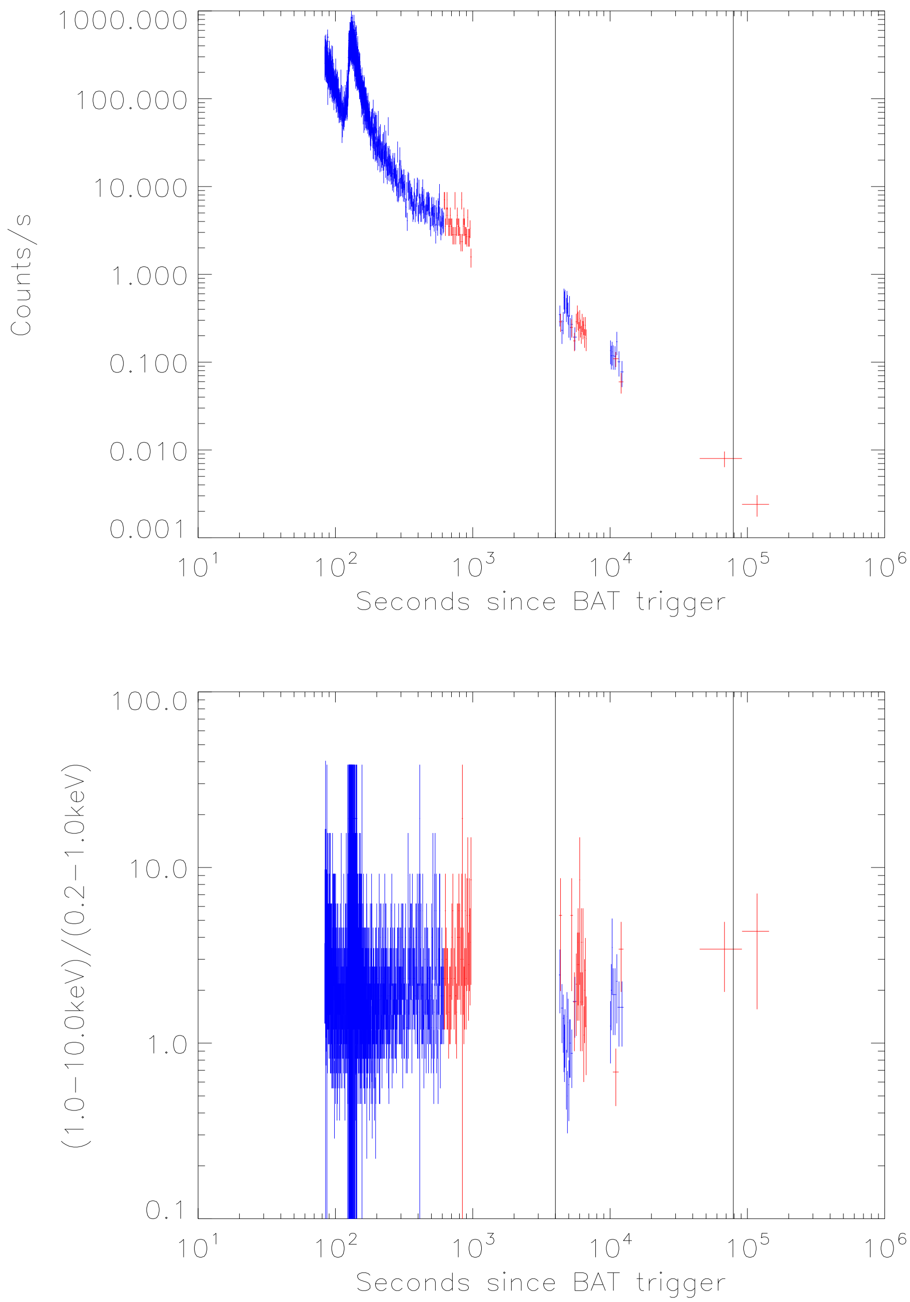

Fig. B.2 GRB060418

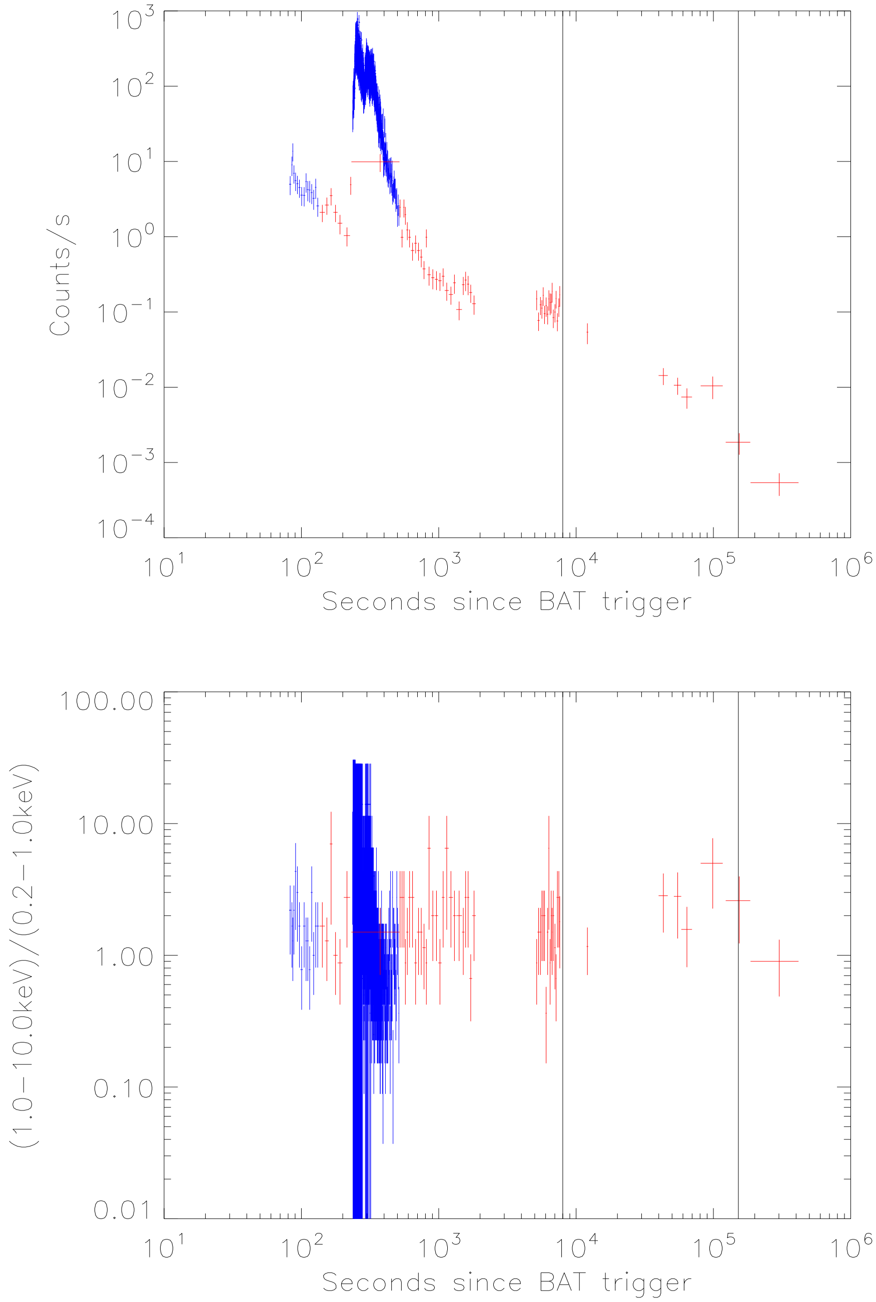

Fig. B.3 GRB060526

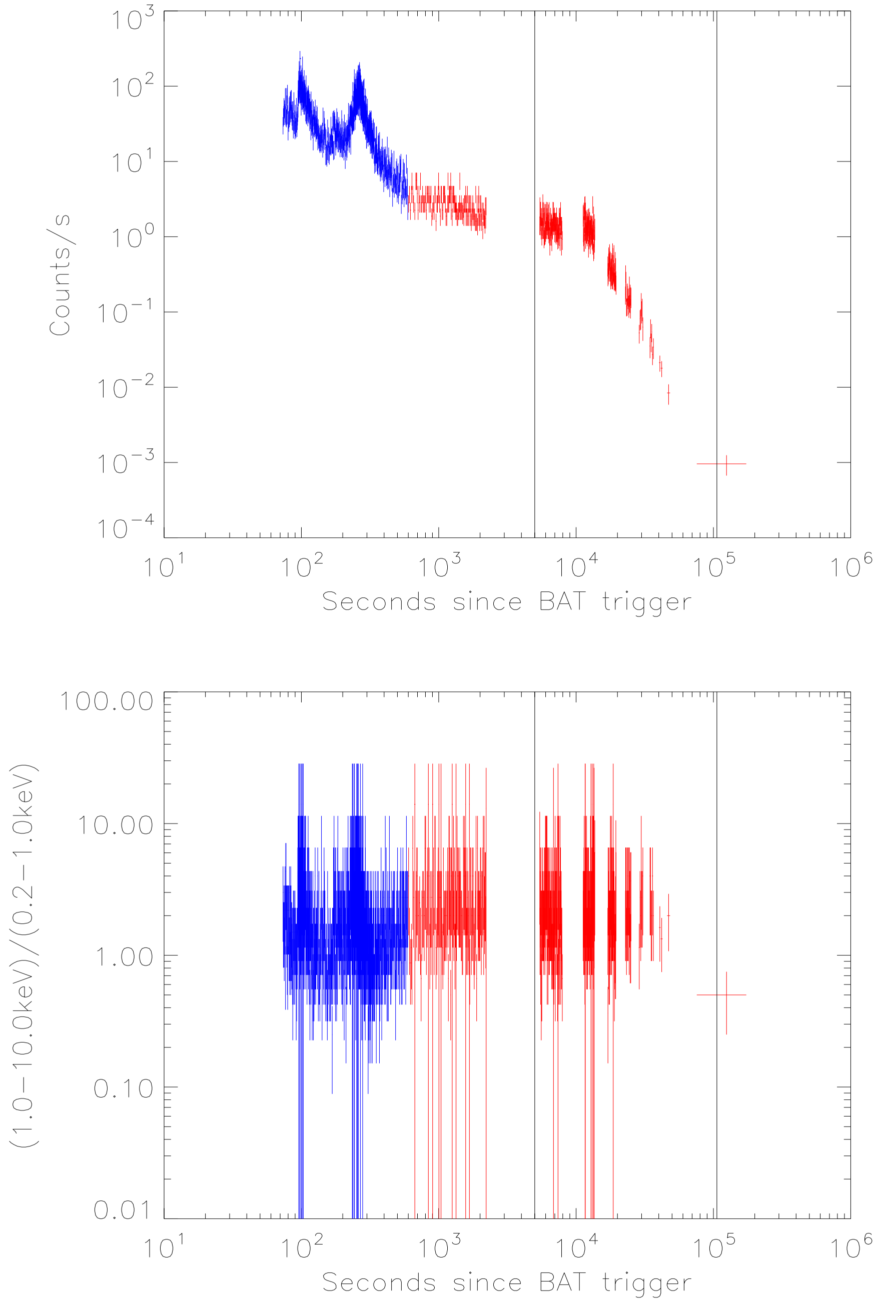

Fig. B.4 GRB060607A

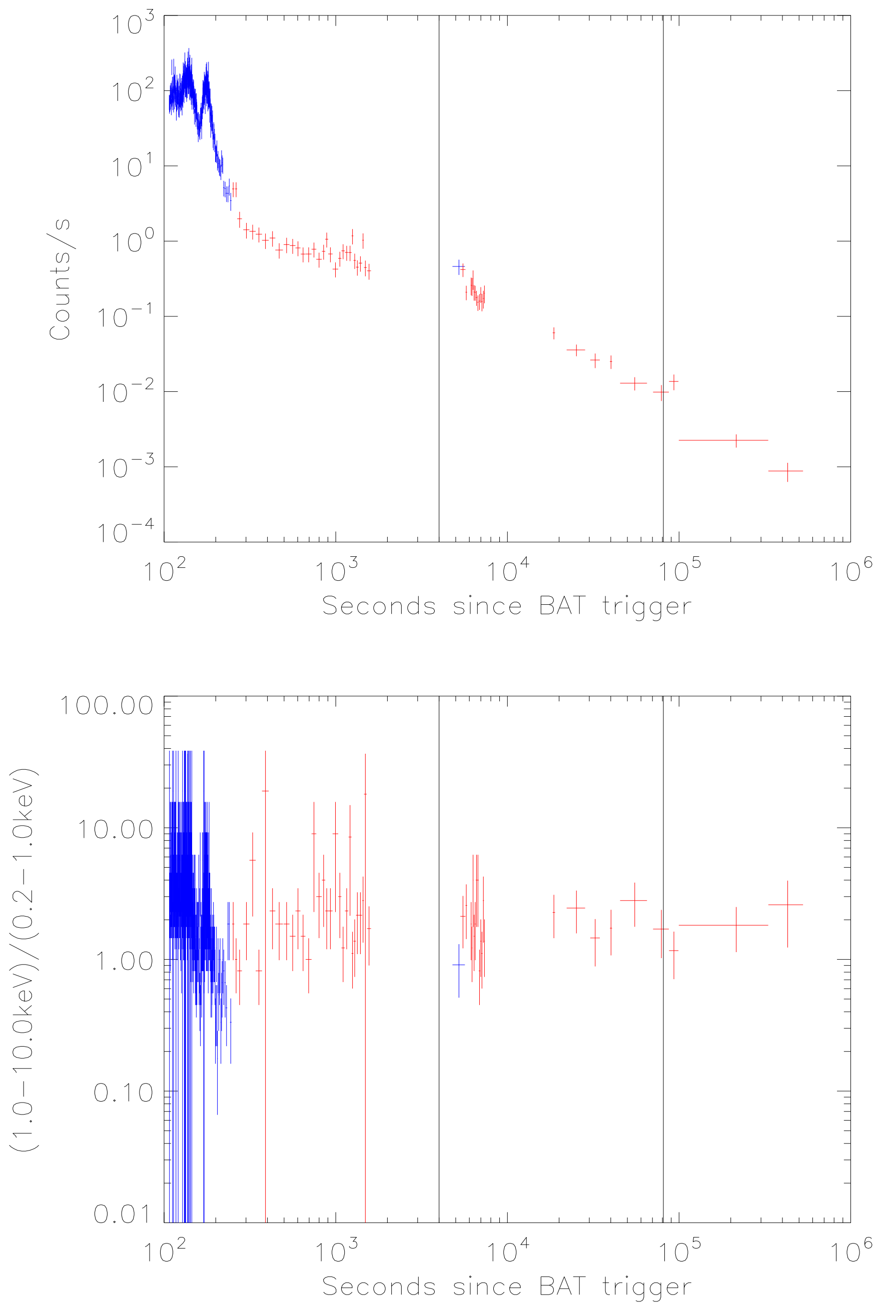

Fig. B.5 GRB060714

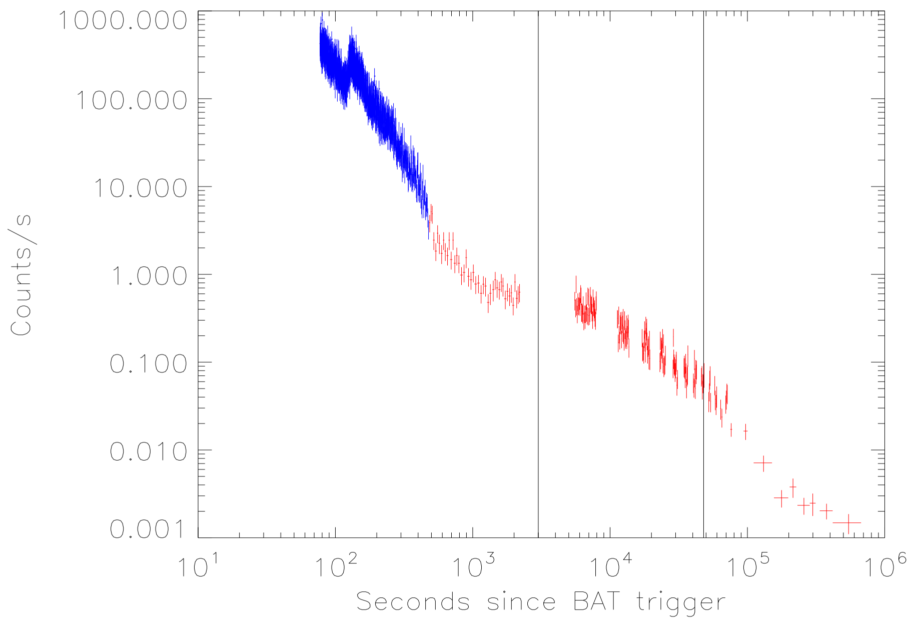

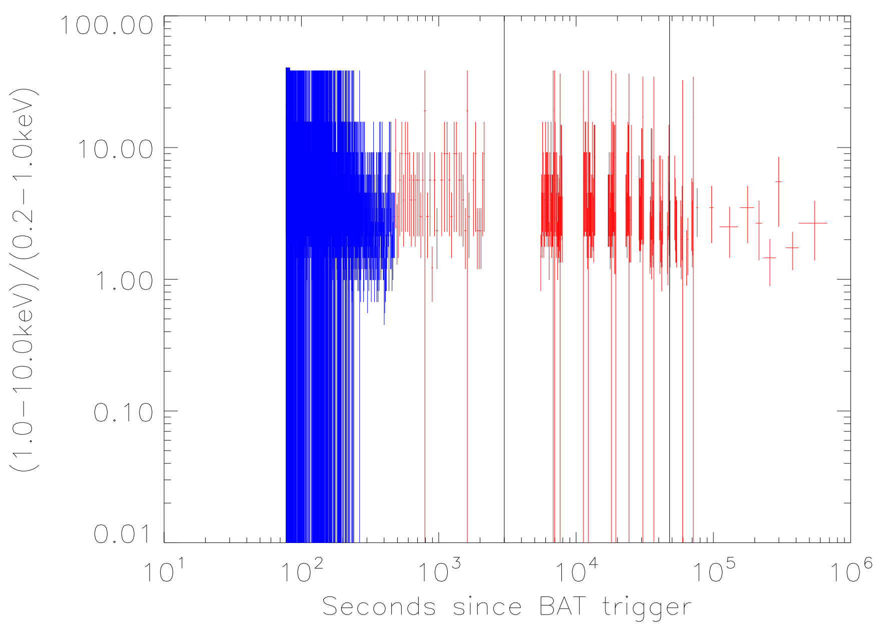

Fig. B.6 GRB060814

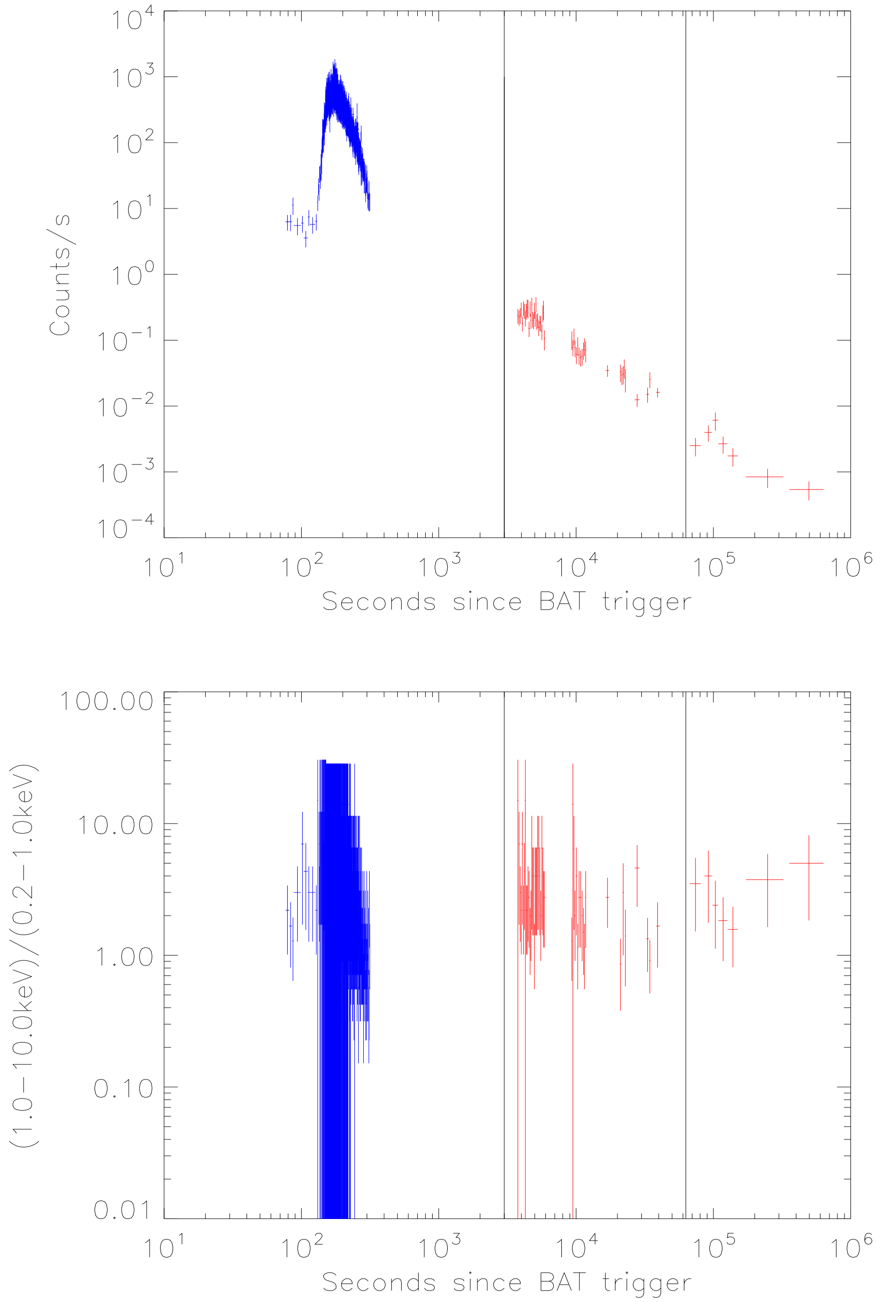

Fig. B.7 GRB060904B

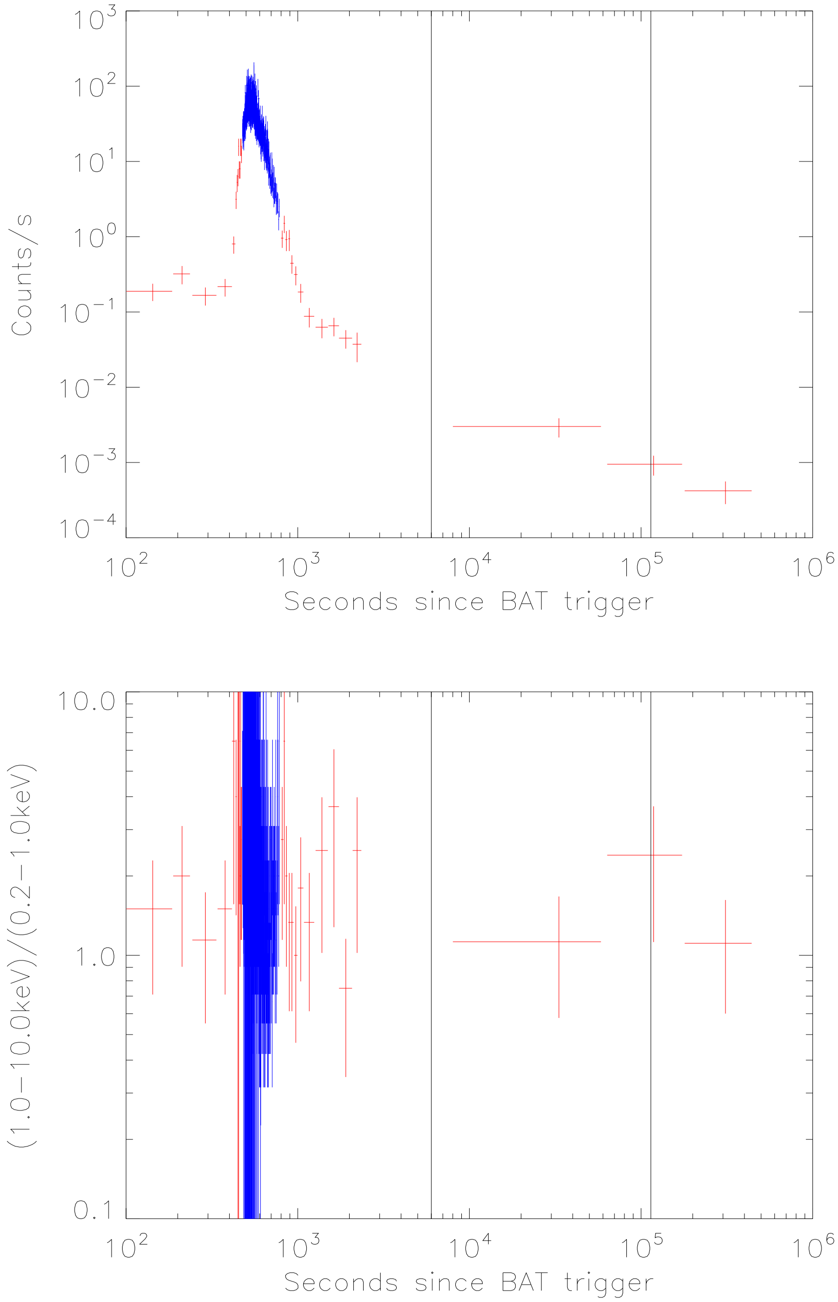

Fig. B.8 GRB060929

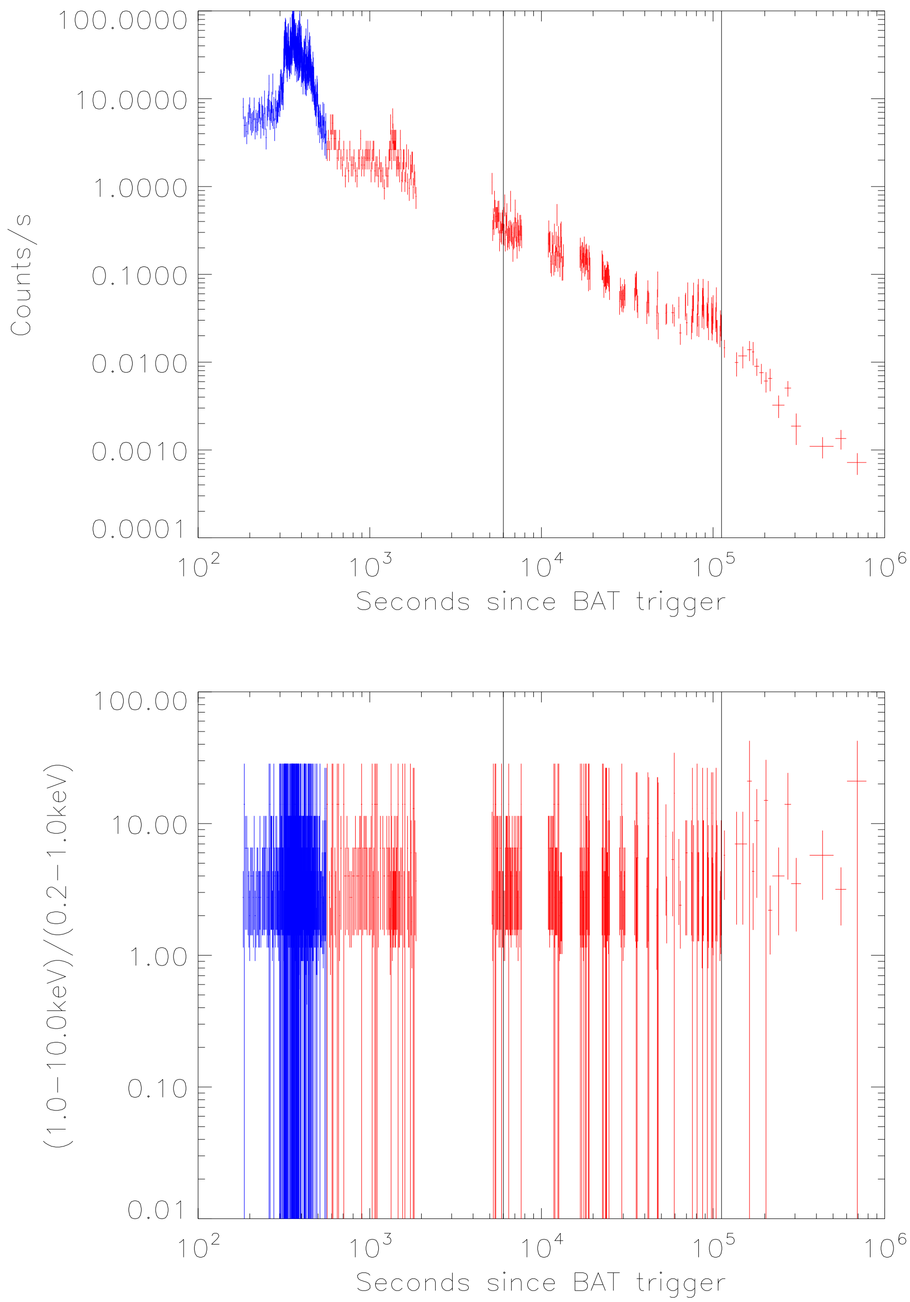

Fig. B.9 GRB070107

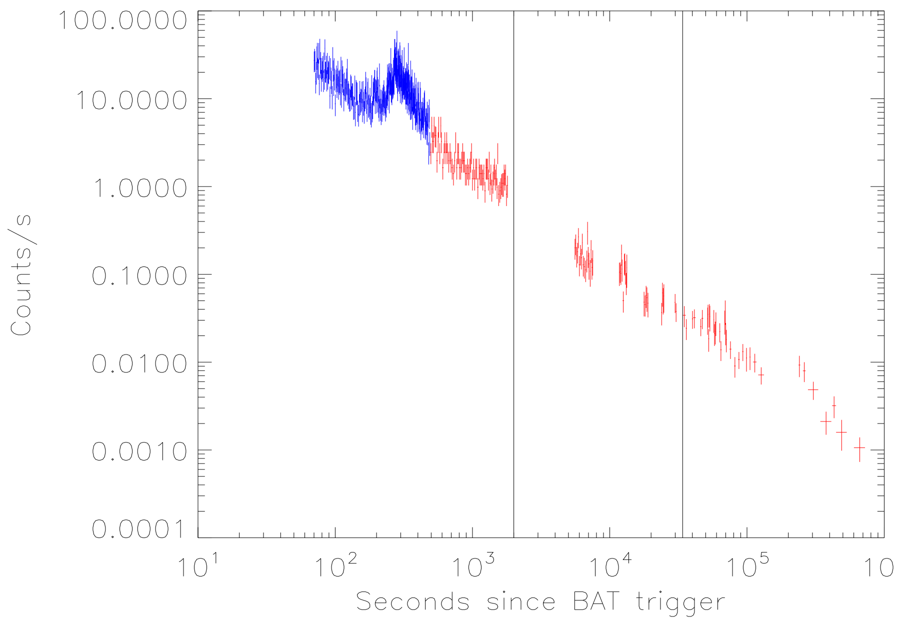

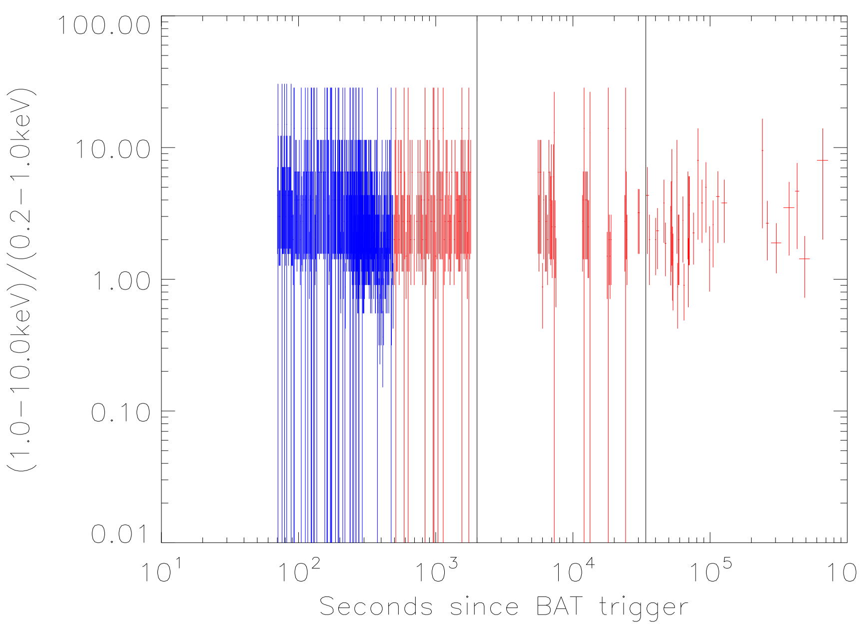

Fig. B.10 GRB070318

Appendix C

BAT Properties of Flaring Bursts

X-ray flares are not detected in the afterglows of all Gamma-Ray Bursts. This fact suggests, though does not imply, that there may be a "flaring class" of GRBs and a "non-flaring class". If such an inherent difference exists in GRBs, i.e., if the detection or non-detection of flares is not simply a question of instrumental detection thresholds, then we might expect to find differences in the population properties of the prompt emission of flaring bursts compared to non-flaring bursts. As an admittedly naive example, one can imagine that if GRBs have an approximately constant energy budget (or at least that the distribution of energy budgets of flaring bursts does not differ from non-flaring bursts), then bursts with significant energy accounted for by late time flaring activity must necessarily have a distribution of prompt energy release shifted to lower values compared to non-flaring bursts. Finding such a difference in properties between FB and NFB would therefore shed light on the nature and production mechanism of flares, but likewise, finding the lack of such differences would raise questions regarding what causes flares to appear in some bursts but not others.

In this appendix, we gather a sample of flaring bursts from the *Swift* archive up to a cutoff date of March 30, 2007 and a complementary sample of non-flaring bursts from the same time period. We produce BAT lightcurves and the standard BAT products created by the *batgrbproduct* script for each burst in each of the two samples. We then search for significant differences in the prompt BAT emission properties of the flaring burst sample compared to the non-flaring burst sample.

C.1 Flaring Classification

We begin by defining "flaring behavior" for the purposes of this investigation. Where other flaring studies undertaken in this thesis have required high fluence levels to ensure sufficient fidelity in spectral fitting, and thus have been limited to samples of a relatively small number of bursts, this study has no such requirement, allowing us to cast many more GRBs into the flaring burst (FB) category than in previous chapters. Nevertheless, it seems reasonable to believe that bursts with more significant flaring behavior (more flares or bigger flares or both) are likely to be more representative of any unique characteristics of FBs as compared to bursts which only show a single small flare. In order to maintain the distinction between the highly flaring bursts and those with only marginal flare detections, we define the following classification scheme: bronze (B) - any GRB exhibiting a 3-σ excess in fluence above the underlying GRB afterglow; silver (S) - multiple 3-σ flares or at least 1 10-σ flare; gold (G) - multiple 10-σ flares or at least 1 30-σ flare; platinum (P) - at least one flare which exceeds 100-σ or multiple 30-σ flares.

We further restrict our classification of a burst as a FB by requiring that flares occur after the prompt emission has ended, as signaled by the beginning of the "rapid-decay" phase, apparent in either the XRT or BAT lightcurves. Imposing this requirement avoids including in the FB sample those GRBs for which BAT triggered on a precursor, the *Swift* slew was completed before the main burst emission began, and the NFIs therefore viewed the prompt emission. In such cases, the XRT would observe pulse-like behavior in its observations, but the pulse-like behavior would be attributed to the prompt emission itself rather than late-time X-ray flares.

To make the determination of signal to noise ratio level for each flare and thus categorize each FB as B,S,G or P, we use a similar technique to that described in Chapter 2 to select flares above the 3-σ threshold for analysis throughout this thesis. In addition, we impose the aforementioned restriction that an emission episode (a pulse) is only qualified as a flare if it occurs during or after the "rapid decay" phase of the burst. We also note that the data sample in this study is extended to all available data at the time of analysis, namely bursts up to GRB070330, inclusive. Finally, we note that we will only include *Swift* triggered GRBs in our sample and only bursts to which *Swift* slewed promptly and for which the XRT localized an afterglow.

C.2 BAT Data Analysis

The majority of BAT parameters which will be discussed in this appendix are drawn directly from the data processing summary report produced by the standard BAT GRB processing script, *batgrbproduct*, using HEADAS version 6.2. Two metrics will be discussed in this appendix which are not generated by the standard processing script, the duration of the first BAT 'pulse' ($P1_N$) and the duration of the first BAT 'episode of emission' ($E1_N$).

$P1_N$ and $E1_N$ are duration measurements of the prompt emission of a GRB, where N describes a flux threshold as a percentage of the peak flux reached by the GRB in the BAT 15-350keV bandpass during the entire duration of the burst. $P1_{90}$, then, is the duration of time that the first BAT pulse that crosses the 90% threshold spends above the 90% threshold before crossing back below the 90% threshold. $E1_{90}$ is the duration of time elapsed from the first crossing of the 90% threshold (ascending) to the last crossing of the 90% threshold (descending). Note that the $E1_N$ measure does not care (or measure) whether or how many times the BAT flux crosses the N% threshold, it only records the duration of time from first to last crossing. We also note a nuance of the $P1_N$ measure, that the different $P1_N$ measures of a particular GRB (e.g., the N=10%, N=50%, N=90% values) may refer to different pulses within the burst if the first pulse of the burst emission is not also the brightest pulse of the burst.

These parameters are intended to provide a measurement of the duration of the prompt emission which is independent of the presence of later flare emission. The standard measures T50, T90, etc, for instance, are a biased measure since late time flares contribute to the total GRB energy output, ranging from typical values of 10% to as much as 50% of the overall energy (see Chapter 4, Falcone et al. (2007)). By focusing on the duration of the first emission pulse alone (as in the P1 statistic) we avoid such bias. In the E1 statistic, one could argue that a late, bright, hard X-ray flare could push the BAT emission back above a given threshold value, however X-ray flares have two properties which make this possibility unlikely; firstly, X-ray flares are generally much softer than the prompt emission (with typical E_{PEAK} values for X-ray flares in the 0.1-10 keV range, while E_{PEAK} of the prompt emission is generally several hundred keV or more); and secondly, X-ray flares, by our definition, occur after the burst afterglow has undergone a rapid decay in overall flux level, typically by ~ 2 orders of magnitude. The combination of these two properties implies that emission in the BAT 15-350 keV band at the time of a late flare is likely to be extremely weak, if at all detectable (indeed, this implication is borne out by the XRT-BAT SEDs of X-ray flares analyzed in Chapter 5, where the BAT flux is typically low).

To build a catalog of $P1_N$ and $E1_N$ values for each burst, we have used the 64ms 4-channel BAT lightcurve products produced by the BAT standard processing script. The 64ms data is highly variable on its intrinsic time resolution, so we smooth the lightcurve to a time resolution of 1 second and create lightcurves in each of the four BAT bands (15-25 keV, 25-50 keV, 50-100 keV, 100-350 keV) and in the total 15-350 keV band. We then create $P1_N$ and $E1_N$ values for each of the five lightcurves produced at nine thresholds ranging from 10% to 90% at increments of 10%.

C.3 Properties

In discussing the properties found from our analysis in the following section, we initially consider our results for the entire flaring sample (bronze-silver-gold-platinum classes) and incrementally refine the sample (silver-gold-platinum, then gold-platinum and finally platinum alone) to look for trends present in our results as we distill the sample to bursts with increasingly higher degrees of flaring activity. Furthermore, approximately 40% of the bursts in our sample have redshift measurements (as do approximately 40% of the bursts in the Swift sample overall), and we will use this subsample to investigate whether trends which may appear in the flaring sample persist in the redshift corrected sample.

C.3.1 Peak Flux Measurement

The peak flux distribution which we discuss in this section is the peak 1 second flux measured in the BAT 15-350 keV band using a powerlaw fit. This value is a standard output product of the *batgrbproduct* processing script, as noted in the previous section. In Figure C.1, we show the distribution of peak flux in the non-flaring sample (in black) and corresponding peak flux distribution of the flaring sample (in red). The four panels correspond to the entire flaring sample, bronze through platinum (upper left panel), the silver through platinum flare sample (upper right panel), the gold-platinum flare sample (lower left panel) and the platinum flare sample alone (lower right panel). While the overall shape of the distributions are similar (both with peak frequency at ~ 1 ph/cm^2/s), the tail of the non-flaring distribution that extends to several tens of ph/cm^2/s is absent from the flaring distribution. The lack of the high flux tail in the flaring distribution becomes more apparent in the more highly distilled flare samples (i.e., the gold-platinum and platinum only samples).

To examine the distributions in a more quantitative way, we plot, in Figure C.2, the fraction of non-flaring bursts that cross a given BAT flux threshold (color coded for various thresholds) versus the fraction of flaring bursts that cross the same BAT threshold. Once again, the 4 panels in the figure represent progressively more refined flaring samples ranging from the full flaring sample in the upper left panel to the platinum flaring sample alone in the lower right panel. We overplot the line x=y for reference. Panels 1-3 of the figure show that non-flaring bursts are more likely than flaring bursts to show bright fluxes in the BAT, where the 'bright' level seems to begin at approximately

2 ph/cm^2/s. The trend is less apparent in the platinum flare-only sample (panel 4) but this is likely due to the small number of bursts in this exclusive sample (8) and the associated large uncertainty.

The figures discussed so far have been presented in observer frame flux units, as is necessary in order to examine the entire sample since redshift measurements are available for only approximately 40% of *Swift* GRBs. There are, however, measured redshifts for 30/67 of the flaring bursts in our sample and for 36/102 of the non-flaring bursts. For this subsample, we can improve the physical significance of the plots shown in Figures C.1 and C.2 by transforming to rest frame flux. Histograms of the flaring and non-flaring bursts, similar to Figure C.1 but now corrected for redshift by scaling the peak flux values by the square of the luminosity distance and also by an additional factor of (1+z) to account for the time dilation effect, are shown in Figure C.3. This figure again uses the 4-panel format, progressing from the full sample (with measured redshifts) in the upper left panel, to the platinum sample alone (with measured redshifts) in the lower right panel. In these redshift corrected histograms, we can see that the apparent lack of high flux objects in the flaring sample, seen previously in Figure C.1, has largely been removed. The non-flaring flux distribution remains peaked at low flux values (approximately 1-5 ph/cm^2/s) as was seen in the sample uncorrected for redshift, but the flaring distribution appears to be more flatly distributed, with a less pronounced peak at low flux levels, particularly when one considers the gold-platinum and platinum only samples.

Figure C.4 shows the redshift corrected figure of non-flaring fraction versus flaring fraction above a given flux threshold. We note that we have scaled the flux threshold values up by a factor of 3 to account for the boost in flux values produced by the redshift correction. The figure shows that after redshift correction, the excess of very bright sources in the non-flaring sample relative to the flaring sample has been removed. In each panel of the figure, all datapoints lie within the expected error of the line of equality with the exception of the datapoint corresponding to flux > 6 ph/cm^2/s, which is likely due to random variation.

C.3.2 $\mathbf{P}_N$ and $\mathbf{E}_N$ Measurement

We now consider the prompt burst duration measures defined previously (see §6.2). Once again using a four panel plot to represent the 4 separate classes of flares, Figure C.5 shows the results of the E_N measure for all bursts in our sample using a time duration of 25s. The figure shows the percentage of all bursts which exceed a duration of 25s at progressively larger flux thresholds, beginning with a flux threshold set at 10% of the peak flux of the burst (represented by the smallest size symbol in the figure) and progressing to a maximum flux threshold set at 90% of the peak flux of the burst (represented by the largest size symbol in the figure). There appears to be a slight excess of flaring bursts at nearly all flux thresholds in all panels except the platinum only sample, where the small number of sources and associated large uncertainties seem to mask any inherent trend.

Figure C.6 shows the P_N measure of all bursts using a time duration of 10s. Here we see a trend for the first pulse of flaring bursts to be longer in duration than that of the non-flaring sample. The trend is apparent in all divisions, but is most obvious in the gold-platinum sample. All four panels show a similar pattern in which the lower threshold datapoints (points corresponding to 10%, 20% and 30% thresholds) show little difference between the flaring and non-flaring sample, mid-level threshold datapoints (points corresponding to 40%, 50% and 60% thresholds) show a significant excess of flaring bursts, and high-level threshold datapoints (points corresponding to 70%, 80% and 90% thresholds) again show little difference between the flaring and non-flaring sample.

As in the peak flux analysis, we can improve these results for the subset of flares for which redshift measurements are available. Figure C.7 shows the redshift corrected E_N plots and Figure C.8 shows the redshift corrected P_N plots. Correcting for redshift removes nearly all traces of the trends seen in the previous figures, which were not corrected for redshift. The redshift corrected P_N plots show that nearly every datapoint now lies within one standard deviation of being on the line of equality. The redshift corrected E_N plots similarly show that most datapoints lie within 1 standard deviation of being on the line of equality except for a small deviation that persists at the highest threshold datapoints, corresponding to the 80% and 90% threshold values. The nature and significance of this small residual excess is still under investigation.

C.4 Discussion

C.4.1 Implications on Flares Production Mechanism

The motivation behind this analysis was to investigate whether inherent differences could be found in the prompt emission of flaring GRBs compared to their non-flaring counterparts. The results of the analysis have shown that apparent trends exist in the observer frame in both the peak flux of the prompt emission (measured in the BAT 15-350 keV band) and in the duration of time spent above a given flux threshold in a particular burst (i.e., a measure of the 'peakyness' of the prompt emission). It has also been shown, however, that these trends largely disappear when a (smaller) sample of bursts with available redshift measurements is analyzed, correcting for the known redshift and thereby presenting the results in the rest frame.

This result implies that the prompt emission of GRBs, at least as it can be parametrized by the peak flux and duration, has no knowledge of or impact upon whether late time X-ray flares will be present in the burst afterglow. This result is somewhat surprising given the large fraction of the total burst energy which has been observed in late time X-ray flares in some bursts, namely up to 50% of the total burst energy (Falcone et al. 2006). Since many X-ray flares are likely due to late time activity of the GRB central engine (as argued earlier in this thesis), one would expect some interplay between the amount of energy released in the prompt emission phase and in the flaring phase. Such interplay is not apparent in our analysis, suggesting either that flares are not associated with central engine activity, or that the phases of central engine activity which produce the prompt emission and which produce the late time X-ray flares are independent. Given the multitude of other pieces of evidence in favor of X-ray flares as products of central engine activity (Burrows et al. 2005b; Falcone et al. 2006; Liang & Zhang 2006; Zhang et al. 2006; Butler & Kocevski 2007; Morris et al. 2007) the latter interpretation is favored.

An alternative view of late time X-ray flare production suggests that flares are due to the interaction of relativistic shells emitted early in the lifetime of the burst but which only interact at late times to produce radiation. In this scenario, one might expect that the presence of late time X-ray flares is more likely in GRBs in which the distribution of Lorentz factors of the expanding shells in the forward shock is relatively broad. Having such a broad distribution of shell Lorentz factors, however, would lower the likelihood of a large numbers of shells interacting rapidly during the early stages of the prompt emission, which is the scenario expected to create an extremely sharp, bright prompt pulse. Such a broad Γ distribution would increase the likelihood of smaller numbers of shells colliding over a longer period of time, producing prompt profiles lower in peak flux but characterized by multiple peaks of somewhat comparable flux. This is the effect that the P_N measure is expected to test, but as the results of the previous section have shown, no such signature is found in the rest frame. Together with arguments against this mechanism due to low efficiency (Ioka et al. 2005; Lazzati & Perna 2007), our results suggest that the majority of flares are not likely to be produced through this mechanism.

C.4.2 Flare-Redshift Relationship

We have found trends in the prompt emission characteristics of flaring GRBs compared to non-flaring GRBs when analyzed in the observer frame but these trends are removed when we consider a redshift corrected subsample of bursts. Furthermore, the nature of the trends in the observer frame data suggests that flaring bursts tend to appear both slightly fainter and slightly longer (by the P_N and E_N measures, see S6.2) than non-flaring bursts. The fact that these trends disappear in the rest frame analysis suggests that flaring GRBs tend to be found at higher redshifts than non-flaring bursts.

To investigate this suggestion, we show, in Figure C.9, the histogram of redshifts for the 36 non-flaring bursts in our sample and overplot the histogram of redshifts of the 30 flaring bursts in our sample. While both the flaring and non-flaring sample show a peak in the distribution at low redshifts, near 1.0, the flaring burst sample also appears to show a secondary peak in the distribution at redshift ~ 3 which is absent from, or at least suppressed, in the non-flaring sample. The flaring sample distribution also appears to have a better populated tail to very high redshifts (above 4.5) compared to the non-flaring sample. The mean and median of the non-flaring sample are z=1.7 and z=1.5 respectively with a standard deviation of 1.4 while the mean and median of the flaring sample are z=2.6 and z=2.7 respectively with a standard deviation of 1.7. The overall sample mean and median are z=2.1 and z=2.0 respectively, with a standard deviation of 1.6, in agreement with the overall *Swift* redshift distribution found in previous studies (z=2.6, Jakobsson et al. (2006b)).

The large values of the standard deviation of each of the samples makes a simple comparison of means $\pm 1\ \sigma$ rather unrevealing. So we turn to the Kolmogorov-Smirnov (KS) test. The KS D value found for these two samples is 0.35 with an associated probability that the two redshift samples are drawn from the same distribution of 0.027. This suggests reasonable confidence (just less than 3-σ) that the apparent bias for bursts in our flaring sample to occur at higher redshifts relative to non-flaring bursts is real. It merits notice here that in previous work by Falcone et al. (2007) (also Chapter 4), the redshift distribution of a smaller sample of flaring bursts (33 bursts encompassing roughly the first year of *Swift* data, 11 of which had measured redshifts) was analyzed and found to be consistent with the published overall *Swift* GRB redshift value of z=2.65. We have analyzed those 11 flaring bursts with redshifts together with 20 non-flaring bursts from the same time period (up to January, 2006) using the KS test and find a KS D value of 0.37 for a probability that the two redshift samples are drawn from the same distribution of 0.21, confirming the result from this previous study that, based on the data sample used, it could not be ruled out that both the flaring and non-flaring redshift samples had been drawn from the same distribution. It is only by using a larger sample of redshifts that a significant difference between the two samples can be claimed.

Having shown that there is an apparent bias for flaring bursts to be found at higher redshifts than non-flaring bursts, the question naturally follows whether a relation can be found between the characteristics of flaring bursts and the redshift of the burst. We will not consider in detail the possible reasons for such a relationship here (there are several, the most obvious of which is simple time dilation effects shifting prompt emission pulses to late enough times to be observed by the *Swift* NFIs after slewing, though this simple effect seems unlikely to be able to explain all flares observed) but rather will simply speculate that a relationship may exist between the degree of flaring activity observed in the *Swift* XRT lightcurve of GRBs and the redshift of the GRB. We proceed to suggest several speculative forms that such a relation might take and test each to see whether a well constrained relation exists.

We begin with the rather natural assumption that later flares and larger flares are both indicative of larger redshifts. As a measure of the flare time we use the intersection of a powerlaw fit to the rising portion of the flare with a powerlaw fit to the underlying afterglow present beneath the flare (for details of this fitting process see Chapter 2). As a measure of the size or magnitude of the flare, we use the signal to noise level of the flare, defined as $\frac{P_{tot}-P_{ag}}{\sqrt{P_{ag}}}$ where P_{tot} is the total events collected during the time period of the flare and P_{ag} is the projected number of events expected from the afterglow at the time of the flare as determined by the powerlaw fit to the afterglow data (for details of the calculation methodology see Chapter 2). We then test the simple relation $z \propto \sum T_{fl_{start}} * \frac{S_{fl}}{N_{fl}}$ where z is redshift, $T_{fl_{start}}$ is the flare start time and $\frac{S_{fl}}{N_{fl}}$ is the signal to noise ratio of the flare. Figure C.10 shows the fit of this function to all bursts from the first year of *Swift* data with measured redshifts. The figure shows a log-linear relationship between the redshift and the computed flare function, with a Pearson correlation coefficient of 0.77 between the redshift and the logarithm of the flare function.

Through inspection of the outliers to the fit, we make the observation that the time of the flares is more significant to the redshift relationship than the size of the flare, and therefore we modify the flare function to $z \propto \log \sum T^2_{fl_{start}} * \frac{S_{fl}}{N_{fl}}$. The result of this modified function is shown in Figure C.11. We again see a log-linear relationship and the Pearson correlation coefficient has improved to 0.82. The slope of the relation is 0.86. Through further inspection of the outliers to this fit, we make the observation that the importance of the size of the flare to the flare function should be mitigated by the initial BAT burst peak flux (this seems a reasonable assumption and is essentially a coarse method of normalizing the size of the flares to the prompt burst brightness). The newly modified function is $z \propto \log \sum T^2_{fl_{start}} * \frac{S_{fl}}{N_{fl}} * \frac{1}{P_{BAT}}$ where P_{BAT} is the peak flux of the prompt BAT emission measured in ph/cm^2/s. The result of the modified function is shown in Figure C.12, again displaying a log-linear relationship with a further improved Pearson correlation coefficient of 0.86.

This result is clearly speculative as we have not addressed considerations such as how to include bursts in the relation which show no obvious flaring behavior or, alternatively, how to justify leaving such bursts out from the relation. A more accurate treatment of the non-flaring bursts is warranted but is left as future work.

C.5 Summary and Conclusions

We have presented the results of an investigation into whether the prompt emission characteristics of GRBs that display X-ray flares are significantly different from the prompt emission characteristics of GRBs that do not display flares. Specifically, we have examined the 1-s peak flux values in the BAT 15-350 keV energy band and the 'peakiness' of the prompt emission as measured by 2 parameters defined in this appendix; P_N, measures the amount of time the burst spends above a given flux threshold before first dropping below that threshold; E_N measures the amount of time the burst spends above a given flux threshold before dropping below that threshold for the final time (this is similar to the T_{45} parameter of the Firmani relation (Firmani et al. 2006)).

We have searched the first 27 months of *Swift* GRB data (up to GRB070330 inclusively) for evidence of flaring behavior in the X-ray afterglow lightcurves. Our final flaring sample contains 57 GRBs divided into 4 categories of increasingly significant flaring activity; Bronze FB - any burst with at least 1 3-σ deviation above the underlying X-ray afterglow; Silver FB - any burst with multiple 3-σ flares or at least 1 10-σ flare; Gold FB - any burst with multiple 10-σ flares or at least 1 30-σ flare; and Platinum FB - any burst with multiple 30-σ flares or at least 1 100-σ flare. The non-flaring sample contains 102 bursts which show no flaring activity or flaring activity below the 3-σ

level. The remaining *Swift* detected GRBs from this time period are excluded from our sample due to delayed slews (due to observing constraints), non-slews (due to observing constraints) or non-detection by the XRT after a prompt slew.

Comparing the fraction of flaring bursts that exceed a series of increasing flux thresholds to the fraction of non-flaring bursts which exceed the same thresholds, we find that a tendency exists in the observer frame for flaring GRBs to have slightly lower peak BAT prompt flux values as well as slightly longer durations, both by the P_N measure and by the E_N measure. We find, however, that neither of these trends persists after we correct for redshift using the subset of bursts in our sample that have available measured redshifts (30 in the flaring sample and 36 in the non-flaring sample). This result, together with evidence from other works suggesting that GRB flares are produced by late time central engine activity, suggests that X-ray flares, while products of central engine activity, do not have any direct observable relation to the intensity or structure of the prompt emission phase.

Finally, since the trends toward lower peak flux and longer duration seen in flaring bursts in the observer frame are removed by translating to the rest frame, a redshift bias for flaring bursts is implied. Flaring bursts tend to be observed at higher redshifts in our sample than their non-flaring counterparts. We carry this suggestion forward by investigating 3 simple relations between redshift and the characteristics of our flare sample:

$$z \propto \log \sum T_{fl_{start}} * \frac{S_{fl}}{N_{fl}}$$

$$z \propto \log \sum T^2_{fl_{start}} * \frac{S_{fl}}{N_{fl}}$$

$$z \propto \log \sum T^2_{fl_{start}} * \frac{S_{fl}}{N_{fl}} * \frac{1}{P_{BAT}}$$

We find that the lattermost relation produces a log-linear fit to the flaring sample with correlation coefficient of 0.82 with coefficients of the fit b=3.96 and m=0.86 where b is the constant of proportionality and m is the slope of the logarithmic fit. We note that in fitting these relations we have not properly included the non-flaring bursts with measured redshifts, the proper analysis of which is left for future work.

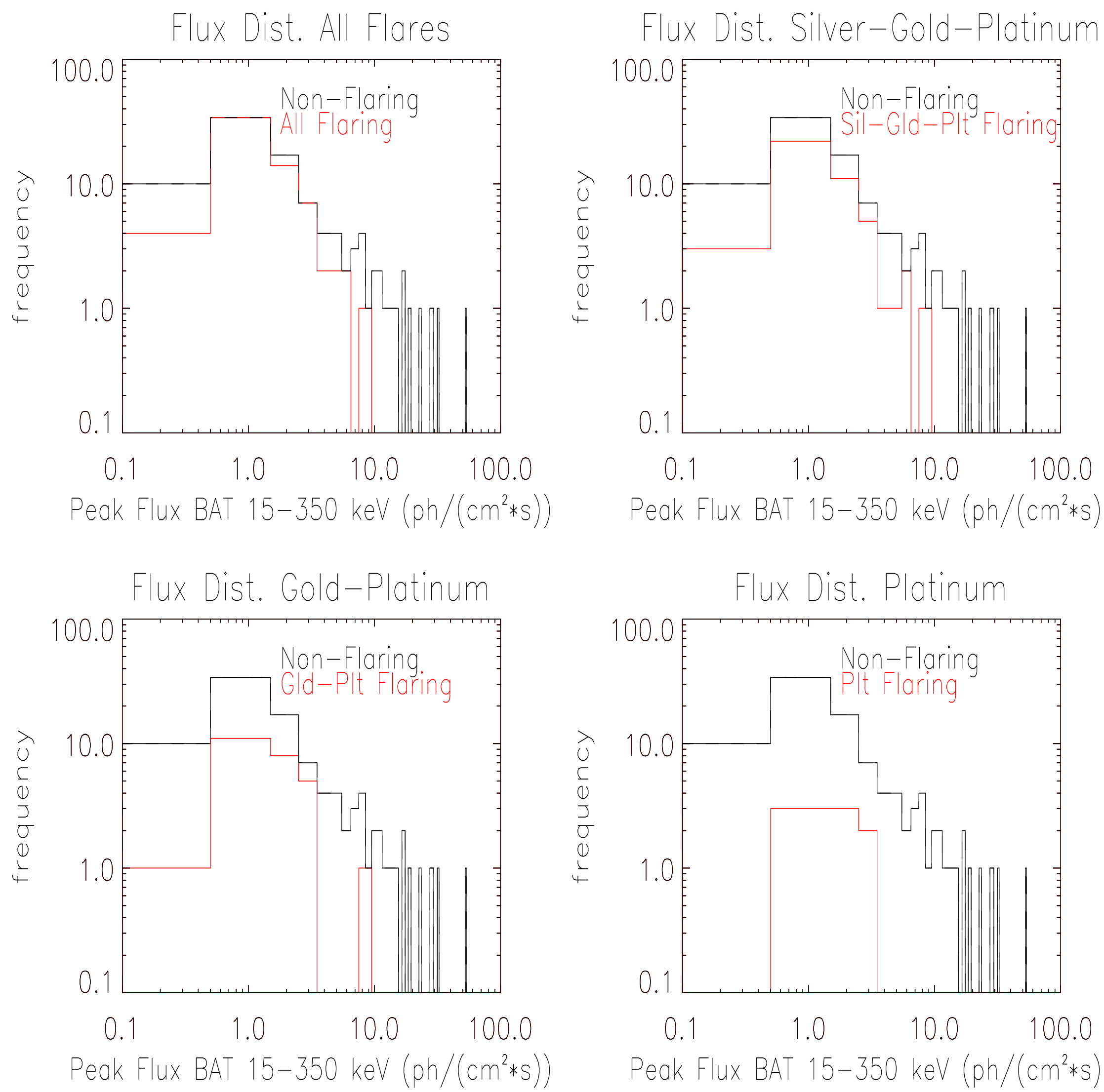

Fig. C.1 Histograms of 1-s peak flux values of the flaring burst sample (black) and the non-flaring burst sample (red) in the observer frame. The four panels correspond to increasing levels of flaring activity. The upper left panel shows to the entire flaring sample, the upper right panel shows the silver-gold-platinum sample, the lower left panel shows the gold-platinum sample and the lower right panel shows the platinum sample alone. Notice the apparent absence of the high-flux tail to the flaring distribution. Data are not corrected for redshift.

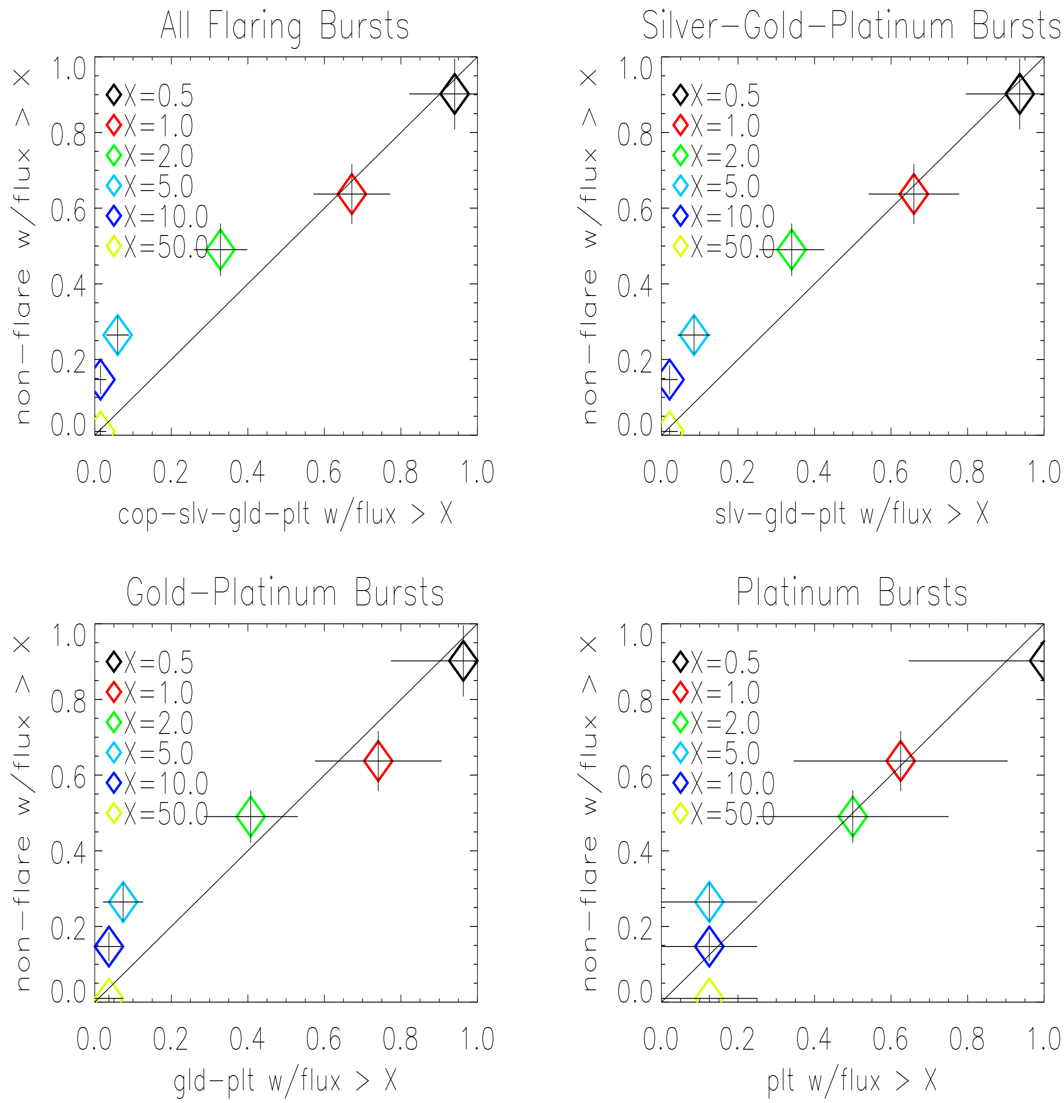

Fig. C.2 Flux-flux plot of flaring vs non-flaring burst samples. Each datapoint represents the fraction of bursts in the non-flaring sample which exceed the BAT flux threshold (in the 15-350 keV band) indicated by the color coding, versus the fraction of bursts in the flaring sample which exceed the same BAT flux threshold. Flux thresholds are measured $ph/cm^2/s$ and are not corrected for redshift. The four panels correspond to increasing levels of flaring activity. The upper left panel shows to the entire flaring sample, the upper right panel shows the silver-gold-platinum sample, the lower left panel shows the gold-platinum sample and the lower right panel shows the platinum sample alone. Notice the excess of non-flaring bursts above threshold values of 2, 5 and 10 $ph/cm^2/s$, particularly visible in the first 3 panels. The lack of such a noticeable trend in the 4th panel is likely due to the smaller number of bursts in the platinum sample alone.

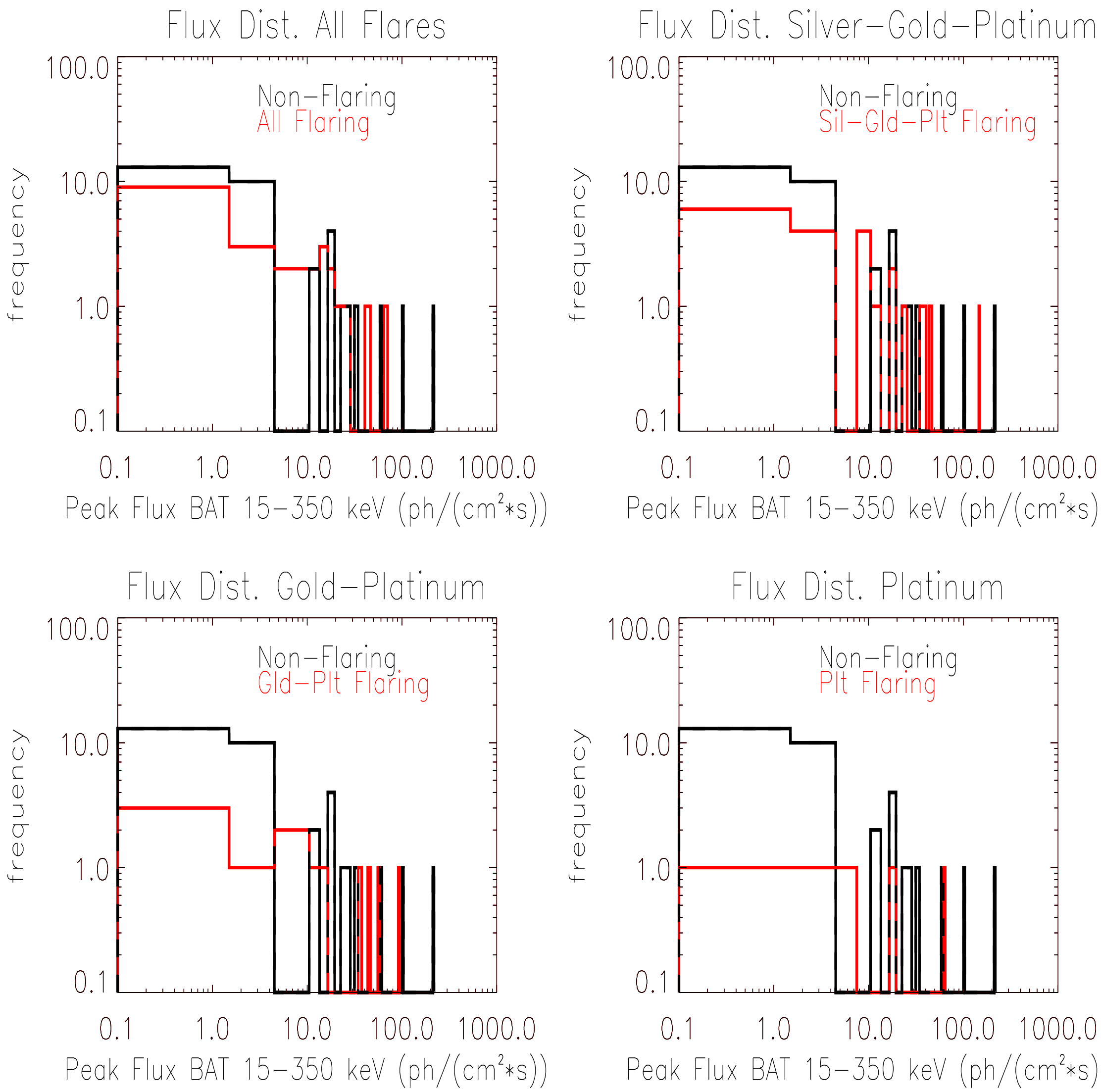

Fig. C.3 Histograms of 1-s peak flux values of the flaring burst sample (black) and the non-flaring burst sample (red) in the rest frame. The four panels correspond to increasing levels of flaring activity. The upper left panel shows to the entire flaring sample, the upper right panel shows the silver-gold-platinum sample, the lower left panel shows the gold-platinum sample and the lower right panel shows the platinum sample alone. Notice that the high-flux tail of the flaring distribution is much more well populated in the redshift corrected analysis.

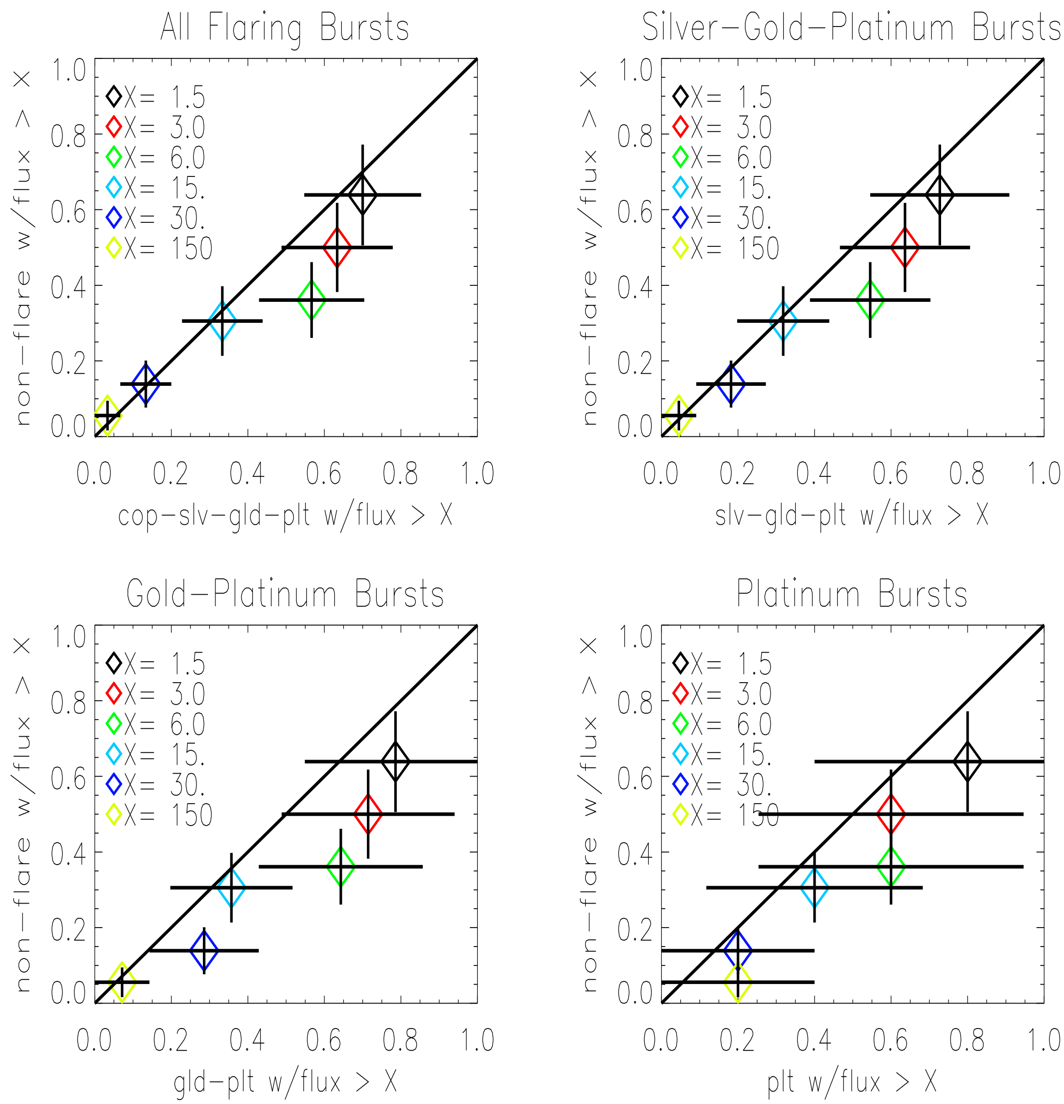

Fig. C.4 Flux-flux plot of flaring vs non-flaring burst samples. Each datapoint represents the fraction of bursts in the non-flaring sample which exceed the BAT flux threshold (in the 15-350 keV band) indicated by the color coding, versus the fraction of bursts in the flaring sample which exceed the same BAT flux threshold. Flux thresholds are measured $ph/cm^2/s$ and are corrected for redshift. The flux thresholds have been scaled up by a factor of 3 to correspond roughly to the flux amplification due to the redshift correction. The four panels correspond to increasing levels of flaring activity. The upper left panel shows to the entire flaring sample, the upper right panel shows the silver-gold-platinum sample, the lower left panel shows the gold-platinum sample and the lower right panel shows the platinum sample alone. Notice that nearly all data points lie on the line of equality here, unlike in the observer frame version of this figure where clear deviations are present.

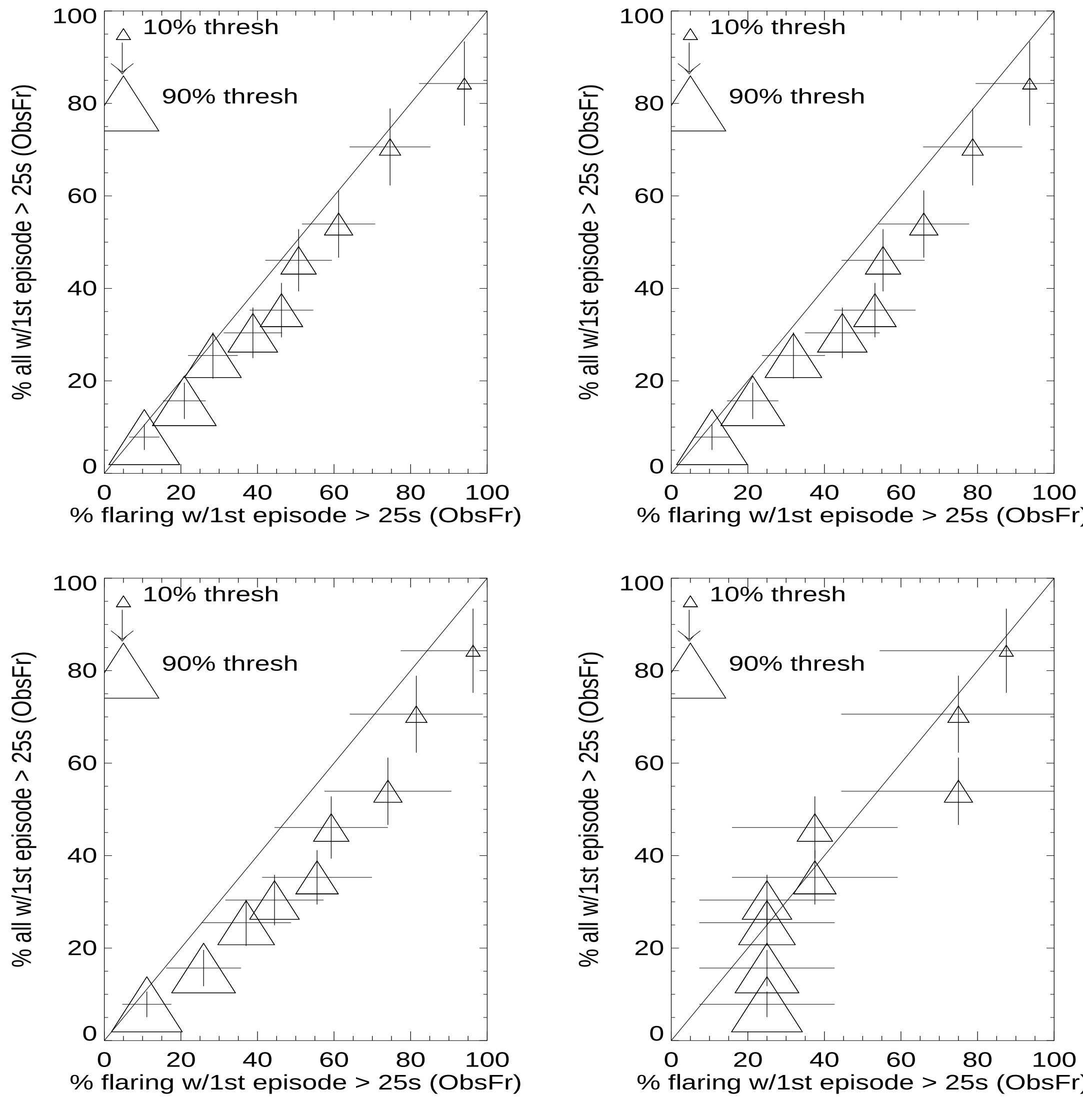

Fig. C.5 E_N for 25s duration. The datapoints represent the fraction of bursts in each sample (non-flaring versus flaring) for which progressively higher flux threshold values are exceeded for a duration of 25s in the observer frame before the BAT flux drops below the given threshold value for the last time. The smallest datapoint represents the 10% threshold level and each progressively larger datapoint represents an increase in threshold level of 10% up to the largest datapoint which represents the 90% threshold level. The four panels correspond to increasing levels of flaring activity. The upper left panel shows to the entire flaring sample, the upper right panel shows the silver-gold-platinum sample, the lower left panel shows the gold-platinum sample and the lower right panel shows the platinum sample alone. There is the suggestion of a trend for flaring bursts to be slightly elongated compared to non-flaring bursts though most datapoints lie within approximately 1-σ of the line of equality, meaning that the trend is weak.

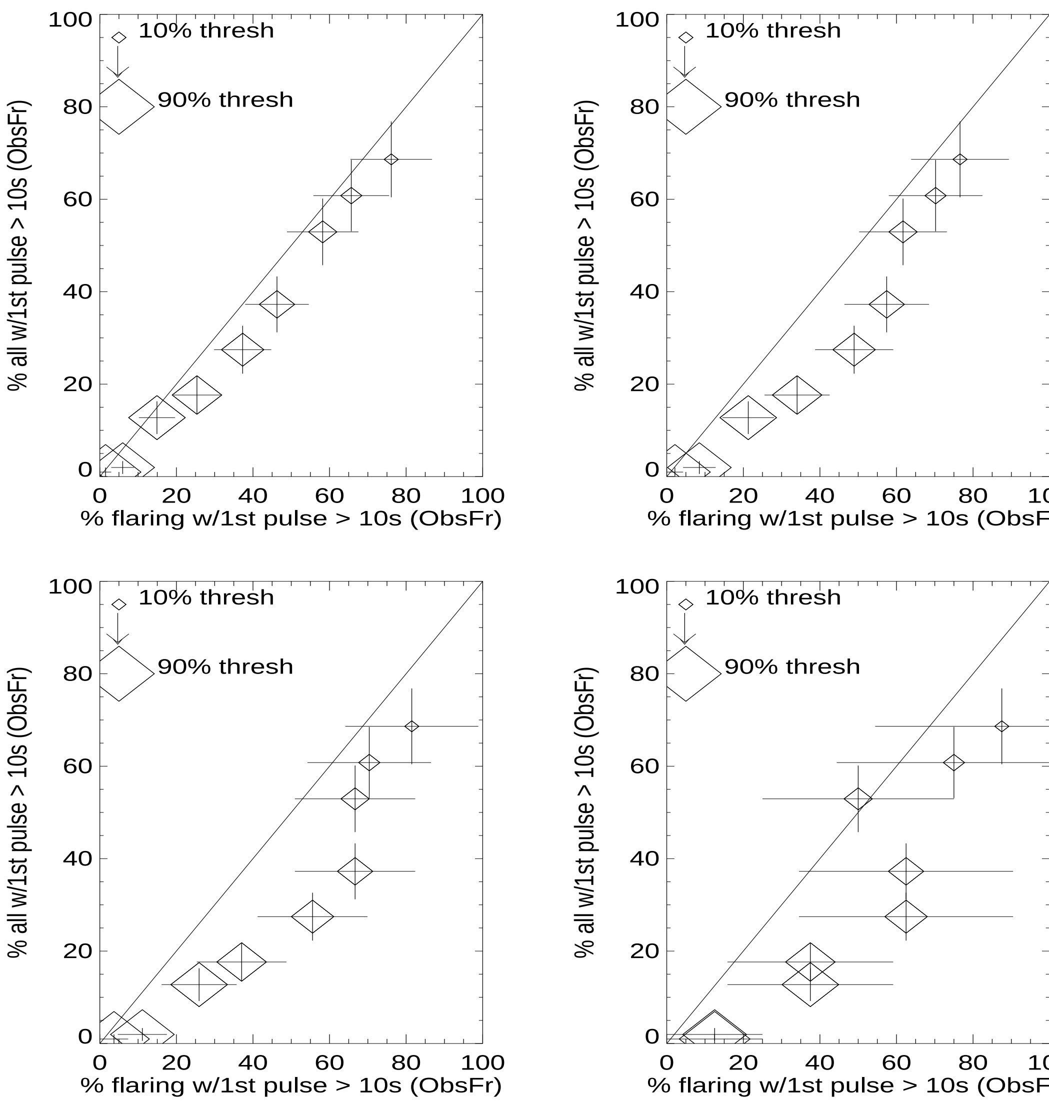

Fig. C.6 P_N for 10s duration. The datapoints represent the fraction of bursts in each sample (non-flaring versus flaring) for which progressively higher flux threshold values are exceeded for a duration of 10s in the observer frame before the BAT flux drops below the given threshold value for the first time. The smallest datapoint represents the 10% threshold level and each progressively larger datapoint represents an increase in threshold level of 10% up to the largest datapoint which represents the 90% threshold level. The four panels correspond to increasing levels of flaring activity. The upper left panel shows to the entire flaring sample, the upper right panel shows the silver-gold-platinum sample, the lower left panel shows the gold-platinum sample and the lower right panel shows the platinum sample alone. There is a trend for the 'first pulse' of flaring bursts to be slightly elongated compared to non-flaring bursts.

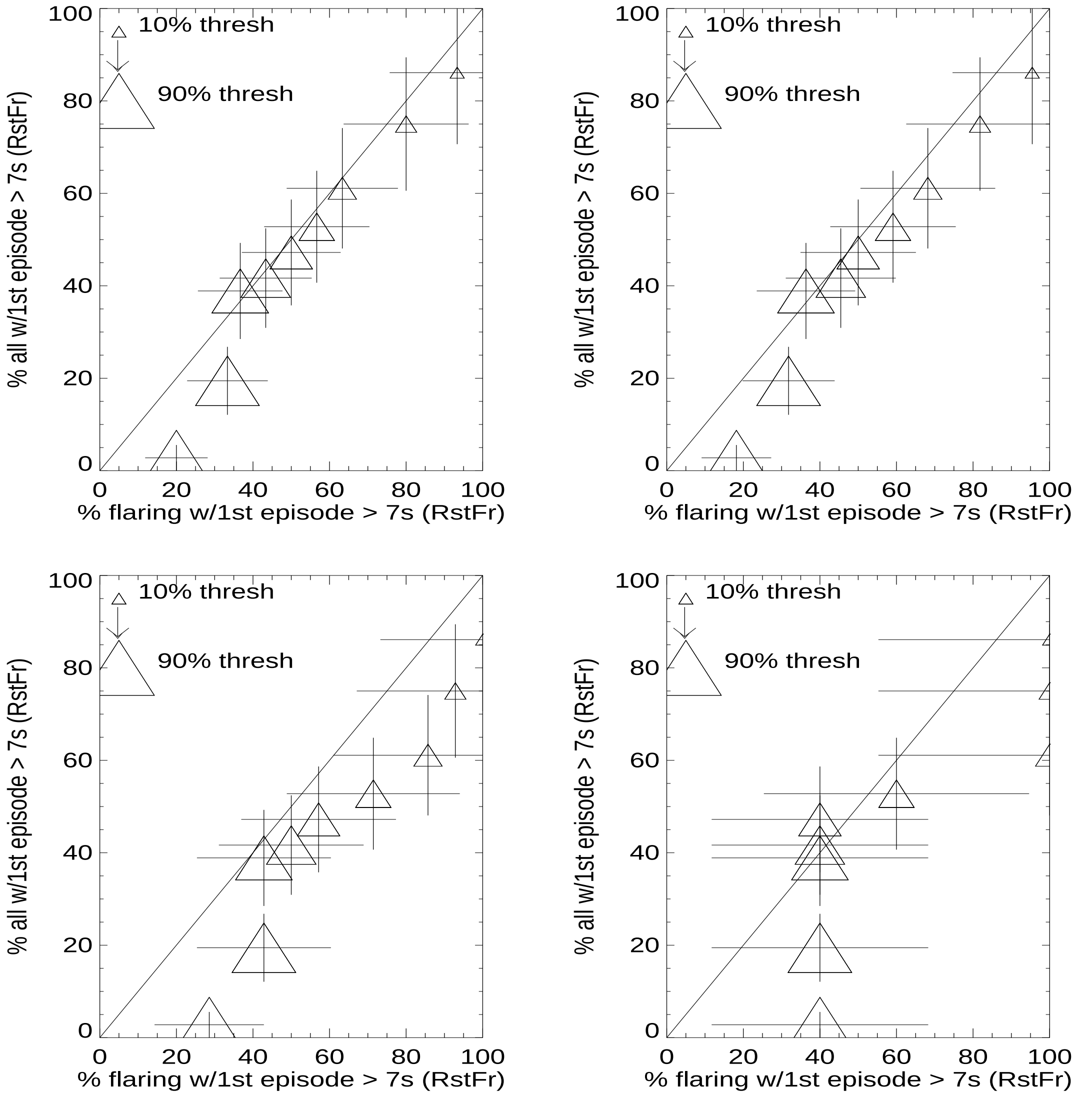

Fig. C.7 E_N for 7s duration, redshift corrected. The datapoints represent the fraction of bursts in each sample (non-flaring versus flaring) for which progressively higher flux threshold values are exceeded for a duration of 7s in the rest frame before the BAT flux drops below the given threshold value for the last time. The smallest datapoint represents the 10% threshold level and each progressively larger datapoint represents an increase in threshold level of 10% up to the largest datapoint which represents the 90% threshold level. The four panels correspond to increasing levels of flaring activity. The upper left panel shows to the entire flaring sample, the upper right panel shows the silver-gold-platinum sample, the lower left panel shows the gold-platinum sample and the lower right panel shows the platinum sample alone. There appears to be no noticeable trend in the data as all datapoints are consistent with the line of equality except for the 80% and 90% threshold datapoints. The significance of these datapoints is still under investigation.

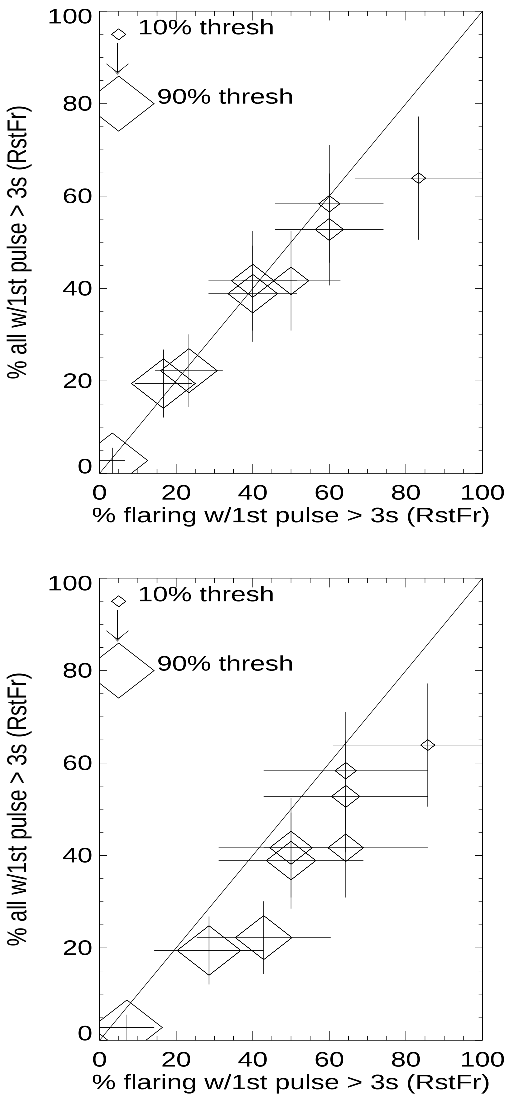

Fig. C.8 P_N for 3s duration, redshift corrected. The datapoints represent the fraction of bursts in each sample (non-flaring versus flaring) for which progressively higher flux threshold values are exceeded for a duration of 3s in the rest frame before the BAT flux drops below the given threshold value for the first time. The smallest datapoint represents the 10% threshold level and each progressively larger datapoint represents an increase in threshold level of 10% up to the largest datapoint which represents the 90% threshold level. The four panels correspond to increasing levels of flaring activity. The upper left panel shows to the entire flaring sample, the upper right panel shows the silver-gold-platinum sample, the lower left panel shows the gold-platinum sample and the lower right panel shows the platinum sample alone. There is no apparent trend in the data, contrary to the observer frame version of this figure, suggesting that the observer frame effect is a product of redshift bias.

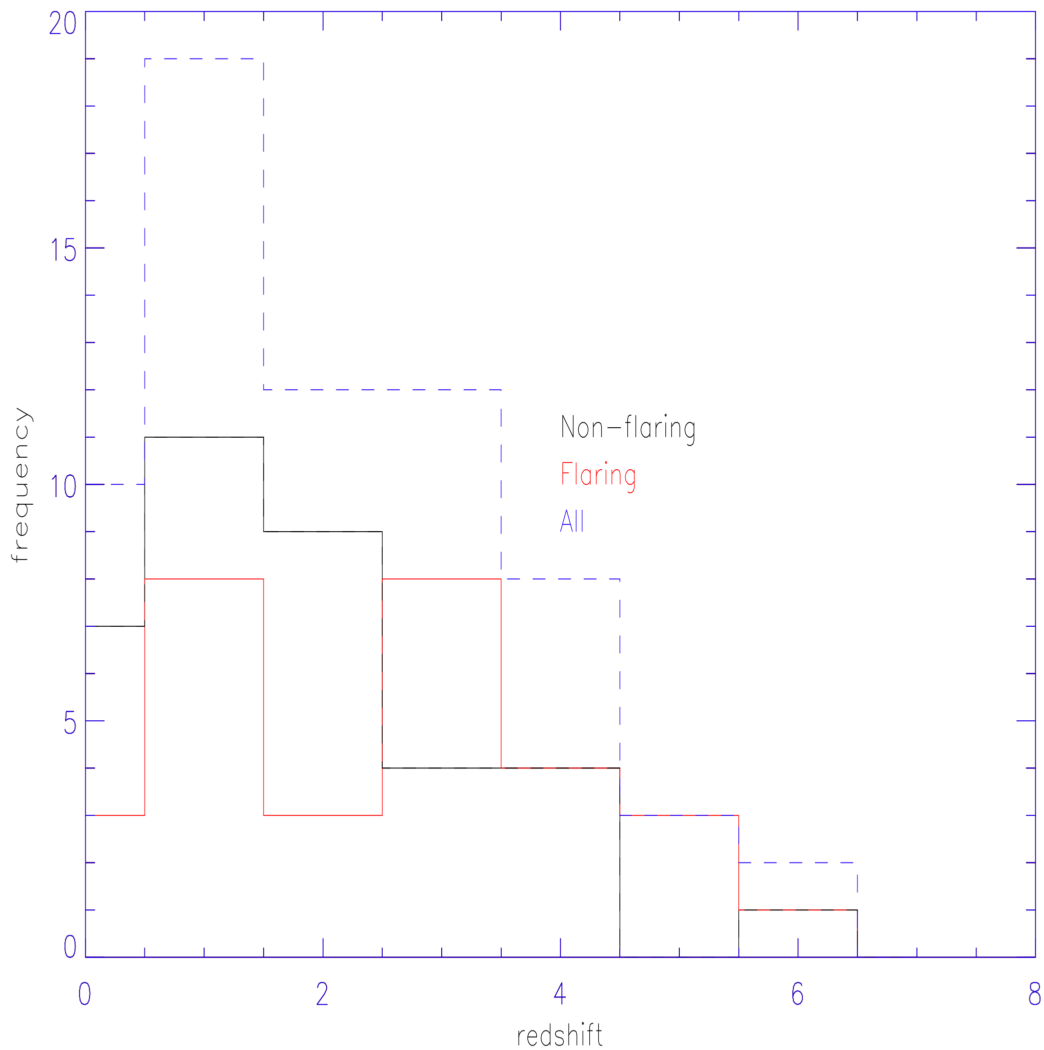

Fig. C.9 Flaring versus non-flaring redshift histogram. The redshift values for the 30 flaring bursts (red) and 36 non-flaring (black) bursts in our sample are shown. The overall sample superposition is shown as the blue dashed line. Both the flaring and non-flaring distributions have a peak at z∼1.0 but the flaring bursts also show a secondary peak in the distribution (or possibly an extended tail) at higher redshifts of 3 and above. The mean of the overall distribution is z=2.1 while the mean of the flaring distribution is z=2.6 and the mean of the non-flaring distribution is z=1.7. The K-S test suggests that the flaring and non-flaring redshift samples are drawn from separate distributions at 97.3% probability.

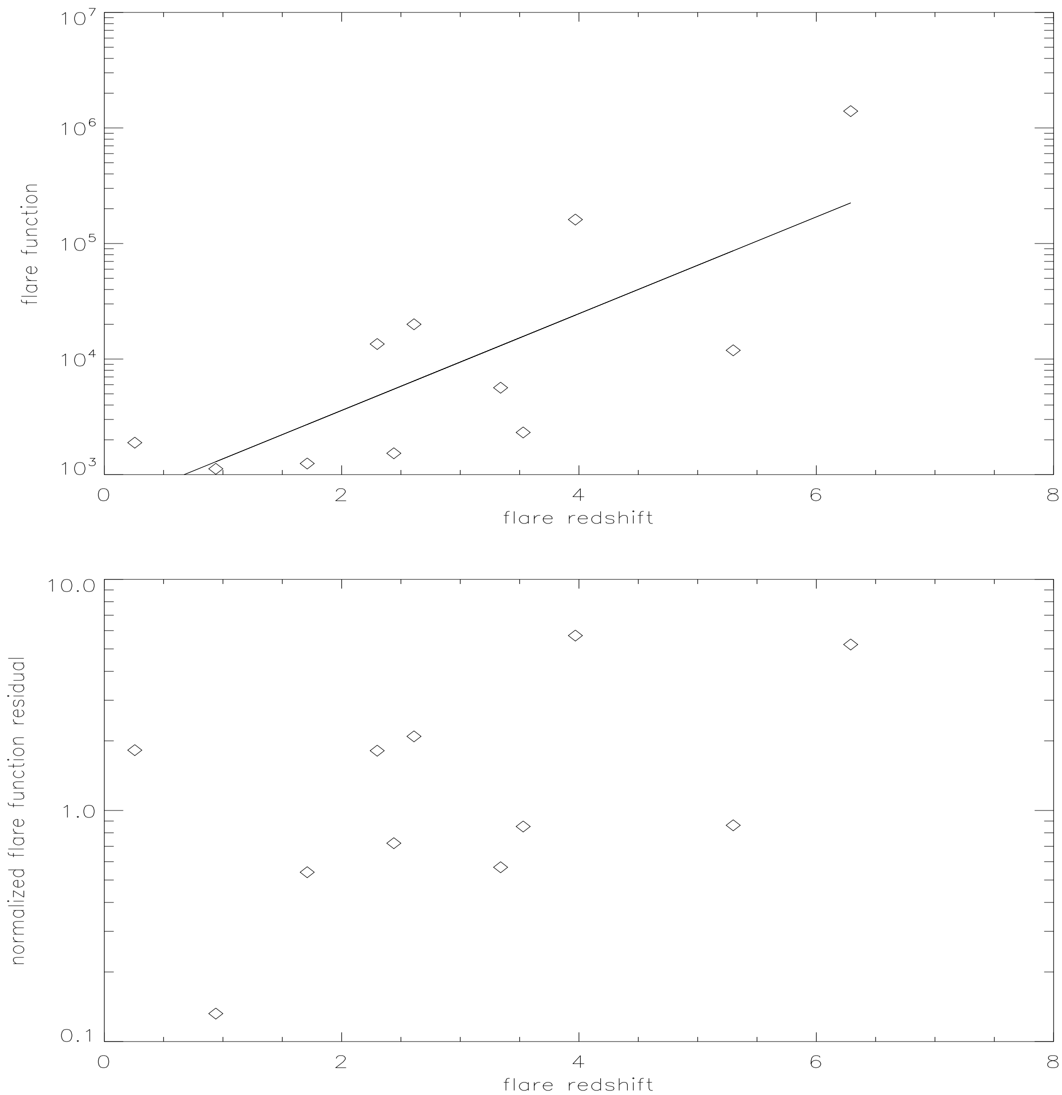

Fig. C.10 Flare-Redshift relation 1. $z \propto \log \sum T_{fl_{start}} * \frac{S_{fl}}{N_{fl}}$

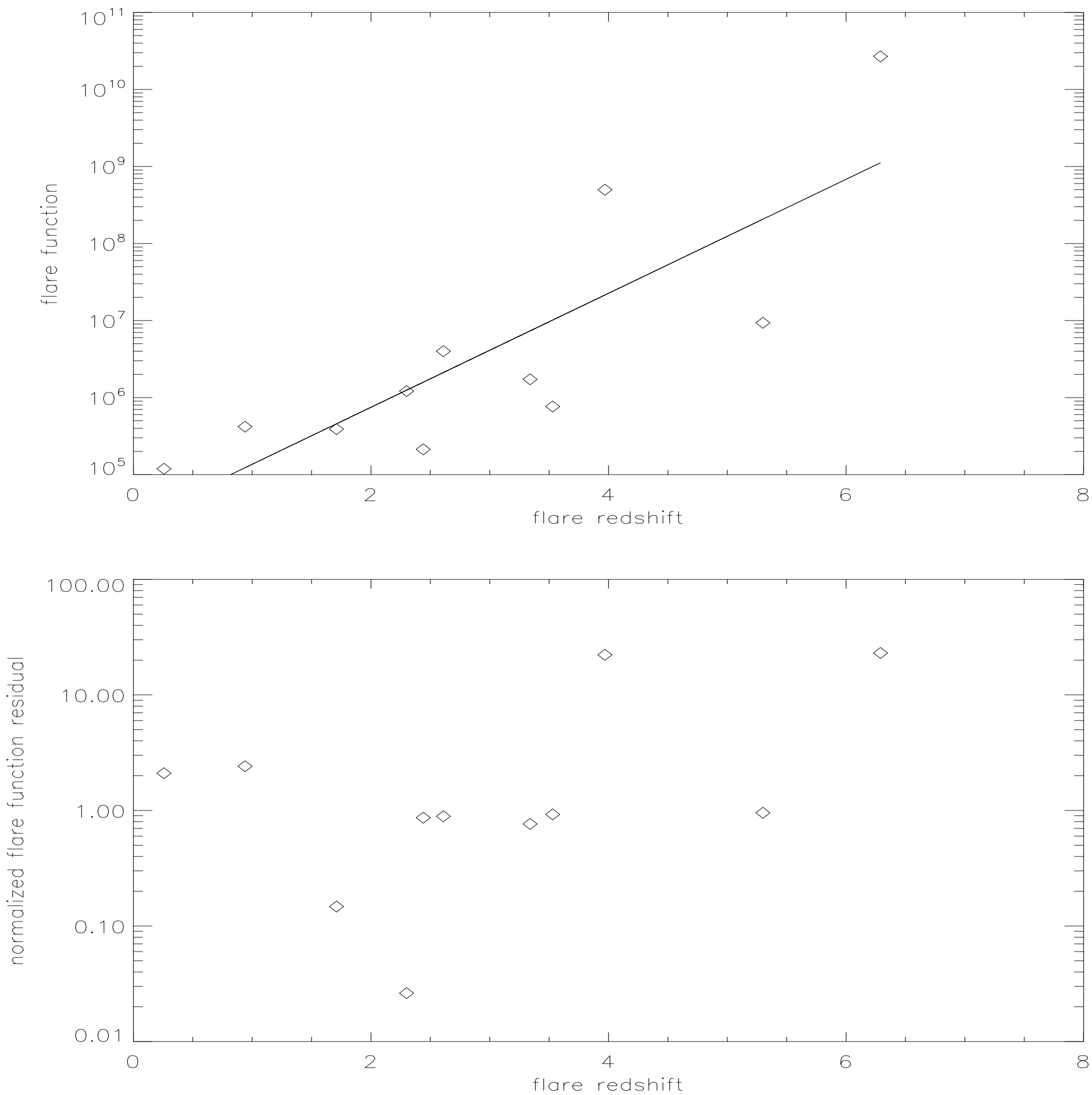

Fig. C.11 Flare-Redshift relation 2. $z \propto \log \sum T^2_{fl_{start}} .* \frac{S_{fl}}{N_{fl}}$

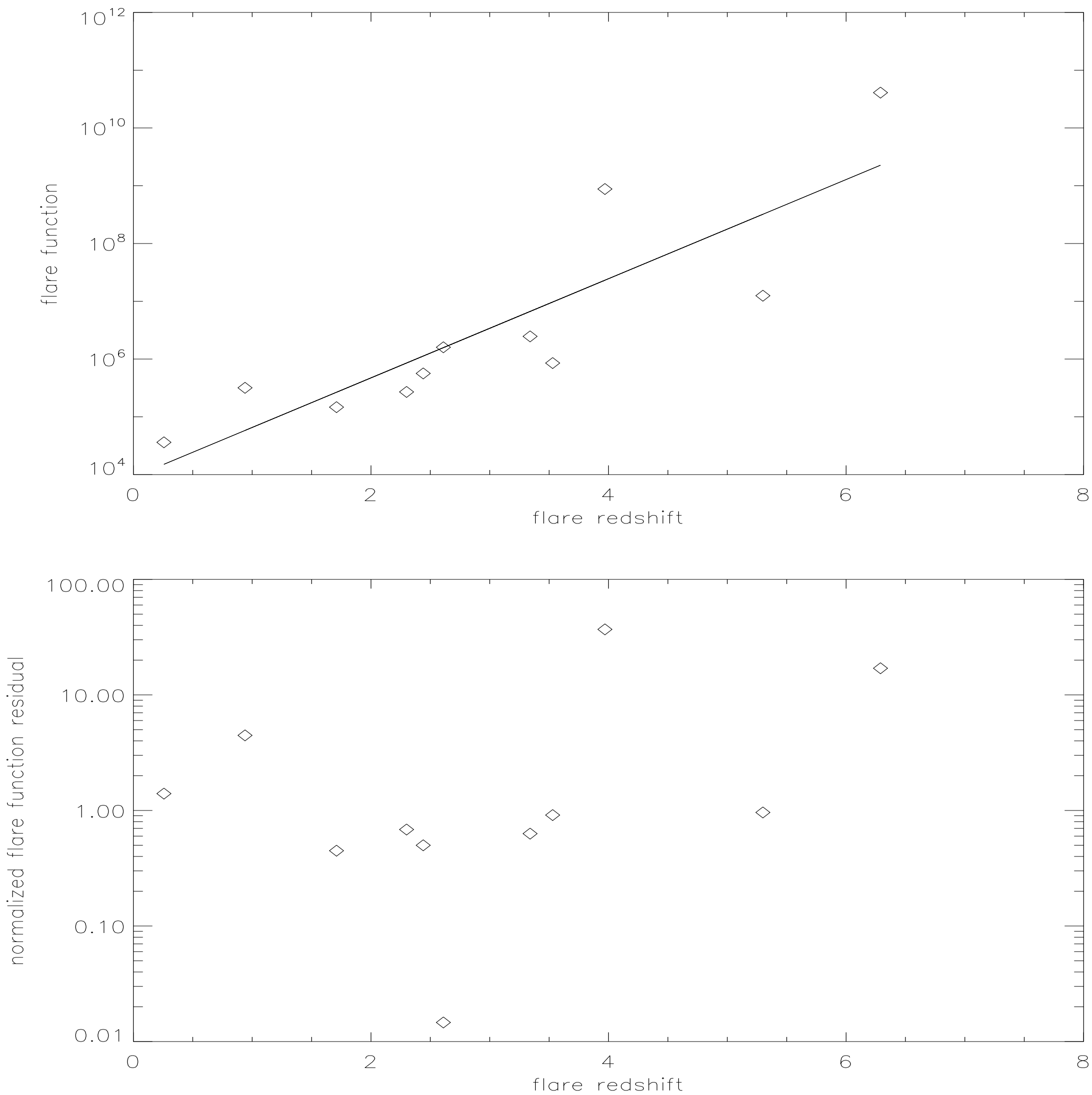

Fig. C.12 Flare-Redshift relation 3. $z \propto \log \sum T_{fl_{start}}^2 .* \frac{S_{fl}}{N_{fl}} * \frac{1}{P_{BAT}}$

Bibliography

Albert, J., Aliu, E., Anderhub, H., Antoranz, P., Armada, A., Asensio, M., Baixeras, C., Barrio, J. A., Bartelt, M., Bartko, H., Bastieri, D., Bavikadi, R., Bednarek, W., Berger, K., Bigongiari, C., Biland, A., Bisesi, E., Bock, R. K., Bretz, T., Britvitch, I., Camara, M., Chilingarian, A., Ciprini, S., Coarasa, J. A., Commichau, S., Contreras, J. L., Cortina, J., Curtef, V., Danielyan, V., Dazzi, F., De Angelis, A., de los Reyes, R., De Lotto, B., Domingo-Santamaría, E., Dorner, D., Doro, M., Errando, M., Fagiolini, M., Ferenc, D., Fernández, E., Firpo, R., Flix, J., Fonseca, M. V., Font, L., Galante, N., Garczarczyk, M., Gaug, M., Giller, M., Goebel, F., Hakobyan, D., Hayashida, M., Hengstebeck, T., Höhne, D., Hose, J., Jacoń, P., Kalekin, O., Kranich, D., Laille, A., Lenisa, T., Liebing, P., Lindfors, E., Longo, F., López, J., López, M., Lorenz, E., Lucarelli, F., Majumdar, P., Maneva, G., Mannheim, K., Mariotti, M., Martínez, M., Mase, K., Mazin, D., Meucci, M., Meyer, M., Miranda, J. M., Mirzoyan, R., Mizobuchi, S., Moralejo, A., Nilsson, K., Oña-Wilhelmi, E., Orduña, R., Otte, N., Oya, I., Paneque, D., Paoletti, R., Pasanen, M., Pascoli, D., Pauss, F., Pavel, N., Pegna, R., Persic, M., Peruzzo, L., Piccioli, A., Prandini, E., Rhode, W., Rico, J., Riegel, B., Rissi, M., Robert, A., Rügamer, S., Saggion, A., Sánchez, A., Sartori, P., Scalzotto, V., Schmitt, R., Schweizer, T., Shayduk, M., Shinozaki, K., Shore, S., Sidro, N., Sillanpää, A., Sobczyńska, D., Stamerra, A., Stark, L. S., Takalo, L., Temnikov, P., Tescaro, D., Teshima, M., Tonello, N., Torres, A., Torres, D. F., Turini, N., Vankov, H., Vardanyan, A., Vitale, V., Wagner, R. M., Wibig, T., Wittek, W., & Zapatero, J.

2006, ApJL, 641, L9

Amati, L. 2006, MNRAS, 372, 233

Aptekar, R. L., Frederiks, D. D., Golenetskii, S. V., Ilynskii, V. N., Mazets, E. P., Panov, V. N., Sokolova, Z. J., Terekhov, M. M., Sheshin, L. O., Cline, T. L., & Stilwell, D. E. 1995, Space Science Reviews, 71, 265

Band, D., Matteson, J., Ford, L., Schaefer, B., Palmer, D., Teegarden, B., Cline, T., Briggs, M., Paciesas, W., Pendleton, G., Fishman, G., Kouveliotou, C., Meegan, C., Wilson, R., & Lestrade, P. 1993, ApJ, 413, 281

Barthelmy, S. D., Barbier, L. M., Cummings, J. R., Fenimore, E. E., Gehrels, N., Hullinger, D., Krimm, H. A., Markwardt, C. B., Palmer, D. M., Parsons, A., Sato, G., Suzuki, M., Takahashi, T., Tashiro, M., & Tueller, J. 2005a, Space Science Reviews, 120, 143

Barthelmy, S. D., Chincarini, G., Burrows, D. N., Gehrels, N., Covino, S., Moretti, A., Romano, P., O'Brien, P. T., Sarazin, C. L., Kouveliotou, C., Goad, M., Vaughan, S., Tagliaferri, G., Zhang, B., Antonelli, L. A., Campana, S., Cummings, J. R., D'Avanzo, P., Davies, M. B., Giommi, P., Grupe, D., Kaneko, Y., Kennea, J. A., King, A., Kobayashi, S., Melandri, A., Meszaros, P., Nousek, J. A., Patel, S., Sakamoto, T., & Wijers, R. A. M. J. 2005b, Nature, 438, 994

Berger, E., Sari, R., Frail, D. A., Kulkarni, S. R., Bertoldi, F., Peck, A. B., Menten, K. M., Shepherd, D. S., Moriarty-Schieven, G. H., Pooley, G., Bloom, J. S., Diercks, A., Galama, T. J., & Hurley, K. 2000, ApJ, 545, 56

Bloom, J. S., Djorgovski, S. G., & Kulkarni, S. R. 2001a, ApJ, 554, 678

Bloom, J. S., Frail, D. A., & Sari, R. 2001b, AJ, 121, 2879

Boella, G., Butler, R. C., Perola, G. C., Piro, L., Scarsi, L., & Bleeker, J. A. M. 1997, A&AS, 122, 299

Borgonovo, L. & Ryde, F. 2001, ApJ, 548, 770

Burrows, D. N., Falcone, A., Chincarini, G., Morris, D., Romano, P., Hill, J. E., Godet, O., Moretti, A., Krimm, H., Osborne, J. P., Racusin, J., Mangano, V., Page, K., Perri, M., & Stroh, M. 2007, ArXiv Astrophysics e-prints

Burrows, D. N., Hill, J. E., Nousek, J. A., Kennea, J. A., Wells, A., Osborne, J. P., Abbey, A. F., Beardmore, A., Mukerjee, K., Short, A. D. T., Chincarini, G., Campana, S., Citterio, O., Moretti, A., Pagani, C., Tagliaferri, G., Giommi, P., Capalbi, M., Tamburelli, F., Angelini, L., Cusumano, G., Bräuninger, H. W., Burkert, W., & Hartner, G. D. 2005a, Space Science Reviews, 120, 165

Burrows, D. N., Romano, P., Falcone, A., Kobayashi, S., Zhang, B., Moretti, A., O'Brien, P. T., Goad, M. R., Campana, S., Page, K. L., Angelini, L., Barthelmy, S., Beardmore, A. P., Capalbi, M., Chincarini, G., Cummings, J., Cusumano, G., Fox, D., Giommi, P., Hill, J. E., Kennea, J. A., Krimm, H., Mangano, V., Marshall, F., Mészáros, P., Morris, D. C., Nousek, J. A., Osborne, J. P., Pagani, C., Perri, M., Tagliaferri, G., Wells, A. A., Woosley, S., & Gehrels, N. 2005b, Science, 309, 1833

Burrows, D. N. & The XRT Team. 2006, in American Institute of Physics Conference Series, Vol. 836, Gamma-Ray Bursts in the Swift Era, ed. S. S. Holt, N. Gehrels, & J. A. Nousek, 215–223

Butler, N. R. & Kocevski, D. 2007, ApJ, 663, 407

Campana, S., Lazzati, D., Ripamonti, E., Perna, R., Covino, S., Tagliaferri, G., Moretti, A., Romano, P., Cusumano, G., & Chincarini, G. 2007, ApJL, 654, L17

Campana, S., Tagliaferri, G., Lazzati, D., Chincarini, G., Covino, S., Page, K., Romano, P., Moretti, A., Cusumano, G., Mangano, V., Mineo, T., La Parola, V., Giommi, P., Perri, M., Capalbi, M., Zhang, B., Barthelmy, S., Cummings, J., Sakamoto, T., Burrows, D. N., Kennea, J. A., Nousek, J. A., Osborne, J. P., O'Brien, P. T., Godet, O., & Gehrels, N. 2006, A&A, 454, 113

Chincarini, G., Moretti, A., Romano, P., Falcone, A. D., Morris, D., Racusin, J., Campana, S., Guidorzi, C., Tagliaferri, G., Burrows, D. N., Pagani, C., Stroh, M., Grupe, D., Capalbi, M., Cusumano, G., Gehrels, N., Giommi, P., La Parola, V., Mangano, V., Mineo, T., Nousek, J. A., O'Brien, P. T., Page, K. L., Perri, M., Troja, E., Willingale, R., & Zhang, B. 2007, ArXiv Astrophysics e-prints

Costa, E., Frontera, F., Heise, J., Feroci, M., in't Zand, J., Fiore, F., Cinti, M. N., Dal Fiume, D., Nicastro, L., Orlandini, M., Palazzi, E., Rapisarda#, M., Zavattini, G., Jager, R., Parmar, A., Owens, A., Molendi, S., Cusumano, G., Maccarone, M. C., Giarrusso, S., Coletta, A., Antonelli, L. A., Giommi, P., Muller, J. M., Piro, L., & Butler, R. C. 1997, Nature, 387, 783

Cusumano, G., Mangano, V., Chincarini, G., Panaitescu, A., Burrows, D. N., La Parola, V., Sakamoto, T., Campana, S., Mineo, T., Tagliaferri, G., Angelini, L., Barthelmy, S. D., Beardmore, A. P., Boyd, P. T., Cominsky, L. R., Gronwall, C., Fenimore, E. E., Gehrels, N., Giommi, P., Goad, M., Hurley, K., Immler, S., Kennea, J. A., Mason, K. O., Marshal, F., Mészáros, P., Nousek, J. A., Osborne, J. P., Palmer, D. M., Roming, P. W. A., Wells, A., White, N. E., & Zhang, B. 2007, A&A, 462, 73

de Jager, O. C. & Stecker, F. W. 2002, ApJ, 566, 738

Dermer, C. D. 2007, ArXiv Astrophysics e-prints

Dickey, J. M. & Lockman, F. J. 1990, ARAA, 28, 215

Donato, D., Sambruna, R. M., & Gliozzi, M. 2005, A&A, 433, 1163

Falcone, A., Palmer, D., Blustin, A., Barthelmy, S., Cummings, J., Krimm, H., Burrows, D., Morris, D., Gronwall, C., Markwardt, C., Page, K., & Gehrels, N. 2005, GRB Coordinates Network, 3581, 1

Falcone, A. D., Burrows, D. N., Lazzati, D., Campana, S., Kobayashi, S., Zhang, B., Mészáros, P., Page, K. L., Kennea, J. A., Romano, P., Pagani, C., Angelini, L., Beardmore, A. P., Capalbi, M., Chincarini, G., Cusumano, G., Giommi, P., Goad, M. R., Godet, O., Grupe, D., Hill, J. E., La Parola, V., Mangano, V., Moretti, A., Nousek, J. A., O'Brien, P. T., Osborne, J. P., Perri, M., Tagliaferri, G., Wells, A. A., & Gehrels, N. 2006, ApJ, 641, 1010

Falcone, A. D., Morris, D., Racusin, J., Chincarini, G., Moretti, A., Romano, P., Burrows, D. N., Pagani, C., Stroh, M., Grupe, D., Campana, S., Covino, S., Tagliaferri, G., Willingale, R., & Gehrels, N. 2007, ApJ, 671, 1921

Fan, Y. Z. & Wei, D. M. 2005, MNRAS, 364, L42

Firmani, C., Ghisellini, G., Avila-Reese, V., & Ghirlanda, G. 2006, MNRAS, 370, 185

Fox, D. B., Frail, D. A., Price, P. A., Kulkarni, S. R., Berger, E., Piran, T., Soderberg, A. M., Cenko, S. B., Cameron, P. B., Gal-Yam, A., Kasliwal, M. M., Moon, D.-S., Harrison, F. A., Nakar, E., Schmidt, B. P., Penprase, B., Chevalier, R. A., Kumar, P., Roth, K., Watson, D., Lee, B. L., Shectman, S., Phillips, M. M., Roth, M., McCarthy, P. J., Rauch, M., Cowie, L., Peterson, B. A., Rich, J., Kawai, N., Aoki, K., Kosugi, G., Totani, T., Park, H.-S., MacFadyen, A., & Hurley, K. C. 2005, Nature, 437, 845

Frontera, F., Costa, E., dal Fiume, D., Feroci, M., Nicastro, L., Orlandini, M., Palazzi, E., & Zavattini, G. 1997, A&AS, 122, 357

Galli, A. & Piro, L. 2006, A&A, 455, 413

Gehrels, N., Chincarini, G., Giommi, P., Mason, K. O., Nousek, J. A., Wells, A. A., White, N. E., Barthelmy, S. D., Burrows, D. N., Cominsky, L. R., Hurley, K. C., Marshall, F. E., Mészáros, P., Roming, P. W. A., Angelini, L., Barbier, L. M., Belloni, T., Campana, S., Caraveo, P. A., Chester, M. M., Citterio, O., Cline, T. L., Cropper, M. S., Cummings, J. R., Dean, A. J., Feigelson, E. D., Fenimore, E. E., Frail, D. A., Fruchter, A. S., Garmire, G. P., Gendreau, K., Ghisellini, G., Greiner, J., Hill, J. E., Hunsberger, S. D., Krimm, H. A., Kulkarni, S. R., Kumar, P., Lebrun, F., Lloyd-Ronning, N. M., Markwardt, C. B., Mattson, B. J., Mushotzky, R. F., Norris, J. P., Osborne, J., Paczynski, B., Palmer, D. M., Park, H.-S., Parsons, A. M., Paul, J., Rees, M. J., Reynolds, C. S., Rhoads, J. E., Sasseen, T. P., Schaefer, B. E., Short, A. T., Smale, A. P., Smith, I. A., Stella, L., Tagliaferri, G., Takahashi, T., Tashiro, M., Townsley, L. K., Tueller, J., Turner, M. J. L., Vietri, M., Voges, W., Ward, M. J., Willingale, R., Zerbi, F. M., & Zhang, W. W. 2004, ApJ, 611, 1005

Gendre, B., Galli, A., Corsi, A., Klotz, A., Piro, L., Stratta, G., Boër, M., & Damerdji, Y. 2007, A&A, 462, 565

Ghirlanda, G., Ghisellini, G., Firmani, C., Celotti, A., & Bosnjak, Z. 2005, MNRAS, 360, L45

Godet, O., Page, K. L., Osborne, J., Zhang, B., Burrows, D. N., O'Brien, P. T., Hill, J. E., Racusin, J., Beardmore, A. P., Goad, M. R., Falcone, A., Morris, D. C., & Ziaeepour, H. 2007, A&A, 471, 385

Golenetskii, S. V., Mazets, E. P., Aptekar, R. L., & Ilinskii, V. N. 1983, Nature, 306, 451

Hill, J. E., Burrows, D. N., Nousek, J. A., Abbey, A. F., Ambrosi, R. M., Bräuninger, H. W., Burkert, W., Campana, S., Cheruvu, C., Cusumano, G., Freyberg, M. J., Hartner, G. D., Klar, R., Mangels, C., Moretti, A., Mori, K., Morris, D. C., Short, A. D. T., Tagliaferri, G., Watson, D. J., Wood, P., & Wells, A. A. 2004, in Presented at the Society of Photo-Optical Instrumentation Engineers (SPIE) Conference, Vol. 5165, X-Ray and Gamma-Ray Instrumentation for Astronomy XIII. Edited by Flanagan, Kathryn A.; Siegmund, Oswald H. W. Proceedings of the SPIE, Volume 5165, pp. 217-231 (2004)., ed. K. A. Flanagan & O. H. W. Siegmund, 217–231

Hill, J. E., Morris, D. C., Sakamoto, T., Sato, G., Burrows, D. N., Angelini, L., Pagani, C., Moretti, A., Abbey, A. F., Barthelmy, S., Beardmore, A. P., Biryukov, V. V., Campana, S., Capalbi, M., Cusumano, G., Giommi, P., Ibrahimov, M. A., Kennea, J., Kobayashi, S., Ioka, K., Markwardt, C., Mészáros, P., O'Brien, P. T., Osborne, J. P., Pozanenko, A. S., Perri, M., Rumyantsev, V. V., Schady, P., Sharapov, D. A., Tagliaferri, G., Zhang, B., Chincarini, G., Gehrels, N., Wells, A., & Nousek, J. A. 2006, ApJ, 639, 303

Hurley, K., Dingus, B. L., Mukherjee, R., Sreekumar, P., Kouveliotou, C., Meegan, C., Fishman, G. J., Band, D., Ford, L., Bertsch, D., Cline, T., Fichtel, C., Hartman, R., Hunter, S., Thompson, D. J., Kanbach, G., Mayer-Hasselwander, H., von Montigny, C., Sommer, M., Lin, Y., Nolan, P., Michelson, P., Kniffen, D., Mattox, J., Schneid, E., Boer, M., & Niel, M. 1994, Nature, 372, 652

Ioka, K., Kobayashi, S., & Zhang, B. 2005, ApJ, 631, 429

Jager, R., Mels, W. A., Brinkman, A. C., Galama, M. Y., Goulooze, H., Heise, J., Lowes, P., Muller, J. M., Naber, A., Rook, A., Schuurhof, R., Schuurmans, J. J., & Wiersma, G. 1997, A&AS, 125, 557

Jakobsson, P., Fynbo, J. P. U., Ledoux, C., Vreeswijk, P., Kann, D. A., Hjorth, J., Priddey, R. S., Tanvir, N. R., Reichart, D., Gorosabel, J., Klose, S., Watson, D., Sollerman, J., Fruchter, A. S., de Ugarte Postigo, A., Wiersema, K., Björnsson, G., Chapman, R., Thöne, C. C., Pedersen, K., & Jensen, B. L. 2006a, A&A, 460, L13

Jakobsson, P., Levan, A., Fynbo, J. P. U., Priddey, R., Hjorth, J., Tanvir, N., Watson, D., Jensen, B. L., Sollerman, J., Natarajan, P., Gorosabel, J., Castro Cerón, J. M., Pedersen, K., Pursimo, T., Árnadóttir, A. S., Castro-Tirado, A. J., Davis, C. J., Deeg, H. J., Fiuza, D. A., Mykolaitis, S., & Sousa, S. G. 2006b, A&A, 447, 897

Jensen, B. L., Fynbo, J. U., Gorosabel, J., Hjorth, J., Holland, S., Möller, P., Thomsen, B., Björnsson, G., Pedersen, H., Burud, I., Henden, A., Tanvir, N. R., Davis, C. J., Vreeswijk, P., Rol, E., Hurley, K., Cline, T., Trombka, J., McClanahan, T., Starr, R., Goldsten, J., Castro-Tirado, A. J., Greiner, J., Bailer-Jones, C. A. L., Kümmel, M., & Mundt, R. 2001, A&A, 370, 909

Kaneko, Y., Preece, R. D., Briggs, M. S., Paciesas, W. S., Meegan, C. A., & Band, D. L. 2006, ApJS, 166, 298

Kelly, B. C. 2007, ApJ, 665, 1489

King, A., O'Brien, P. T., Goad, M. R., Osborne, J., Olsson, E., & Page, K. 2005, ApJL, 630, L113

Klebesadel, R. W., Strong, I. B., & Olson, R. A. 1973, ApJL, 182, L85+

Kneiske, T. M., Bretz, T., Mannheim, K., & Hartmann, D. H. 2004, A&A, 413, 807

Kobayashi, S., Mészáros, P., & Zhang, B. 2004, ApJL, 601, L13

Kobayashi, S., Zhang, B., Mészáros, P., & Burrows, D. 2007, ApJ, 655, 391

Kocevski, D., Butler, N., & Bloom, J. S. 2007, ApJ, 667, 1024

Kocevski, D., Ryde, F., & Liang, E. 2003, ApJ, 596, 389

Kouveliotou, C., Meegan, C. A., Fishman, G. J., Bhat, N. P., Briggs, M. S., Koshut, T. M., Paciesas, W. S., & Pendleton, G. N. 1993, ApJL, 413, L101

Krimm, H. A., Granot, J., Marshall, F. E., Perri, M., Barthelmy, S. D., Burrows, D. N., Gehrels, N., Mészáros, P., & Morris, D. 2007, ApJ, 665, 554

Kulkarni, S. R., Frail, D. A., Wieringa, M. H., Ekers, R. D., Sadler, E. M., Wark, R. M., Higdon, J. L., Phinney, E. S., & Bloom, J. S. 1998, Nature, 395, 663

Kumar, P. & Panaitescu, A. 2000, ApJL, 541, L51

Lazzati, D. 2005, MNRAS, 357, 722

Lazzati, D. & Perna, R. 2002, MNRAS, 330, 383

—. 2007, MNRAS, 375, L46

Liang, E. & Zhang, B. 2006, MNRAS, 369, L37

Malesani, D., D'Avanzo, P., Palazzi, E., Israel, G. L., Chincarini, G., Stella, L., & Pedani, M. 2005, GRB Coordinates Network, 3582, 1

Meszaros, P. & Rees, M. J. 1992, MNRAS, 257, 29P

—. 1993, ApJL, 418, L59+

Mészáros, P. & Rees, M. J. 1999, MNRAS, 306, L39

Meszaros, P., Rees, M. J., & Papathanassiou, H. 1994, ApJ, 432, 181

Metzger, M. R., Djorgovski, S. G., Kulkarni, S. R., Steidel, C. C., Adelberger, K. L., Frail, D. A., Costa, E., & Frontera, F. 1997, Nature, 387, 878

Mirzoyan, R. & et al. 2005, in International Cosmic Ray Conference, Vol. 4, International Cosmic Ray Conference, 23–+

Moretti, A., Campana, S., Mineo, T., Romano, P., Abbey, A. F., Angelini, L., Beardmore, A., Burkert, W., Burrows, D. N., Capalbi, M., Chincarini, G., Citterio, O., Cusumano, G., Freyberg, M. J., Giommi, P., Goad, M. R., Godet, O., Hartner, G. D., Hill, J. E., Kennea, J., La Parola, V., Mangano, V., Morris, D., Nousek, J. A., Osborne, J., Page, K., Pagani, C., Perri, M., Tagliaferri, G., Tamburelli, F., & Wells, A. 2005, in Presented at the Society of Photo-Optical Instrumentation Engineers (SPIE) Conference, Vol. 5898, UV, X-Ray, and Gamma-Ray Space Instrumentation for Astronomy XIV. Edited by Siegmund, Oswald H. W. Proceedings of the SPIE, Volume 5898, pp. 360-368 (2005)., ed. O. H. W. Siegmund, 360–368

Morris, D. C., Reeves, J., Pal'shin, V., Garczarczyk, M., Falcone, A. D., Burrows, D. N., Krimm, H., Galante, N., Gaug, M., Golenetskii, S., Mizobuchi, S., Pagani, C., Stamerra, A., Teshima, M., Beardmore, A. P., Godet, O., & Gehrels, N. 2007, ApJ, 654, 413

Norris, J. P., Share, G. H., Messina, D. C., Dennis, B. R., Desai, U. D., Cline, T. L., Matz, S. M., & Chupp, E. L. 1986, ApJ, 301, 213

Nousek, J. A., Kouveliotou, C., Grupe, D., Page, K. L., Granot, J., Ramirez-Ruiz, E., Patel, S. K., Burrows, D. N., Mangano, V., Barthelmy, S., Beardmore, A. P., Campana, S., Capalbi, M., Chincarini, G., Cusumano, G., Falcone, A. D., Gehrels, N., Giommi, P., Goad, M. R., Godet, O., Hurkett, C. P., Kennea, J. A., Moretti, A., O'Brien, P. T., Osborne, J. P., Romano, P., Tagliaferri, G., & Wells, A. A. 2006, ApJ, 642, 389

O'Brien, P. T., Willingale, R., Osborne, J., Goad, M. R., Page, K. L., Vaughan, S., Rol, E., Beardmore, A., Godet, O., Hurkett, C. P., Wells, A., Zhang, B., Kobayashi, S., Burrows, D. N., Nousek, J. A., Kennea, J. A., Falcone, A., Grupe, D., Gehrels, N., Barthelmy, S., Cannizzo, J., Cummings, J., Hill, J. E., Krimm, H., Chincarini, G., Tagliaferri, G., Campana, S., Moretti, A., Giommi, P., Perri, M., Mangano, V., & LaParola, V. 2006, ApJ, 647, 1213

Pagani, C., Morris, D. C., Kobayashi, S., Sakamoto, T., Falcone, A. D., Moretti, A., Page, K., Burrows, D. N., Grupe, D., Retter, A., Racusin, J., Kennea, J. A., Campana, S., Romano, P., Tagliaferri, G., Hill, J. E., Angelini, L., Cusumano, G., Goad, M. R., Barthelmy, S., Chincarini, G., Wells, A., Giommi, P., Nousek, J. A., & Gehrels, N. 2006, ApJ, 645, 1315

Palmer, D., Barthelmy, S., Barbier, L., Cummings, J., Fenimore, E., Gehrels, N., Hullinger, D., Krimm, H., Markwardt, C., Nousek, J., Parsons, A., Sakamoto, T., Sato, G., Suzuki, M., Tripicco, M., & Tueller, J. 2005, GRB Coordinates Network, 3597, 1

Panaitescu, A. & Kumar, P. 2000, ApJ, 543, 66

Perna, R., Armitage, P. J., & Zhang, B. 2006, ApJL, 636, L29

Piro, L., Amati, L., Antonelli, L. A., Butler, R. C., Costa, E., Cusumano, G., Feroci, M., Frontera, F., Heise, J., in 't Zand, J. J. M., Molendi, S., Muller, J., Nicastro, L., Orlandini, M., Owens, A., Parmar, A. N., Soffitta, P., & Tavani, M. 1998, A&A, 331, L41

Piro, L., De Pasquale, M., Soffitta, P., Lazzati, D., Amati, L., Costa, E., Feroci, M., Frontera, F., Guidorzi, C., in't Zand, J. M. J., Montanari, E., & Nicastro, L. 2005, ApJ, 623, 314

Preece, R. D., Briggs, M. S., Mallozzi, R. S., Pendleton, G. N., Paciesas, W. S., & Band, D. L. 2000, ApJS, 126, 19

Primack, J. R., Bullock, J. S., & Somerville, R. S. 2005, in American Institute of Physics Conference Series, Vol. 745, High Energy Gamma-Ray Astronomy, ed. F. A. Aharonian, H. J. Völk, & D. Horns, 23–33

Proga, D. & Zhang, B. 2006, MNRAS, 370, L61

Protassov, R., van Dyk, D. A., Connors, A., Kashyap, V. L., & Siemiginowska, A. 2002, ApJ, 571, 545

Rees, M. J. & Meszaros, P. 1998, ApJL, 496, L1+

Romano, P., Moretti, A., Banat, P. L., Burrows, D. N., Campana, S., Chincarini, G., Covino, S., Malesani, D., Tagliaferri, G., Kobayashi, S., Zhang, B., Falcone, A. D., Angelini, L., Barthelmy, S., Beardmore, A. P., Capalbi, M., Cusumano, G., Giommi, P., Goad, M. R., Godet, O., Grupe, D., Hill, J. E., Kennea, J. A., La Parola, V., Mangano, V., Mészáros, P., Morris, D. C., Nousek, J. A., O'Brien, P. T., Osborne,

J. P., Parsons, A., Perri, M., Pagani, C., Page, K. L., Wells, A. A., & Gehrels, N. 2006, A&A, 450, 59

Roming, P. W. A., Schady, P., Fox, D. B., Zhang, B., Liang, E., Mason, K. O., Rol, E., Burrows, D. N., Blustin, A. J., Boyd, P. T., Brown, P., Holland, S. T., McGowan, K., Landsman, W. B., Page, K. L., Rhoads, J. E., Rosen, S. R., Vanden Berk, D., Barthelmy, S. D., Breeveld, A. A., Cucchiara, A., De Pasquale, M., Fenimore, E. E., Gehrels, N., Gronwall, C., Grupe, D., Goad, M. R., Ivanushkina, M., James, C., Kennea, J. A., Kobayashi, S., Mangano, V., Mészáros, P., Morgan, A. N., Nousek, J. A., Osborne, J. P., Palmer, D. M., Poole, T., Still, M. D., Tagliaferri, G., & Zane, S. 2006, ApJ, 652, 1416

Ryde, F. 2005a, A&A, 429, 869

—. 2005b, ApJL, 625, L95

Ryde, F. & Petrosian, V. 2002, ApJ, 578, 290

Sahu, K. C., Livio, M., Petro, L., Macchetto, F. D., van Paradijs, J., Kouveliotou, C., Fishman, G. J., Meegan, C. A., Groot, P. J., & Galama, T. 1997, Nature, 387, 476

Sakamoto, T., Barthelmy, S. D., Barbier, L., Cummings, J. R., Fenimore, E. E., Gehrels, N., Hullinger, D., Krimm, H. A., Markwardt, C. B., Palmer, D. M., Parsons, A. M., Sato, G., Stamatikos, M., Tueller, J., Ukwatta, T. N., & Zhang, B. 2007, ArXiv e-prints, 707

Sari, R., Narayan, R., & Piran, T. 1996, ApJ, 473, 204

Sari, R. & Piran, T. 1999a, ApJL, 517, L109

—. 1999b, ApJ, 520, 641

Schady, P., Mason, K. O., Page, M. J., de Pasquale, M., Morris, D. C., Romano, P., Roming, P. W. A., Immler, S., & vanden Berk, D. E. 2007, MNRAS, 377, 273

Schlegel, D. J., Finkbeiner, D. P., & Davis, M. 1998, ApJ, 500, 525

Starling, R. L. C., Vreeswijk, P. M., Ellison, S. L., Rol, E., Wiersema, K., Levan, A. J., Tanvir, N. R., Wijers, R. A. M. J., Tadhunter, C., Zaurin, J. R., Gonzalez Delgado, R. M., & Kouveliotou, C. 2005, A&A, 442, L21

Stocke, J. T. & Rector, T. A. 1997, ApJL, 489, L17+

Strong, I. B., Klebesadel, R. W., & Olson, R. A. 1974, ApJL, 188, L1+

Tagliaferri, G., Antonelli, L. A., Chincarini, G., Fernández-Soto, A., Malesani, D., Della Valle, M., D'Avanzo, P., Grazian, A., Testa, V., Campana, S., Covino, S., Fiore, F., Stella, L., Castro-Tirado, A. J., Gorosabel, J., Burrows, D. N., Capalbi, M., Cusumano, G., Conciatore, M. L., D'Elia, V., Filliatre, P., Fugazza, D., Gehrels, N., Goldoni, P., Guetta, D., Guziy, S., Held, E. V., Hurley, K., Israel, G. L., Jelínek, M., Lazzati, D., López-Echarri, A., Melandri, A., Mirabel, I. F., Moles, M., Moretti, A., Mason, K. O., Nousek, J., Osborne, J., Pellizza, L. J., Perna, R., Piranomonte, S., Piro, L., de Ugarte Postigo, A., & Romano, P. 2005, A&A, 443, L1

Thompson, C., Mészáros, P., & Rees, M. J. 2007, ApJ, 666, 1012

van Paradijs, J., Groot, P. J., Galama, T., Kouveliotou, C., Strom, R. G., Telting, J., Rutten, R. G. M., Fishman, G. J., Meegan, C. A., Pettini, M., Tanvir, N., Bloom, J., Pedersen, H., Nørdgaard-Nielsen, H. U., Linden-Vørnle, M., Melnick, J., van der Steene, G., Bremer, M., Naber, R., Heise, J., in't Zand, J., Costa, E., Feroci, M., Piro, L., Frontera, F., Zavattini, G., Nicastro, L., Palazzi, E., Bennet, K., Hanlon, L., & Parmar, A. 1997, Nature, 386, 686

Wang, X.-Y., Li, Z., & Mészáros, P. 2006, ApJL, 641, L89

Watson, D., Hjorth, J., Fynbo, J. P. U., Jakobsson, P., Foley, S., Sollerman, J., & Wijers, R. A. M. J. 2007, ApJL, 660, L101

Wren, J., Vestrand, W. T., Wozniak, P., White, R., & Evans, S. 2005, GRB Coordinates Network, 3604, 1

Wu, X. F., Dai, Z. G., Wang, X. Y., Huang, Y. F., Feng, L. L., & Lu, T. 2007, Advances in Space Research, 40, 1208

Zhang, B., Fan, Y. Z., Dyks, J., Kobayashi, S., Mészáros, P., Burrows, D. N., Nousek, J. A., & Gehrels, N. 2006, ApJ, 642, 354

Zhang, B. & Mészáros, P. 2002a, ApJ, 581, 1236

—. 2002b, ApJ, 566, 712

—. 2004, International Journal of Modern Physics A, 19, 2385

Vita
David Morris

Education

The Pennsylvania State University State College, Pennsylvania 2002–2008
Ph.D. in Astronomy & Astrophysics, expected in May 2008
Area of Specialization: Gamma-Ray Bursts

University of Massachusetts Amherst, Massachusetts 1991–1995
B.S. in Physics and Astronomy, Minor in Mathematics

Awards and Honors

Pennsylvania Space Grant Consortium Fellowship	2006-2007
Certificate for Outstanding Performace on the Swift Mission	2005
Nellie H. and Oscar L. Roberts Fellowship	2002-2003
NASA Group Award for Contributions to the Chandra X-ray Center	2001
Smithsonian Institution Certificate of Award for Special Achievement	2000

Research Experience

Doctoral Research The Pennsylvania State University 2002–2008
Thesis Advisor: Prof. David N. Burrows
Multiwavelength Studies of X-ray Flares in GRBs

Graduate Research The Pennsylvania State University 2003–2004
Research Advisor: Prof. Michael Eracleous
Study of the X-ray Baldwin Effect in Radio-Loud/Radio-Quiet Quasars

Undergraduate Research University of Massachusetts 1993–1995
Research Advisor: Prof. Michael F. Skrutskie
Infrared Variability of Stars in the Orion Nebula Cluster

Teaching Experience

Teaching Assistant The Pennsylvania State University 2002-2003
Taught and graded introductory astronomy labs.